EXPERIMENTAL STUDY OF THE GEOMETRIC CHARACTERISTICS OF BUBBLES/DROPLETS PASSING THROUGH A PORE SPACE

by

Shadi Ansari

A thesis submitted in partial fulfillment of the requirements for the degree of

Doctor of Philosophy

in

Mechanical Engineering

Department of Mechanical Engineering
University of Alberta

Abstract

The multi-phase flow motion of droplets and bubbles through porous media has been reported for different applications. The importance of the effect of the presence of emulsions on the performance of steam-assisted gravity drainage (SAGD) for oil extraction is discussed as a relevant process. SAGD models of these flow conditions have a major limitation by commonly adopting the single-phase flow assumption in their analyses. Researchers have reported the likelihood of the emulsification processes to prevail at SAGD conditions. The issue has been addressed in a limited number of works that demonstrated a modeling improvement by applying a multi-phase assumption. The pore-scale interactions of the multi-phase flow in a porous region is a complex phenomenon that needs to be studied in detail.

The difference between the mobility of the phases and the presence of interfacial forces acting on the interface lead to various flow characteristics. The development of a methodology to evaluate multi-phase flow motion and investigation of the interaction of multi-phase flow passing through pore geometries is outlined in detail. A theoretical model used to evaluate the motion of an isolated dispersed phase, a bubble, in a confined geometry showed that the pressure difference between the leading and the trailing edge describes the motion of an isolated dispersed phase and required energy to mobilized trapped phases. An indirect pressure measurement technique to calculate the pressure field of a multi-phase flow in the porous media using non-intrusive velocity measurement was introduced and discussed in detail. Using the proposed method, the effect of discontinuous phase size and the flow rate of the continuous flow on the pressure was investigated. The importance of the phase pinning phenomenon was also considered in the motion of the flow.

The developed method for measurement of the pressure of the dispersed phase was also applied to a refractive index-matched dispersed phase, a droplet, to expand its capability. Pore-

scale velocity measurements were achieved using microparticle shadow velocimetry (µ-PSV). By detailed measurement of velocity and applying theoretical relations that suit the flow field under study, the resultant pressure field was determined. The results of the velocity measurement of the continuous phase were used to determine the pressure field calculated from a simplified Navier-Stokes expression of the flow, discretized using an Eulerian approach. The pressure determined from the shape analysis technique and the velocity measurements were also compared to validate the results.

The interaction of between the dispersed phase and also the confined solid geometry was studied using the proposed method. In this part of the study, pore geometries having different surface roughness and confined shapes were considered. The results of the study showed that phase pinning intensifies as the roughness of the pore structure increases. The higher number of pinning events in the motion of a dispersed phase results in an increase in the transit time required for the flow passage. Larger bubbles also had a longer transit time through a pore structure due to higher deformation.

The interaction of the dispersed phases in a loosely packed bubbly flow was studied using different arrangements of the array and matrix of the bubble flow entering a pore geometry. Bubbles in both arrangements experience deformation as they pass through the pore structure. The bubbles decelerate before they reach the pore and accelerate as they pass through the pore throat due to the deformation of the phase. The motion of the bubble entering the pore in the matrix arrangement leads to a temporary repelling of the competing bubble from the pore. In this condition, the bubbles decelerate further as they get closer to the pore due to the competition to enter the pore geometry.

This study makes a major contribution to research on multi-phase flow through porous region by providing analytical and experimental insights on the pore scale interaction and accounting for three-phase contact line pinning. The results of the study indicated that the size of the dispersed phase, flow rate of the continuous phase and solid interface properties are the factors effecting the required transit time of the phase passage and the energy to mobilize trapped phases.

Preface

This thesis represents the original work by Shadi Ansari. All experiments and development methodology discussed in the current thesis were performed using facilities of the Applied Thermofluids Laboratory under the supervision of Prof. David S. Nobes. Some of the contents of the thesis have been published as papers and there are as following.

Chapter 2 with some modifications in the application of the current study has been published as **(J-1)** Ansari, S[1]., Sabbagh, R., Yusuf, Y., and Nobes, D. S. (2019). “The Role of Emulsions in Steam-Assisted-Gravity-Drainage (SAGD) Oil-Production Process: A Review”. *Society of Petroleum Engineers*. doi:10.2118/199347-PA

Chapter 3 with major modifications is submitted as **(J-2)** Ansari, S., and Nobes, D. S. (2021). “The effect of phase pinning on the passage of an isolated bubble passing through a pore confinement” Manuscript submitted for publication to the Journal, *Physics of fluids*.

Chapter 4 with minor modifications have been originally published as Ansari S. [2], Yusuf Y., Sabbagh R., Soltani H., Kinsale L., and Nobes D. S. (2018) “An imaging derivation of the pressure field of a multi-phase flow in a porous media using µ-SPIV”, *19th International Symposium on the Application of Laser and Imaging Techniques to Fluid Mechanics* Lisbon | Portugal July 16 – 19, 2018 and published an invited article as: **(J-3)** Ansari, S. [3], Yusuf, Y., Sabbagh, R., and Nobes,

---

[1] Contributions: Review of literature, preparation of manuscripts, generation of the figures, analysis and interpretation of data

[2] Contributions: Review of literature, design and manufacture flow channels for experiments, data collection, , analysis and interpretation of data, methodology development

[3] Contributions: Review of literature, design and manufacture flow channels for experiments, data collection, methodology development, analysis and interpretation of data

D. S. (2019). “Determining the pressure distribution of a multi-phase flow through a pore space using velocity measurement and shape analysis”. *Measurement Science and Technology*, 30(5), 054004.

Chapter 5 with some modifications will be submitted as **(J-4)** Ansari, S., and Nobes, D. S. (2020). “The effect of surface properties of a pore-scale confined geometry on the passage of a multi-phase flow”. Manuscript is prepared for submission.

Chapter 6 with some modifications has been published as **(J-5)** Ansari, S., and Nobes, D. S. (2020). “Interaction of loosely packed bubbly flow passing through a pore space.” *Journal of Visualization*. 23: 649-660.

Shadi’s contributions as the lead author in the above publications were setting up and conducting experiments, developing a methodology for processing, analyzing data, generating plots, and preparing manuscripts.

Shadi has also been involved in other research projects that are not included in the current thesis that has been published as:

Journal Papers:

J-6. Raffel, J., Ansari, S., and Nobes, D. S. (2021). “An experimental investigation of flow phenomena in a multi-stage micro Tesla valve.*”(Manuscript submitted for publication to Journal of Fluids Engineering)*

J-7. Ansari, S., Rashid, M.I., Waghmare, P.R., and Nobes, D. S. (2020). “Measurement of the flow behavior index of Newtonian and shear-thinning fluids via analysis of the flow velocity characteristics in a mini-channel.” *SN Appl. Sci.* **2,** 1787 https://doi.org/10.1007/s42452-020-03561-w

J-8. Sabbagh, R, Ansari, S., and Nobes, D. S. (2020). “An imaging approach for in-situ measurement of the refractive index of a porous medium.” *Optics and Lasers in Engineering*. 134:

Conference papers:

C-1. **Ansari, S.** and Nobes, D.S. (2019) “Effect of the pore geometry on pressure distribution within a bubble penetrating a single pore”, *13th International Symposium on Particle Image Velocimetry – ISPIV 2019*, Munich, Germany, July 22-24, 2019

C-2. Yusuf, Y., **Ansari, S.,** Sabbagh, R. and Nobes, D.S. (2019) “Pressure field calculation from streamline behavior in the flow-through adjacent rectangular orifices”, *13th International Symposium on Particle Image Velocimetry – ISPIV 2019*, Munich, Germany, July 22-24, 2019

C-3. Kamble, P., **Ansari, S.** and Nobes, D.S. (2019) “Prediction of the calcium carbonate growth rate in a vertical slot due to the effect of pressure drop”, *13th International Symposium on Particle Image Velocimetry – ISPIV 2019*, Munich, Germany, July 22-24, 2019

C-4. Yusuf Y., Kinsale L., **Ansari S.,** Sabbagh R., and Nobes D. S. (2019) “The behavior of streamlines in the flow convergence region in SAGD”, *4th Thermal And Fluids Engineering Conference,* Las Vegas, NV, USA 2019

C-5. Kinsale L., Yusuf Y., **Ansari S.,** Sabbagh R., and Nobes D. S. (2019) “A study of fines migration in the near-slot region of SAGD operations using PSV”, *4th Thermal And Fluids Engineering Conference,* Las Vegas, NV, USA 2019

C-6. **Ansari S.,** Yusuf Y., Kinsale L., Sabbagh R. and Nobes D. S. (2018) “Visualization of fines migration in the flow entering apertures through the near-wellbore porous media”, *2018 SPE Thermal Well Integrity and Design Symposium Banff* , Canada, Nov 27-29 2018

C-7. **Ansari S.,** Yusuf Y., Sabbagh R., Soltani H., Kinsale L., and Nobes D. S. (2018) "An imaging derivation of the pressure field of a multi-phase flow in a porous media using μ-SPIV*", 19th International Symposium on the Application of Laser and Imaging Techniques to Fluid Mechanics Lisbon,* Portugal July 16 – 19, 2018

C-8. **Ansari S.,** Sabbagh R., Soltani H. and Nobes D. S. (2018) "Flow visualization of a droplet penetration through a porous media in SAGD process using μPIV", 5*th International Conference on Experimental Fluid Mechanics – ICEFM 2018 Munich*, Munich, Germany, July 2-4, 2018

C-9. Soltani H., **Ansari S.,** Azadi R., Baldygin A. and Nobes D. S. (2018) "Developing quantitative information of oil droplets rising through a rectangular confinement", *5th International Conference on Experimental Fluid Mechanics – ICEFM 2018 Munich*, Munich, Germany, July 2-4, 2018

C-10. **Ansari S.,** Bayans M., Rasimarzabadi F. and Nobes D.S. (2018) "Flow visualization of the Newtonian and non-Newtonian behavior of fluids in a Tesla-diode valve", *5th International Conference on Experimental Fluid Mechanics – ICEFM 2018 Munich*, Munich, Germany, July 2-4, 2018

C-11. Yusuf Y., **Ansari S.,** Bayans M., Sabbagh R., El Hassan M. and Nobes D. S. (2018) "Study of flow convergence in rectangular slots using particle shadowgraph velocimetry", *5th International Conference on Experimental Fluid Mechanics – ICEFM 2018 Munich*, Munich, Germany, July 2-4, 2018

C-12. **Ansari, S.,** Sabbagh, R. and Nobes, D.S., (2017). "Flow visualization and pressure calculation of electrokinetically driven flows through slots in SAGD process", *67th Canadian Chemical Engineering Conference*, Edmonton, Alberta, Canada, (2017)

C-13. Sabbagh, R., **Ansari, S.,** and Nobes, D.S., (2017). "Investigation of the transport of fines in porous media using a refractive index matching technique", *67th Canadian Chemical Engineering Conference*, Edmonton, Alberta, Canada, (2017)

C-14. **Ansari, S.,** Sabbagh, R., and Nobes, D.S., (2017). "Flow visualization through slots in SAGD process and migration of particles in the presence of electric field" *Proceedings of Okanagan Fluid Dynamics Meeting*, Kelowna, (2017).

C-15. **Ansari, S.,** Sabbagh, R., Rasimarzabadi, F., Leitch, M., Waghmare, P.R., and Nobes, D.S. , (2017) " Visualization of an electro kinetic driven flow-through mini-channels in SAGD wells" *Proceedings of the 2nd Thermal and Fluid Engineering Conference and 4th International Workshop on Heat Transfer*, Las Vegas, TFEC-IWHT2017-18389, (2017).

C-16. Rasimarzabadi, F.,Ghaemi, S., **Ansari, S.,** Leitch, M., and Nobes, D.S.," Measurement of the flow field out of high aspect ratio slots" *Proceedings of the 2nd Thermal and Fluid Engineering Conference and 4th International Workshop on Heat Transfer*, Las Vegas, TFEC-IWHT2017-18390, (2017).

C-17. Rasimarzabadi, F., Leitch, M., **Ansari, S.,** and Nobes, D.S., "Flow visualization for performance measurement across sand control orifices," *SPE Latin America and Caribbean Heavy and Extra Heavy Oil Conference*, Peru, SPE-181164-MS, (2016).

To my Husband, Ali Baladi, for constantly being by my side

To my son, Liam – may you never stop learning

And to all my family and friends, who believed in me

Acknowledgments

I would like to express my sincere gratitude to my supervisor Prof. David S. Nobes for his continuous support during my study. I am so thankful for his patience, motivation, and immense knowledge. He was not only my supervisor, his guidance helped me in my research, life, and career. I could not have imagined having a better supervisor and mentor for my graduate studies.

Thanks to my lab mates and friends for their help, support, and friendship. My special thanks go to Dr. Reza Sabbagh for his help and motivation during my PhD studies. I thank my colleague and friend, Dr. Yishak A. Yusuf, who was always there for me.

Special thanks go to my loving husband, Ali Baladi, who has not only been a husband but also the greatest friend, and one to truly rely on for anything anytime. Finally, the greatest thank you to my parents and my brother for supporting me during my whole life and believing in me all along.

Thanks to the funding support for this project provided by RGL Reservoir Management Inc., the Natural Sciences and Research Council (NSERC) of Canada, the Alberta Ingenuity Fund, and the Canadian Foundation for Innovation (CFI).

Table of Contents

List of Figures

List of Tables

Nomenclature

Acronyms

EOR	Enhanced oil recovery
O/W	Oil-in-water emulsion
O/W/O	Oil-in-water-in-oil emulsion
PSD	Particle size distribution
PSV	Particle shadowgraph velocimetry
PIV	Particle image velocimetry
SAGD	Steam assisted gravity drainage
W/O	Water-in-oil emulsion
W/O/W	Water-in-oil-in-water emulsion

Greek Symbols

μ	Dynamic viscosity of the fluid, Pa.s
μ_c	Dynamic viscosity of the continuous phase, Pa.s
μ_{em}	Dynamic viscosity of the emulsion, Pa.s
μ_i	Dynamic viscosity of component *i*, Pa.s
μ_o	Dynamic viscosity of the oil, Pa.s
μ_r	Relative apparent dynamic viscosity of emulsion, Pa.s
η	Intrinsic viscosity parameter, dimensionless
θ	contact angle
κ	Permeability, m^2
ϕ	Porosity, dimensionless
α	Reservoir thermal diffusivity, m^2/s
α_L	Contact angle of the phase and the solid interface at the leading edge

Nomenclature (continues)

α_T	Contact angle of the phase and the solid interface at the trailing edge
ν	Kinematic viscosity of the oil, m^2/s
ν_r	Kinematic viscosity at the reservoir conditions, m^2/s
τ	The ratio of the viscosity of the dispersed phase to the continuous phase, dimensionless
$\Gamma(\cdot)$	Gamma function, N/A
γ_{cd}	Interfacial tension between the phases
γ_c	Interfacial tension of continuous phase
γ_d	Interfacial tension of dispersed phase
σ	Interfacial tension for two immiscible fluids, N
λ	Oil mobility, m^3.s/kg
Φ	Dispersed phase concentration, kg/m^3
Φ_m	Maximum packing concentration in an emulsion, kg/m^3
Φ^o	Dispersed phase concentration for a relative viscosity of 100, kg/m^3
ρ_0	Oil density at standard temperature and pressure, kg/m^3
ρ	Density of the fluid
$\dot{\gamma}$	Shear rate, s^{-1}
z_L	Location of contact lines

Other symbols

ΔS_o	Difference in oil saturation, initial value minus the residual saturation, N/A
ΔP	Pressure drops along the droplet, Pa
ΔP_c	Capillary pressure, Pa
$\Delta p_{d-Velocity}$	Pressure of the disperse phase calculated from the velocity, Pa
$\Delta\theta_L$	Cropping angle for leading-edge, °

Nomenclature (continues)

$\Delta\theta_L$	Cropping angle for trailing edge, °
ΔR	Variation in the calculated radius, mm
$\Delta R_{corrected}$	Corrected change in the inverse of the radii of curvature, mm
Δt	Time between sequential frames, s
Δx	Distance between the bubbles, mm
$\frac{\partial P}{\partial x}$	Pressure drop over the length of the bed, Pa/m
$\frac{\partial}{\partial \mathrm{t}}$	Partial derivative
∇	Divergence operator
A_i	Model parameter of component *i* , N/A
A	Cross-sectional area of flow, m^2
A_c	Cross-sectional area of the channel, m^2
a	Model parameter, N/A
$\mathrm{B_A}i$	Bubble label in an array arrangement, N/A
$\mathrm{B_M}i$	Bubble label in a matrix arrangement, N/A
b	Model parameter, N/A
c	Model parameter, N/A
Ca	Capillary number, dimensionless
Ca_{crit}	The capillary number below trapping of the phase, dimensionless
Co	Corey's coefficient, N/A
d	Model parameter, N/A
D	Diameter, mm
D_{eq}	Equivalent diameter, mm
g	Gravitational acceleration, m/s^2
h_f	Net pay, m

Nomenclature (continues)

h	Physical distance between any two points (x_1 and x_2), mm
k	Experimental factor, N/A
K_0	Hydration factor, N/A
$K_f(\dot{\gamma})$	Flocculation factor, N/A
κ_{rocw}	The relative permeability of oil at the water saturation, N/A
m	Dimensionless parameter (between 3 to 5), dimensionless
$N_{Re,p}$	Particle Reynolds number, dimensionless
$O(\cdot)$	The second-order approximation function
p	Model parameter, N/A
P	Pressure, Pa
q	Model parameter, N/A
Q	Volumetric flow rate, m^3/s
R_d	The radius of the dispersed phase, mm
R_b	The radius of the bubble, mm
R_L	The radius of the leading edge, mm
R_T	The radius of the trailing edge, mm
T	Temperature, ˚C
T_r	Reservoir temperature, ˚C
T_s	Steam temperature, ˚C
t	Time, s
t_p	Transit time, s
u	The velocity in x-direction, mm/s
U	Characteristic velocity, m/s
$\bar{U}$	The average flow velocity in the constructed channel, mm/s

Nomenclature (continues)

U_t	Terminal velocity, mm/s
U_c	Centroid velocities, mm/s
V_f	The volume fraction, N/A
V_{f-d}	The volume fraction of dispersed-phase, N/A
V_d	Volume of the bubble, mm^3
V_c	Volume of the channel, mm^3
V_0	Volume of bubble inside of the channel, mm^3
X_i	Molar fraction of component i, N/A
x_c	x -location of the centroid, mm
y_c	y-location of the centroid, mm
y_L	y -location of the leading edge, mm
y_T	y-location of the trailing edge, mm
$y_{\max\_L}$	y-location of the maximum width at the upper part of the bubble, mm
y_p	y-location of the pore throat, mm
y_{Cut-L}	y-location to crop the leading edge, mm
y_{Cut-T}	y-location to crop the trailing edge, mm
y	Model parameter, N/A
y^*	Normalized y-position based on the width of the pore throat, dimensionless
y^o	Normalized y-position based on the radius of the bubble, dimensionless
w_{major}	Major width, mm
w_{minor}	Minor width, mm
w	Width of pore throat, mm

Chapter 1: Introduction

1.1 Motivation

Multi-phase flow refers to a wide range of mixtures such as suspended solid material, emulsions, bubbly flow, and slurries. The motion of these immiscible mixtures in confined geometries has been observed in many applications that include the food industry [1], macromolecular delivery [2], [3], and oil reservoirs [4], [5]. In multi-phase flows, the phases have different mobility and ultimately different pressure distributions, the main driving force in the flow. The motion of multi-phase flow can result in encapsulation or the deposition of material in different locations in the application [3], [6], phase trapping [7]–[10], and selective material motion in confined geometries [11]. The motion of these flows in the porous region in application such as steam-assisted gravity drainage process (SAGD) results in the decrease in the half of the oil production reported for the single-phase flow assumption [12]. A better understanding of the motion of the phases and their interaction with the surrounding fluid and solid geometry is beneficial to predict the internal motion of the encapsulated material, mobilization of the trapped phase, and effect of solid material on the motion of emulsion flows.

Several attempts have been made to study the motion of the multi-phase flows in confined geometries [13]–[17]. Research to date has tended to focus on a single bubble motion in a confining geometry having a constant cross-sectional area [13], numerical simulation of bubble flow in pore geometry [14], [15], and bulk motion of multi-phase flow in pore geometry [16], [17]. It has been reported the capillary number representing the viscosity, surface tension, and the velocity of the phases has a significant effect on the deformation and the interaction of the phase with the confined geometry [13], [14], [18]–[29] The motion of a rising bubble both stationary and flowing with constant velocity in a confined geometry has shown that for a bubble larger than a confined channel, the presence of the walls results in the reduction of the bubble rising velocity [14], [30], [31]. It could be expected that the effect of the aforementioned parameters on the motion of the phases will become more pronounced in cases of confined geometries with varying cross-sectional areas such as a pore space, where the capillary number varies due to the change in the velocity of the dispersed phase.

Studies on the bulk motion of multi-phase flows passing through a pore space indicate that more resistance to the motion exists due to an excessive pressure drop introduced by the motion of the phases [21], [32], [33]. An increase in the pressure drop compared to a single-phase flow is caused by the presence of interfacial forces between the phases. The deformation of the dispersed phase as it passes through the confining geometry will result in more resistance and ultimately higher pressure drop. Much of the current literature on the deformation of the isolated phase pays particular attention to the deformation of motion of soft matters passing through a confined geometry [7]–[10]. Several attempts have been made to study the effect of the pore geometries on the motion of soft material entering a pore [7]–[10] as a function of pressure distribution and the deformation of the dispersed phase [25], [34], [35]. It is reported that the pressure within the dispersed phase is not uniform at different locations along the pore due to the deformation of the phase as it passes through the different cross-sectional areas [27]. The relation between the shape of the dispersed phase and the pressure is discussed by the Laplace law and the Jamin effect [36]–[38] [35], [37]. [11], [39]–[41]. The experimental studies in this field have only focused on the critical pressure needed for them to enter the pore[42]–[45].

The main questions addressed in this thesis are: a) How significant is the effect of multi-phase flows on the performance of an oil recovery method such as the SAGD process? b) What is the effect of pore-scale interaction of bubble flows in pore geometry and how to develop a methodology to instantaneously track the motion of a bubble to evaluate the field parameters such as pressure distribution? c) How to extend the methodology to study the interaction of the phases in liquid-liquid systems? d) What is the effect of the pore surface properties on the motion of the dispersed phase in a confined geometry? , and finally, e) what is the interaction of the competing dispersed phase approaching a pore geometry?

1.2 Thesis scope

This thesis was prepared in a paper-based format therefore some overlap in the motivation, theory, and experimental setup can be observed. The thesis is divided into five main sections, each of which presents the results relating to one of the research questions.

In Chapter 2, the importance of the emulsification process in oil recovery methods such as SAGD process is studied. Reservoir conditions are assessed to identify whether or not the effect of the emulsion is strong enough to encourage the use of a multi-phase assumption instead of a single-phase for the modeling of the process. The effect of operating conditions on the stability of emulsions in the formation is discussed. The review also covers the nature and extent of effects from emulsions on the flow mechanics through pore spaces and other flow passages that result from the well completion and downhole tubing such as sand/flow control devices.

Chapter 3 starts with an introductory section providing a brief overview of the theory used to determine the pressure change in the dispersed phase motion in confined geometry. The experimental setup and image processing to quantify the pressure change in the bubble motion inside the round pore space are explained. The third part of this chapter describes the two methods developed in this investigation in greater detail. The results obtained from the combination of these methods and the experimental study are described in the last section by accounting for the effect of the size of the dispersed phase, the velocity of the flow field, and phase pinning.

In Chapter 4, the methodology introduced in Chapter 3 is extended to the motion of the liquid-liquid multi-phase flow. In this section, the motion of a refractive index-matched droplet is studied for different droplet sizes and flow rates. The internal velocity of the fluid within both phases has been studied using the particle image velocimetry method and the shape of the interface between the droplet and the surrounding fluid was used for the shape analysis. The results of the pressure change determined by shape analysis are also compared and validated by the pressure field obtained from the particle image velocimetry technique.

Chapter 5 discusses the effect of the shape and the roughness of the confined geometry on the motion of an isolated bubble. Different flow conditions and bubble sizes were considered for comparison of the results. The effect of the pore geometry on the pressure change, pinning of the phase and ultimately the required transit time for the bubble passage will be considered.

Chapter 6 investigates the interaction of dispersed phases passing through a simulated microscale pore geometry. This will be undertaken using image analysis techniques to track the position of the bubbles and their change in shape. Two different cases of a linear array of bubbles and a loosely packed matrix of bubbles are studied to investigate the effect of the number and the arrangement of bubbles on their entrance and exit to a single pore space. This combination of findings will provide a better understanding of the multi-phase flow interaction and the importance of the dispersed phase orientation when a loose-packed dispersed phase passing through the pore space geometries. The final chapter of this dissertation is the conclusion section. A summary of the main findings and of the main issues and suggestions which have arisen in this discussion are provided in this chapter.

Chapter 2: The Role of Emulsions in Steam Assisted Gravity Drainage (SAGD) Oil Production Process: A Review [4]

This chapter reviews more than 100 prior publications that are related to the SAGD process and SAGD modeling approaches. Based on these studies, the emulsification process is confirmed in the reservoir condition and it is suggested a strong relationship between the emulsion formation mechanisms and reservoir properties at SAGD conditions which affect thermodynamic phenomena. The chapter covers the nature and extent of effects and importance of emulsification on the flow mechanics through pore spaces and other flow passages.

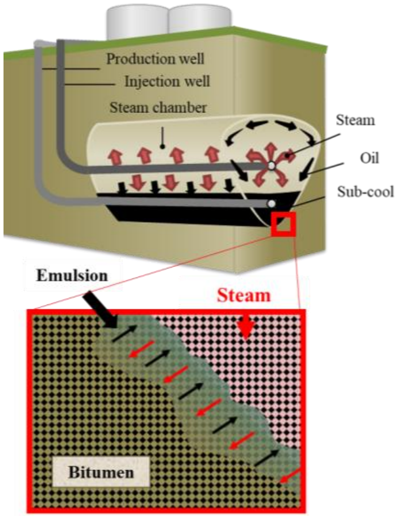

Graphical Abstract Chapter 2

2.1 Introduction

Canada has the third-largest oil reserves in the world following Venezuela and Saudi Arabia [46]. In western Canada, a large majority of this resource is composed of oil sand. Oil sand is a mixture of highly viscous bitumen with a viscosity of up to 5×10^5 cP at 20 °C [47] and sand that has a lithology and particle size distribution (PSD) that varies based on the location and depth

---

[4] This chapter with some modifications in the conclusion has been published as: Ansari, S., Sabbagh, R., Yusuf, Y., and Nobes, D. S. (2019).” The Role of Emulsions in Steam-Assisted-Gravity-Drainage (SAGD) Oil-Production Process: A Review”. *Society of Petroleum Engineers Journal.* doi:10.2118/199347-PA

of the reservoir [48], [49]. To recover immobile oil from oil sand reservoirs, enhanced oil recovery (EOR) techniques are often used to modify the flow properties of the oil [50]–[52]. The properties of the oil such as viscosity and interfacial tension can be manipulated using one of the three main EOR methods such as thermal, chemical, and/or gas injection [50]–[52] to enable a mobile oil. Steam assisted gravity drainage (SAGD) [53], is one of the more common in-situ thermal oil recovery methods that can be used to achieve an increased oil production recovery by up to 60% [52]. The highly viscous oil becomes mobile as a result of injecting the steam into the reservoir that heats the bitumen and lowers its viscosity [52], [54], [55]. The mobilization of oil is further enhanced in solvent-assisted-SAGD process [56] by the co-injection of steam and a solvent into the reservoir. Given the importance of these processes, an understanding of how the process can be modelled in an efficient manner for designing and operating a well is vital.

The main focus of this review is to highlight the approaches taken for modeling a SAGD process and the important consequences of assumptions made by researchers in the literature. As with the modeling of any physical phenomenon, assumptions used in the model’s development affect model performance. The assumption of whether to model the flow bitumen as a single-phase fluid or as a multi-phase flow (a mixture of bitumen and condensed steam) is investigated by reviewing the performance of models documented in the literature. The potential presence of multi-phase flow that is important for justifying the use of an emulsion model, is investigated by reviewing the potential emulsion formation mechanisms in the SAGD process.

2.1.1 The SAGD Process and Solvent-Assisted-SAGD Process

SAGD process was first introduced by Butler [57] in 1970 and it is most effective in reservoirs with high vertical permeability [52], [54], [55]. As a result, a standard SAGD well completion would be similar to the schematic shown in Figure 2-1. It requires the drilling of two parallel horizontal wells with a typical length of 500 to 1000 m separated by a vertical distance of 4 to 6 m [58]. The upper injection well is used for steam injection while the lower well, the producer, is used to collect the flowing bitumen. To initiate and start the process, proper communication between the two wells should be established. This communication is undertaken by circulating steam through both wells [59]. The establishment of this communication along the well is influenced by the rate of heat transfer and fluid convection into the reservoir formation. Continued steam injection after establishing the communication between the upper and lower wells develops the steam chamber [60]. This process can be either pressure-balanced or unbalanced in terms of the difference in pressure between the two wells [58]. In the underbalanced operation, where the pressure in the two wells is equal, the steam injection will result in the smallest achievable net flow of steam. The unbalanced operation, typically on the order of 100 kPa, can be used to enhance the heat convection to increase the heating of the oil in the reservoir and to shorten the start-up period [58].

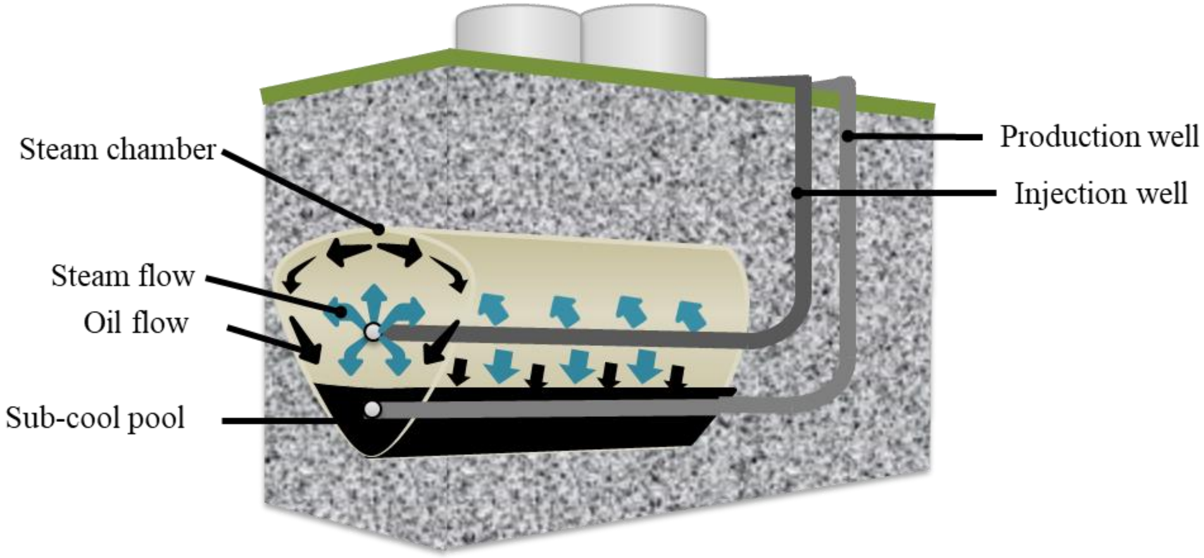

Figure 2-1. Schematic of steam-assisted gravity drainage (SAGD) oil recovery method.

Recently, solvent-steam assisted gravity drainage (solvent-SAGD) has been introduced to enhance SAGD operation which decreases the required energy for bitumen mobilization. In this operation, in addition to the injected steam, hydrocarbon solvents such as light n-alkanes and other solvents with mutual solubility in water and oleic phase are injected into the reservoir to enhance the oil recovery efficiency [56]. The interaction of the steam and the solvent with the bitumen, further reduces the viscosity of the mixture due to the heat and mass transfer between the phases Different experimental research has confirmed the enhancement of the recovery performance as a result of oil phase dilution [61]–[63]. Studies show that the steam-to-oil ratio of the process decrease by ~25-50 %. Such a decrease can be achieved with less than 5-6 % (volumetric fraction) of solvent injection [64]. Understanding the system behavior and reservoir characteristics in SAGD and the solvent-SAGD process is required to determine the mobilization process and the effect of components such as a solvent on the changes in the system performance.

2.1.2 Properties of bitumen and reservoir

The rise of the steam in the formation above the injection well results in the development of a steam-saturated zone known as the steam chamber, shown in Figure 2-1. The conditions under which the SAGD process operates are different depending on the properties of the reservoir. Some typical process conditions along with reservoir properties collected from SAGD wells in Alberta Canada are summarized in Table 2-1 [65], [66]. The pressure of the reservoir at the beginning of the process is between 1.75 MPa to 2.25 MPa [67]. After the steam injection, the pressure of the reservoir is increased to 2.5 MPa to 3 MPa. The temperature in the steam chamber also becomes the same as that of the saturated steam at the prevailing reservoir operating pressure of between 200 to 250 °C [58], [68].

Table 2-1. Typical process conditions along with SAGD reservoir properties. The lower and upper bounds are values from the resources used in this study [65], [66] and do not represent the limits. Sample values represent the most common value observed in the collected data.

Process conditions	Example value	Lower bound	Upper bound
Well Pair Length (m)	850	700	1100
Well Pair Spacing (m)	100	100	120
Depth (m)	400	120	500
Net Pay (m)	25	7	42
Porosity (%)	32	31	36
Horizontal Permeability (Darcy)	5	1.7	10
Vertical Permeability (Darcy)	4	0.9	10
Oil Saturation (%)	80	65	85
Initial Reservoir Absolute Pressure (MPa)	1.7	0.4	2.7
Initial Reservoir Temperature (°C)	12	8	20
Maximum Operating Pressure -MOP (MPa)	5.5	1.5	10.5
Chamber Temperature (°C)	230	210	250
Chamber Absolute Pressure (MPa)	2.5	1.5	4
Cumulative SOR (bbl/bbl)	3	1.7	5.2
Instantaneous SOR (bbl/bbl)	3	1.3	3.9
Recovery Factor %	40	5	62
pH	6.8-8.8	7	11

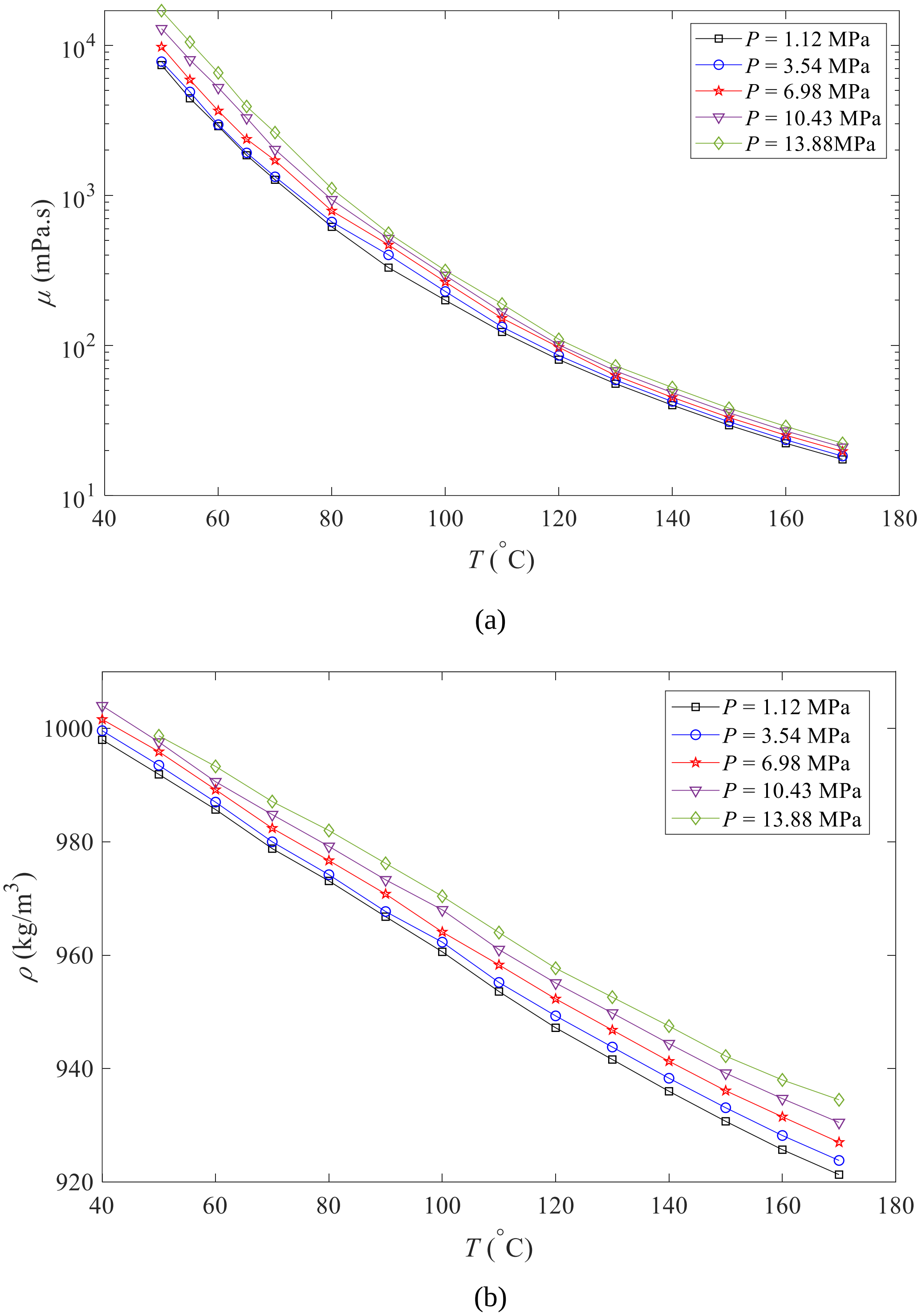

Figure 2-2. Change in the (a) viscosity and (b) density of bitumen as a function of temperature at different pressures. Data from [69].

The change in the viscosity and density of bitumen for temperature from the experimental study by [69] is plotted in Figure 2-2 (a) and (b). In the steam chamber, the heat transfer between the steam and oil leads to a significant reduction in the viscosity of the bitumen, as high as three orders of magnitude as shown in Figure 2-2 (a) [69], [70]. The density of the bitumen also decreases as the temperature increases as shown in Figure 2-2 (b) [69]. It is also seen in Figure 2-2 that increasing the chamber pressure increases both the viscosity and density of bitumen.

The exchange of heat from the steam to the bitumen results in the condensation of the steam in the chamber. The condensed steam will mix with water in the reservoir and form water droplets with different salinities, depending on the salts present in the reservoir. Major minerals observed in SAGD produced water in Alberta Canada are summarized in Table 2-2. The information in Table 2-2 was extracted from a set of data for produced water analysis obtained from different fields in Alberta Canada and the available data in the literature [65], [71]. The lower and upper bounds in the table do not necessarily belong to the same water sample and the average value represents the arithmetic average of the available data.

The interaction between the mobilized bitumen and the soluble or dissolved materials in the water may affect the flow and fines transport. The flow of mobilized fluid through the reservoir represents a complex phenomenon that depends on the reservoir properties. Thus, the study of the flow of mobilized bitumen is vital in characterizing the performance of the oil recovery process. Understanding the SAGD modeling approaches is an important step toward such a flow characterization.

Table 2-2. The concentration of major components in produced water in the SAGD process. [65], [71] units are mg/L

Components	Symbol	Average	Lower bound	Upper bound
Cations	Na	417	74	3000
	K	24	15	240
	Ca	4	1.2	52
	Mg	1	0.4	14
Anions	Cl	406	11	4800
	HCO3	335	140	2700
	SO4	161	5.1	669
Alkalinity (CaCO3)		277	120	1400
TDS (Total Dissolved Solids)		1882	690	4510

2.1.3 Modeling the SAGD Process

A review of the modeling approaches for SAGD provided in the literature allows the development of an understanding of their benefits and limitations. The approach taken here is to provide a fundamental description of the different modeling approaches in detail for comparison and evaluation. In the initial SAGD model, it is assumed that the heat transfer only occurs at the edge of the steam chamber [57] and that the temperature of the steam chamber is essentially the same as that of the injected steam. The reservoir in this model was assumed to provide a homogeneous and isotropic relative permeability to the flow of bitumen. Capillary forces in the reservoir were neglected in this initial SAGD model due to the assumption of high relative permeability available for the flow of oil compared to that of water and steam. This approach implied that the flow of mobile bitumen is the only fluid motion considered and that the presence of other phases such as steam and water was neglected. The main driving force in the steam chamber was defined as the drainage process due to the rapid reduction of the viscosity of bitumen caused by heat transfer. Details of the drainage models proposed by Butler in 1985 are discussed in [68], [72].

The development of models for the flow of mobilized bitumen within the reservoir has been based on Darcy's law [72]–[74]. Darcy's law describes the volumetric flow rate, Q through a porous bed as a linear function of an intrinsic sand property, it's permeability, κ the applied pressure drop over the length of the bed, $\frac{\partial P}{\partial x}$, the viscosity of the fluid, μ and the cross sectional area of flow, A:

$$Q = -\frac{\kappa A}{\mu}\frac{\partial P}{\partial x} \tag{2-1}$$

The combination of this equation with the heat conduction theory is what Butler [58], [75] used to give the final equation to estimate the oil production rate, Q as:

$$Q = \sqrt{\frac{2\phi \Delta S_o \kappa g \alpha h_f}{m\nu}} \tag{2-2}$$

where α is the reservoir thermal diffusivity, ϕ is the porosity of the reservoir, ΔS_o is initial oil saturation minus the residual oil saturation, h_f is the net pay, m is a dimensionless parameter (between 3 to 5) dependent on the oil viscosity-temperature relationship, g is the gravitational acceleration and ν is the kinematic viscosity of the oil. The term, net pay, refers to the height of the drainage region [76]. Following the derivation in the development of the model [75], the net pay can be broadly defined as the relative height (thickness) of the steam chamber. The parameter m is included to account for the viscosity-temperature relationship and is defined as:

$$Qm = \left[\nu \int_{T_r}^{T_s} \left(\frac{1}{\nu} - \frac{1}{\nu_r} \right) \frac{dT}{T - T_r} \right]^{-1} \tag{2-3}$$

where T is temperature and subscripts s and r represent steam and initial reservoir conditions, respectively.

In the development of Butler's model, the oil viscosity was considered to vary with temperature, which changes with relative distance between the inside and the edge of the steam chamber and is incorporated in the parameter m. The thermal conductivity of the reservoir beyond the steam chamber was assumed to remain unchanged. The steady-state temperature distribution was also assumed for locations beyond the edge of the steam chamber

Various modifications have been proposed to improve the assumptions in Butler's model. Modified versions of the model for the effect of the heterogeneity of the reservoir permeability have also been introduced by [72] and [77]. The effect of a transient temperature distribution of the steam interface on the steam chamber growth was added by [78].

In general, comparisons between the estimated oil production from Butler's model and data from field observations showed that the original model overestimates oil production rates [79]. Critical assessments of the Butler SAGD model highlights its shortcomings in capturing all the physical phenomena involved in the process [79]–[81]. Subsequent improvements to Butler's original model have suggested accounting for reservoir heterogeneity [72]., temperature variation at the edge of the steam chamber [80], and change in the position and velocity of the steam chamber interface [78], [82]

Despite the modifications, discrepancies remain between predicted rates and field results [79]. Butler's model for SAGD did not include any particular consideration for the presence of multi- phase flows such as emulsions. The model can be seen as a single-phase model where a constant temperature distribution is assumed at the edge of the steam chamber [83]. The fractional composition of the fluid flowing towards the producer also assumed the presence of only water condensate and oil droplets near the edge of the steam chamber as two immiscible continuous phases. This can be an indication of why there is a significant disagreement between the predicted results from the model and the field observations.

2.1.4 Introducing a multi-phase assumption

The models introduced so far to determine the performance of the SAGD process, only account for a single-phase flow through the reservoir [72], [77], [78], [84]–[86]. For instance, in Eq. (2-1), a single term for the permeability of the reservoir is seen but no term for relative permeability. The viscosity term in the equation is for pure bitumen instead of a multi-phase fluid. A typical production stream, however, contains micro-droplets of water suspended in the continuous phase of oil which forms an emulsion [87]. The literature also shows that sand and fines are also carried with the emulsion toward the production well. These observations conflict with the single-phase permeability and the viscosity terms included in Eq. (2-1) [88]–[94].

Investigations have shown that emulsions in SAGD are mainly produced due to capillary forces present in the steam chamber at the pore scale [88]. Heat and mass transfer between the oil and the steam in the steam chamber can also have a significant effect on the capillary forces and hence the formation of emulsions [88] and their stability. The stability of the produced emulsions in the reservoir is also a function of the crude oil characteristics and the reservoir conditions [95]–[101].

Knowing that the oil-water emulsion is an unavoidable part of the SAGD process, the presence of water droplets in the reservoir, raises two important questions. 1) Does the multi-phase flow of emulsions affect the performance of SAGD oil recovery? 2) Is it imperative for engineers and researchers to always work in the single-phase or multi-phase domain regardless of the areas they are investigating? The implications of these two questions can have significant effects on the performance of any predictive model for a SAGD process.

The validity of the single-phase assumption for the flow of bitumen in a SAGD reservoir has been studied by independent researchers [17], [70], [79]. Azom and Srinivasan (2009) [102] developed a numerical model by coupling a simulation of the reservoir and the emulsion model introduced by Taylor (1932) [103]. Taylor's emulsion model describes the variation of the viscosity of an emulsion as a function of the volume fraction of the dispersed phase and the viscosities of the dispersed and continuous phases such that:

$$\frac{\mu_{em}}{\mu} = 1 + V_f\left[2.5\left(\frac{\tau + 0.4}{\tau + 1}\right)\right] \tag{2-4}$$

where μ_{em} and μ are the viscosities of the emulsion and the continuous phase, respectively, τ is the ratio of the viscosity of the dispersed to the continuous phase, and V_f is the volume fraction of the dispersed phase. Ezeuko et. al. (2013) modified the viscosity of the emulsion in Taylor's model by considering the effect from the variation of temperature during the growth of the steam chamber. Butler's single-phase model was further numerically improved by Mojarad and Dehghanpour (2016) [70] assuming a multi-phase flow. In the modifications of Butler's model, the flow of emulsions was again described using Darcy's law, which assumes that the transport of dispersed phase of water to be the same as the continuous oil phase. In particular, the multi-phase flow was assumed to have no two-phase interaction.

Sharma and Gates (2010) considered the effect of temperature on the viscosity of bitumen to give a modified form of Butler's equation as:

$$Q = 2L\sqrt{\frac{2\alpha\kappa\kappa_{rocw} g\phi\Delta S_o h_f \Gamma(m)\Gamma(Co+1)}{\nu\Gamma(m+Co+1)}} \tag{2-5}$$

where κ_{rocw} is the relative permeability of oil at the water saturation, $\Gamma(\cdot)$ is the gamma function [104] and Co is Corey's coefficient [79], [105]. The presence of a relative permeability term in this equation shows that multi-phase phenomena are indeed accounted for. The comparison of Butler's model in Eq.(2-2) with Sharma and Gates (2010) in Eq. (2-5) gives the difference between these models to be a gamma function of only m and a [79].

2.1.5 Review objectives

The discussion so far highlights that multi-phase flow mechanics should be considered during the development of a model of the SAGD process for an improved prediction of the production rate. This strongly suggests that the emulsification phenomenon present in SAGD needs to be accounted for. There has also been evidence for the existence of emulsions in the reservoir at typical SAGD process conditions. The aim of the current study is to provide a review regarding the emulsification process strictly in relation to its influence on the SAGD process to identify and understand its potential effects on production and its modeling. The review also attempts to determine the extent to which the single-phase flow assumption for bitumen flow holds.

In the sections that follow, possible mechanisms of emulsion formation in the SAGD steam chamber reported by experimental studies and augmented by some numerical investigations are introduced. This is followed by a discussion on the stability characteristics and properties of the emulsions formed at reservoir conditions. The effect of multi-phase flow through porous media on reservoir properties such as effective permeability on the oil mobility is reviewed. Comparing the single- and multi-phase assumption consequences, the importance of multi-phase flow assumption influence on the SAGD oil production estimation is emphasized.

2.2 Crude oil emulsification

An emulsion refers to any stable mixture of two or more immiscible fluids whereas the process of its formation is termed emulsification [95]–[97]. In such a mixture, one (or more) dispersed phase of fluid is formed within a continuous phase of another immiscible fluid. Different kinds of emulsions can be formed depending on the properties of the immiscible fluids and conditions at which the emulsification occurs. These different types of emulsions are highlighted in the schematic shown in Figure 2-3 [3]. An emulsion in crude oil can be categorized into one of the three main groups which are (a) water-in-oil (W/O), (b) oil-in-water (O/W), and (c) multiple or complex emulsions such as water-in-oil-in-water (W/O/W) or oil-in-water-in-oil (O/W/O) [93], [95]–[97], [106].

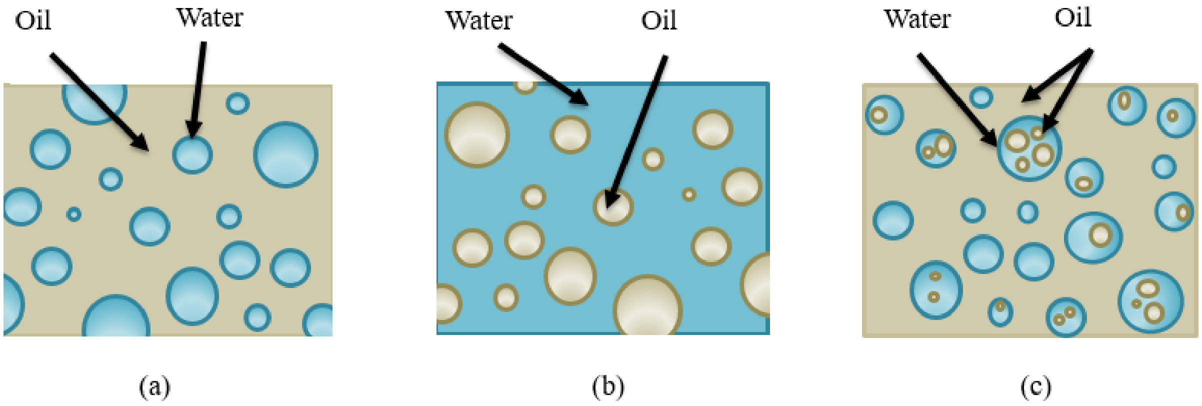

Figure 2-3. Graphical representation of different types of emulsions (a) W/O, (b) O/W, and (c) O/W/O emulsion.

Both W/O and O/W emulsions have been observed in SAGD reservoirs [88]–[95]. An O/W emulsion is also referred to as a “reverse” emulsion. It has been reported that the W/O emulsions are predominant in the oil recovered using SAGD [88]–[92], [95]. For W/O emulsions, the water droplet size distribution ranges from 0.1 μm to 50 μm [95]. Emulsion formation and the size of the water droplets in SAGD depend on the state and conditions of the reservoir after drilling and well completion and the natural properties of the formation such as the temperature, pressure, and type of minerals and their relative composition.

Different mechanisms of emulsification in oil recovery processes are suggested in the literature. For the SAGD process, emulsification occurs as a result of conduction/convection heat transfer, displacement of immiscible fluids [107], [108], mixing of the fluid at the pore bodies, the snap-off mechanism and steam condensation[92], [109]. The presence of the emulsion in solvent-SAGD has been also studied using numerical approaches [64]. It has been shown in the literature that emulsification mostly occurs in the steam chamber [88]. The emulsification mechanisms at the growing steam chamber and heat and mass transfer phenomena in this region have a significant contribution to emulsion formation during the SAGD process.

2.2.1 Steam chamber growth and emulsification mechanisms in SAGD

The steam chamber develops in SAGD as a result of the different mechanisms of counter-current flow, co-current flow, water imbibition [110] emulsification, steam fingering [82] and dimensional movement (lateral vs. vertical) [74], [107], [111], [112]. A schematic of the SAGD steam chamber that is typically used in modelling is shown in Figure 2-4. The injected steam is the source of water condensate that facilitates emulsion formation. Since the injected steam has a lower density compared to the oil, the steam chamber grows vertically upwards [74], [107], [111],

[112]. Steam also moves laterally outwards to displace the oil that is recovered from the reservoir. At the pore scale, the flow of steam takes the profile of a plug flow [92]. To have efficient oil production, there should not be any contact between the steam chamber and the production well, otherwise, the undesirable phenomenon known as "steam breakthrough" can occur [113]. To avoid this issue, the desired region of an accumulated pool of oil at the bottom of the steam chamber which is called the sub-cool region [108], [114] decreases the possibility of the steam channeling and breaking through to the production well [114]. This sub-cool layer also prevents non-uniform oil production from different locations of the well, damage to the well and equipment, and further emulsification [113].

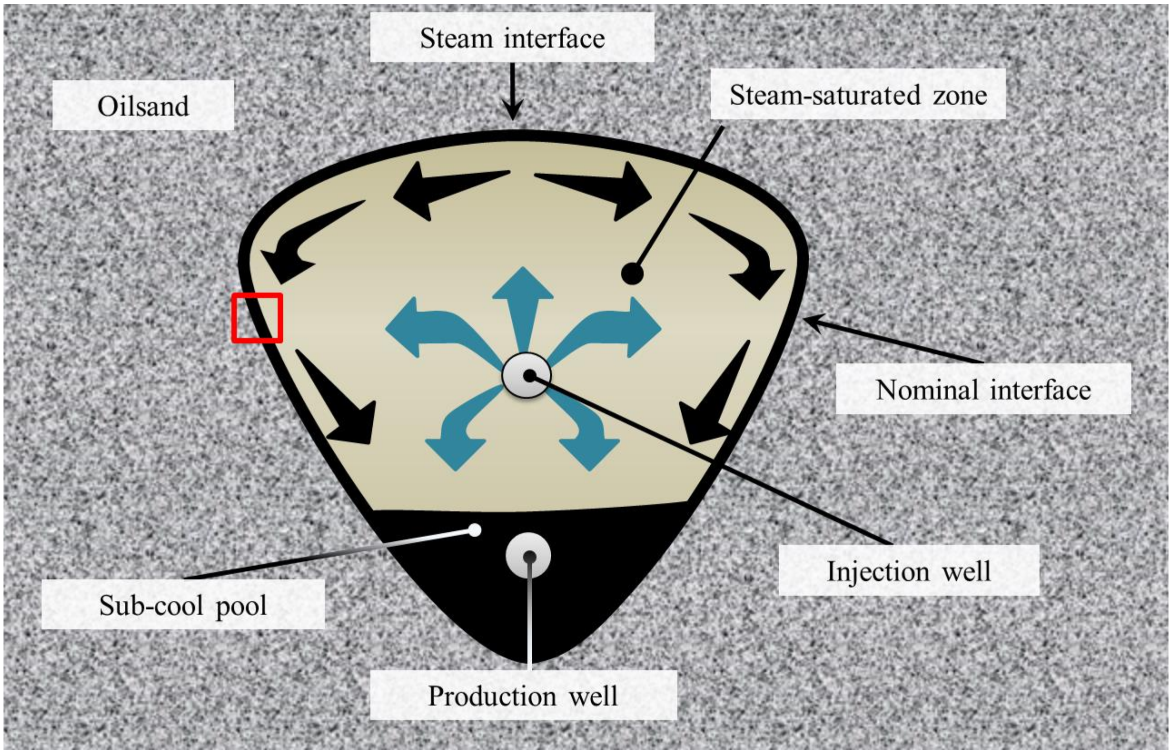

Figure 2-4. Schematic of the steam chamber in the SAGD process (black arrows represent bitumen motion and blue represent steam motion and the red square is the detailed view shown in Figure 2-5).

Also shown in Figure 2-4 are the steam-saturated zone, the steam interface at the top of the steam chamber, and the nominal interface zone in the lateral direction. In an ideal SAGD process, the steam chamber can be divided into three zones that have different steam stability and hence possibilities for emulsification. The bottom of the steam chamber is stable due to the continuous steam injection. The top and side steam interface, however, is not stable since it grows with respect to time due to the expansion of the chamber [92]. At the interface, a counter-current flow of steam and bitumen is responsible for the chamber growth. A schematic interpreting the results of experiments by [92], whose observation was on the nominal interface, is shown in Figure 2-5. The results of the experimental study confirm that the presence of counter-current flow configuration between the steam and bitumen at the interface is the main cause for heat and mass transfer between the reservoir and the growing steam chamber.

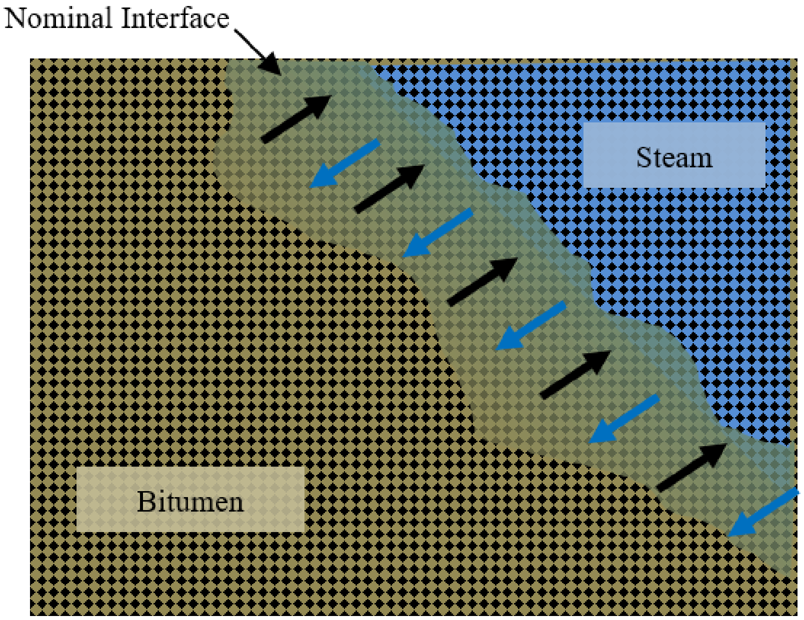

Figure 2-5. A picture of the steam chamber nominal interface in the SAGD process shown by the red box in Figure 2-4.

The most stable form of steam in the reservoir is found in the steam-saturated zone of the steam chamber [92]. In this region, steam is the primary flowing phase moving through the pores to the upper interface of the steam chamber. The difference in the available permeability for the steam and bitumen in this region results in different flow conditions. The small relative permeability of oil in this zone prevents the oil from being present as a continuous phase. In the steam saturated zone, the mobilized oil moves vertically as a result of the counter current or it may move laterally to merge with the draining mobile oil at the nominal interface [89], [92], [115].

The upward moving steam interface at the top of the steam chamber increases the reservoir temperature. In this direction of steam chamber growth, there is no plug flow of steam that displaces the oil but rather steam fingering occurs [111], [116]. This fingering occurs due to the presence of an unstable steam flow below the heating heavy oil. This scenario, visualized in Figure 2-6, can be characterized by the heat conduction due to counter-current flow between steam and colder bitumen [74], [112]. The mobilized oil, having a lower viscosity, drains to the lower level as a film around the steam fingers with the help of gravity [108], [111], [116]. The heated bitumen then forms the top stream chamber interface and drains downward to the production well following the path of the steam chamber nominal edge [112].

The nominal interface along the lateral expansion of the steam chamber is the most important zone in the emulsification process. This region has a more complex flow regime than the steam-saturated zone and the top interface of the steam chamber. In this zone, the mobilized oil produced in other zones is drained toward the production well due to gravitational and capillary forces. The bitumen proceeds along with the interface between the steam saturated zone and cold bitumen towards the producer well. Here, the steam condenses on the falling face of the oil at the interface containing steam, oil, and water and initiates the emulsification process. The lateral growth of the steam chamber interface occurs by displacing the mobile oil in the pores where the capillary forces play the primary role in emulsification [92], [107], [117], [118].

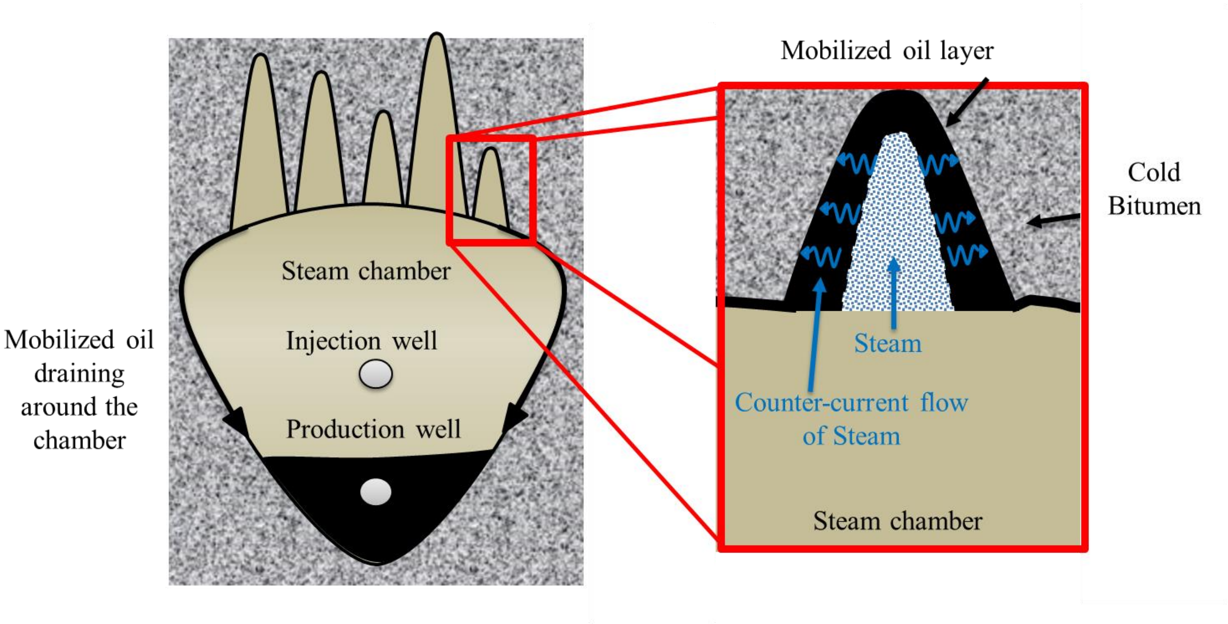

Figure 2-6. Schematic of steam fingering in the steam chamber in the SAGD process.

In oil-wet formations (with hydrophobic sand particles), the process of displacing bitumen (wetting phase) with steam/water (non-wetting phase) is called drainage [92], [119]–[121]. In this kind of formation, the wetting fluid remains in the continuous phase, and the non-wetting fluid moves as a dispersed phase [119], [120], [122]. In the drainage process, two of the main important capillary emulsification mechanisms in a steam chamber are condensation and snap-off [92]. The literature, however, contains little information regarding the conditions under which the condensation and snap-off mechanisms can occur and the respective details therein. The presence of such phenomena, nonetheless, leads to the formation of W/O emulsions.

2.2.1.1 Emulsification through condensation of steam in bitumen

The mechanism which is believed to be mainly responsible for emulsion formation in the SAGD process is the condensation of steam in bitumen [64], [92]. At the pore scale, the condensation of steam occurs due to the local decrease in the temperature of steam below its local dew point. A schematic of this process is shown in Figure 2-7 for the nominal interface [92]. Three zones that have a fluid with different compositions can be found in the figure. On the outer- and innermost faces of the steam chamber interface, porous media is saturated with cold bitumen and steam, respectively, represents the single-phase portions of these zones. In the zone in between, the three components are all present and interact to form an emulsion.

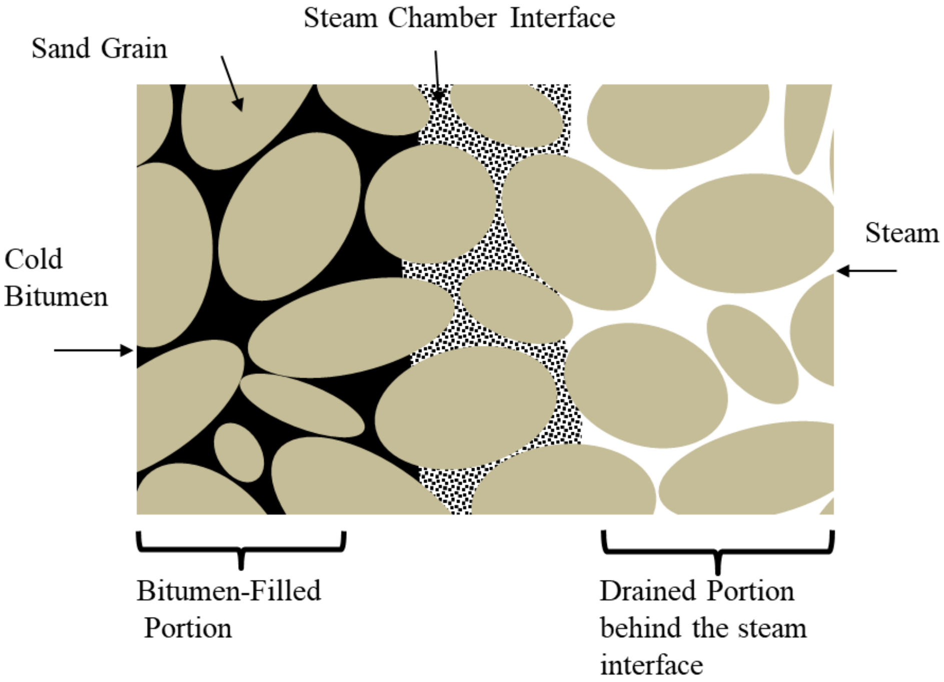

Figure 2-7. Schematic of condensation of steam in pore-scale in the falling film of bitumen at the edge of the steam chamber.

Experimental observations of [92] have confirmed the presence of multiple phases at the nominal interface (water, oil, and steam in this case). Micro-droplets of water form as the steam condenses due to the heat transfer at the interface of the steam chamber to the cold bitumen. These micro-droplets penetrate into the reservoir and the falling face of the oil with the help of gravity-capillary interactions. The penetration of the small droplets into the bitumen falling phase creates a W/O emulsion. The fraction of water in the emulsion changes along the edge of the steam chamber towards the direction of the production well. In general, this fraction increases as the distance to the production well decreases and the steam condensate keeps on accumulating in the falling face [123].

2.2.1.2 Emulsification through snap-off

The other pore-scale mechanism by which emulsions form is known as the snap-off of water flow in a pore throat and is depicted schematically in Figure 2-8. In this mechanism, before a droplet forms in a drainage process, the displacing phase approaches the pore throat as a continuous phase as shown in Figure 2-8 (a). As shown in Figure 2-8 (b), when the front face of the continuous phase is sufficiently (~ seven diameters of the pore throat) far from the pore throat [92], [117], [118], the curvature of the front face creates a pressure gradient within the oil film. This pressure difference makes the oil film moving towards the central axis of the throat in both upward and downward directions to create a lamella. This is a thin, membrane-like structure that separates the newly formed droplet from the continuous phase upstream [92], [117], [118] as indicated in Figure 2-8 (c). The displaced oil surrounds the water and generates a micro-droplet of water in the pore throat. The sizes of the micro-droplets formed after the lamella formation are typically larger than the pore throat [117], [118] [92]. Once the micro-droplet is generated, it penetrates to the falling phase of the mobile oil, and the micro-droplet is carried with the continuous fluid phase (oil) through the pores. The pressure drop along the pore with respect to the curvature of the droplet or bubble is explained by the Jamin effect [36].

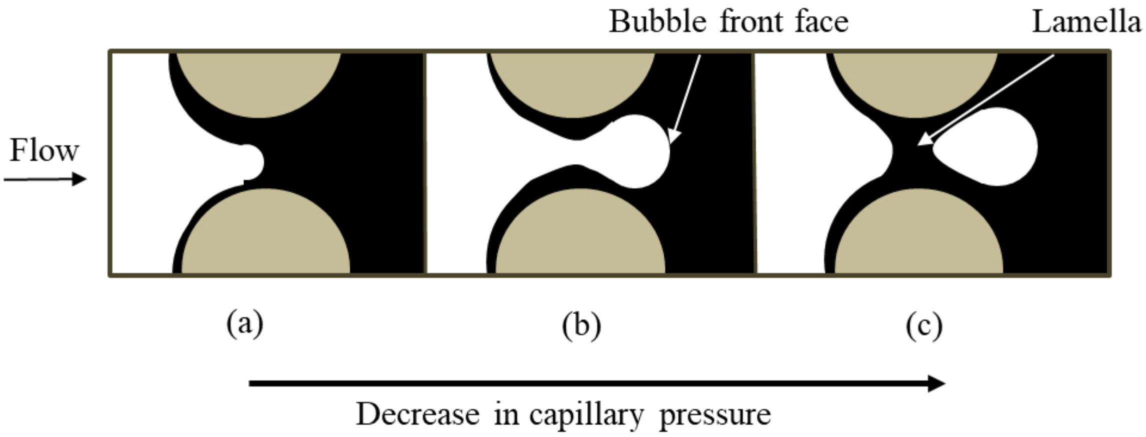

Figure 2-8. Schematic of drainage snap-off stages. Black represents pore oil, white is water, and brown is a solid particle.

The snap-off mechanism described above is also applied to a droplet or a bubble of the dispersed phase approaching a pore throat as long as its size is larger than the pore throat. The snap-off mechanism, in this case, is mainly associated with the breaking up of the dispersed phase into smaller, daughter bubbles [32]. Figure 2-9 shows a schematic of the experimental study of Wu et al. (2017) [32], which demonstrates the snap-off of a nitrogen bubble passing through 100 µm pore throat and create daughter bubbles. Results showed that the formation of daughter bubbles is continued until the capillary pressure difference along the pore throat becomes low enough that the formation of the lamella is not possible. This process will occur for the dispersed phase is either a gas or a liquid.

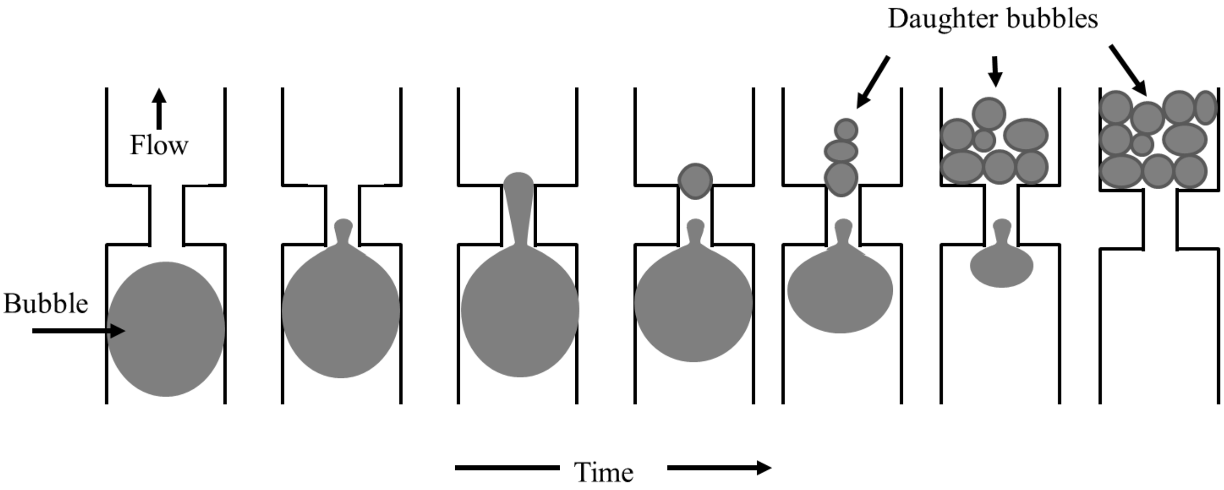

Figure 2-9. The snap-off mechanism leading to the formation of the daughter bubble.

The number and the size of the daughter bubbles (or droplets) can be described by the capillary number, Ca. This is a function of viscous force exerted by the continuous phase on the dispersed phase that is represented by the dynamic viscosity of the liquid, μ, characteristic velocity, $U,$ and the surface tension, σ between the fluid and solid or the interfacial tension between the two fluid phases [32], [124] in the relationship:

$$Ca = \frac{\mu \mathrm{U}}{\sigma} \tag{2-6}$$

The droplet/bubble size decreases as the Ca increases until the critical value is reached. Beyond its critical value, Ca does not influence the diameter of the daughter droplets/bubbles [32], [124].

2.2.2 Enhanced SAGD emulsification

The formation of emulsions in SAGD can further prevail if the steam chamber does not grow ideally along the length of the well. Figure 2-10 shows different configurations that the steam chamber can take at the heel and toe of a SAGD well [113]. The ideal steam distribution is shown in Figure 2-10 (a) where the production well is fully below the level of the sub-cool region. In this case, emulsification occurs at the nominal interface of the steam chamber as described above.

For a non-ideal steam distribution and hence the growth of the chamber, however, there are different possibilities for emulsification in the reservoir depending on the well condition that includes non-uniform steam injection and variation in the reservoir permeability [113]. In Figure 2-10 (b), the sub-cool region is ideal at the heel but extends to cover the injection well at the toe. Therefore, at the toe of the well, the steam injection will be into a pool of an already-mobilized bitumen. Due to the penetration of the steam into this mobilized bitumen, there is the possibility for steam fingering which results in an increased emulsion formation. Figure 2-10 (c) shows the steam breakthrough phenomenon at the heel. In this case, a direct flow path of steam is formed between the injection well and the production well at the heel. At the toe of the well, however, an ideal sub-cool level is achieved. Therefore, the production at the toe is limited as a result of the steam breakthrough at the heel which can result in emulsification. The dominant flow in the well at the heel will be steam and bitumen mostly flows in the toe of the well. This creates a high shear interface between the two flows which results in emulsion formation [113].

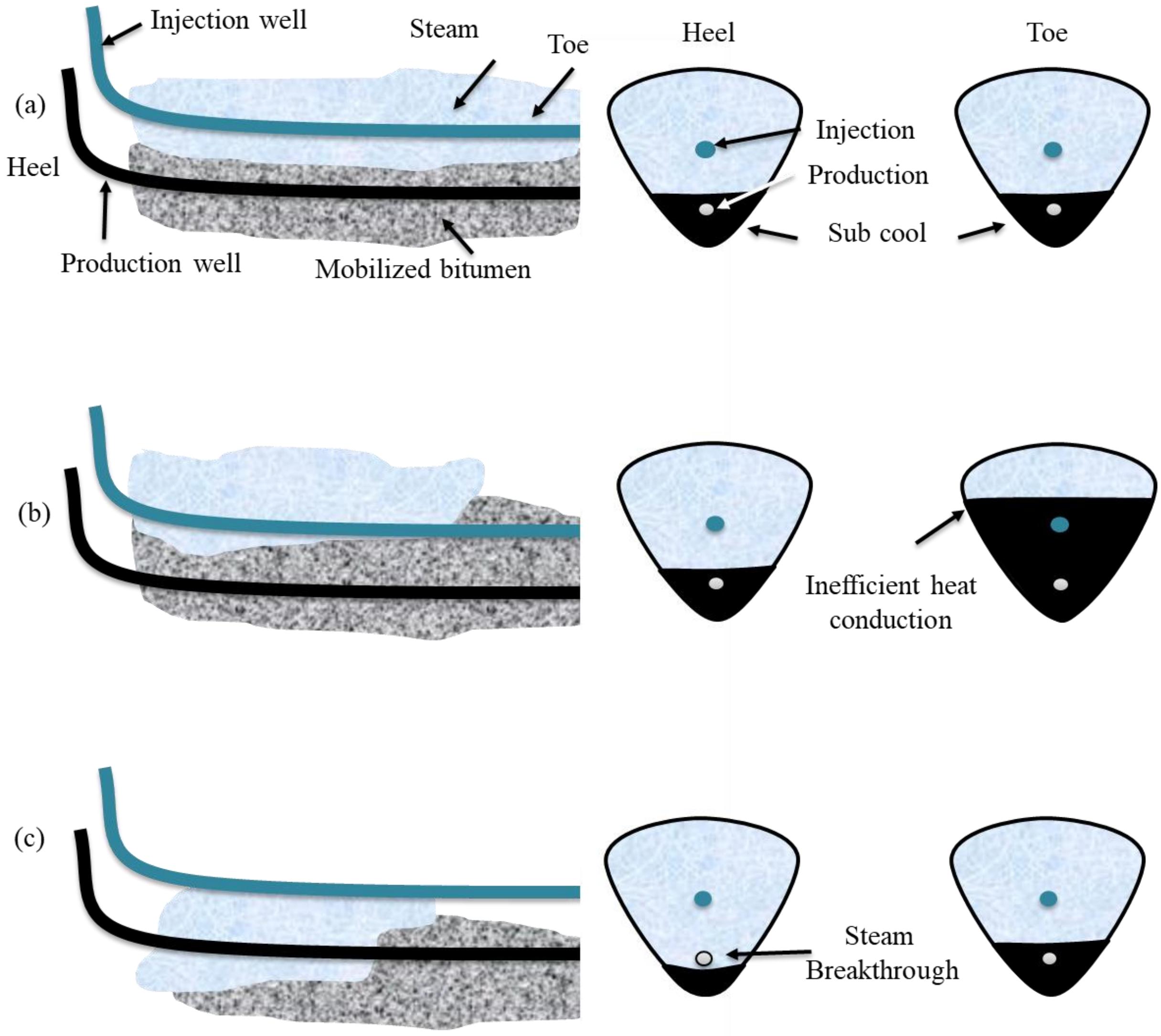

Figure 2-10. Schematic of non-ideal steam chamber growth (a) ideal subcool (b) inefficient heat conduction near the toe and (c) steam breakthrough at the heel. The possibility of emulsification increases in cases (b) by steam fingering at the toe and (c) by steam breakthrough at the heel.

In all of the aforementioned scenarios of the emulsification process in SAGD, it has been shown [92] that it forms an integral part of both pore scale and bulk scale phenomena. Once the presence of emulsions and their potential influence on the performance of the system is established, equal attention should be given to their stability properties [92]. In view of the discussion so far, the possible pathways of emulsification in the SAGD process have been covered in the literature. However, the question regarding whether or not emulsions are present in the production of the SAGD process and how they will affect the performance of SAGD cannot be addressed yet. The stability properties of emulsions and their effects on reservoir properties and other transport phenomena have to first be considered. To achieve this, the behavior of emulsions with respect to their motion and interactions with compounds that are present in the reservoir needs to be established.

2.3 Stability of emulsions in SAGD processes.

The stability of an emulsion refers to the tendency of the dispersed phase to remain in the form of a droplet or bubble. The natural tendency of dispersed phases, however, is to have the minimum possible contact area with the immiscible fluid. This mainly results in emulsions of the dispersed phase having a smaller cross-sectional area to volume ratio [95], [97].

Emulsification is not a spontaneous process but one that requires enough energy to overcome the natural tendency of the dispersed phase to form bubbles/droplets of larger size. Emulsifiers, as interface active components, can reduce this energy requirement. An emulsifier decreases the W/O or O/W interfacial tensions to a lower energy level by forming a film at the phase interface (hence interface active) to produce emulsions that are more stable [95], [97]. The interfacial film is an insoluble cover with high interfacial viscosity on the surface of the droplet. Different types of interfacial layers may be produced depending on the mobility of the interfacial film. This can be categorized into two groups of mobile/liquid films or rigid/solid films [95], [97]. When emulsifiers are used, the viscosity of the interfacial layer increases as a result of the film formation [95], [97] despite the decrease in the interfacial tension. This will enhance the stability of the emulsion.

In heavy oil reservoirs, there are naturally present components such as asphaltene, resin, and fines that can behave as emulsifiers. Other compounds that are injected into the formation during well completion can also have an emulsifying effect at process conditions. The presence of natural components and sand results in a change in the physical [100] and chemical properties of the reservoir. The change in the physical properties such as permeability and porosity of the reservoir can be caused due to the migration of fines and their plugging in the pore geometries. The motion of the natural minerals can also result in a change of the pH and salinity which ultimately will lead to their participation in reactions to generate scale formation in the pore geometry. Any change in the physical and chemical properties of the reservoir can lead to the formation of an interfacial layer around the water droplets in the reservoir to stabilize the emulsion flows [98], [99], [125], [126].

2.3.1 Asphaltene and resin effects

Asphaltene and resins are found to be the more important emulsifiers in heavy oil reservoirs [95], [99]–[101], [126]–[130]. It has been confirmed that these components enhance the stability of emulsions by producing a rigid layer on the surface of droplets [99]–[101], [126], [127], [129], [130]. Analysis of Athabasca bitumen as an example of heavy oil has shown that the oil mixture contains a significant amount of asphaltene (~19 wt.%) and resin (~17 wt.%) [131]. These compounds are natural emulsifiers that lead to increased stability of emulsions formed in SAGD.

The association of asphaltene with resin defines the solubility extent of the aggregate because the ends of molecular forms of asphaltene and resin have different polarities [126]. Figure 2-11 shows a representation of separate molecules of asphaltene, Figure 2-11 (a), and resin, Figure 2-11 (b), along with a stabilized aggregate shown in Figure 2-11 (c) and (d). In a solubilized aggregate, it can be seen in Figure 2-11 (c) and (d) that the resins attached to asphaltene with the polar attraction of two polar functional groups. The tendency of asphaltene to form such aggregates depends on factors such as the relative proportion of asphaltene to that of resin, and the respective concentration of polar functional groups [126], [132]

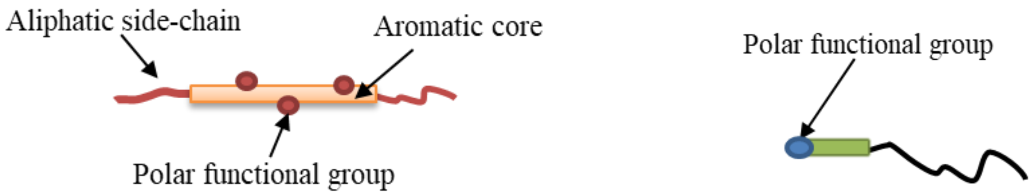

(a) Asphaltene molecule (b) Resin molecule

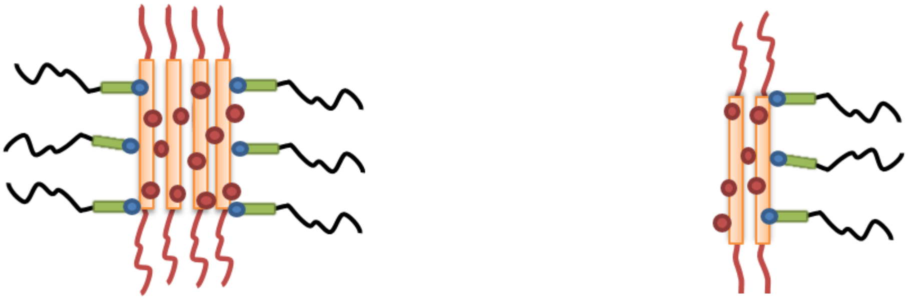

(c) Resin- solublized asphaltene aggregate (d) Partially resin-solublized asphaltene aggregate

Figure 2-11. A schematic of resin-asphaltene aggregation.

SAGD favors the precipitation of asphaltene due to the presence of injection water which provides a significant source of a polar component. Asphaltene aggregates that have lowered free energy, become partially stabilized as shown in Figure 2-11 (d) where it has an exposed end of a polar functional group. During the emulsification that occurs at the edge of the steam chamber, this partially solvated asphaltene [126] attaches to the surface of droplets due to the attraction of polar ends [95], [98]–[101], [125]–[127], [133]–[135]. A rigid/solid interfacial film thus forms on the surface of the droplet preventing coalescence of the droplets, as shown in Figure 2-12 [95], [99]–[101], [126], [127].

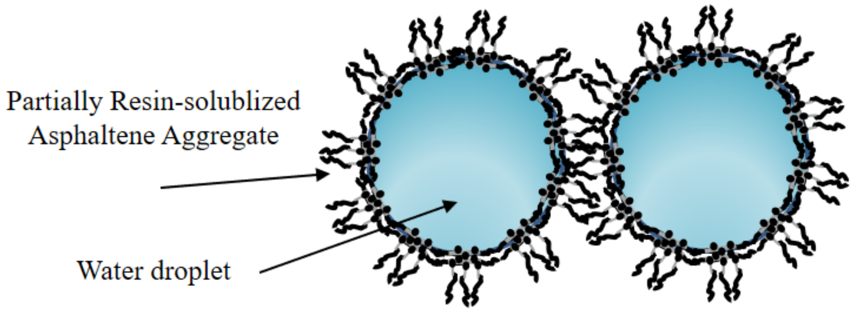

Figure 2-12. Schematic of adsorption of asphaltene aggregates on the surface of the droplet asphaltene- stabilized water droplet and droplet resist fusion due to steric stabilization.

2.3.2 Fine and coarse sand effect

The presence of sand affects emulsion stability through its influence on asphaltene and resin. Sands may further stabilize the interfacial layer formed by asphaltene and resin [95], [99], [101] if the particles attach to the interface of a droplet. The strength and stability of this adhesion depend on the size, wettability, and state of dispersion of the solid phase. Particles that are smaller than the droplet can also have an impact on the emulsion stability. At SAGD conditions, fines smaller than 1 µm in diameter can enhance the stability of the droplets [95], [99], [101]. Particles that are larger by up to several orders of magnitude can also have enhancing effects on the stability of the emulsions depending on their relative proportion in the formation.

Formation sand in oil reservoirs can have a PSD that ranges from fines (< 45 µm) to coarse (> 45 µm) [136]. The specific distribution of fine and coarse sand and their effects on emulsion stabilization are summarized in Figure 2-13. Experimental studies [137] show that droplets are more stable if there is a fractional area ratio of fines to asphaltene of 1:2. For a high fractional area of fines, there will not be enough asphaltene to remain on the interface to mobilize the solids whereas for high content of asphaltene there will be insufficient solid that is available to generate an effective barrier [137], [138]. It is expected that clay particles that are less than 4 µm in size, enhance the stability of the emulsions due to their high contact area to volume ratio by form a stable layer on the surface of the droplets [139], as shown in Figure 2-13 (a).

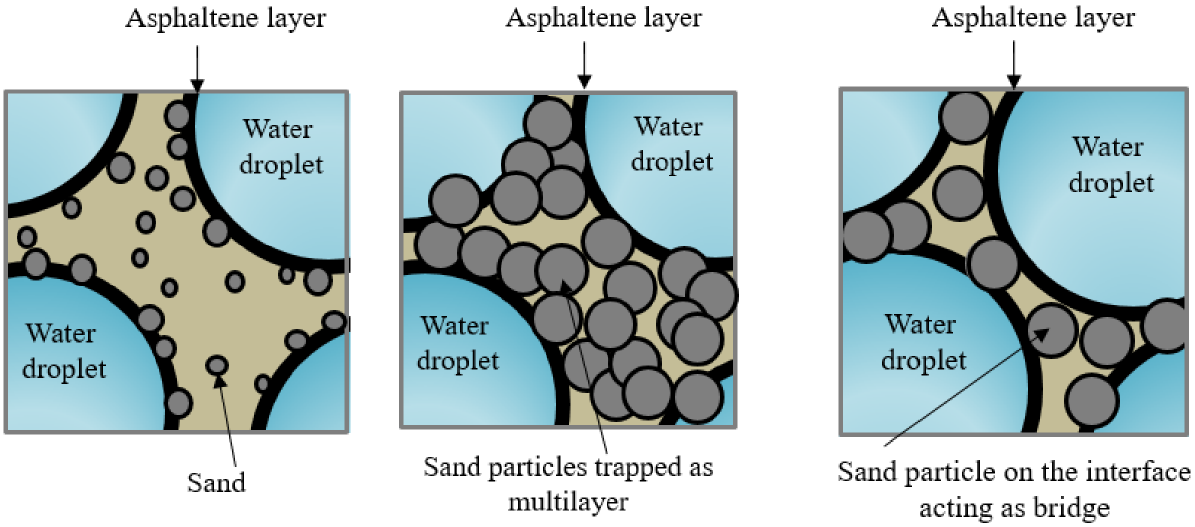

(a) (b) (c)

Figure 2-13. Distribution of coarse and fine sands in an emulsion; (a) fine particles (b) low concentration of coarse particles, and (c) high concentration of coarse particles.

The presence of coarse sands may enhance or reduce the stability of the interfacial layer as per the particle concentration between droplets of the dispersed phase. It has been experimentally shown [137] that when the concentration of coarse sands is low (< 10 kg per m^3 of reservoir volume) as shown in Figure 2-13 (b), the sand particles produce a bridge between two droplets resulting in a higher possibility of droplet coalescence. As shown in Figure 2-13 (c), for a high concentration of coarse sands, however, sand particles can be trapped between the droplets as multilayers, which enhances the stability of the emulsions [137].

2.3.3 Sand wettability effect

In addition to the PSD of the sand, the wettability of the sand is another influencing parameter that plays an important role in the stabilization of the emulsion [95], [99], [101]. Sand particles can be water-wet or oil-wet depending on their interaction with oil. Water-wet sands have more tendency to remain in contact with water than oil [119], [122]. Such particles can stabilize the oil droplets in the water (O/W) by acting as a barrier between the oil and the water phase. Oil-wet sands, however, stabilize W/O emulsions in the reservoir [95], [99], [101]. Findings from experimental studies on the wettability of clay in the reservoir also indicate that the wettability property of clay also depends on its surface properties [139].

Clays in the reservoir typically consist of chlorite, smectite, illite, kaolinite, and a mixed-layer illite/smectite [140]. Chlorite, illite, and smectite are water-wet, whereas kaolinite has shown oil-wet behavior [139]. SAGD reservoirs with the presence of chlorite, illite, and smectite are expected to enhance the stability of the W/O emulsions, while stabilization of O/W emulsions can be enhanced in reservoirs with the presence of kaolinite.

The amount of clay components present in the formation varies between reservoirs and hence its role in the stabilization of the emulsion. As an example, in the Athabasca oil sand formation, kaolinite is present in the largest amount (~ 80 %) which is followed by illite (~ 20 %) [136], [141], [142]. Based on the discussion on the wettability, the presence of kaolinite and illite clays in the Athabasca formation in large amounts is expected to enhance the stabilization of both W/O and

O/W emulsions in Athabasca oil production. A summary of studies on the clay distribution of the Athabasca oil sand can be found in Kaminsky et al. (2009) [136].

2.3.4 Other reservoir properties effect

Emulsions have different stability characteristics depending on the size of droplets suspended in the fluid. They may be categorized based on their size as tight or loose emulsions. Tight emulsions contain small droplets of the dispersed phase whereas loose emulsions are made of large droplets of the dispersed phase [143]. Emulsions made of smaller droplets will be more stable and harder to break than emulsions containing larger droplets [100], [101]. Large droplets in a loose emulsion can be separated even by body forces. The water that can be separated from such emulsions within the period of five minutes is called free water [143]. The amount of water that remains in the emulsion may vary from 1 to 60 % depending on the oil. In light crude oil (with density < 933.1 kg/m^3) emulsions, the water content is typically from 5 to 20 vol % [143]. In heavy oils (with a density ≥ 933.1 kg/m^3), the water content increases to 10 to 35 vol % [144]. This is due to the prevalence of tight emulsions production in SAGD operation [143].

In addition to emulsifiers contained in a reservoir, other properties including droplet size distribution in the emulsion, and conditions such as temperature and pH of the water have significant effects on the stability of the droplets [95], [99], [101]. Temperature and pH of the water influence the interfacial layer that forms around the droplets [95], [99]–[101], [145]. The interfacial layer becomes less stable as the temperature increases. An increase in the temperature also reduces the viscosity and the interfacial forces of a droplet and the continuous phase and changes in the interfacial and physical properties of the components in the interfacial film. The motion of the droplets within the continuous phase is also affected by the temperature. A droplet within the continuous phase fluctuates more once temperatures increases. This fluctuation of the droplets leads to an increase in the coalescence rate of the droplets [95], [99].

The pH of SAGD reservoirs typically varies from 7.3 to 11 as outlined in Table 2-1 [146]–[151]. This change in the pH is due to the relative proportion of organic and inorganic components that are present in the reservoir [150]. The major organic components in the reservoir can be categorized into four different groups of aliphatic, aromatics, polar, and fatty acid components. The major inorganic components commonly found in the produced water are cations such as Na^{+}, K^{+}, Ca^{2+}, Mg^{2+}, Ba^{2+}, Sr^{2+}, Fe^{2+} and anions such as Cl^{-}, SO_4^{2-}, $\mathrm{CO}_3^{2-}$and HCO_3^{-} [150], [151]. The presence of inorganic acids and bases in emulsions will affect the rigidity of the interfacial film by changing the ionization inside the film. Whereas W/O emulsions are typically formed in low pH reservoirs, O/W emulsions are mostly expected for high pH reservoirs [95], [152]. To have a stabilized emulsion, different ranges of optimum pH exist depending on the properties of the crude oil. As discussed in the literature [149]–[151], the pH in the reservoir is within the range which favors stabilities of both W/O and O/W emulsions and the presence of O/W emulsions in addition to W/O emulsions in SAGD reservoirs can be attributed to this [88]–[95].

2.3.5 Dispersed phase migration in SAGD emulsions

Water droplets that are generated due to the condensation or snap-off at the edge of the steam chamber migrate as the dispersed phase. This migration occurs inside the continuous phase of an immiscible fluid in the pores of the formation medium. The interaction between individual droplets and a surrounding medium depends on their size, geometry of the passage (pore), and capillary forces. Such an interaction can affect the emulsion properties through droplets' shapes, sizes, and motion within the emulsion flow.

Droplets may coalesce to form larger droplets that move like a slug or they may break into smaller droplets [153]–[158]. This can be attributed to different factors such as external forces, geometrical effects [153]–[158], viscosity, and droplet size [153], [159]. A major external force that affects the interaction of droplets, is one from the presence of an electric field. Charged particles or droplets result in forming an electric field within the pores [160], [161]. To the best of the authors’ knowledge, the effect of an induced electric field on an emulsion in the reservoir condition has not been covered with substantial information or findings in the literature.

The effect geometry and properties of the pore spaces have been reported to have significant effects on the interactions between the emulsion droplets. One important geometric parameter that affects is the cross-section of the pores through which a droplet passes by affecting the velocity of passing droplets. Due to the change in the velocity, droplets that have different sizes or viscosities can coalesce while passing through the pore [159]. Droplets of the same size, however, can coalesce within the exit region of the pore space due to the increase in the available cross-sectional area for the flow. At such conditions, the velocity of the droplets varies as they move through the pore [153], [159]. Droplets passing through a pore throat can coalesce at the pore exit due to the acceleration of the droplets. Droplets with different sizes may also coalesce in the capillaries in the SAGD formation.

The breakup and/or coalescence of droplets is affected by the topology and morphology of the occupying and nearby pores, properties of the continuous phase, the capillary pressure, and the size, shape, and orientation of the droplets [162], [163]. These parameters also influence the time required for a droplet to break-up (break-up time). In a shorter break-up time, smaller and more dispersed droplets are produced. Larger droplets will be produced in a slower break-up time. In SAGD reservoirs where the viscosity of cold bitumen as the continuous phase is high, the break-up time is higher compared to light oil reservoirs. This results in the formation of larger droplets in SAGD oil recovery as opposed to the light oil recovery. However, due to the interfacial forces, the possibility of coalescence of the droplets in the flow of heavy oils is higher than that of light oils due to the oil viscosity [163]. The higher viscosity of the oil in the SAGD heavy oil recovery leads to a higher water production content compared to light oil reservoirs [162], [163].

2.4 The effect of emulsion on SAGD reservoirs properties

Snap-off and condensation of the steam in bitumen inside the steam chamber, followed by coalescence and breakup of the droplets in the continuous phase, results in further stabilization of emulsions in the produced oil. Understanding the effects resulting from the flow of emulsions in the reservoir is necessary to judge the validity of the single-phase flow assumption when modeling the SAGD process. This effort can begin by considering the motion of an individual droplet in a single pore and further considering the interaction between multiple droplets and a bed of porous media.

The flow of an emulsion through a porous media at the pore scale and over a large scale have been studied with respect to different applications [5], [21], [30], [33], [83], [88], [92], [109], [123], [164], [165] that can be related to the emulsion flow phenomenon in SAGD. Experimental studies have indicated that additional capillary pressure is introduced in the porous media due to the motion of droplets or bubbles [21], [33], [35], [36], [166]. This is the presence of the Jamin effect [36] in emulsion flows at SAGD conditions which results in a higher pressure drop in the reservoir [38]. It has been shown that the capillary pressure introduced by the Jamin effect is affected by different factors such as droplet and pore throat sizes, interfacial forces, and velocity of the carrying fluid (continuous phase) [21], [25], [33], [35], [36], [166].

2.4.1 Effect of emulsion on permeability

At SAGD process conditions, droplets having sizes significantly smaller than the pore throat may be trapped in the pore space and remain on the surface of the sand particles. For droplets that are only slightly smaller than the pore throat size, accumulation at the entrance of the throat may result in the blockage of the pore throat. For droplets that are larger than the pore size, an excessive driving force based on the pores capillary pressures will be required to move the droplets in the pores [21], [33], [35], [36], [166]. Capillary forces are affected by interfacial tension forces between the droplet and the carrying fluid. As the presence of emulsion flows in the SAGD process requires excessive pressure drop to pass through the pore, the effective permeability of the reservoir is expected to decrease based on Darcy's law at a constant flow rate [167] to conserve the mass. The change in the effective permeability of the reservoir due to the flow of emulsions highlights the importance of accounting for it in the SAGD processes investigations.

The emulsions flow rate can also have an impact on the changing rate of the apparent permeability of the SAGD reservoirs. Lower effective permeability is expected at lower flow rates compared to single-phase flow. At higher flow rates, having sufficient driving force to overcome the induced capillary pressure, a higher effective permeability is expected compared to lower emulsion flow rates. The effective permeability asymptotes toward the permeability of the single-phase flow with increasing the emulsion flow rate [21], [30]. At such conditions, due to the deformability of the dispersed phase, more plugged droplets can deform and pass through the pore spaces. This implies that at low flow rates, such as those in SAGD producer wells, the flow of emulsions in porous media is more apparent and influential.

Investigations on large-scale oil recovery processes have also indicated that the flow of a multi-phase fluid through porous media may also have a favorable effect on the oil recovery in contrast to the case of single-phase flow [21], [33], [121]. One reason for this is the interaction of emulsions and the porous media. Such interactions emerge in the reservoir due to the Jamin effect that prevails at the pore scale [33]. Studies of foam passing through porous media indicated that the presence of a multi-phase flow can also result in mobilizing the trapped oil in the pore. This occurs due to the increase in the flow resistance in the existing fracture or high-permeability zones [121]. This ultimately results in decreasing the permeability available for fluid flow and decreasing the potential locations where channeling and breakthrough can occur [21], [33].

Table 2-3. Some of the proposed models on the relation of the viscosity of bitumen and temperature.

Model name	Equation
Batzle, 2004; Beggs, 1975 [168], [169]	$\log_{10}(\mu + 1) = 0.505y(17.8 + T)^{-1.163}$ where $\log_{10}(y) = 5.693 - 2.863/\rho_0$
Mehrotra, 1986 [170]	$\ln(\ln(\mu)) = 22.855 - 3.5784\ln(T) + 0.00511938\, P_g$
Butler, 1991[102]	$\log[\log(\mu + 0.7)] = a.\log_{10}(T + 273.15) + b,$ $a = 0.6464 - 0.4127b$
Edmunds, 1998 [171]	$\mu = \exp\{\exp[-23.56614.\ln(T + 273.15) + 22.7975] - 6.9078\}$
Al-Gawfi, 2019 [172]	$\mu = \exp\big(222.73\exp(7.85 \times 10^{-6}T^2 - 0.0158T - 0.000887P^2 + 0.016P + 1.06)\big)$

2.4.2 Effect of emulsification on viscosity

How the viscosity of pure bitumen varies with temperature has been studied by a number of researchers [102], [168]–[173]. Some of the models developed to estimate the viscosity of the bitumen with respect to temperature are shown in Table 2-3. Emulsions in SAGD have different apparent viscosity compared to pure bitumen. Several models have been proposed by researchers to estimate the viscosity of the emulsions and some of these models are presented in Table 2-4

Table 2-4. Some of the proposed models to estimate the viscosity of emulsions

Model name	Equation
Simon, 1968 [174]	$\mu_r = \frac{\mu_{em}}{\mu_c} = \exp(k\Phi)$ k =7 (w/o emulsions,$V_{f-d} \leq 0.75$) k =8 (o/w emulsions,$V_{f-d} > 0.75$)
Bloomfield, 1971 [175]	$\log(\mu_{em}) = X_1\log(\mu_1) + X_2\log(\mu_2)$
Camy, 1975 [176]	$\mu_r = \frac{\mu_{em}}{\mu_c} = \exp(k\Phi)$ k =-4 to -3 (w/o emulsions) k = 6 to 7 (o/w emulsions)
Barnea, 1976 [177]	$\mu_r = \frac{\mu_{em}}{\mu_c} = \exp\left(\frac{2.66\Phi}{1-\Phi}\right)$
Smith, 1987 [144]	$\mu_r = \frac{\mu_{em}}{\mu_c} = 1 + 2.5\Phi + 14.1\Phi^2$
Pal, 1985, 1989 [178], [179]	$\mu_r = \frac{\mu_{em}}{\mu_c} = \left[1 + \frac{(\Phi/\Phi^o)}{1.187 - (\Phi/\Phi^o)}\right]^{2.49}$
Elgibaly, 1997 [180]	$\mu_{em} = p\dot{\gamma}^q \exp[c\Phi + \Phi d/T_{[°C]}]$
Pal, 1998 [181]	$\Phi_m^{0.5}\left[1 - \mu_r^{-\frac{1}{\eta\Phi_m}}\right] = A_0 + A_1\log(N_{Re,p}) +$ $A_2[\log(N_{Re,p})]^2$ For $\Phi \geq 0.70$ $\Phi_m^{0.5}\left[1 - \mu_r^{-\frac{1}{\eta}}\right] = A_0 + A_1\log(N_{Re,p})$ For Φ <0.70
Li-ping, 2012; Pal et al., 1985 [179], [182]	$\mu_r = \frac{\mu_{em}}{\mu_c} = [1 - K_0K_f(\dot{\gamma})\Phi]^{-2.5}$
Dou, 2006 [183]	$\mu_r = [1 - K_f(\dot{\gamma})K_f(\Phi)\Phi]^{-2.5}$ $K_f(\Phi) = a\Phi^b$

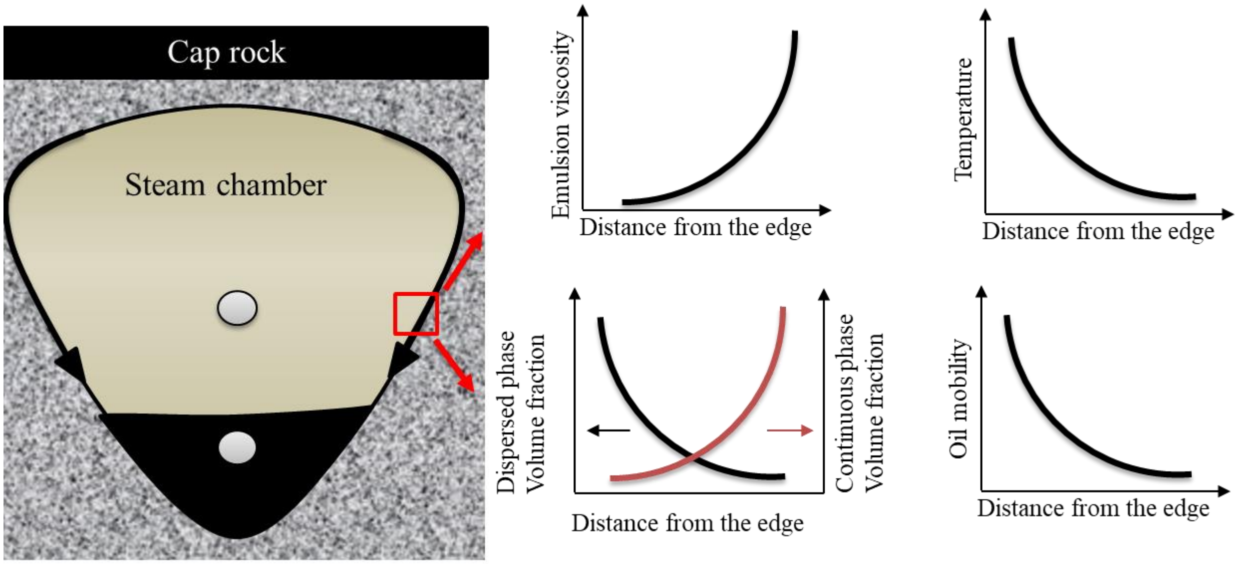

Figure 2-14. Schematic of the steam chamber and plots of changes in temperature, dispersed phase and continuous phase volume fraction, emulsion viscosity, and oil mobility with respect to the distance from the steam chamber edge (e).

The temperature itself varies with the distance from the steam chamber edge which ultimately affects local viscosity. According to the analytical models, the reservoir properties such as volume fraction (V_f), emulsion viscosity (μ_{em}), and oil mobility (λ) change with respect to the relative distance from the edge of the steam chamber [79], [83], [95]. Figure 2-14 shows a schematic of a steam chamber and the changes in the emulsion viscosity along with other properties with respect to the distance from the edge of the steam chamber [79]. As shown in the figure, the oil mobility, the dispersed phase volume fraction, and the temperature have their highest values at the edge of the steam chamber. The viscosity of the emulsion and the continuous phase volume fraction, however, have their lowest values in this region. The temperature in the reservoir decreases as the distance from the edge increases and hence the viscosity of the emulsion increases

Numerical studies on emulsion flows in SAGD have indicated that the apparent viscosity of the bitumen increases due to the presence of microbubbles of water and their fraction in the emulsion [95]. Rheological studies on tight W/O emulsions produced in crude oils showed that the emulsions behave as a Newtonian fluid when the water cut (water volume fraction) is less than 30 % [95]. Emulsions having high water cut typically behave as non-Newtonian fluids [95], [184]. They behave as shear-thinning or pseudoplastic fluids depending on the water cut. For such fluids, viscosity decreases as the shear rate increases. The fluid starts to behave as a non-Newtonian fluid (shear thinning) as the water cut becomes greater than 30 % and continues up to 80 %. At a water cut of > 80 %, however, the emulsion starts to invert and the water droplets coalesce such that an O/W emulsion is produced [95].

The viscosity of SAGD emulsions is affected not just by the water cut (water volume fraction) but also depends on the type of emulsion as heightened with the data from Kokal (2005), shown in Figure 2-15. Emulsions with large and widely distributed droplets (loose emulsions) have lower relative viscosity (the ratio of the viscosity of emulsion to the viscosity of pure oil) than emulsions with small and closely distributed droplets (tight emulsions).

It should also be noted that although it is convenient to assume a uniform viscosity throughout the reservoir, in reality, it may change with the location within the reservoir laterally and vertically. Up to a ten-fold difference has been reported [185], [186]. Therefore, the quality of the viscosity data and the predictive models should be verified and the results should be applied with caution with respect to the assumptions and measuring procedures [187].

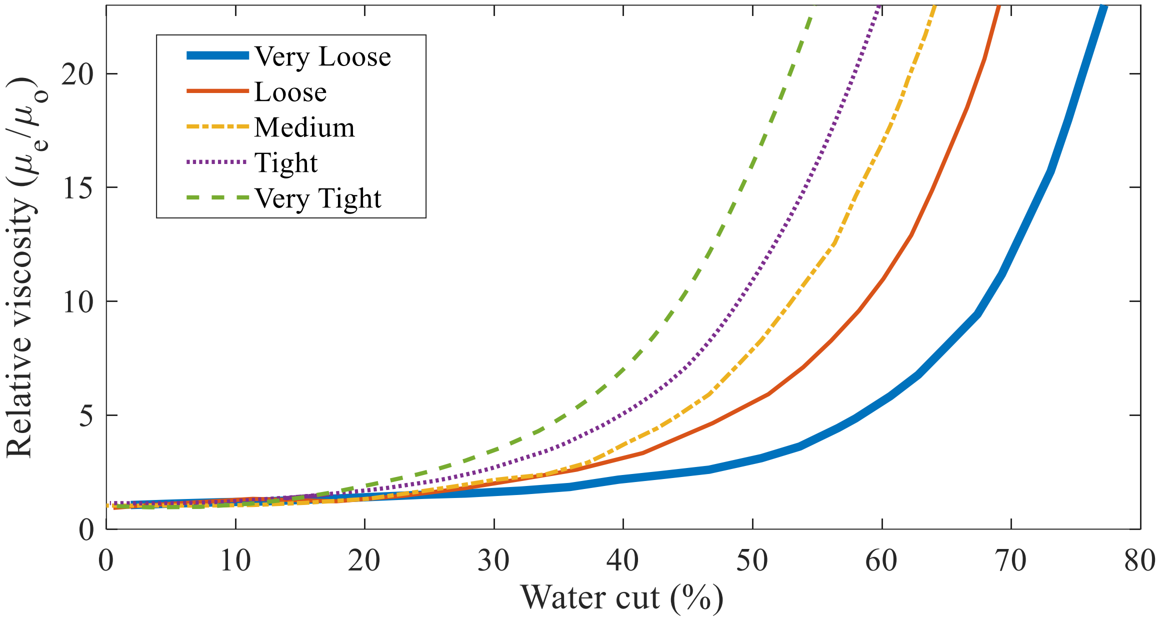

Figure 2-15. Experimental results of relative viscosities of different types of emulsions. [95]

2.4.3 Effect of emulsification on oil mobility

Different models have been proposed to describe the oil mobility in SAGD reservoirs [17], [70], [79], [83]. Based on Butler's model, the oil-phase mobility exponentially decreases with increasing distance from the steam chamber edge, as shown in Figure 2-16, as it is a function of the viscosity (as can be seen from Figure 2-14). Figure 2-16also shows the results from two other models. The results from the model, which accounts for multi-phase flow [79] also indicate the decrease in mobility of the oil as proposed by Butler. Sharma's model [83], however, shows lower oil mobility within the reservoir with a different trend from the other models shown in the figure. The decrease in the oil mobility ratio of this model as compared to Butler's model suggests a strong effect of the emulsification on the mobility of the oil.

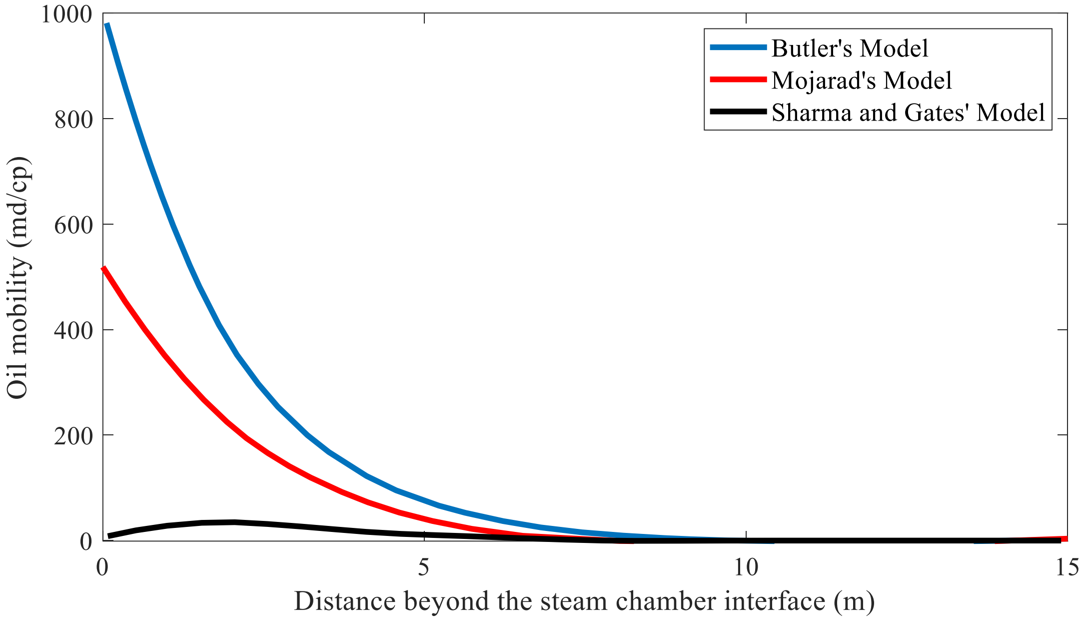

Figure 2-16. Comparison of oil mobility from Butler’s model, Sharma s’ model, and Mojarad’s model. After [79]

In single-phase flow, higher oil mobility is expected as the pore networks are only available to the flow of a single fluid. For multi-phase flow, however, the relative permeability should be considered for its effects on the bulk flow [83]. [79] Proposed a model to obtain the oil mobility by ignoring multi-phase effects in the presence of an emulsion but by accounting for the dynamic emulsion viscosity effects. The results show the same exponential trend proposed by Butler. The values of the oil mobility, however, are lower as a result of the emulsion effect which was accounted for [79].

2.4.4 Emulsification models and production estimation

The result of the oil production proposed by the models of Butler [84], [85], Sharma [83], Mojarad [79], and data for the oil recovery from six different fields were compared by Mojarad and Dehghanpour (2016) and are re-represented in Figure 2-17. The reader can refer to [79] for further details about the properties of the oil fields and calculations of oil production. It can be observed from the figure that Butler's model overestimates the oil recovery and this is strongly due to the single-phase flow assumption. The results from an oil field, however, are in good agreement with the results proposed by Sharma et.al [83] and Mojarad et.al [79] for the range that the models proposed. The results show a substantial effect of emulsion flows in the reservoir properties and the oil recovery. The comparison between analytical results [79], [83], [95] for the oil production and field results [95] and the effect of emulsification raises a question on the importance of emulsion formation in the SAGD process. The discussion above indicates that the single-phase flow of the produced bitumen is not an accurate assumption in SAGD flows. This requires further investigations regarding the emulsion flow under SAGD operating conditions.

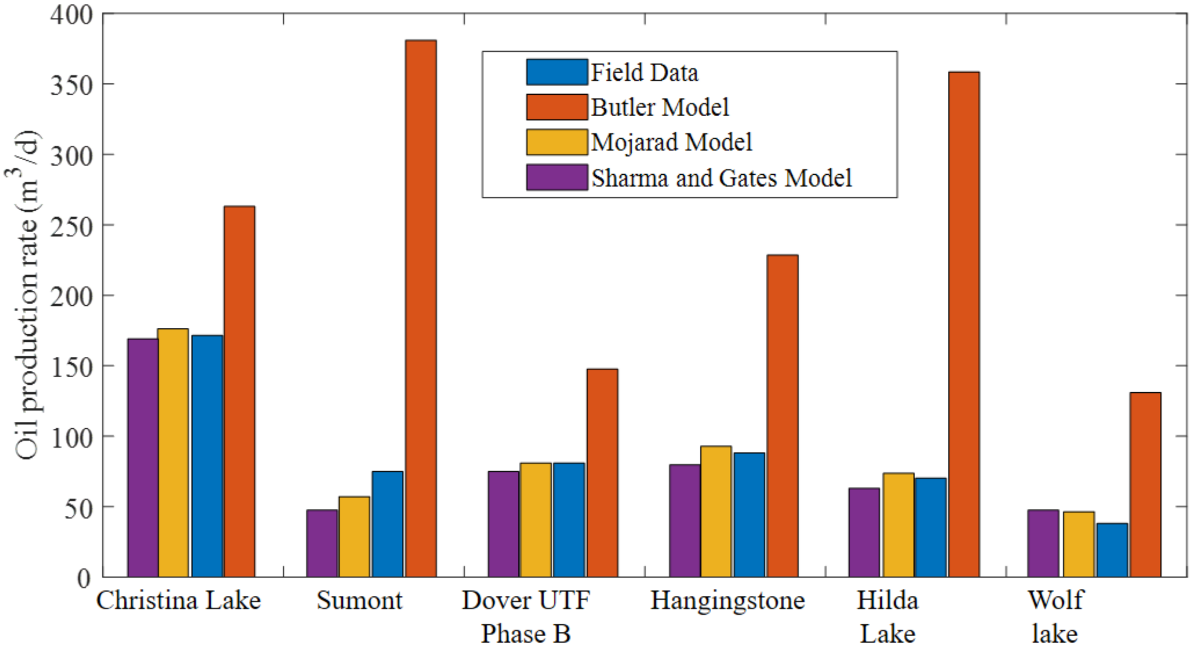

Figure 2-17. Comparison of SAGD models for different field-operations data. After [79]

2.5 Conclusion

A review has been conducted to discuss the physics of the emulsification process in SAGD reservoirs and its effect on the validity of the assumptions considered in models estimating SAGD process performance. A major observation in popular SAGD models is the assumption of the single-phase flow phenomenon in the reservoir. Considering the emulsification phenomena that could prevail in oil reservoirs, however, this could be seen as a significant limitation. Therefore, the mechanisms of emulsion formation in porous media are also discussed with respect to the processing conditions that prevail in SAGD. The effect of emulsion flow in the reservoir on characteristics such as permeability, viscosity, and oil mobility in the reservoir expressed as porous media was discussed in detail. It is evident from the literature that SAGD conditions lead to the formation of stable emulsions in the reservoir. Edges of the steam chamber are considered as regions of pronounced effects of emulsion formation. These effects location will extend to other regions such as the sub-cool zone, and the near-entrance regions of the sand/flow control devices. An implication of this finding is that the single-phase assumption does not well account for the change in the effective permeability, mobility, and consequently oil production in the presence of emulsions in the reservoir.

Focusing on the reservoir properties for the SAGD process, models based on the single-phase assumption do not well capture the effect of temperature and pressure on the viscosity, density, and other thermal- and flow-related properties of the reservoir to the level that a multi-phase flow model assumption will. While substantial mathematical simplicity might be gained through the single-phase assumption, neglecting the role of emulsions present in the reservoir will result in a different estimation of oil production rate at SAGD conditions and is the main limitation of using these models. Models developed specifically to the SAGD process by Sharma and Gates (2010) and Mojarad and Dehghanpour (2016) verify the benefits of including multi-phase flow properties. The assumption of single-phase flow results in an overestimation of the oil production, whereas, estimated production rate by accounting for the effect of emulsion flow closely matches the field data obtained for different reservoirs in Canada. The results of these studies emphasize the importance of consideration of the emulsion flow characteristics in the estimation of oil production.

The multi-phase assumption in developing the SAGD models can affect new and developing trends in SAGD operations. The significance of emulsions and their contributions are crucial features of solvent-SAGD processes where the presence of the solvents may further stabilize the emulsions. A detailed investigation is needed to specify the reservoir properties such as temperature, pressure, and effective permeability and the effect of solvent selection at the early stages of the modeling. Future work modeling a SAGD system would be best undertaken using the assumption of multi-phase flow phenomena. This would have the best possibility of reliable prediction of main parameters such as production rate, and steam-to-oil ratio can be achieved. In addition, the effect of emulsion flows on the flow properties such as pressure drop is only studied using the bulk motion of the flow. A further study with more focus on multi-phase flow in pore-scale is therefore suggested to have a clear understanding of the flow phenomena in this scale and its effect on the change in the permeability for the system.

Chapter 3: An experimental investigation of the effect of three-phase contact line pinning on the passage of an isolated bubble passing through a pore confinement [5]

This chapter describes and discusses the experimental investigation and methods developed to analyze the shape of an isolated dispersed phase to evaluate the internal pressure change. The first section discusses the theory considered to evaluate the pressure of the phase and highlights its limitation. The second part moves on to describe the methodology developed for image processing from two different perspectives in greater detail.

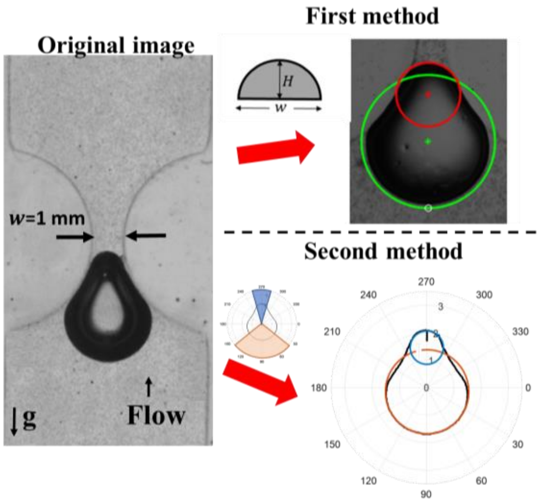

Graphical Abstract Chapter 3

The developed method is utilized to study the motion of different sizes of isolated bubbles moving with a bulk motion of glycerol in the pore-scale at different flow rates.

3.1 Introduction

Multi-phase flow displacement in confined geometries is a common practice found in different industries such as oil recovery [4], [5], heat exchangers [188], mechanical valves [189], the food industry [1], and macromolecular delivery [2], [3]. In these flows, a continuous phase of a liquid flow containing isolated gas bubbles or liquid droplets passes through constant cross-sectional

---

[5] This chapter with major modifications is submitted as Ansari, S., and Nobes, D. S. (2021). “The effect of phase pinning on the passage of an isolated bubble passing through a pore confinement” Manuscript submitted for publication to *Journal of Physics of fluids.*

areas or varying geometries depending on the applications [35], [190]. The motion of such a multi-phase fluid showed significantly different flow characteristics compared to a single-phase flow motion [21], [34], [191].

In multi-phase flows, the phases have different mobility and ultimately different pressure distributions. The variation between the pressure of the phases of multi-phase flows in industries such as the food industry [1] and macromolecular delivery [6] is desired since it results in solid particle and colloid removal from the system [150], [192]–[195]. In mechanical valves, however, the presence of a gas phase is not preferred as it is concentrated in the core vortex which ultimately leads to the separation of the liquid boundary layer along the valve's walls [189]. Despite the application of multi-phase flow and the importance of its pressure distribution, very few studies have experimentally investigated these cases.

In recent years, there has been an increasing amount of literature on the passage of a dispersed phase through macro and micro-geometries [13], [24]–[28]. Several studies investigating multi-phase flow have been carried out by focusing on the motion of an isolated dispersed phase in a confined geometry [18], [24]–[29]. The findings from these studies indicated that the size of the dispersed phase, interfacial interaction, density, and the viscosity of the phases have a significant effect on the difference in the mobility of the phases [14], [21]. The motion of a rising bubble both stationary and flowing with constant velocity in a confined geometry showed that for a bubble larger than a confined channel, the presence of the walls results in the reduction of the bubble rising velocity [14], [30], [31]. The motion of the liquid-liquid flow through a pore space also highlighted the reduction in the mobility of the fluid [21]. The studies all discussed the effect of the confined wall of the channel on the velocity of the phase. However, little attention has been paid to the change in the shape of the phase and its ultimate impact on the internal pressure of the dispersed phase.

Studies on the bulk motion of multi-phase flows passing through a pore space indicate that more resistance to the motion exists due to an excessive pressure drop introduced by the motion of the phases [21], [32], [33]. An increase in the pressure drop compared to a single-phase flow is caused by the presence of the interfacial forces between the phases. The deformation of the dispersed phase as it passes through the confining geometry will result in more resistance and ultimately higher pressure drop. Much of the current literature on the deformation of the isolated phase pays particular attention to the deformation of motion of soft matters passing through a confining geometry [7]–[10]. The difference in the deformation of the dispersed phase, based on its properties and the pore geometry, leads to the separation or trapping of the dispersed phase in different applications.

Several studies investigating biological cell separation have been carried out on the design of microfluidic devices that can trap separate soft material at different locations [11], [39]–[41]. It has been reported that the change in the pressure can be determined using shape analysis of the dispersed phase or pressure distribution of the continuous phase. The relation between the shape of the dispersed phase and the pressure is discussed by the Laplace law and the Jamin effect [36]–[38]. The Laplace law has been used for pressure calculation in numerical and experimental studies [42]–[45]. Numerous studies have attempted to explain the motion of soft material entering a pore [7]–[10]. These studies, however, only focused on the critical pressure needed for them to enter the pore. Several attempts have been made to evaluate the motion of the soft material at different locations along the confined geometry [7], [35]. However, approaches of this kind carry various limitations and further research is needed to account for the limitation of this modeling approach such as the inclusion of the pinning effect and the influence of an asymmetric shape of the dispersed phase on the fluid motion. These limitations can be reduced using experimental studies where all the conditions are accounted for and the forces acting on the fluid are present in the study.

There are two primary aims for this study. The first is to introduce a methodology of the pressure determination using the existing theory and the second is to ascertain the effect of dispersed phase pinning on the pressure of the dispersed phase. This paper examines the significance of phase pinning on the motion of an isolated bubble passing through a round pore at different flow rates. A non-intrusive method is utilized to evaluate the interaction and the motion of the isolated bubble carried by the motion of a bulk flow in single pore space. The images obtained from the study are further analyzed to evaluate the interface of the phase and the curvature of the phase at different locations along the pore to determine pressure. A novel methodology to evaluate the pressure will be introduced. The methods used for the pressure calculation can be extended to 3-D flow motion and the motion of multi-phase flow in porous media.

3.2 Theory

3.2.1 The pressure of a dispersed phase

The presence of interfacial forces acting on the surface of an isolated droplet/bubble results in a pressure difference between the continuous phase and the dispersed phase. The pressure is uniformly distributed within the entire volume of the dispersed phase when the phase is not deformed. This pressure is known as the capillary pressure (ΔP_c)[196]:

$$\Delta P_c = \frac{2\gamma_{cd}}{R_d} \tag{3-1}$$

where γ_{cd} is the interfacial tension and R_d is the radius of the dispersed phase.

The dispersed phase passing through a confined geometry will experience deformation and ultimately change in the pressure of the phase. The variation in the internal pressure of a dispersed phase passing through confined geometries such as a pore space is discussed by different groups of researchers [7], [15], [26], [197], [198]. A schematic of a deformed droplet/bubble passing through a pore space is shown in Figure 3-1. For the motion of a dispersed phase that the deformation is purely due to the interaction of the phase and the solid geometry, the pressure change can be determined using the Young–Laplace equation. In this condition, the dispersed phase should also have partially wetting properties with the contact angle of $\frac{\pi}{2} < \theta < \pi$ with the pore.

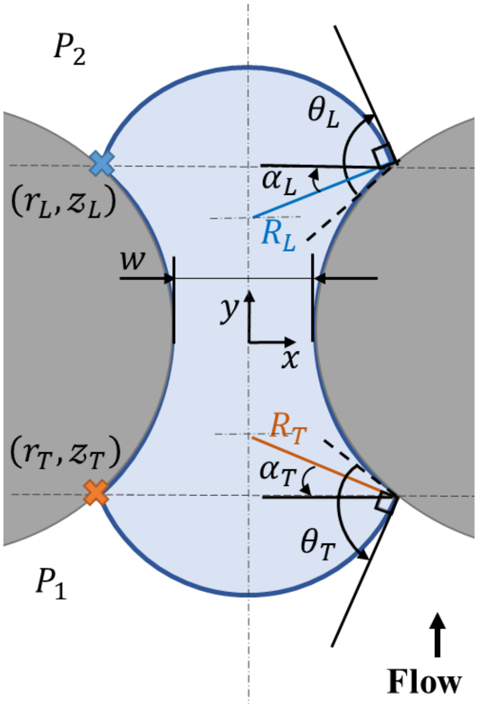

Figure 3-1. A schematic of a deformed bubble passing through a pore.

When undertaking a numerical study, the change in the pressure of the phase is evaluated by accounting for the change in the contact angle of the phase and the solid interface at the leading (α_L) and trailing (α_T) of the edge [7] as defined in Figure 3-1 using:

$$\Delta P = P_1 - P_2 = 2\gamma_{cd}\left(\frac{\cos\alpha_T}{\mathrm{r}(z_L)} - \frac{\cos\alpha_T}{\mathrm{r}(z_T)}\right) \tag{3-2}$$

$$\alpha_i = \theta + \arctan\left[\frac{dr(z_i)}{dz}\right] - \pi \tag{3-3}$$

where $z_L$and z_T are the location of contact lines, and $r(z_L)$ and $r(z_T)$ are the radius at the contact line of leading and trailing edges, respectively. These equations are commonly being used to design two-phase flows in microfluidic confined geometry. Several important limitations are needed to be considered for using these equations. The current model is valid in a quasi-static case and some studies have reported a sharper bubble/droplet surface curvature or backflow for simulations in non-static cases [199]. The other limitation is that the motion of a non-Newtonian fluid and accompanying effect of viscosity variation is not considered in this model [200]. It also does not consider the wetting behavior of the phase in the motion of the flow in a confined geometry with sharp corners [197], [201].

Having a detailed experimental visualization of the motion of a two-phase flow passing through a confined geometry can overcome the limitations that arise in numerical studies. In the current study, the pressure difference between the leading and trailing of the bubble is determined by shape analysis of the motion of the dispersed phase in a round pore geometry. Having the radius of curvature of the edges of the phase, the pressure can be calculated by the change of the inverse of its radius of curvatures of the leading (R_L) and trailing (R_T) edge and surface properties (γ_{cd}):

$$\Delta P^* = P_1 - P_2 = \gamma_{cd}\left(\frac{1}{R_\mathrm{L}} - \frac{1}{R_\mathrm{T}}\right) \tag{3-4}$$

3.2.2 Transit Time

The required time for the bubble/droplet to move from the inlet to the outlet of a confined geometry is termed the transit or residence time. Studies have shown [197], [202]–[204] that the transit time is highly affected by the physical properties of the phases and the interaction of the dispersed phase with the solid surface. Some of these parameters are the pressure and velocity of the system, contact angle of the phases, channel length, and the confinement radius.

Study [202] has shown that the transit time, t_p, as a function of the volume of the droplet (V_d), the volume of the channel (V_c), the volume of the droplet inside of the channel (V_0), the average flow velocity in the constructed channel ($\bar{U}$) and the area of the channel (A_c) can be defined as:

$$t_p = \frac{V_d + V_c - 2V_0}{\bar{U} A_c} \tag{3-5}$$

It was also reported [205] that the t_p is inversely proportional to the capillary number Ca and the capillary number below trapping of the phase Ca_{crit} as:

$$t_p \propto (Ca - Ca_{crit})^{-\frac{1}{3}} \tag{3-6}$$

The proposed models to evaluate the transit time have some limitations. These models cannot predict the motion of the flow in a channel with a varying cross-section as the area and the velocity of the phase varies at different locations. In these conditions, an experimental study can be utilized to evaluate t_p by accounting for the change in the geometry of the confined channel. In experimental studies, the transit time can be determined directly by evaluating the required time for the dispersed phase to pass through the confining geometry.

3.3 Experimental setup

The particle shadowgraph velocimetry (PSV) experimental setup, shown in Figure 3-2, is used to study the motion of an isolated dispersed phase passing through a pore space [206]–[208]. The setup includes two main sections of an optical system and a flow loop. The optical section consists of a camera, a light source, and data acquisition. The flow loop is made up of two syringe pumps one for each phase and a flow channel mounted vertically.

A camera (4M180, IO Industries Inc.) with a resolution of 2048 × 2048 pixels operating at a frame rate of 50 Hz is used to capture the motion of the phases in the flow channel. The camera is coupled to a 105 mm SLR lens to focus on the pore space. The camera is connected to a computer through a direct storage unit (DVR Express Core 2, IO Industries Inc.) to provide high-speed data collection. The flow field is illuminated using a LED panel (BX0404-520 nm; Advanced Illumination Inc.) operating in a continuous mode.

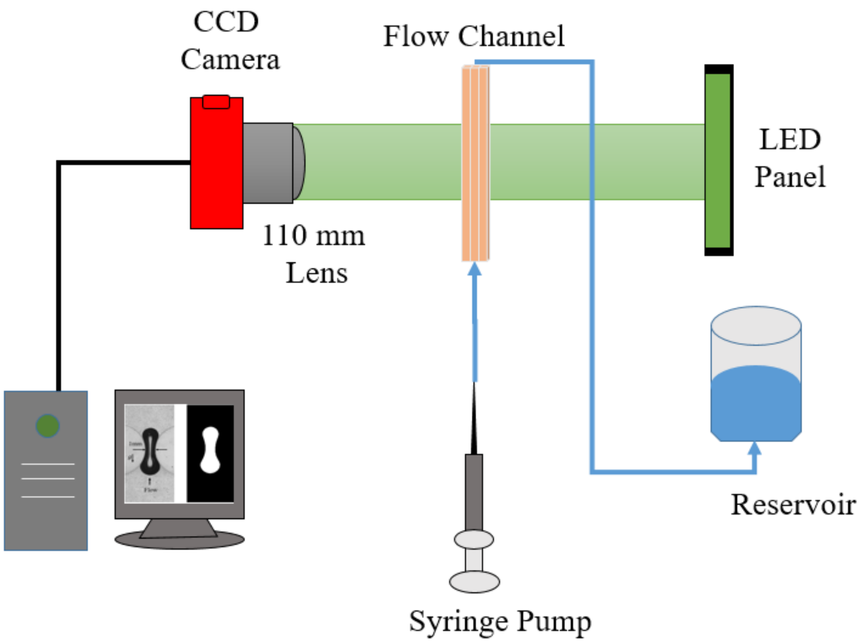

Figure 3-2. The schematic of the experimental setup.

A schematic of the manufactured flow channel is shown in Figure 3-3. The flow assembly has two layers of an optical access window (made of an acrylic sheet) and the main flow channel. The main flow channels are designed using commercial software (SOLIDWORKS, Dassault Systèmes SOLIDWORKS Corp.) and the desired features are developed from a photo-reactive resin using stereolithography (SLA) additive manufacturing technique (Form 2, Formlabs Inc. USA). As shown in the detailed view of Figure 3-3, two adjacent particles in the porous media are modeled using two cylindrical pillars. The pillars were designed to have 2 mm in diameter and they were separated by 1 mm at the pore throat. Two separate inlets for the continuous and the dispersed phase were designed at the bottom of the flow channel.

An air bubble and glycerol are chosen as the dispersed phase and continuous phase, respectively. The difference in the density of the fluid will result in the relative motion of the air bubble in the fluid. The glycerol used in this study is 100 % pure (Glycerol (Molecular Biology), Fisher BioReagents™, USA) with a viscosity of 1.412 Pa.s and density of 1.261 g/cm³ [209]. The continuous phase in each experiment is injected at two different flow rates of 0.1 and 0.2 ml/min using the designed inlet for the continuous phase. To generate an isolated dispersed phase, the air was injected from the bottom of the channel at specific time intervals.

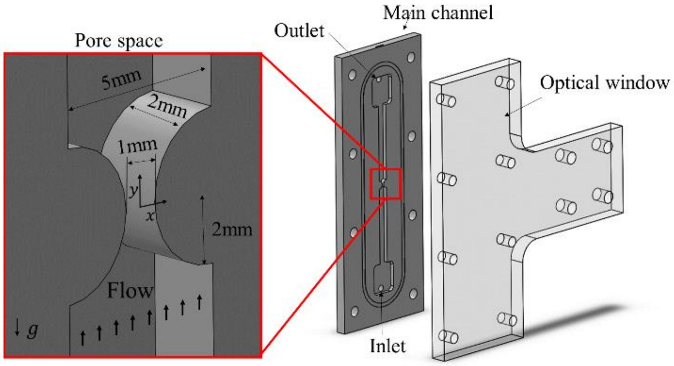

Figure 3-3. Schematic of manufactured flow channel containing a pore space.

3.4 Image processing to evaluate the pressure of the dispersed phase

Two different methodologies were developed to evaluate the pressure change in a dispersed phase passing through a confined geometry. In these methods, the images of the dispersed phase are cropped to the lower and upper portion of the phase to evaluate the radius of curvature of leading and trailing edges. The cropping location is highly affected by the shape of the phase and its location in the confined geometry. The first method was developed based on the relative location of the centroid of the dispersed phase and pore throat. The main disadvantage of this method arises when the exact location of the pore is not detectable. Therefore, a second method was developed where the curvature detection is independent of the confined geometry. This approach was introduced based on the change in the curvature around the bubble. Having the location where the bubble's interface curvature changes, the radii of the curvature will be evaluated. This section will begin by describing the first methodology introduced based on the pore geometry. It will be then discussing the limitation of the developed method. The next section will be on the development of the second method and some sample results.

3.4.1 The pressure difference in an isolated dispersed phase (bubble) based on the pore throat

To determine the instantaneous pressure change of the dispersed phase, a custom image processing algorithm was developed. A summary of the main steps analyzing the shadowgraphed images is provided in Figure 3-4. The process starts with the pre-processing of the original image to determine a binary image. As can be seen in the sample of an original image, the dispersed phase is captured as a black hollow region due to the difference between the refractive index of the fluids. The binary image was used to isolate the bubble and the dispersed phase was detected with an edge recognition function using the change in the intensity of the images (function `edge`, Matlab2018a the MathWorks, Inc.). The hollow region inside the dispersed phase was also filled (function `imfill`, Matlab2018a the MathWorks, Inc.). The next step was to evaluate the dispersed phase properties such as the location of its centroid (x_c, y_c), equivalent diameter (D_{eq}) of the projected area, major and minor axis ($2R_{b,major}$and $2R_{b,minor}$), (function `regionprops`; Matlab R2019a, The MathWorks, Inc.).

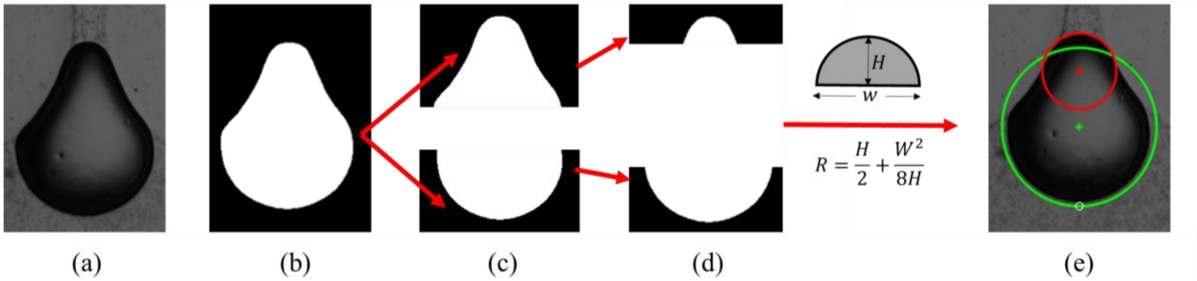

Figure 3-4. Shape analysis steps (a) original image, (b) pre-processed image (c) image cropped from the center of the projected area, (d) image cropped for calculating the leading and trailing curvature, and (e) image of the bubble with a fitted radius of curvatures.

The next step was to crop the image to the upper and lower portion of the phase from the center of the projected area as shown in Figure 3-4 (c). After this stage depending on the location of the bubble relative to the pore throat, different locations were used to crop the image to determine the radius of the leading and trailing edge. After detecting the proper location of the leading and trailing edge, the bubble was cropped further as shown in Figure 3-4 (d). The radius of the leading and trailing edge were determined based on the height (*H*) of the arc and the width (*w*) of the cropped location. A sample of the calculated radius of curvature fitted on the original image is shown in Figure 3-4 (e).

The stages of bubble deformation can be categorized into seven case as shown in Figure 3-5. In these steps, the leading and trailing edges are at different locations along the pore. The cropping location for calculation of the radius of curvature, location of Figure 3-4 (d), varies depending on the stages of the bubble deformation. The samples of the cropping locations for the leading and trailing edge are shown by the green and red dashed lines in Figure 3-5. In the following sections, the details of the cropping locations for these steps will be discussed.

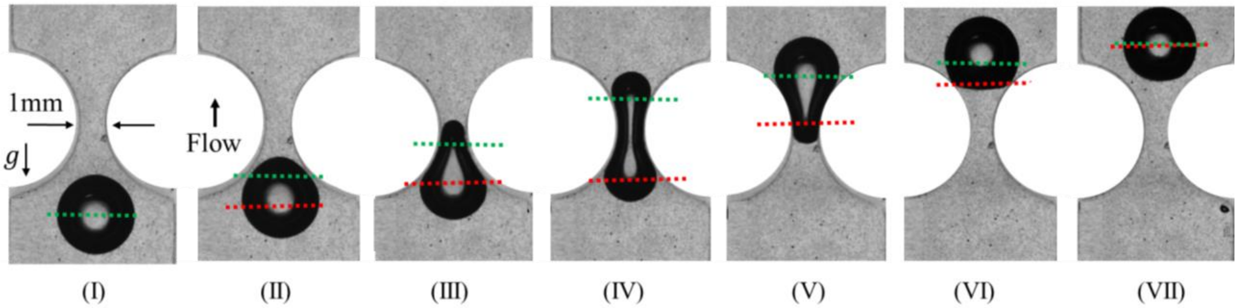

Figure 3-5. Different stages of bubble deformation and the image cropping locations for curvature calculation.

- **Stage (I) and (VII)**

The stages of a dispersed phase approaching or leaving a pore geometry are shown in Figure 3-5 (I) and (IV). This condition occurs when the solid surfaces of the channel before and after the pore space is further away from the bubble and the effect of confined geometry in these locations can be neglected. As the bubble is moving in a free surface geometry, it is assumed to have a spherical shape with uniform pressure distribution. The pressure between the continuous phase and dispersed phase also known as a capillary pressure (ΔP_c) can be calculated using Eq.(3-1)

To determine these conditions, the sphericity of the bubble will be determined using the ratio of the minor and the major axis. If the sphericity is higher than 0.95, the bubble is assumed to be in its spherical shape. The elevation of the centroid,y_c, is the best estimation of the cropping location to evaluate the radii of curvature. In this condition, the radius of curvature of the leading and the trailing edge will be considered the same as the radius of the projected area.

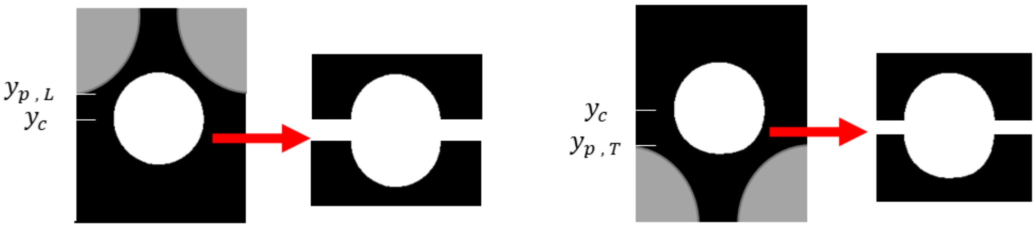

(a) (b)

Figure 3-6. The cropping location of the radius of the curvature for stage (a) I and (b) VI.

This condition is highly affected by the ratio of the size of the bubble (R_d) and the pore throat (w). In the case of a small bubble compared to the pore geometry, $2R_d/w \ll 1$, the bubble will not be affected by the pore interface. The bubble will not be deformed and the current condition can occur through the passage of the dispersed phase. When $2R_d/w>1$ the bubble starts to deform as it passes through the confined geometry. As the ratio increases, the deformation occurs further upstream before it reaches the pore and further downstream as it exists in the pore space.

- **Stage (II)**

As a bubble with $2R_d/w>1$ enters the pore geometry, it starts to deform as shown in Stage II of Figure 3-5. The deformation is caused by the impact of the confinement walls introduced as a result of the decrease in the cross-sectional area available for the flow. To evaluate this stage, the location of the leading edge of a bubble (y_L) will be compared to the pore throat (y_p). This stage will be detected if the bubble's leading face is between the trailing part of the pore ($y_{p,T}$) and the pore throat as shown in Figure 3-7 (a).

To calculate the radius of curvature of each face, the first step is to divide the bubble into two sections of the leading and trailing from the centroid as indicated in Figure 3-7 (b). The trailing section which is cut from the centroid is a good assumption for the curvature calculation of the trailing edge. For the leading edge, however, the centroid results in the over-estimation of the radius of the leading edge. Therefore, the leading curvature will be evaluated at the location 1/3 of the distance from the leading edge and the centroid $\left(y_L - \frac{1}{3}(y_L - y_c)\right)$. The finalized stage for the curvature evaluation of the leading and trailing edge is shown in Figure 3-7 (c).

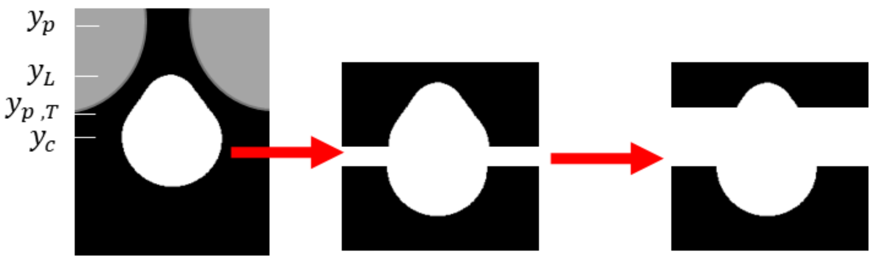

(a) (b) (c)

Figure 3-7. The location of the determination of the radii of the curvature of the stage (II).

- **Stage (III)**

Stage (III) corresponds to the location where the bubble leading edge passes the pore throat. To evaluate this stage, the locations of the leading (y_L) and trailing edge (y_T) were compared to the pore throat (y_P). If the location of the leading edge is on a higher elevation of the pore throat and the trailing edge (y_T) is lower than the pore throat $(y_{P,T})$, this is defined as stage (III). The location with the maximum width of both upper and lower portions will be detected. In this condition, only one maximum width will be detected which will coincide with the location of the centroid. Therefore, the trailing portion will be cut from the centroid and the location of the pore throat will be used to determine the radius of the leading part as depicted in Figure 3-8 (c).

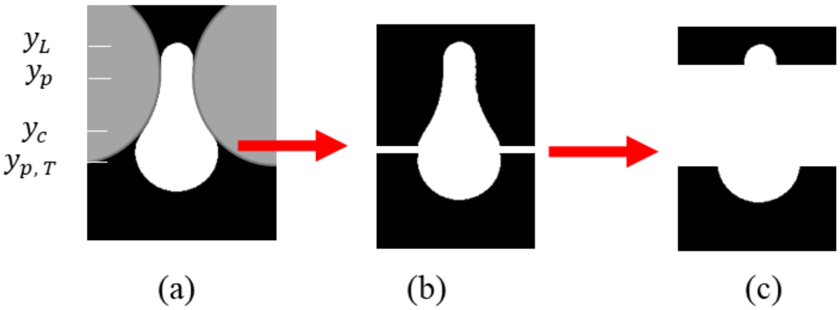

Figure 3-8. The location of the determination of the radii of the curvature of the stage (III).

- **Stage (IV)**

As the leading edge of the bubble passes through the pore throat, the radius of curvature of the leading face starts to increase. Stage (IV) occurs when the location detected for the maximum widths of the bubble are located before and after the pore throat. In this case, to evaluate the radius of the curvature of the faces, the maximum location of the leading and the trailing edge will be calculated and that location will be chosen as the cropping location as shown in Figure 3-9 (c).

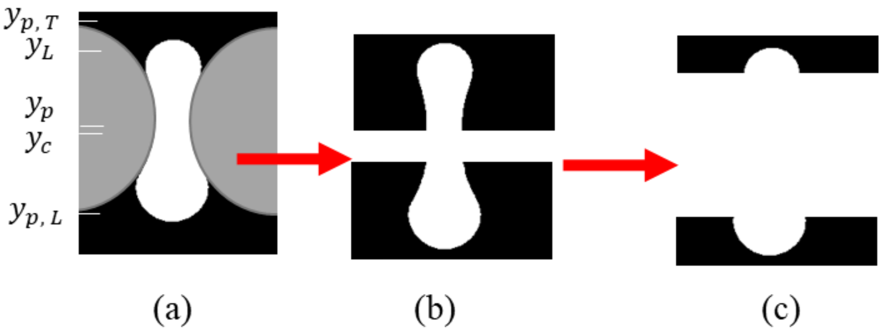

Figure 3-9. The location of the determination of the radii of the curvature of the stage (IV).

- **Stage (V)**

This stage is the condition where the dispersed phase's center of the projected area has passed through the pore throat. A similar approach as discussed in section (III) is considered for the of calculation curvature. In this stage, the leading edge has passed the pore throat and the trailing edge is in the lower elevation of the pore throat. To evaluate this stage the bubble will be cropped from the pore throat for the trailing edge and maximum width of the leading edge for leading edge calculation.

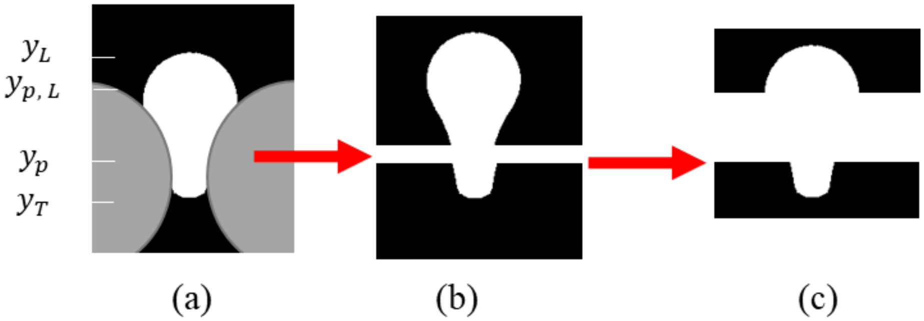

Figure 3-10. The location of the determination of the radii of the curvature of the stage (V).

- **Stage (VI)**

As the bubble passes the pore space, the interaction between the dispersed phase and the solid geometry leads to the further deformation of the trailing edge. In this condition the location of the centroid will be a good estimation for the calculation of the leading edge, for the trailing edge. However, this location will lead to underestimation of the radius of the trailing edge. Therefore as discussed in stage (II), 1/3 of the distance from the trailing edge and the centroid of the bubble $\left(y_T + \frac{1}{3}(y_c - y_T)\right)$.will be selected for the radius of the trailing edge calculation.

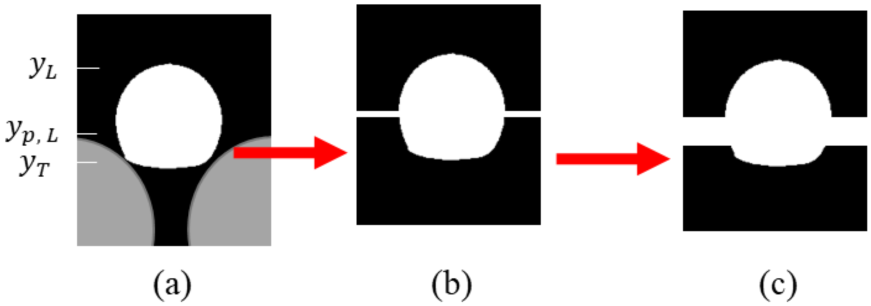

Figure 3-11. The location of the determination of the radii of the curvature of the stage (VI).

A summary of the all cropping location selected for the trailing and the leading edge of the dispersed phase at different stages are shown in Table 3-1. The flow chart of the developed algorithm is also represented in Figure 3-12.

Table 3-1. The location of the leading and trailing edge cut.

Bubble stage	y_{Cut-L}	y_{Cut-T}
(I)	y_c	y_c
(II)	$y_L - \frac{1}{3}(y_L - y_c)$	y_c
(III)	y_p	$y_{\mathrm{Wmax},\ T}$
(IV)	$y_{\mathrm{Wmax},\ L}$	$y_{\mathrm{Wmax},\ T}$
(V)	$y_{\mathrm{Wmax},\ L}$	y_p
(VI)	y_c	$y_T + \frac{1}{3}(y_c - y_T)$

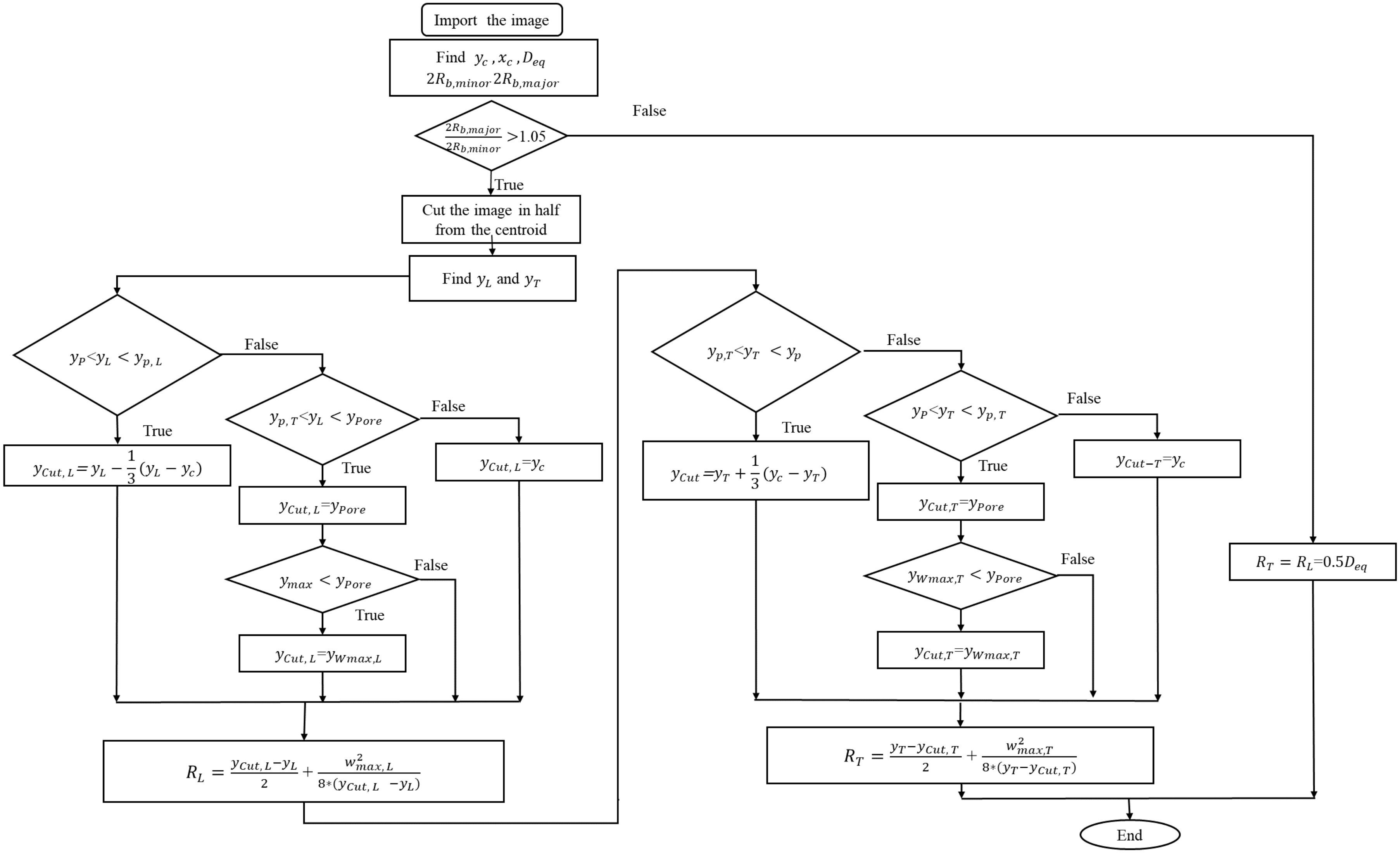

Figure 3-12. The flow chart of the algorithm used to determine the radii of the curvature of trailing and leading edge of a bubble at different locations along the pore.

- **Limitation of the method**

Some important limitations need to be considered for this method. First, to determine the pressure of the phase, the location of the pore geometry (specifically the pore throat) is required. Also, the bubbles leading and trailing edge can have different characteristics depending on the flow rate and the interaction with the solid geometry. This methodology can be applied to the case where there is not a strong interaction of the phase with the surroundings and other information such as the presence of phase pinning and the location of the pore throat is known. This code can be further developed to evaluate the motion of multi-bubble and multi-pore that are required for the motion of multi-phase flow in porous media. To address the limitations of this methodology, a second approach was also developed in which the curvature of the bubble is determined only based on the interface of the phase and independent of the pore geometry.

3.4.2 The pressure difference in an isolated dispersed phase (bubble) using shape analysis

This process is also started with the detection of the bubble as discussed in section 3.4.1. Once the bubble was located, the process proceeds by assessing the boundary of the dispersed phase (function: `bwboundaries`; Matlab R2019a, The MathWorks, Inc.) and plotting it in polar coordinates as shown in Figure 3-13. The bubble was cropped from its symmetric axis and the instantaneous change in the curvature of the boundary of each side can then be determined. The curvature is evaluated by scanning the bubble interface and by curve-fitting over a sliding window of a specific size that slides around the bubble edge to determine the local curvature (function `polyfit`; Matlab R2019a, The MathWorks, Inc.). The curvature gradient was determined by the average change in the curvature in the scanning window. Based on the change in the curvature of the bubble the cropping angle to determine the leading edge and the trailing edge could then be identified. Finally, R_{L} and R_{T} are determined by using a curve fitted to the cropping location.

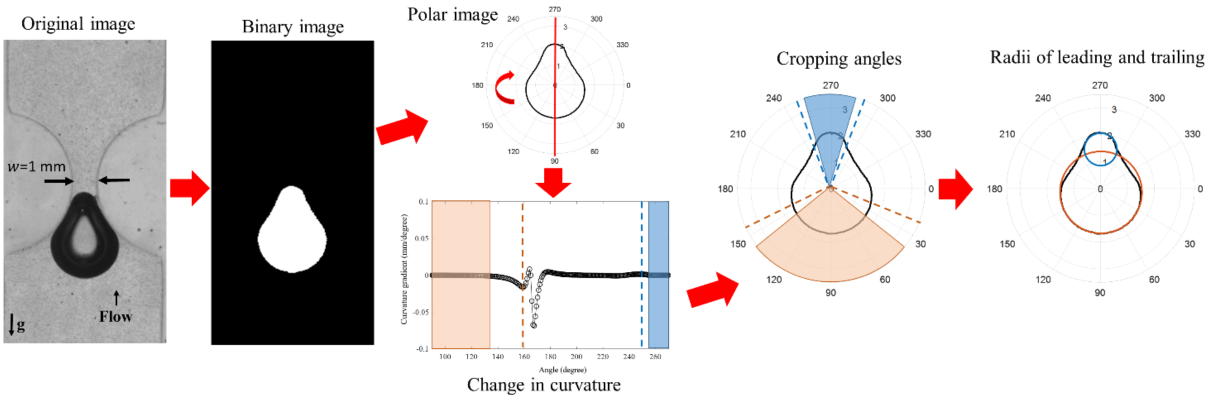

Figure 3-13. The pre-processing of shadowgraph images and steps used to evaluate the curvature of leading and trailing edge.

An example of the change in the curvature with respect to the angle around the left side of a bubble is shown in Figure 3-14. The leading and trailing edges of the bubble are located at $\theta = 270°$ and $\theta = 90°$, respectively. The best location to evaluate the radius of the edges is the constant curvature ranges located for $\theta > 90°$ and $\theta < 270°$ highlighted in the shaded regions in the figure. The extent of locations is determined by the location of the first peaks representing a local change in the surface curvature (function `findpeaks`; Matlab R2019a, The MathWorks, Inc.). The first detected peak, (located ~ 115°) indicates a location where there is a in the local curvature of the trailing edge of the bubble and the last peak (located ~ 245°) represents the leading edge curvature change. The same approach is also utilized to evaluate the location of θ_T and θ_L of the right side of the bubble. The regions of constant curvature evaluated at the leading and the trailing of the bubble ($\Delta\theta_L$ and $\Delta\theta_T$) will be used to determine the curvature of the bubble.

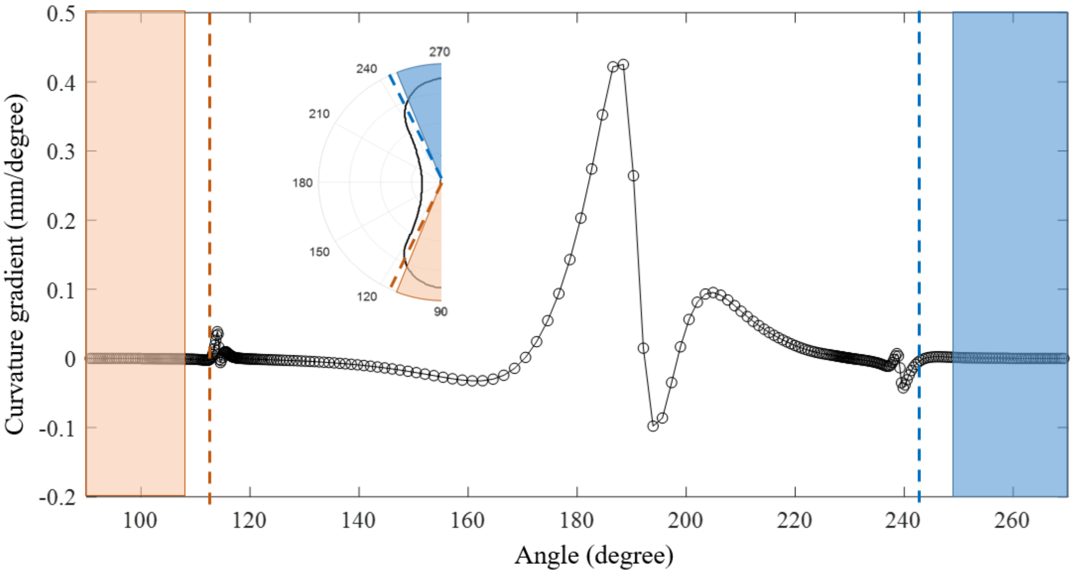

Figure 3-14. The change in the curvature along the left side of the bubble having R_b=1.58 mm at different angles.

The location of the evaluated value of $\Delta\theta_T$ and $\Delta\theta_L$ varies depending on the shape of the bubble. Some examples of different stages of the bubble passing through a pore with their detected locations of the trailing and leading edges are shown in Figure 3-15. Their corresponding evaluated radius of curvature of the leading and trailing edges are also depicted in Figure 3-16. These examples are taken as the bubble passes through the pore at different locations, which are summarized in Figure 3-17 (a).

The bubble has an equilibrium, spherical shape before it reaches the pore geometry. The same shape can be also observed when the bubble exits the pore space. These cases are shown in stages (I) and (VII) of Figure 3-15. The stated stage resembles the condition where the bubble is not affected by the confined wall. In the developed algorithm these stages are detected by the sphericity of the bubble using the ratio of the minor and the major axis $\left(2R_{b,minor}/2R_{b,major}\right)$. If the ratio is higher than 0.98, the bubble is assumed to be in its spherical shape. In this condition, the radius of curvature of the leading and the trailing edge is the same as the radius of the projected area ($R_L = R_T = R_b = D_{eq}/2$).

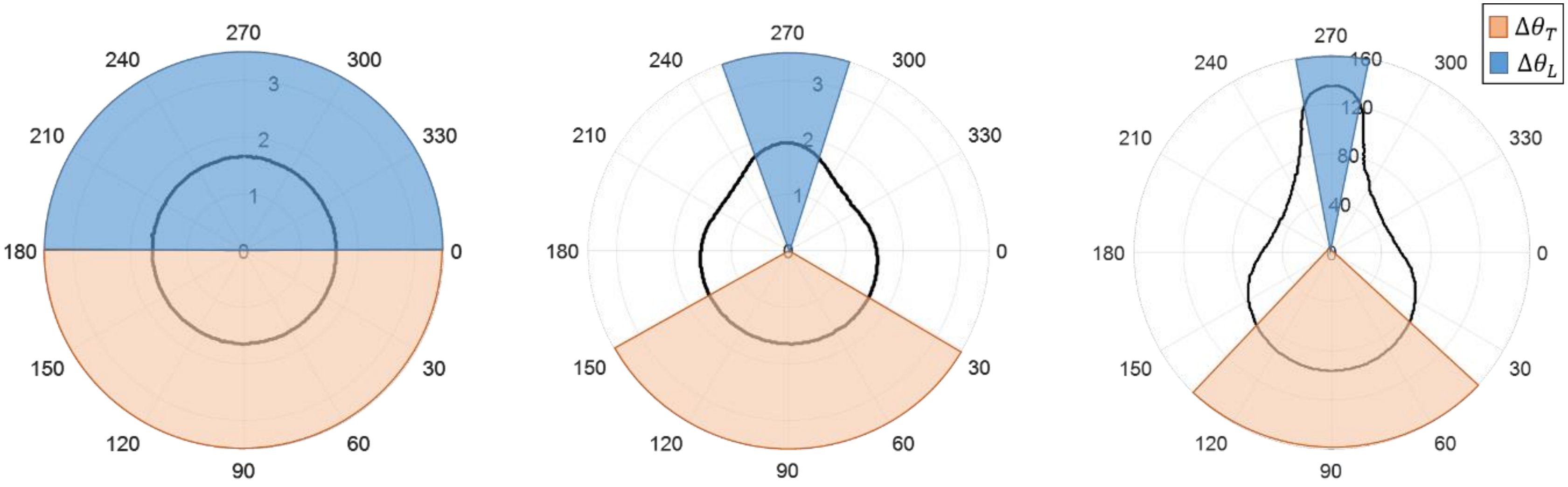

Stage (I) and (VII) **Stage (II)** **Stage (III)**

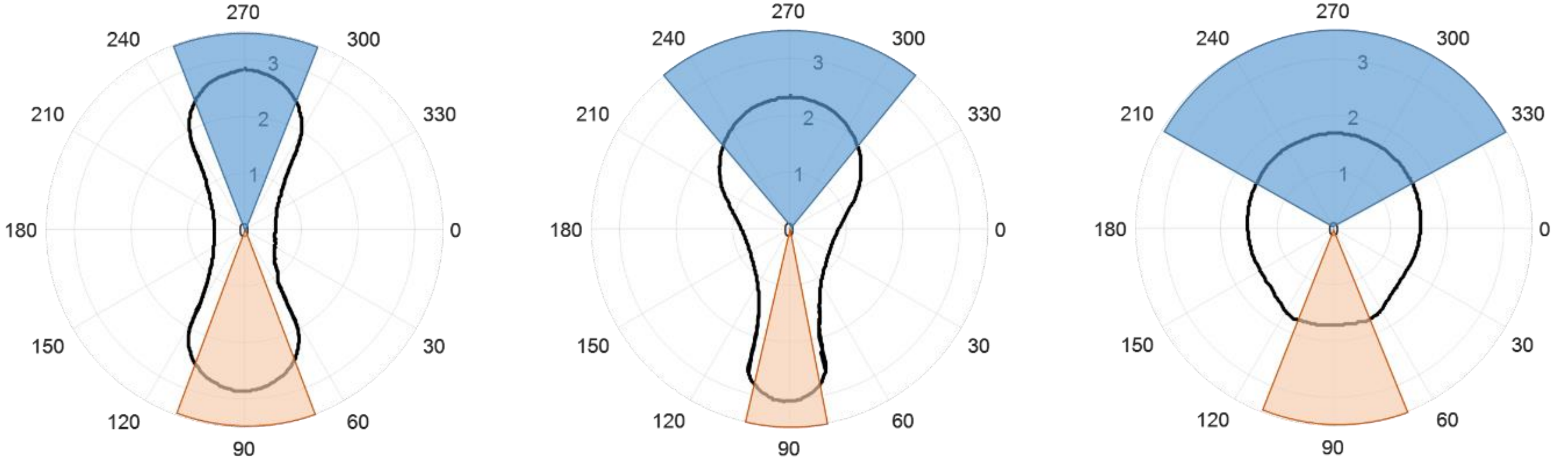

Stage (IV) **Stage (V)** **Stage (VI)**

Figure 3-15. The cropping angles evaluated for leading($\Delta\theta_L$) and trailing edge ($\Delta\theta_T$) at different stages of dispersed phase deformation.

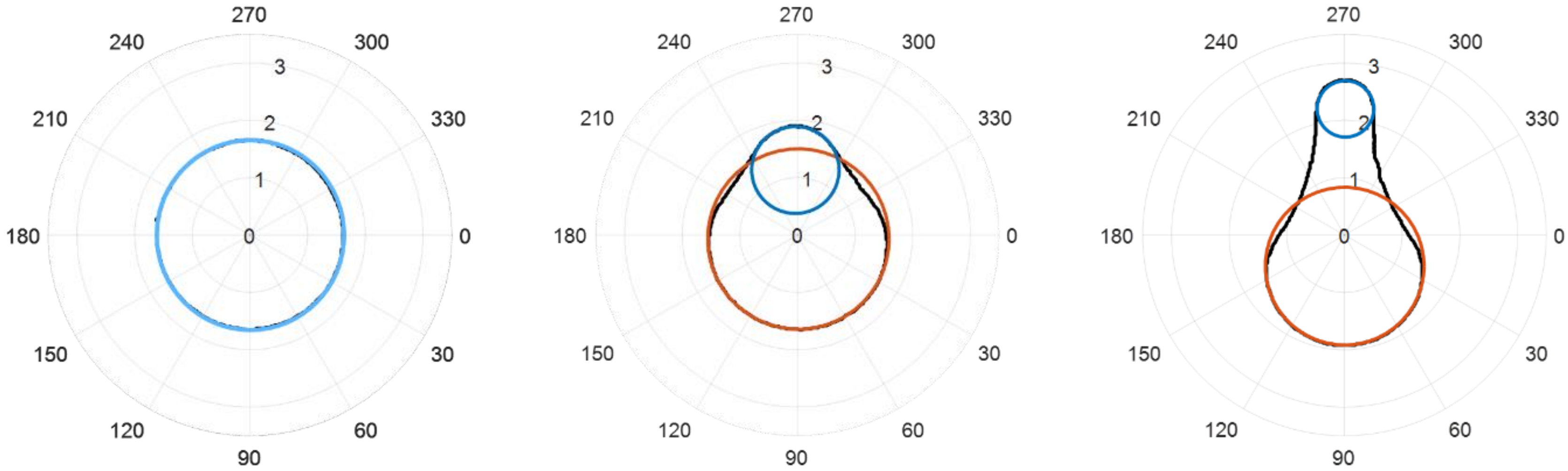

Stage (I) and (VII) **Stage (II)** **Stage (III)**

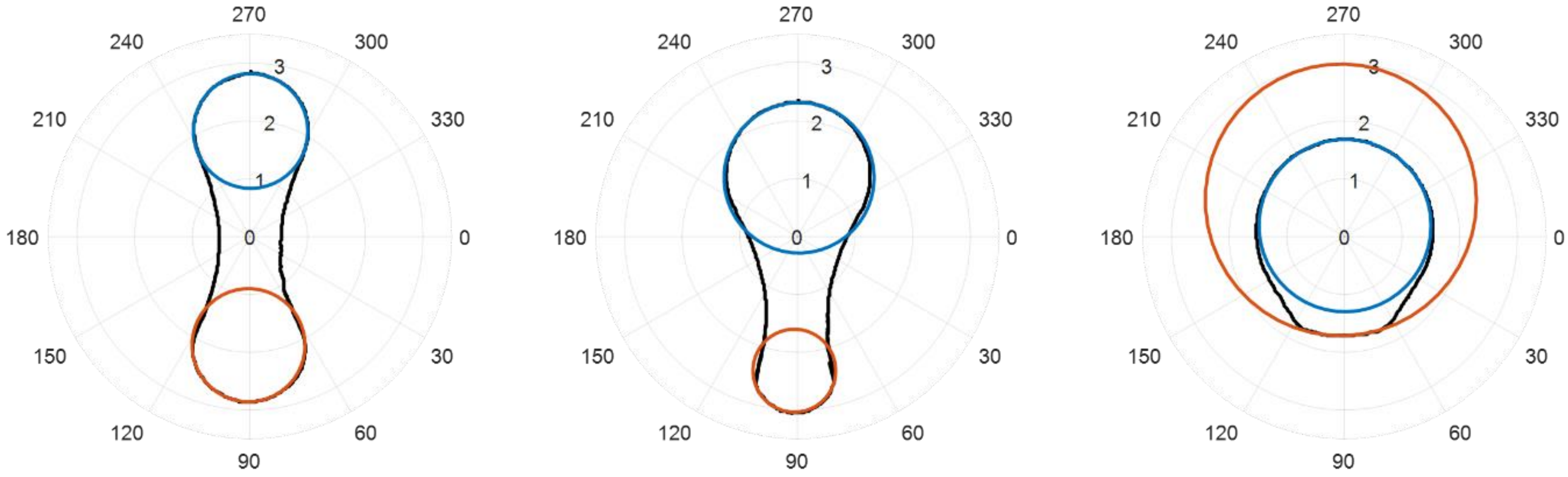

Stage (IV) **Stage (V)** **Stage (VI)**

Figure 3-16. The boundary of bubble and the curvature of leading and trailing at different stages for R_b=1.58 mm.

As shown in Figure 3-15, $\Delta\theta_L$ and $\Delta\theta_T$ of a bubble in stages (I) and (VII) are equal to 180° and the plotted fitted curvature of the edges are coinciding as indicated in Figure 3-16. The bubble in this condition has a uniform pressure distribution within the phase and the pressure can be determined using Eq. (3-1). This condition is highly affected by the ratio of the size of the bubble (R_b) and the pore space (w). For the case of $2R_b/w \ll 1$, the bubble will not be affected by the pore space and the bubble will maintain its uniform pressure as the bubble passes through the pore.

For the case of a bubble with $2R_b/w > 1$, the bubble deforms as it enters the pore geometry. The first deformation step of the bubble is shown in Stage II of Figure 3-15. In this case, the radius of the leading interface is smaller than the trailing edge and consequently $\Delta\theta_L < \Delta\theta_T$. Shown in Figure 3-16 (II), the leading edge has a smaller radius of curvature. Based on Eq. (3-4), the bubble will have positive ΔP^*. This condition in the bubble will continue and the bubbles trailing edge enters the pore geometry and its radius of curvature decreases.

As the leading edge of the droplet passes the pore throat, the radius of curvature of the leading face starts to increase. Stage (IV) occurs when the leading and trailing edge of the bubble has the same curvature ($\Delta\theta_L = \Delta\theta_T, R_L = R_T$). Based on Eq. (3-4), the pressure of the leading and the trailing edge of the bubble will be equal. As the bubble's leading-edge passes stage (IV), R_L will be higher than the trailing edge. In this condition, the bubble will have a negative ΔP^*. This condition remains until the bubble passes the pore space. An interesting finding is a presence of pinning of the dispersed phase as shown in stage (VI). This condition varies based on the acting forces on the interface and it is controlled by the surface tension, the ration of the bubble size to pore width ($2R_b/w$), and the flow rate of the continuous phase. No previous study has investigated this phase condition and its effect on the calculation of pressure. Pinning of the phase on the solid surface will lead to a delay in the recovery of the shape to its spherical shape and an increase in the transit time.

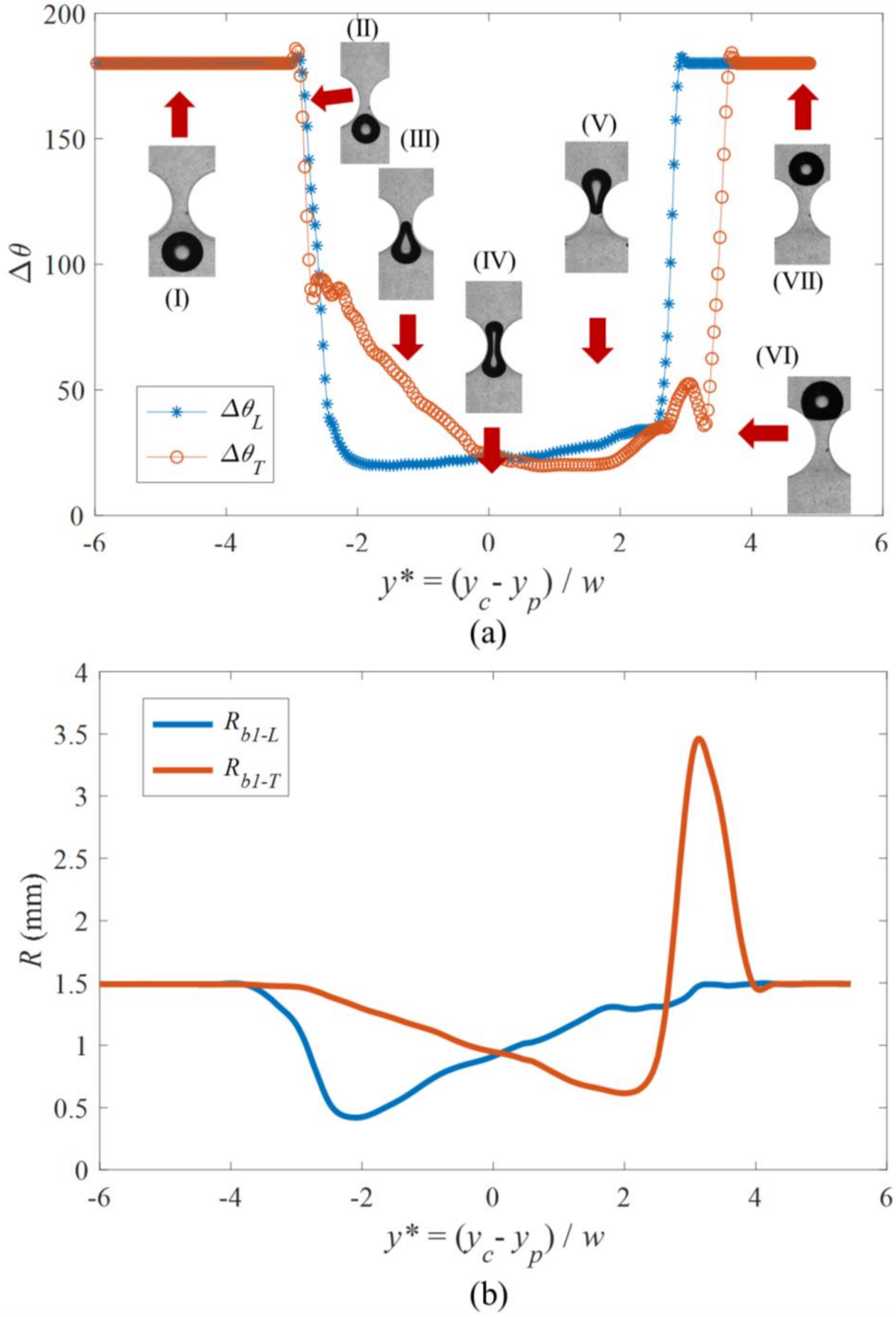

Figure 3-17.The change in (a) the angle to evaluate the curvature and (b) radius of curvature of the leading and trailing edge of a bubble for the location along the pore for a bubble R_b=1.58 mm.

Figure 3-17 (a) presents the instantaneous change in $\Delta\theta$ used to determine the leading and trailing surface curvature and the radius of curvature of the bubble along the pore obtained using the developed method. In these graphs, the location is represented by the normalized location based on the width of the pore throat and offset by the location of the pore space ($y^* = \frac{y_{centroid} - y_{pore}}{w}$). The number of images processed in this study is over 600 which makes the data plotted in the figures essentially a continuous line. Therefore, for clarity of the plots, the data in all further plots are shown as a continuous line.

It can be seen in Figure 3-17 (b) that the bubble has a constant radius of curvature before it reaches the pore located before $y^* = -4$. The same $\Delta\theta$ of 180° is used to evaluate this condition. As the bubble enters the pore geometry due to the reduction in the available area to the flow, the radius of the leading edges of the bubble decreases. With a delay, its trailing edge deforms as it can be seen in Figure 3-17 (a) and (b). The leading edge reaches its minimum value when the leading face is aligned with the pore space ($y^* \sim -2$) and for the case of the trailing edge it occurs further upstream ($y^* \sim 2$) as the bubble exits the pore.

The radius of the leading and trailing edge becomes equal when the bubble's centroid is aligned with the pore throat. This condition can be also seen when the leading and trailing edge have the same $\Delta\theta$ at $y^* = 0$. The radius of the leading edge increases as the bubble moves in the pore and returns to its spherical radius after it exits the pore. For the trailing edge, however, a decrease in the angle and an accompanying peak in the radius are detected (at $y^* \sim -3$). This location corresponds to when pinning of the phase occurs which causes further deformation in the bubble. These conditions are shown in stage (VI) of Figure 3-15 and Figure 3-16.

3.4.3 Repeatability of the shape and velocity measurement calculation

To determine the repeatability of the shape analysis for pressure measurement of a dispersed phase, the deformation of two bubbles with a similar radius of R_{b1} = 1.57 mm and R_{b2} = 1.65 mm at the same flow rate of 0.1 ml/min of the continuous phase are studied. In this comparison, the curvature of the leading and the trailing edges of the bubbles at different locations along the pore throat is determined as shown in Figure 4-18. It can be seen that the change in the radius of the leading curvature of both bubbles starts at the same location and the change and their magnitude are similar. There is a slight change in the magnitude of the highest curvature of the bubble due to the pinning effect. This arises due to the slight difference in the diameter of the bubbles. Based on the result it can be concluded that the image data processing algorithm will give repeatable results.

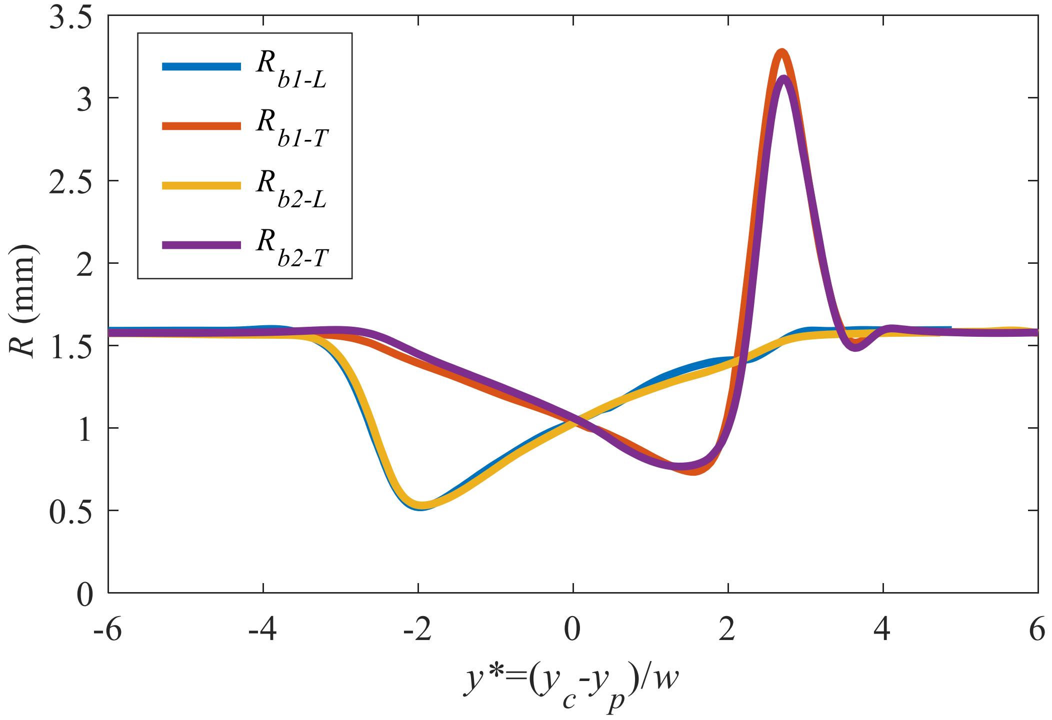

Figure 3-18. Plots of the changes in the leading and trailing face radii of curvatures for two bubbles with similar size R_{b1} =1.57 and R_{b2}=1.65 mm at 0.1 ml/min.

3.4.4 Uncertainty of shape calculation

The first source of uncertainty in the pressure calculation of the dispersed phase is due to the interface detection of the bubble in image binarization. Figure 3-19 shows an example of the detected interface of the bubble and its binarized image. As it can be seen in the detailed view (I), the variation in the intensity of the image at the interface occurs over approximately 2.5 pixels. In this study, the threshold used to evaluate the binary image results in the boundary being at ~1 to 2 pixels in the interface region as depicted in the image.

The next source of error is due to the smoothing of the boundary in the processing of the image to determine the radius of curvature. An example of this step is shown in the detailed view (II) of Figure 3-19. It can be seen that on average, the smoothed boundary will be detected at 1 pixels within the boundary of the binary image. The change in the interface will affect the equivalent and radius of curvature of the phase and ultimately the pressure.

The change in the equivalent diameter (D_{eq}) is determined by comparing the number of pixels describing the interface (~2.5 pixels) with the size of the bubble at its spherical shape (~350 pixels in diameter). Considering the change in the interface in all directions of the bubble, the change in the diameter of a circular bubble is 5 pixels. This value corresponds to a 1-4.5 % error in the diameter calculation.

For the pressure calculated using the detected interface, considering a change of ΔR ~ 2.5 pixels in the radius of curvature of the leading and trailing edge, the corrected change in the radius is:

$$\frac{1}{\Delta R_{corrected}} = \frac{1}{R_L + \Delta R} - \frac{1}{R_T + \Delta R} \tag{3-7}$$

The $\frac{1}{\Delta R_{corrected}}$ has its minimum value for the case of the highest R_T and lowest R_L and has its maximum for vice versa. Considering these locations for the smallest bubble in this study, the change in the radius is:

$$-0.0121 < \frac{1}{\Delta R_{not-corrected}} = \frac{1}{R_L} - \frac{1}{R_T} < 0.0121 \tag{3-8}$$

$$-0.0114 < \frac{1}{\Delta R_{corrected}} = \frac{1}{R_L + \Delta R} - \frac{1}{R_T + \Delta R} < 0.0114 \tag{3-9}$$

The uncertainty associated with this approach will be relative to the size and the overall sphericity of the bubble. The highest number of pixels removed from the interface (2.5 pixels) and the smallest size will be considered to evaluate the highest uncertainty. This variation corresponds to a 5.5 % error in the change in the radius of curvature. This uncertainty will decrease as the size of the bubble increases. Having a smaller field of view for the image will result in a higher number of pixels for the bubble which ultimately leads to a decrease in the uncertainty.

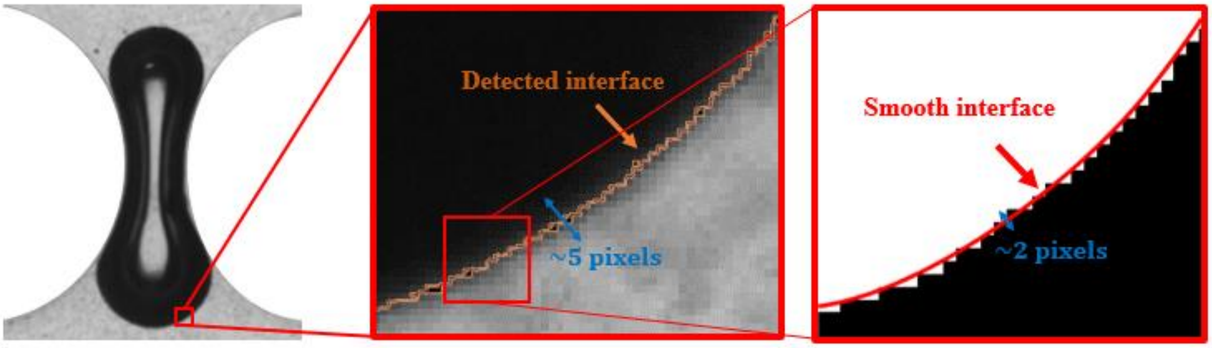

Figure 3-19. The zoomed-in picture of the interface of a bubble and the location of the detected interface.

In addition to the aforementioned source of uncertainty, the accuracy in the curvature detection of the trailing edge of the bubble is also a function of the number of images. This can be highly important when calculating the radius of the curvature in the detachment of the bubble from the surface. As the bubble reaches its maximum radius of the curvature (a flat surface in some cases), having a detailed study of the flow in this condition is highly affected by the number of images at this condition. Therefore it is highly recommended to evaluate the pressure of the dispersed phase using a high-speed camera in a zoomed-in field of view.

3.5 Results

3.5.1 Effect of size and flow rate of bubble on the change of the bubble's leading and trailing curvature

The variation of the radius of curvature of the leading and trailing edges of bubbles having different sizes and flow rates are shown in Figure 3-20. Three different bubble sizes of 1.6, 2, and 2.8 mm were studied at two flow rates of 0.1 and 0.2 ml/min of the continuous phase. The bubbles having the same size are plotted as pairs and for the clarity of the plots, each pair is separated by a constant gap. The radius of these bubbles is determined using the shape analysis approach discussed in Section 4. To have a better comparison of the cases, the location is represented by the normalized difference between the y position of the centroid of the bubble ($y_{centroid}$) at each step and the location of the pore throat (y_{pore}). Using this approach, $y^* = 0$ corresponds to the location where the centroid of the bubble is aligned with the pore space.

As shown in Figure 3-20, a similar trend of the change of the radius of curvature of the leading and trailing edges was observed for all cases. It can be seen that the change in the radius of curvature starts at different locations depending on their size and flow rate. The bubble with a larger radius starts to deform earlier, upstream ($y^{*} \sim -5$ for R_b = 2.8 mm and $y^{*} \sim -2.8$ for R_b = 1.6 mm). This variation is due to larger $\frac{2R_b}{w}$ for the larger bubble that results in more deformation caused by the confined walls compared to the smaller ones.

Comparing the results represented in Figure 3-20 also indicates that the size and the flow rate have significant effects on the change in the shape of the bubbles. Higher peaks were detected for R_b = 2.8 mm when the bubble is detaching from the solid interface. It indicates that at a constant flow rate, the change in the radius of the trailing edge intensifies as the size of the bubble increases. Also, for the same size of the bubble, higher deformation is observed at higher flow rates of the continuous phase.

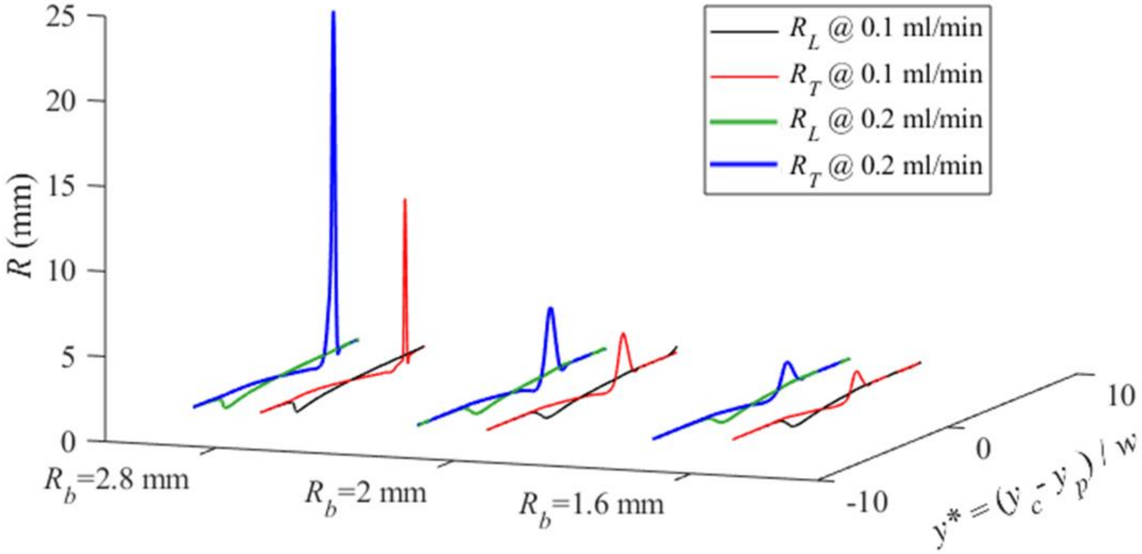

Figure 3-20. The change in the radii of curvature with respect to flow rate for different bubble sizes plotted as pairs.

An increase in the duration of the range of the location of the curvature changes suggest that different length scales can be also used to normalize the location. Figure 3-21 shows that having the size of the bubble (R_b) as the length scale for the normalization of the location shows that the same base phenomenon in the change of shape of the bubble occurs on entering the pore at the same flowrate. It can be seen that for the flow at 0.1 ml/min Figure 3-21 (a)), the bubble starts to deform around a diameter before the pore ($y^o \sim -2$) throat and the bubble gains its spherical shape more than a diameter after the pore ($y^o \sim 2.5$). For the higher flow rate, shown in Figure 3-21 (b), the range of the location where the bubble deforms increases ($-2.5 \leq y^o \leq 3$). This indicates that the region of the interaction of the bubble and interface is proportional to the size and the flow rate of the continuous phase.

For all bubble sizes, the bubbles leading and trailing interfaces decrease as the bubble moves further into the pore until a radius reaches a minimum value. In the case of the leading edge, the minimum occurs when the leading edge of the bubble is aligned with the pore throat ($y^o \sim -$ 1.9 for R_b=2.8 mm and $y^o \sim -$ 1.5 for R_b=1.6 mm). For the trailing edge, the minimum occurs further into the pore when the trailing interface is aligned with the pore throat ($y^o \sim 1.5$ for R_b=2.8 mm and $y^o \sim 1.1$for R_b=1.6 mm). The radius of the leading and the trailing edges of the bubble becomes equal where the centroid is aligned with the pore throat (y^o =0).

One of the interesting findings of this study is observed in stage (VI) of Figure 3-16 which corresponds to the peak detected in the radius of the trailing edge shown in Figure 3-20 ($y^* \sim 4.4$ for R_b = 2.8 mm and $y^* \sim 2.7$ for R_b = 1.6 mm). In this region, the radius of curvature of the trailing edge increases and reaches a value higher than the equivalent radius of the bubble before it reaches the pore. This phenomenon occurs due to the pinning effect when the bubble exists in the pore geometry which leads to further deformation of the bubble. After the bubble passes this stage, it regains its spherical shape in the stage (VII) where the leading and the trailing edge of the bubble are equal to unity. In this study due to the presence of the bulk motion of the continuous phase, the driving force overcomes the interfacial forces and ultimately, detachment of the bubble from the interface occurs.

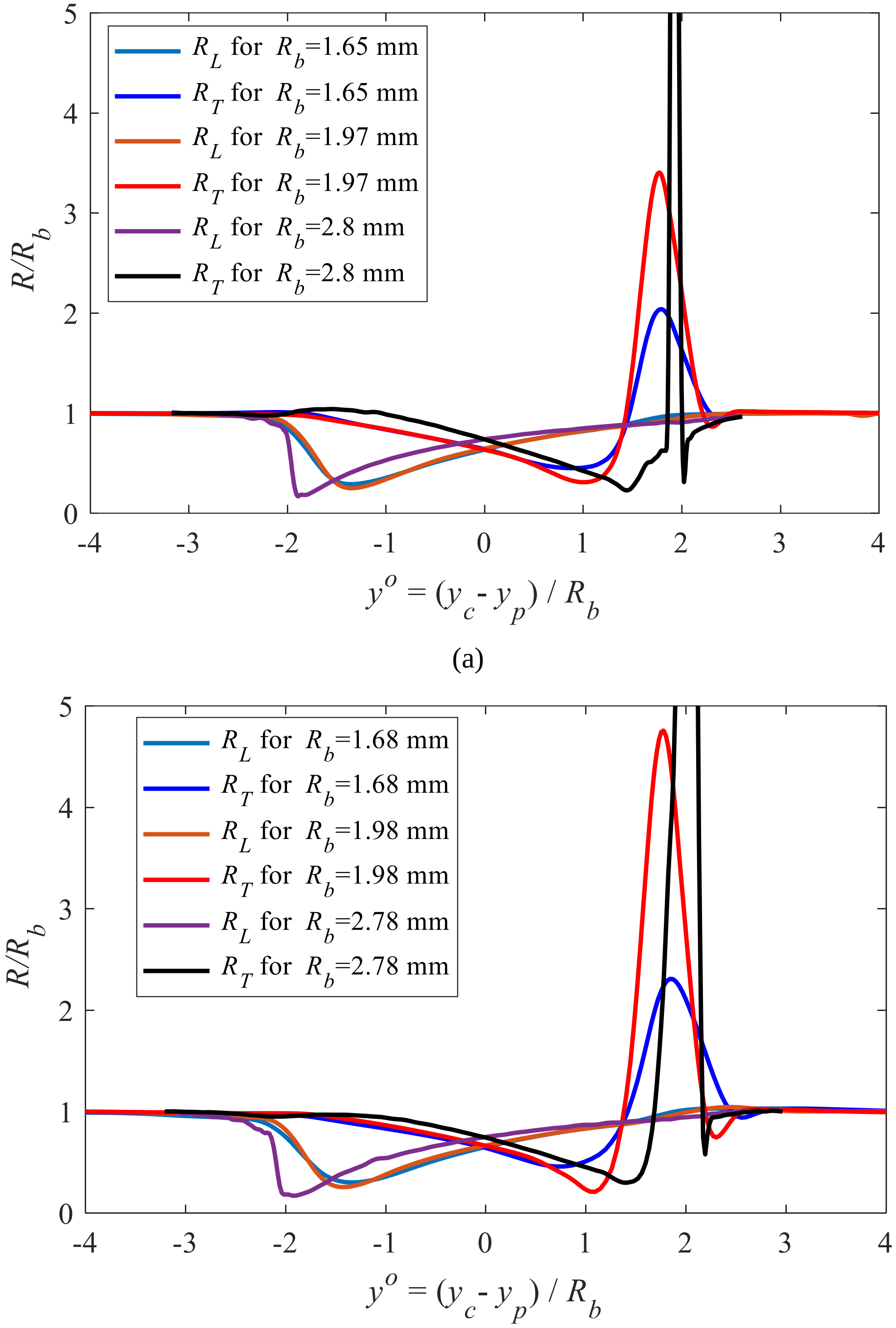

(a)

(b)

Figure 3-21. Plots of the changes in the radii of leading and trailing face of different size of bubbles moving at (a) 0.1 ml/min and (b) 0.2 ml/min, normalized with the size of the bubble (for clarity the graphs are zoomed in and the peak of the RT of the larger bubble is not shown.)

Stages of the deformation of two sizes of bubbles exiting the pore geometry are shown in Figure 3-22. The contact area of the bubble with the pore surface is highlighted by red lines in the sub-figures and the location of the upper contact point is marked by a blue dashed line. It can be seen for both sizes of the bubble shown in Figure 3-22 (a) and (b), as the trailing edge of the bubble passes through the pore geometry the contact area between the bubble and the pore geometry decreases. It can be seen that there is a decrease in the contact area that occurs due to the upward movement of the lower contact point of the bubble with the pore wall due to the upper contact point of the bubble remaining at the same location.

As the bubble moves further, it exits the pore and the trailing edge of the bubble becomes closer to the upper contact point. The bubble maintains its contact point with the solid surface as it exit the geometry. The duration of this stage however varies depending on the size of the bubble. As shown in Figure 3-22 (a), for the case of the smaller bubble, the interaction continues until the trailing edge becomes flat. After this location, the force acting on the bubble due to the bulk motion of the continuous phase moving upward in the channel overcomes the interfacial forces between the interface of the bubble and the pore space. For the larger bubble shown in Figure 3-22 (b), pinning is stronger resulting in more deformation of the trailing edge of the bubble. In this case, the equivalent diameter of the bubble is larger, based on Eq. (3-1), the difference between the internal pressure of the bubble compare to the surrounding fluid is smaller. The bulk motion of the continuous phase will result in more deformation of the interface and the detachment occurs further upstream. This phenomenon results in a concave shape of the trailing edge of the bubble as shown in location (e) of Figure 3-22 (b). Therefore in this condition, the negative radius of curvature of the trailing edge will be expected due to the pinning effect.

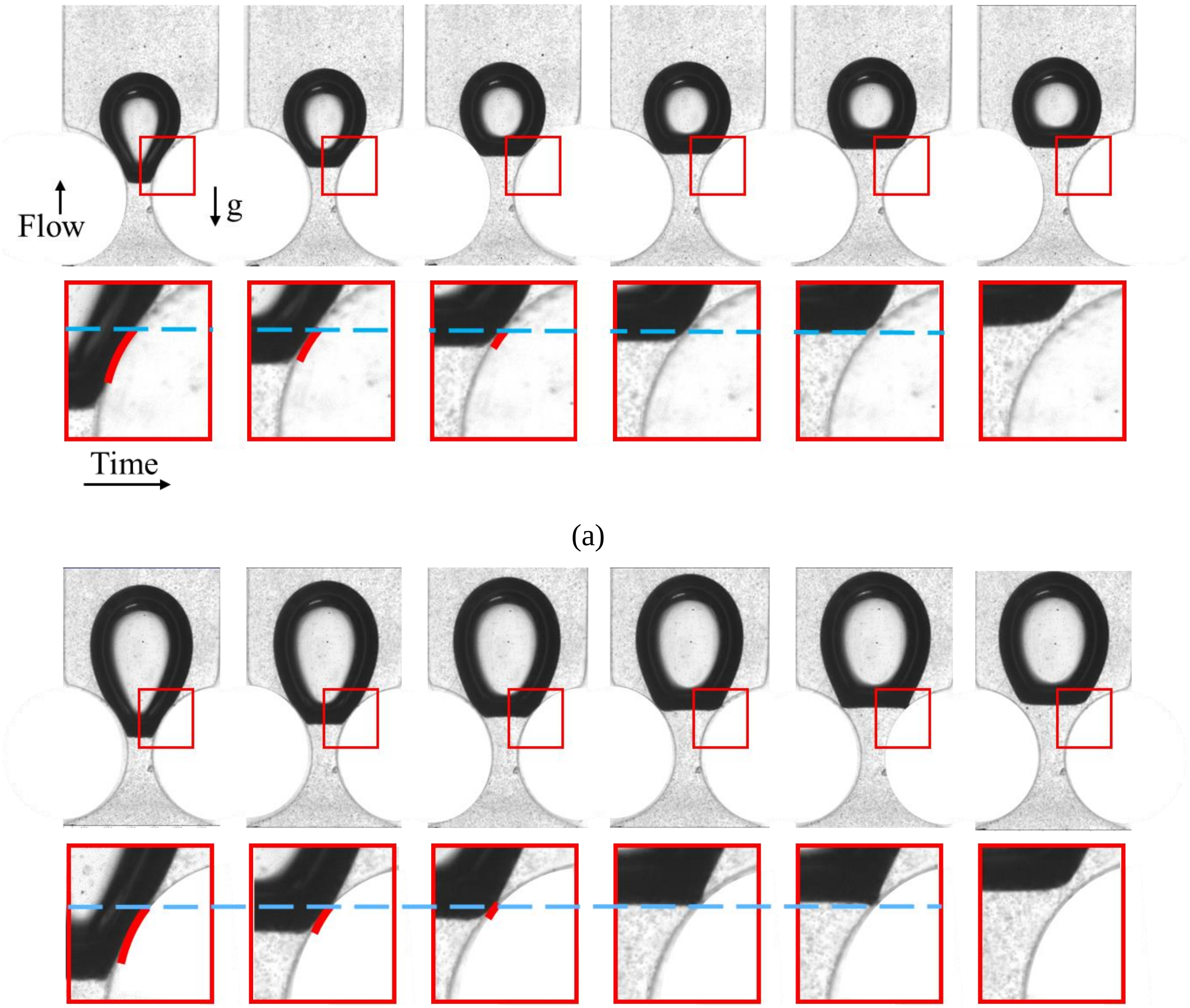

(a)

(b)

Figure 3-22. The change in the contact line of bubbles exiting the pore at 0.2 ml/min for (a) R_b =2.8 and (b) R_b =4.7 mm.

3.5.2 Transit Time and velocity of the bubble

Changes in the instantaneous velocity and the acceleration of the centroid of bubbles passing through the pore are shown in Figure 3-23(a) and (b) for a bubble for R_b =1.65 mm moving at 0.2 ml/min. The pressure change difference between the leading and trailing edges of the bubble was also determined using Eq. (3-4) and represented in Figure 3-21 (c). To have a better comparison of the cases, the velocity is normalized based on the terminal velocity of the bubble before it reaches the pore geometry and the location is normalized using the size of the bubble (R_b).

As shown in Figure 3-23(a) as the bubble gets closer to the pore entrance, the velocity of the centroid increases and reaches a maximum due to the deformation of the leading edge. As the leading edge moves further into the pore, it can be seen that the bubble decelerates and the velocity decreases. As shown in Figure 3-23(c), the pressure difference between the bubble faces has its maximum value which corresponds to the critical pressure required for the bubble to enter the pore. The driving force provided by the continuous phase overcomes this excessive pressure drop and the bubble enters the pore throat.

The bubble accelerates again after it passes the pore and prepares to exit the pore geometry. In this study due to the interaction of the bubble and the pinning of the phase, the bubble velocity decreases further and it reaches a minimum value. The deceleration can be observed at $y^{*}\sim 2.5$ where the phase pinning occurs. An excessive driving force is also required in this location to move the bubble further through the pore. As the bubble detaches from the solid surface its velocity increases and returns but to the bubble's terminal velocity.

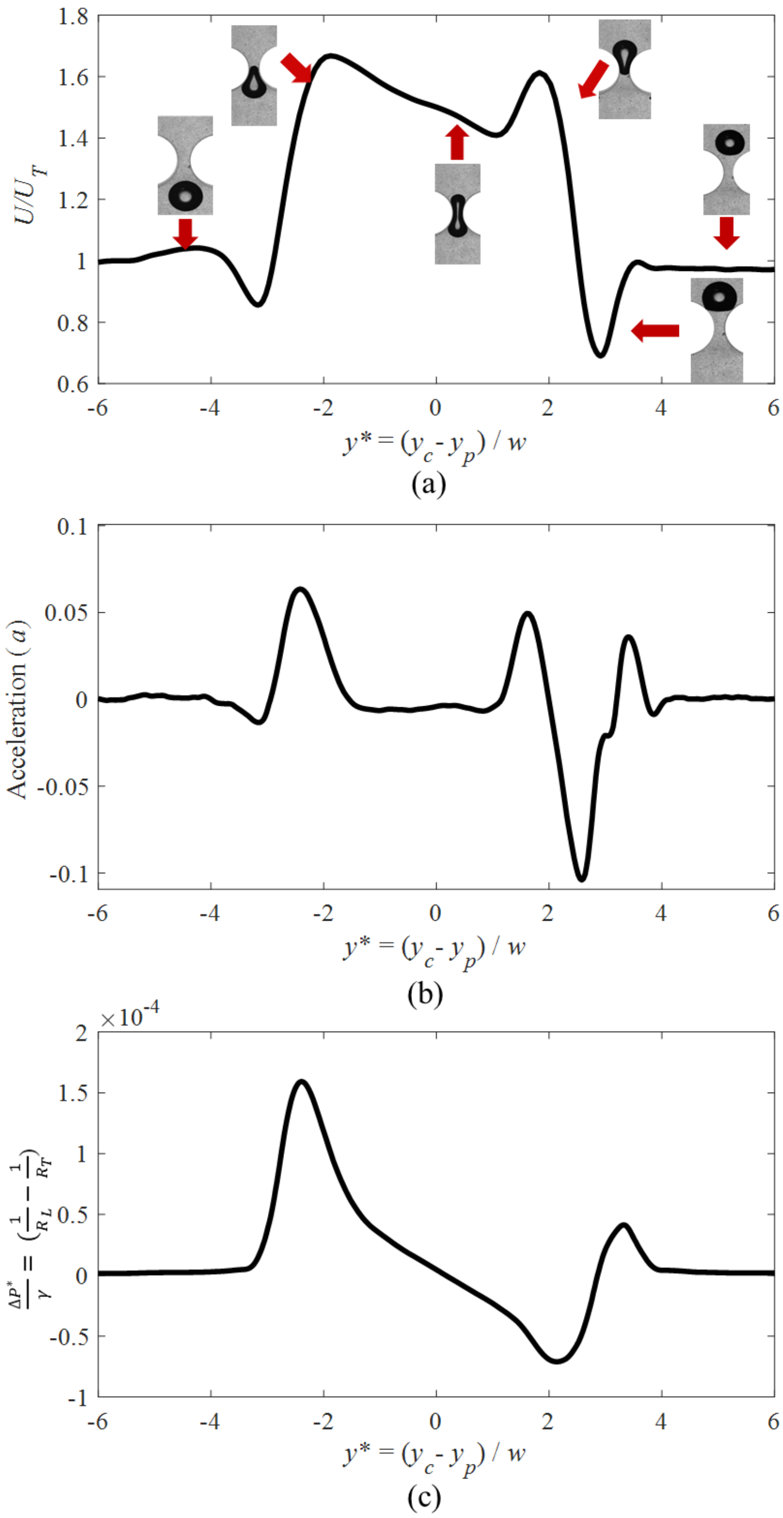

Figure 3-23. Graph of the change in the average (a) velocity (b) acceleration of the centroid and (c) pressure change in the bubble at different locations for R_b =2.8 mm moving at 0.2 ml/min.

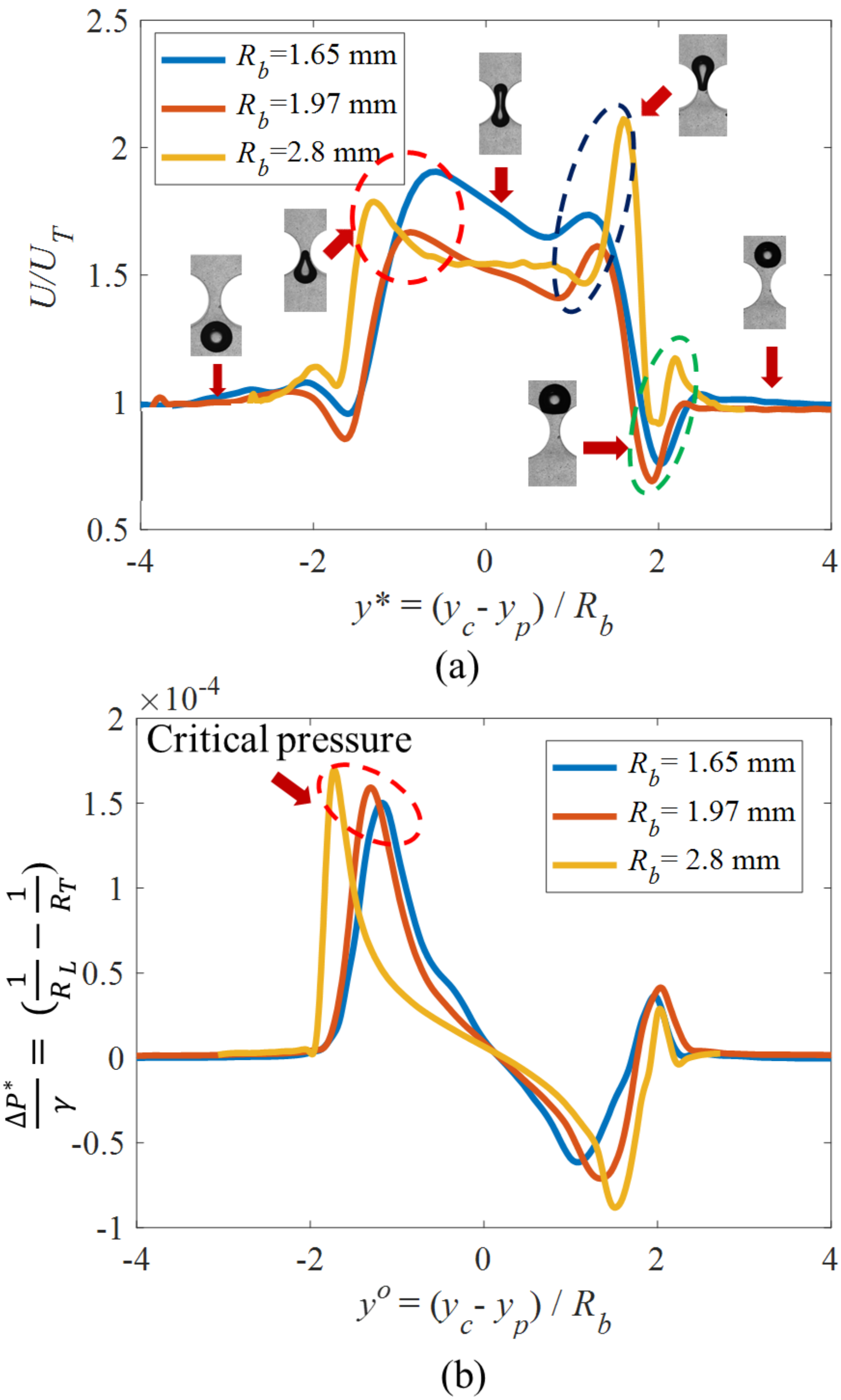

Figure 3-24. Graph of the change in the average velocity of the bubble at different locations.

Changes in the velocity and the pressure of bubbles of different sizes moving at the same flow rates are shown in Figure 3-24. It can be seen that the velocity is highly affected by the size of the bubble. A similar trend of the change in the velocity and pressure is observed for all cases. It can be seen that for the larger bubble, the change in the velocity occurs further downstream and upstream. This can be observed by the location of peaks of the change in velocity as highlighted in Figure 3-24 (a). As the ratio of $2R_b/w$ increases, the deformation occurs further upstream before it reaches the pore and further downstream as it exits the pore space. The constant velocity region in the pore is extended and a higher increase in the velocity is observed for the larger bubbles. The higher peak of the change in the pressure also suggested that a higher driving force is required for the bubble to overcome the entrance pressure.

The transit time required for the bubbles was also determined based on the required time for the bubble to pass the pore geometry and they are summarized in Table 3-2 and Figure 3-25. It can be seen that for the same flow rate more time is required for the larger bubble to pass through the pore. This is due to the difference in the mobility of the phases and the resulting deformation. Bubbles having a similar size move faster at a higher flow rate due to the available driving force provided by the continuous phase to the bubble passage.

Table 3-2.Table of the transit time of bubble passing through a 1 mm pore for different sizes and flow rates

Flow rate (ml/min)	R_b (mm)	Transient time (s)
0.1	1.65	6.81
	1.97	8.60
	2.8	15.00
0.2	1.68	4.71
	1.98	5.26
	2.78	7.14

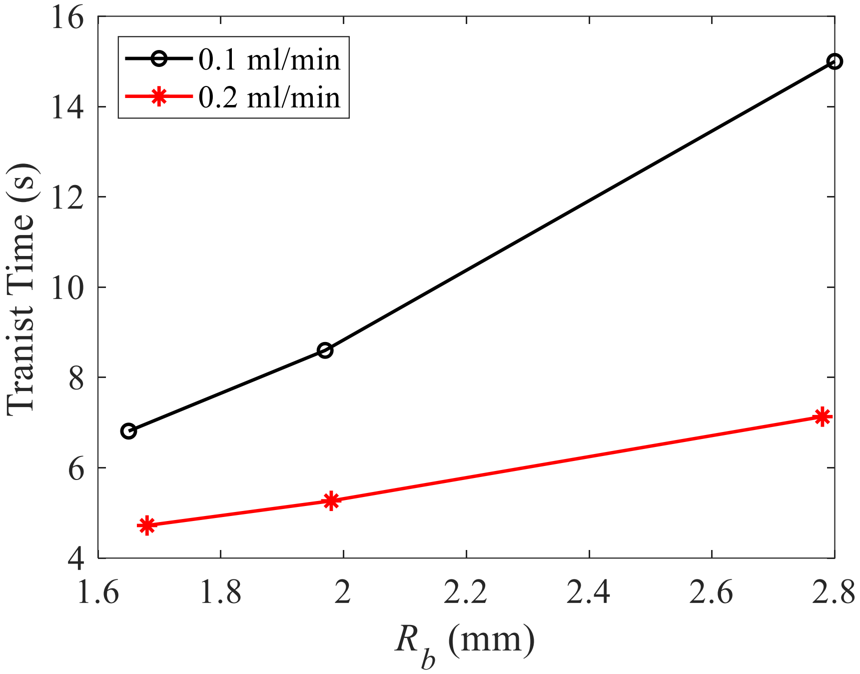

Figure 3-25. The transit time of bubble passing through a 1 mm pore for different sizes and flow rates.

3.6 Conclusion

The present study was designed to introduce a new methodology to evaluate the pressure change of an isolated bubble and determine the effect of phase pinning on the motion of an isolated air bubble passing through a 2D pore. This motion was evaluated by considering the bubble’s deformation, velocity, and pressure change. These characteristics were experimentally evaluated by a non-intrusive imaging system. The images obtained from the study are analyzed to evaluate the interface and the location of the phase. The pressure along the bubble was determined using the combination of image analysis obtained from a shadow-graphic optical system and the Laplace equation.

A novel methodology was introduced to track the bubble deformation and the change in the radius of curvature of the leading and trailing face of the bubble to evaluate the pressure change based on the Jamin effect. In this approach, the interface between the phases was detected and the curvature along the bubble was determined. Using the change in the curvature around the bubble the corresponding locations to evaluate the radius of curvature of the leading and trailing edges were selected. The methodology showed repeatable results and the maximum uncertainty introduced by the edge detection was 5.5%.

Different sizes of bubbles and flow rates were considered to study the effect of flow conditions on the deformation, velocity, and acceleration of the bubble. A similar trend in the motion of the bubble was observed for different sizes and flow rates. Phase pinning was also captured for the bubble exiting the pore. The investigation has shown that the bubble deformation intensified as the size of the bubble and the flow rate of the continuous phase increased. The bubbles’ phase pinning intensified as the size of the bubble and the flow rate increased. It can be seen that a higher flow rate due to the motion of the continuous phase results in the faster passage of the bubble.

However, the effect of the pinning results in a slower motion of the bubble and a resultant increase in the transit time through the pore.

This work contributes to existing knowledge of multi-phase flow through porous media by providing experimental insights on the limitation of previous studies by accounting for phase pinning when a dispersed phase passes through a pore space. The methods used for the pressure calculation may be extended to 3-D flow motion and the motion of multi-bubble/droplet flow in a porous media.

Chapter 4: Determining the pressure distribution of a multi-phase flow through a pore space using velocity measurement and shape analysis[6]

This chapter presents, a novel combination of existing theoretical models and optical diagnosis to determine the pressure distribution in a multiphase flow. The flow of a dispersed phase (glycerol) through a pore geometry in the presence of a stationary continuous phase (canola oil) is considered in the experiments conducted using conventional particle shadowgraph velocimetry (PSV) setup.

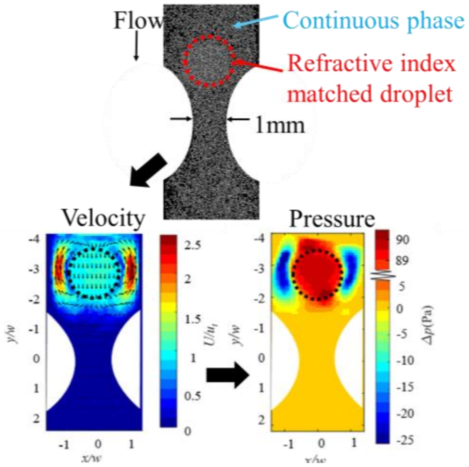

Graphical Abstract Chapter 2

This work shows that quantitative information about the deformation behavior of a dispersed phase can be used to determine the field parameters and investigate the pressure gradient properties of a multiphase flow. Research initiatives that aim at building a stronger understanding of multiphase flow through pore geometries can benefit from this work which demonstrates the capability of the presented combination of experimental and analytical techniques.

4.1 Introduction

The prevalence of the multi-phase flow can have several advantages in different applications such as oil recovery [4], food industry [1], [210], and macromolecular delivery [2], [211]. For in-

---

[6] This chapter with some modifications has been published as Ansari, S. & Yusuf, Y & Sabbagh, R. & Nobes, D. S. (2019). “Determining the pressure distribution of a multi-phase flow through a pore space using velocity measurement and shape analysis”. *Measurement Science and Technology* 30. 10.1088/1361-6501/ab0afc

situ oil recovery processes, however, the presence of an emulsion is typically an undesired phenomenon since it decreases the oil production efficiency by increasing the production of fine sand particles [5], [83], [109], [164]. The transport of emulsions through a medium made up of pore networks leads to the encapsulation of micro-and macro-scale materials in the dispersed phase. This can then result in one of the main failure mechanisms, the blockage of pore spaces that will directly impact the pressure distribution in the system [6], [212], [213]. The resulting pressure loss can also have a cumulative effect by causing the precipitation of salts [214] carried in the fluid due to its effect on the reaction kinetics [215]. To describe the performance of the system behavior with respect to the pressure distribution requires a comprehensive understanding of the interactions between all present phases. To quantitatively characterize the transportation through a pore space the respective influence of the solid boundaries and emulsions on field parameters and the deformation properties of the dispersed phase is therefore important.

Studies on emulsion flow through different geometries show emulsions intensify particle transportation compared to single-phase fluid flows. The flow behavior of emulsions passing through a rectangular channel [19], [20], [195] has shown that the interaction between the dispersed phase and the surface of the particles is a strong function of the dispersed phase's velocity, viscosity, surface tension, and other interfacial properties [19], [20], [22], [23], [195]. In addition to the properties of the phases, geometric characteristics such as the ratio of the size (radius) of the dispersed phase to the size of the channel, channel aspect ratio and the shape of the cross-sectional area of the channel can significantly affect phenomena and transport in all the phases [19], [20], [195]. The effects of these parameters may become more pronounced for a flow within geometries that have varying cross-sections. These types of geometries can be found in flow media such as oil reservoirs where emulsion flows are commonly present in the porous media.

The bulk flow through porous media has been studied using core flooding approaches [216]–[218] and has shown that the flow encounters more resistance within the pores compared to single-phase flows. The presence of emulsions in porous media thus results in a reduction of the permeability of a porous medium due to the pore-level interactions [5], [83], [109], [164]. Therefore, a clear understanding of the interactions between the phases is required. These forces ultimately affected the pressure distribution of phases within the pores.

Studies on two-phase flows discuss the importance of interfacial interactions of the phases on particle transportation [19], [20], [195]. In a stationary two-phase system, particles can be in equilibrium in the dispersed or continuous phases or the interfaces within [192]–[194], [219], [220]. The state of such an equilibrium depends on the balance of gravity, buoyancy, hydrostatic, and the surface tension of the interface. For the flow of emulsions compared to the stationary systems, however, the interface shape also has an effect on the position of the transported particle [192]–[194], [219], [220]. Interface conditions can be expected to be highly influenced by the pressure distribution in the flow field which is affected by the geometry of the channel.

The pressure distribution in the flow of emulsion through porous media can be measured using direct or indirect methods [221], [35]. In most applications, bulk properties determined by direct measurement of pressure are commonly used as design parameters [21], [216]. Such measurements use a core sample as the porous medium which makes the procedure relatively simple to operate. The direct measurement approach provides single-point measurements within the field which often is not sufficient to form a detailed understanding of the interactions between the emulsions and the pores at the pore-scale. Indirect pressure measurements, however, can determine a pressure field which enables in-depth analysis of the interfacial interactions.

The pressure field in the single-phase flow through a controlled geometry can be determined numerically or experimentally [222], [223]. Depending on the spatial and temporal characteristics of the information that needs to be extracted, the pressure gradient can be calculated using either the Eulerian or Lagrangian approach. Determination of the pressure distribution of two-phase flows, however, is a challenging task to achieve since the interfacial forces can be dominant [224]. The application of various numerical methods to determine the pressure field in a flow media that include pore networks have been demonstrated [225], [226].

Having the velocity distribution of the flow enables a pressure calculation by applying equations that govern the system [221], [222]. Particle shadowgraphic velocimetry (PSV) can be applied to determine the velocity distribution in the flow of an oil-in-oil emulsion through pore geometries [13]. To measure the velocities within the phases, the fluids were selected to have the same refractive index to eliminate the effects of light distortion. The velocity in the domain can be determined by measuring the motion of the respective tracer particles added to each phase.

Deformation of the dispersed phase can be related to a pressure distribution or gradient of the capillary pressure within the bubble or droplet. The Jamin effect [21], [35], [166] describes this as the dispersed phase undergoes stretching by assuming longitudinal symmetry and that the system is under equilibrium. Shape analysis of the dispersed phase from image data can therefore be used to interpreted pressure. Deformation of specific features can be used to identify the pressure distribution which can be verified by using results from the indirect determination of pressure, such as calculating pressure from a measurement of the velocity field [227]. To the best of the authors' knowledge, there are only a few numerical and experimental studies that have focused on pore-scale measurement of pressure in a multi-phase flow through porous media [21], [30], [35], [118], [121], [166].

This work develops a methodology to determine the pressure gradient by combining the results from the measurement of the velocity field of an initially-stationary continuous phase and from shape analysis of a dispersed phase that undergoes deformation. The pressure gradient is the parameter that is ultimately sought because its characteristics are directly related to the occurrence of scaling and pore plugging which are the common failure mechanisms [228] for flows in porous media. The flow of a droplet passing through a single-pore geometry in the presence of a stationary continuous phase is considered here to lead to future investigations that will study the flow through a more complex geometry such as an entirely porous medium. The effect of the size of a droplet on the pressure drop is also discussed.

4.2 Experimental setup

Micro shadowgraph velocimetry (μ-PSV) is used to determine the velocity distribution in the flow of both phases. The images are also used to perform a shape analysis of the dispersed phase. The experimental setup is shown in Figure 4-1 consists of a camera, a light source, and an assembly that contains the flow cell. The camera (4M180, IO Industries Inc.) used in the setup has a resolution of 2048 × 2048 pixels and can run at frequencies up to 200 Hz. The camera is coupled with a 50 mm lens to focus on the region of interest including the droplet and the tracer particles added to the phases. The camera is connected to a computer through a direct storage unit (DVR Express Core 2, IO Industries Inc.) to allow high-speed data collection over longer durations (~15 minutes). The flow field in this experiment is illuminated using an LED panel (BX0404-520 nm; Advanced Illumination Inc.) emitting green light in a continuous mode.

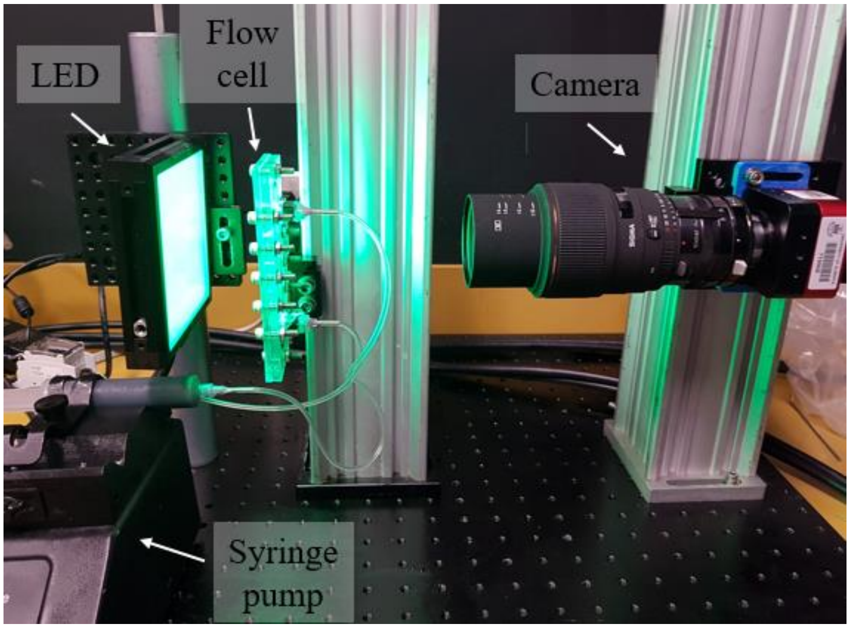

Figure 4-1. An image of the main components of the experimental setup.

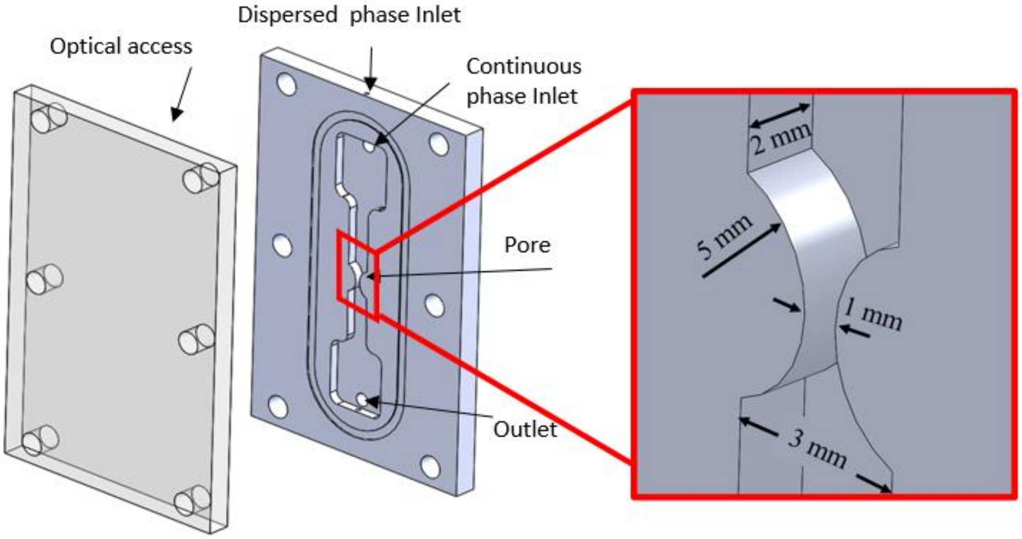

Figure 4-2. A schematic of the manufactured flow cell containing a 1mm pore geometry with the detailed view.

The design of the flow cell containing the single pore geometry is shown in Figure 4-2. The desired features of the channel are manufacturing from a photo-reactive resin using the stereolithography (SLA) additive manufacturing technique (Form 2, Formlabs Inc. USA). Clear optical access to the flow cell is maintained by using a window made from transparent acrylic. As shown in the detailed view in Figure 4-2, the single pore space is constructed as a 2D flow geometry using two pillars having a radius of 5 mm that mimics two adjacent spherical particles separated by 1 mm at the pore throat. The depth of the channel was also set to be 2 mm.

A dispersed phase of a single glycerol droplet flowing in a continuous phase of canola oil is used in the experiments. Table 4-1. The physical properties of fluids at 20 °C [209], [229] summarizes some of the important physical properties of these fluids. They are selected for their similar refractive indices which allows clear imaging of particles within the droplet for velocity determination without light distortion. The refractive indices and viscosities of these fluids are measured using a refractometer (Abbe-3L, Bausch, and Lomb) and a rotational rheometer (Rheolab QC, Anton Paar GmbH), respectively.

Table 4-1. The physical properties of fluids at 20 °C [209], [229].

	Viscosity (Pa.s)	Density (g/cm^3)	Refractive index	Surface tension (mN/m)
Glycerol	1.412	1.26	1.4723	64
Canola oil	0.074	0.92	1.4730	32

The continuous and the dispersed phases are injected from their respective inlet ports as indicated in Figure 4-2. The difference between the densities of these two immiscible phases is the primary driving force for the relative motion of the phases. For these experiments, both fluids were introduced from the top. For all experiments, the continuous phase remained stationary and the dispersed phase was injected as needed using a syringe pump (PHD 2000, Harvard Apparatus) for controlled volume.

A sample raw image for the tracer particle field is shown in Figure 4-3 (a). In order to distinguish between the two phases, two different seeding particles were used. The continuous- and dispersed-phases were seeded with 20 µm and 40 µm spherical polymer beads (Dynoseeds®, Microbeads, Norway), respectively. The interface of the phases cannot be distinguished due to the matching of the refractive indices. The relative motion of the droplet in the continuous phase, however, allows the anticipated location of the dispersed phase to be detected as highlighted in Figure 4-3 (a) by the dashed line. In order to have a clear detection of the location of the droplet, the two phases were masked based on the respective sizes of the tracer particles as shown in Figure 4-3 (b) and (c).

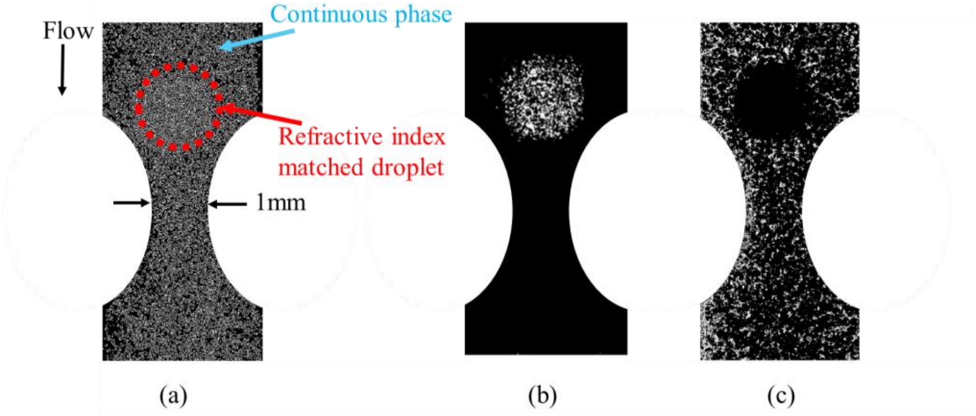

Figure 4-3. An example image of (a) the entire seeded particle field including both continuous and dispersed phases and isolating (b) the continuous phase and (c) the dispersed phase.

The motion (and the deformation) of the phases were calculated from sets of data containing 2,000 images. These images are processed as sequential frames using commercial software (DaVis 8.4, LaVision GmbH) to determine the velocity field. Masking is applied to remove the stationary regions of the flow channel from the raw images. An adjacent frame cross-correlation algorithm with decreasing window size (48 × 48 pixels to 16 × 16 pixels with 50% overlap) was used to obtain the velocity vector map of each phase as shown in Figure 4-4. In this figure, only every 5th vector is shown for clarity and velocities have been scaled here relative to the maximum velocity in each data set.

Uncertainty in the velocities can be estimated by assuming the displacement measurement uncertainty in the PIV analysis approach is ~ 0.1 pixel [230]. Given the typical displacements in this slow flow field (~ 4 pixels) result in an uncertainty in the determination of the velocity of about 2.5%. The uncertainty was also calculated from correlation statistics using commercial software (DaVis 8.4, LaVision GmbH) [231]. The maximum error in the velocity field was calculated to be 2.2% for the velocity in x-direction, 4.6% for the velocity in y- direction and 4.8% for average velocity. This is a preliminary estimate of uncertainty as particle size in this study is significantly larger than optimal for PIV analysis as particle size is used to discern the dispersed phase in the describe method. Further investigation is needed to address this.

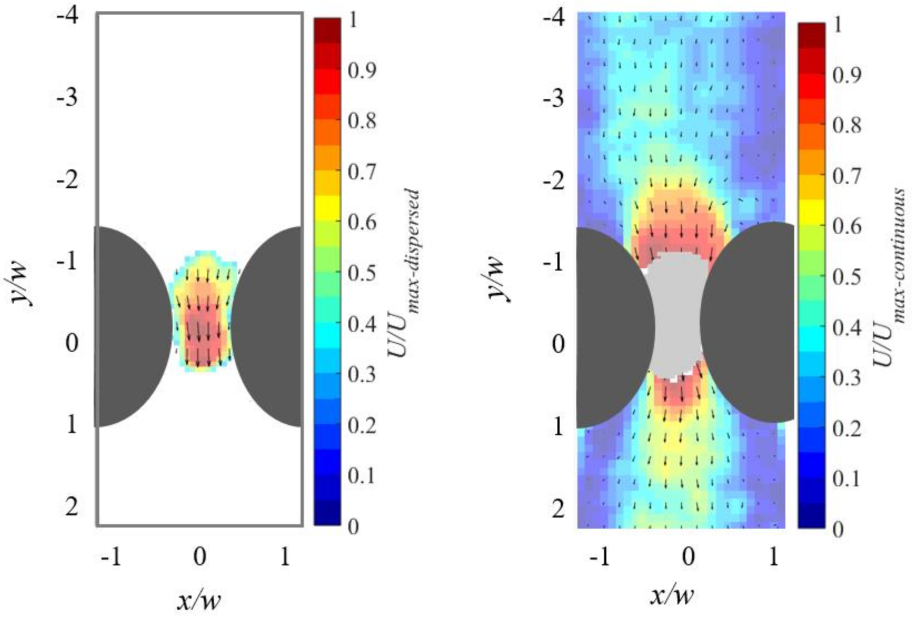

(a) (b)

Figure 4-4. Velocity distribution (a) in the dispersed phase and (b) in the continuous phase passing through a single pore obtained from the experimental data.

4.3 Calculation of Pressure

4.4 Pressure calculation from shape analysis

The pressure inside a spherical droplet in equilibrium with its surrounding is different from the pressure in the continuous phase due to the addition of the surface tension force at the boundary of the different phases. At this condition, due to the symmetry of the shape of the droplet, a uniform pressure distribution can be expected within the droplet. The pressure difference between the inside and the outside of the droplet depends on its size and the interfacial, forces which can be calculated by [196]:

$$\Delta P_c = \frac{2\gamma_{cd}}{R_\mathrm{d}} \tag{4-1}$$

where ΔP_c is the capillary pressure, R_{d} is the radius of the droplet and γ_{cd} is the interfacial tension between the phases. By assuming immiscibility of the two phases, the interfacial tension can be calculated as [196]:

$$\gamma_{cd} = \gamma_c - \gamma_d \tag{4-2}$$

where the subscripts c and d represent the continuous and dispersed phases, respectively. For the experiments in this study, γ_{cd}, is the interfacial tension between the canola oil and glycerol. Based on the values given in Table 3-1, the interfacial force between the phases is 32 mN/m.

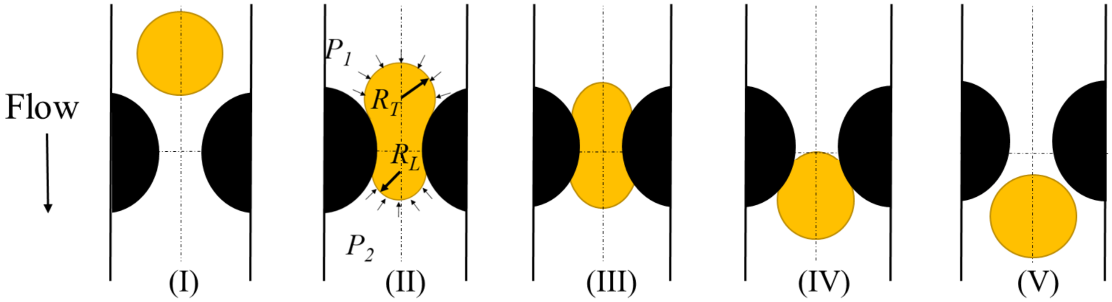

Figure 4-5. A schematic of stages of a droplet deformation through a pore throat. After [35]

The uniform pressure distribution within the droplet changes when the droplet undergoes any deformation. The overall deformation characteristics- of the dispersed phase is a function of its size, its geometry, and the geometry of the surface. For a droplet passing through a single pore, its deformation occurs in different stages as shown in Figure 4-5. The droplet has a spherical shape and uniform pressure distribution before and after it passes through the pore as is seen in Figure 4-5 (I) and (V). In stages (II)-(IV) in Figure 4-5, however, the droplet has a different leading- and trailing-face curvature. This variation in the curvatures of the faces results in a capillary pressure gradient inside the droplet known as the Jamin effect [21], [35], [166] and can be described by:

$$\Delta P^* = P_1 - P_2 = \gamma_{cd}\left(\frac{1}{R_\mathrm{L}} - \frac{1}{R_\mathrm{T}}\right) \tag{4-3}$$

where ΔP^* is the resulting pressure difference introduced by the change in capillary forces, P_1 and P_2 are the pressure of the continuous phase before and after the droplet and R_T and R_L are the trailing-face and leading-face radii of curvatures as described in Figure 4-5 (II). Based on this relation, the pressure gradient within the droplet may have a positive or a negative value depending on the location of the droplet with respect to the pore throat. The pressure gradient generated within the droplet is positive as the droplet enters the pore in the stage seen in Figure 4-5 (II) ($R_\mathrm{L} < R_\mathrm{T}$) leading to an extra resistance to the droplet passage [21], [35], [166].

The positive pressure gradient decreases to zero when the center of the projected area of the droplet is aligned with the pore throat as shown in Figure 4-5 (III). At this location, the leading and trailing faces have the same radius of curvature ($R_\mathrm{L} = R_\mathrm{T}$) resulting in zero pressure gradient. After this stage, the radius of the trailing face decreases as shown in Figure 4-5 (IV) ($R_\mathrm{L} > R_\mathrm{T}$) resulting in a negative pressure gradient. When the trailing face passes the pore throat, shown in Figure 4-5 (V), the pressure starts to recover and it becomes uniform within the droplet [35].

This change in pressure distribution is described by the Jamin effect which is essentially described by Eq. (4-3) [34], [38]. It indicates that the pressure gradient within an element of a dispersed phase is a function of the shape and the interfacial forces between the phases. This highlights that the change in the capillary pressure can be determined by monitoring the change in the shape of the dispersed phase. The pressure can be calculated by measuring the radii of the leading and trailing faces of the droplet as introduced in previous studies [34].

An example of shape analysis to highlight the Jamin effect is shown in Figure 4-6 (a) where for this data set, a gas bubble was used. This allows the interfaces between the phases to be detected due to the strong difference between their refractive indices. The data shown is from an experiment that used an air bubble rising in glycerol. Combining the radius of the curvature shown in Figure 4-6 (a) with Eq. (4-3) provides the change in the pressure distribution of the droplet, which is proportional to the droplet curvature. The pressure gradient calculated is shown in Figure 4-6 (b) which represents the same phenomena as the one described by the Jamin effect [21], [35], [166].

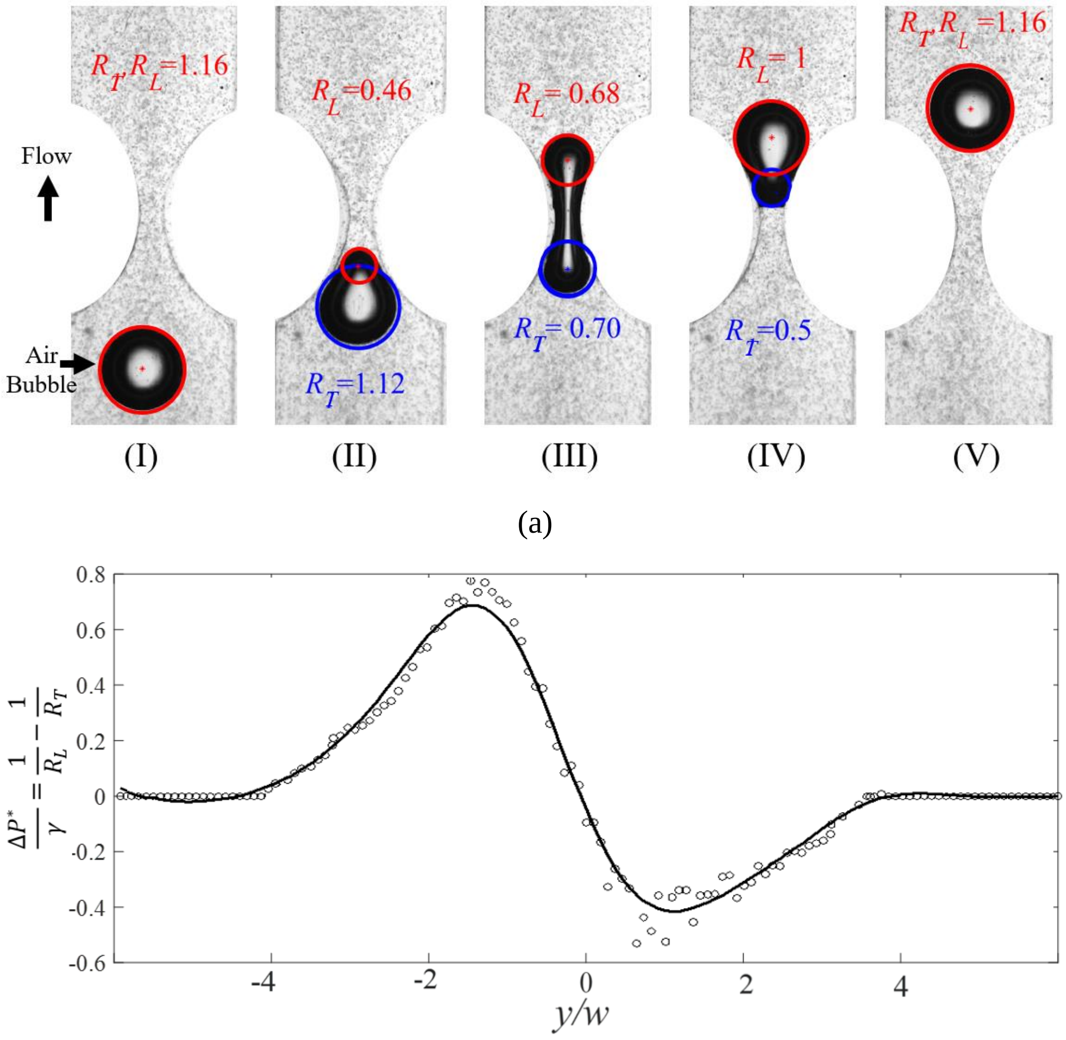

(a)

(b)

Figure 4-6. An example of determining capillary pressure from bubble shape; (a) sample images of a buoyant bubble deforms while passing through a pore throat, (b) measured change of curvature of the bubble with respect to a position with fitted line.

Applying the same approach for fluids with matching refractive indices causes some difficulties as there are no clear visible edges between the phases. The masking procedure described in Figure 4-3, however, shows enough detection of the edges to enable the calculation of ΔP^*. An example of the edge detection process used for droplet detection is shown in Figure 4-7. The difference between the seeding particles of the droplet and the continuous phase can be seen in the raw image shown in Figure 4-7 (a). This highlights the importance of proper seeding of the phases during the experimental setup including the size and concentration of the seeding particles. The intensity of the seeding particles of the dispersed phase can be increased as shown in the inverted image in Figure 4-7 (b).

As shown in Figure 4-7 (c), applying a mask (function bwareaopen, Matlab2018a The MathWorks, Inc.) improves the droplet detection. Masking is applied to remove objects in the image of a pixel size less than a specified value. Since the smaller size of particles (20 µm) are used for seeding the continuous phase, the shape of the droplet can be detected by removing the particles within the continuous phase based on their size. The outer shape of the droplet (function edge, Matlab2018a The MathWorks, Inc.) can be determined as shown in Figure 4-7 (d) This results from the detection of the location of the change in intensity between the seeded region and the background. Applying a smoothing function (function conv2, Matlab2018a The MathWorks, Inc.) around the edge of the detected droplet will result in the evaluation of the location and the shape of the droplet as shown in Figure 4-7 (d). A closer look at the images in Figure 4-7 shows that the system had visible asymmetries along the interface and the location of the droplet. Comparing the final processed image (Figure 4-7 e), with the original image (Figure 4-7 a), confirms that the asymmetry did not result from the edge detection process but was a physical characteristic of the droplet due to its interaction with the flow field.

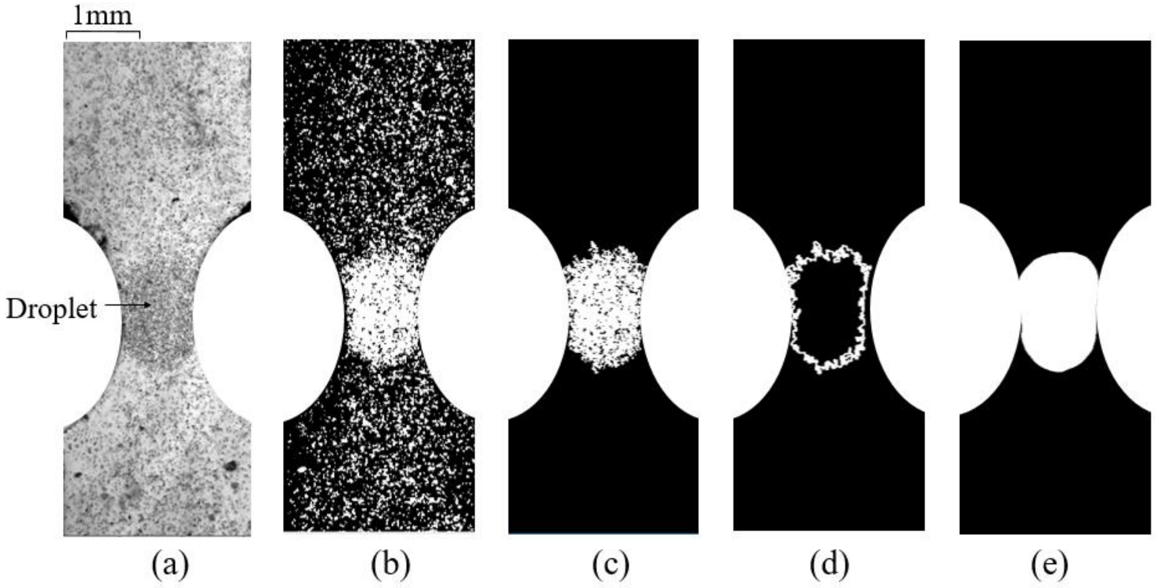

Figure 4-7. Refractive index matched droplet shape analysis (a) raw image (b) intensity enhancement (c) masked droplet (d) outer contour shape and (e) predicted location of the droplet.

The uncertainties in the pressure calculation can result due to the random placement of particles which will affect the edge detection process. Figure 4-8 (a) shows a closer view of the particles in the droplet. The uncertainty introduced will be relative to the size and the overall sphericity of the droplet. The maximum gap between a particle and the edge is around ~3 particle diameters (20 μm). Along the edge of the droplet, the detection algorithm will also capture particles that are not in focus based on the intensity difference.

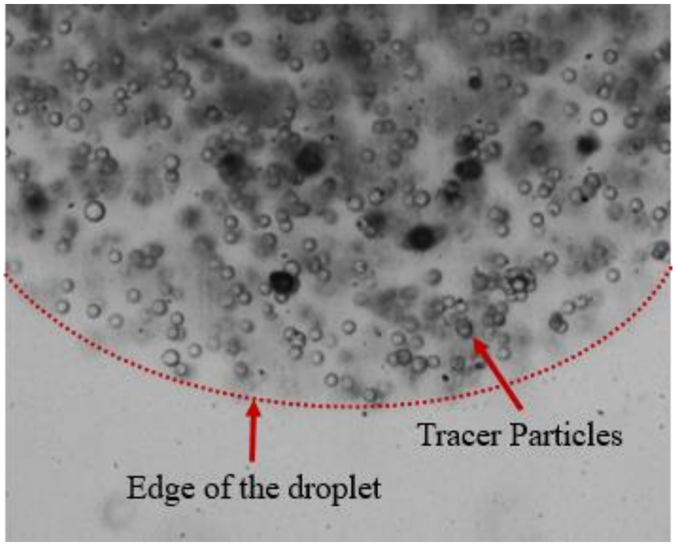

Figure 4-8. The zoomed-in picture of a droplet containing 20 µm seeding particles.

Comparing the size of the tracer particles with the size of the droplet when at its spherical shape (1600 µm and 1100 µm) showed that there are approximately 30 particles separated by an average of 2 particle diameters with its surrounding particles around the edge. Assuming the change in the radius of the curvature, ΔR = 40 µm, the effect on the change in the radius can be accounted by:

$$\frac{1}{\Delta R_{not-corrected}} = \frac{1}{R_L} - \frac{1}{R_T} \tag{4-4}$$

$$\frac{1}{\Delta R_{corrected}} = \frac{1}{R_L + \Delta R} - \frac{1}{R_T + \Delta R} \tag{4-5}$$

where the $\frac{1}{\Delta R_{corrected}}$ has its minimum value when the trailing edge has its maximum radius and the leading has its minimum, and it has its maximum value vice versa. Considering ΔR, the respective ranges for the change in the radii are given as:

$$-0.75 < \frac{1}{\Delta R_{not-corrected}} < 0.75 \tag{4-6}$$

$$-0.7 < \frac{1}{\Delta R_{corrected}} < 0.7 \tag{4-7}$$

Comparing the limits of the ranges given in Eq. (4-6) and (4-7) shows the difference of 0.05 mm- 1 mmwhich amounts to 7% of $\frac{1}{\Delta R_{not-corrected}}$. Therefore, a cumulative uncertainty of ± 7% is taken for the pressure determined from shape analysis. This uncertainty increases as the size of the droplet decreases since the radii of the curvature and ΔR will be at comparable scales. This can be addressed by using smaller particles with higher seeding densities.

The pressure distribution in the fluids can also be determined from the measurement of the velocities inside the droplet and the continuous phase [232]. The change in the pressure gradient within the droplet should have a similar trend as the one represented by the change in the curvatures of the leading and trailing faces of the droplet as shown in Figure 4-6 (b).

Having demonstrated the application of the Jamin effect for obtaining the pressure drop, the results shall be compared with the pressure drop calculated from the velocity measurements. The main purpose of this step is to verify the trend in pressure drop such as the one shown in Figure 4-6 (b). Matching trends will, therefore, validate that analyzing localized deformation behavior of a dispersed phase can be used to deduce the distribution of pressure drop throughout the flow field.

4.4.1 Pressure calculation from the velocity measurement

The pressure field of a flow can be calculated by applying appropriate analytical approaches on measured velocity field results obtained using optical diagnostics techniques [227]. The incompressible Navier–Stokes equations are commonly used to form the link between the velocity field and the corresponding pressure distribution as:

$$\nabla p = -\rho\left(\frac{\partial u}{\partial t} + (u.\nabla)u - \nu\nabla^2 u\right) \tag{4-8}$$

where P is the pressure, ρ is the density of the fluid, u is the velocity in x-direction, $\frac{\partial}{\partial \mathrm{t}}$ is the partial derivative, and ∇ is the divergence operator. The pressure gradient can be determined using either the Lagrangian or Eulerian approach [233]. In this study, an Eulerian approach is selected over a Lagrangian method since it has lower discretization resolution and there is no need to interpolate the data between the tracks of the particles. It is also useful since the velocity measurement of this study is in a fixed spatial location. The second-order central finite difference in time and space were used as defined as [226]:

$$\frac{\partial u}{\partial t}(x,y,z,t) = \frac{u(x,y,z,t+\Delta t) - u(x,y,z,t-\Delta t)}{2\Delta t} + O(\Delta t^2) \tag{4-9}$$

$$\frac{\partial u}{\partial x}(x,y,z,t) = \frac{u(x+h,y,z,t) - u(x-h,y,z,t)}{2h} + O(h^2) \tag{4-10}$$

$$\frac{\partial^2 u}{\partial x^2}(x,y,z,t) = \frac{u(x+h,y,z,t) - 2u(x,y,z,t) + u(x-h,y,z,t)}{h^2} + O(h^2) \tag{4-11}$$

where h is the physical distance between any two points (x_1 and x_2) within the flow field, Δt is the time between sequential frames, and $O(\cdot)$ is the second-order approximation function. The significant difference between the viscosities and densities of the continuous and dispersed phases in this experiment, as given in Table 3-1, emphasizes the importance of including the second-order derivative of the velocity. Therefore, the equations with corresponding viscosity terms are applied to two phases separately. By integrating the pressure gradient, Eq. (4-8) [221], in each phase and combining the respective results, the pressure field for the multi-phase flow can be determined.

The pressure gradient for each case is determined with respect to a relative reference pressure. This reference pressure is selected as the pressure at the top of the field of view (at y/w = -4). The physical distance between any two points is determined by the correlation window size and its overlap in the processing scheme used for the velocity measurement data. This approach provides a uniform rectangular grid discretizing the flow field as per the window size used and the specified overlap.

The no-slip boundary condition is applied to all solid walls in the flow channel by using the masking function in the experiment. This sets the velocity at all liquid-solid interfaces to zero. At the interface between the dispersed and the continuous phase, however, the capillary pressure between the phases is used as the boundary condition. Therefore, the pressure in the dispersed phase is calculated to account for the effect of capillary pressure between the two phases (Eq. 4- 1) such that:

$$\Delta P = \Delta P_{d-Velocity} + \Delta P_c \tag{4-12}$$

where the $\Delta P_{d-Velocity}$is the pressure of the disperse phase calculated from the velocity field and ΔP_c is the capillary pressure between the two phases. A sample showing the details in the pressure calculation for a multi-phase flow is shown here to demonstrate the method. Figure 4-9 (a) and (b) represent the determined pressure field for the velocity distribution of dispersed and the continuous phases measured using µ-PSV illustrated in the experimental section. Note that the velocity field shown in Figure 4-4 for each case has been normalized based on the maximum velocity of the fluid in the phase. The positions have also been normalized using the size of the pore throat (w) in the channel where the origin is located at the centre of the throat. It can be seen that the pressure change in the dispersed phase is on the order of 80 Pa and is significantly higher than the distribution in the continuous phase. This is due to account for the capillary pressure within the phase in the pressure calculation. The figure also shows that the pressure is not uniform within the droplet as a result of the deformation of the droplet as described in the previous section and by the Jamin effect [21], [33], [35], [36], [166]. The pressure change is negligible before the flow enters the pore and it is higher in the converging zone of the pore throat. The asymmetric nature of the flow is also visible in this case.

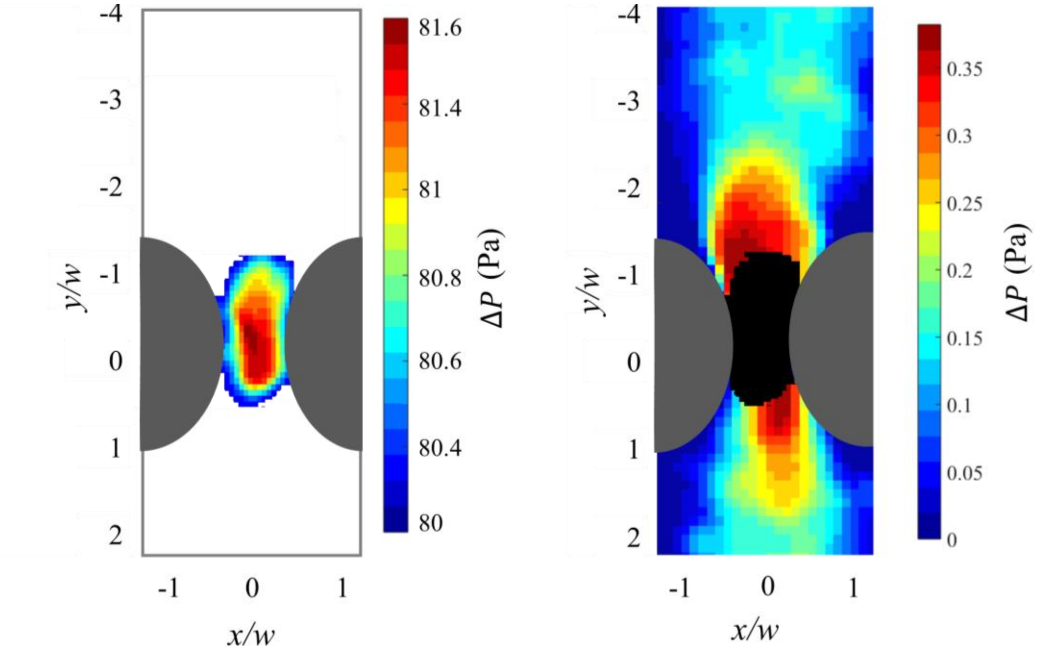

(a) (b)

Figure 4-9. Pressure distribution of (a) the dispersed phase and (b) the continuous phase calculated from the velocity field in Figure 4-4.

The total uncertainty of the determined pressure from the PIV velocity field is the propagation of numbers of error sources [234]. The first group of uncertainty can be categorized by the errors introduced by the velocity field used as an input for the pressure calculation. This consists of the velocity measurement accuracy due to the PIV processing and the accuracy of velocity derivatives which arises from the temporal and spatial resolution of the velocity field. The second group of sources of uncertainty derives from the pressure calculation technique used. In this stage, the uncertainty of velocity material acceleration calculation is highly affected by the calculation approach being either Eulerian or Lagrangian. The selection of the boundary conditions used to evaluate the pressure field also plays an important role in the uncertainty of the pressure gradient calculation [234]. In the case of the multi-phase flow, in addition to the discussed source of uncertainties, the condition used at the boundary of the phases is also important in both velocity and pressure calculation. The uncertainty analysis of deriving pressure from velocity data is an active area of research and further investigation [234], [235] is needed especially to advance it to multi-phase flows.

4.5 Results and Discussion

The velocity distributions of different droplets approaching the pore throat were measured for a stationary continuous phase. The aim of these flow experiments is to have a better description of the balance of forces acting on the droplets. The pressure drop across the pore throat is primarily a function of the capillary forces present due to the pore geometry and buoyancy. The size of the droplet highly influences the distribution of these forces. As such, the droplet diameter is varied in order to capture the interactions from the effects of the parameters.

Raw images showing two droplets of different sizes used in this study are shown in Figure 4-10. The smaller droplet measures slightly larger than the pore throat $\left(\frac{2R_d}{w} = 1.1\right)$. The size of the larger droplet, however, exceeds the pore throat by more than 50 % $\left(\frac{2R_d}{w} = 1.6\right)$. By using the sizes of the droplets and the interfacial tension of the fluid, the capillary pressure difference between the phases (ΔP_c) were calculated using Eq. (4-1) to be 80 and 116 Pa, respectively, for the small and large droplets.

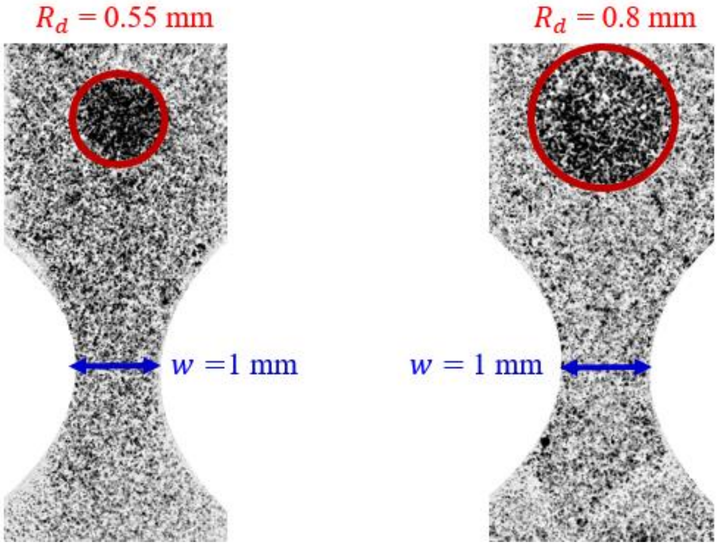

(a) (b)

Figure 4-10. Shape and size of droplets calculated by the shape analysis as they approach the single pore throat.

The corresponding velocity fields were used to calculate the pressure distribution of the dispersed and continuous phases. In all the different analyses, the local velocity in the field (U) is normalized by the maximum velocity of the droplet to ensure a proper comparison between the motion of the different sizes of the droplet. The value of this maximum is taken from the position where the droplet has a spherical shape which also represents its terminal velocity (U_t) within the confinement before the pore. The size of the pore throat is used as a length scale to normalize locations at any position in the channel. Dashed lines are used to signify the position and the shape of the droplet are determined following the masking procedure described in Section 3.1. The same normalization procedure is also applied to the pressure field data.

4.5.1 Velocity field for a droplet in motion

The velocity distributions for the larger droplet in the stationary continuous phase at different positions along the pore geometry are shown in Figure 4-11 (a)-(d). The color map of the velocity distribution has been adjusted to highlight the features of the flow. Figure 4-11 (e)- (i) shows the distribution for the smaller droplet. In both cases, the velocity reaches its highest value when the droplets were approaching the pore as shown in Figure 4-11 (a) and (e) which also shows that the spherical shape of the droplets is maintained. The droplets are moving at their terminal velocity where the dominant driving force is the density difference between the phases. Hence, there is in general, constant velocity observed inside the droplets in both sizes based on the higher viscosity of the dispersed phase

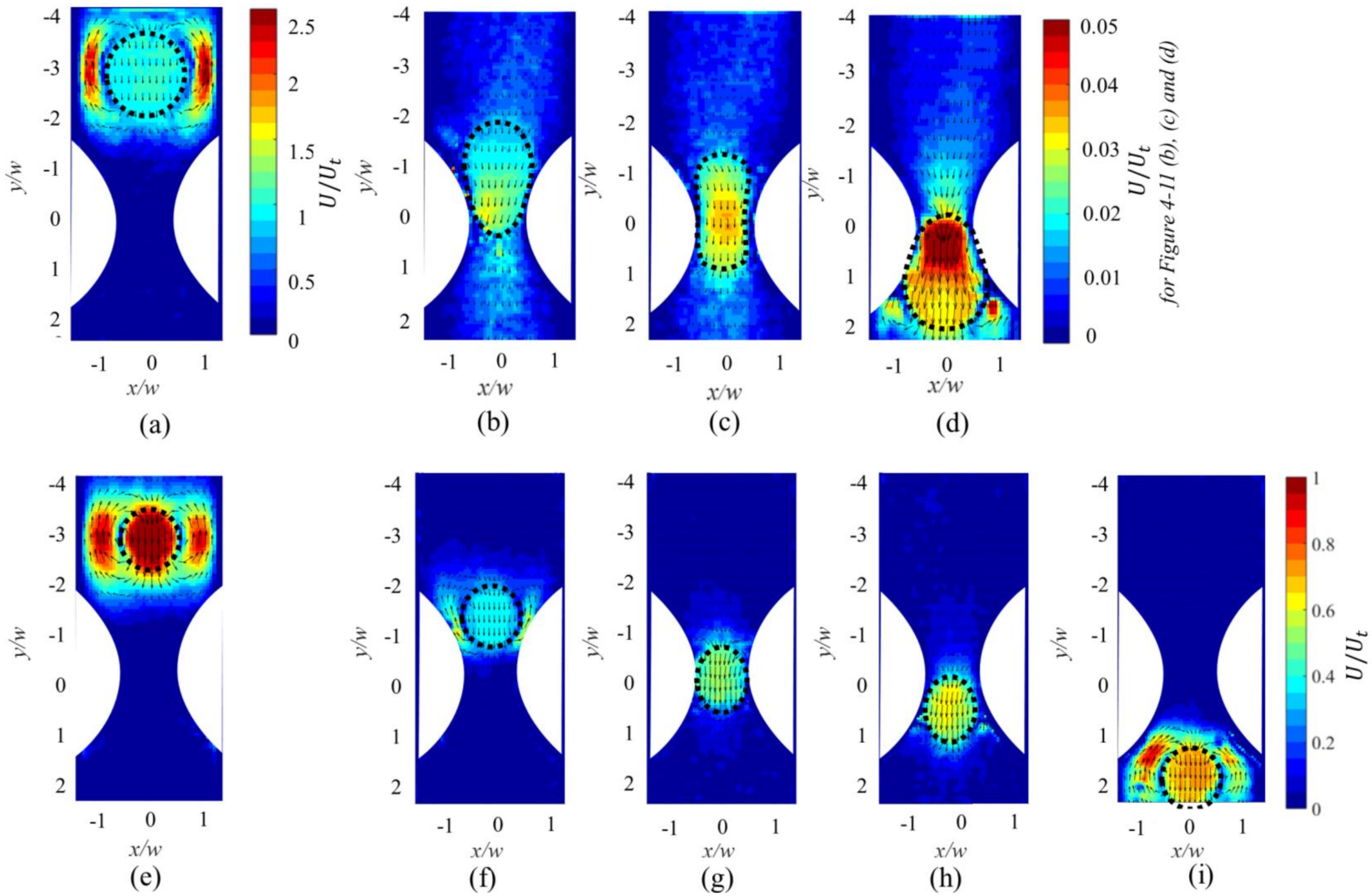

Figure 4-11. Velocity vector maps and the anticipated location of the larger droplet (a) before droplet enters the pore (b) as it enters (c) in the pore throat and (d) exiting the pore throat and the smaller droplet (e) before the droplet enters the pore (f) as it enters (g) in the pore throat and (h) exiting the pore throat, (i) after pore throat.

The continuous phase remains stationary along the pore throat before the droplet approaches. As shown in Figure 4-11 (a) and (e), in regions between the droplets and the confining wall, however, a reverse flow is observed in the continuous phase. This is due to the downward motion of the droplet leading to a counter-current flow in the continuous phase. The magnitude of the maximum velocity of the continuous phase in the larger droplet, shown in Figure 4-11 (a), is almost twice that for the dispersed phase in this case. This is because of the larger size of the droplet which results in a smaller open area to flow between the droplet and the confining wall. For the smaller droplet, however, as shown in Figure 4-11 (e), the droplet and the surrounding fluid have comparable velocity magnitudes due to the small size of the droplet relative to the channel size. This provides greater open space between the edge of the droplet and the confining wall for the continuous phase to flow in the reverse direction.

Figure 4-11 (b) and (f) show the flow field as the droplets enter the pore. The region is mainly characterized by the change in the local velocity distribution due to the contraction and is hence named the converging zone. From Figure 4-11 (b), it can be seen that the droplet has decelerated and has a significant internal velocity gradient when it enters the converging zone. The leading face of the droplet has a higher velocity as compared to the trailing face. It is important to note that there is an order-of-magnitude change in the velocity of the larger droplet compared to its terminal velocity before the pore. This reduction in the velocity is much higher than in the case for a smaller size droplet that is shown in Figure 4-11 (f). It is also observed that the smaller droplet has a slightly higher leading-face velocity and lower trailing-face velocity upon entering the pore. The overall magnitude of the velocity change is, however, not as significant.

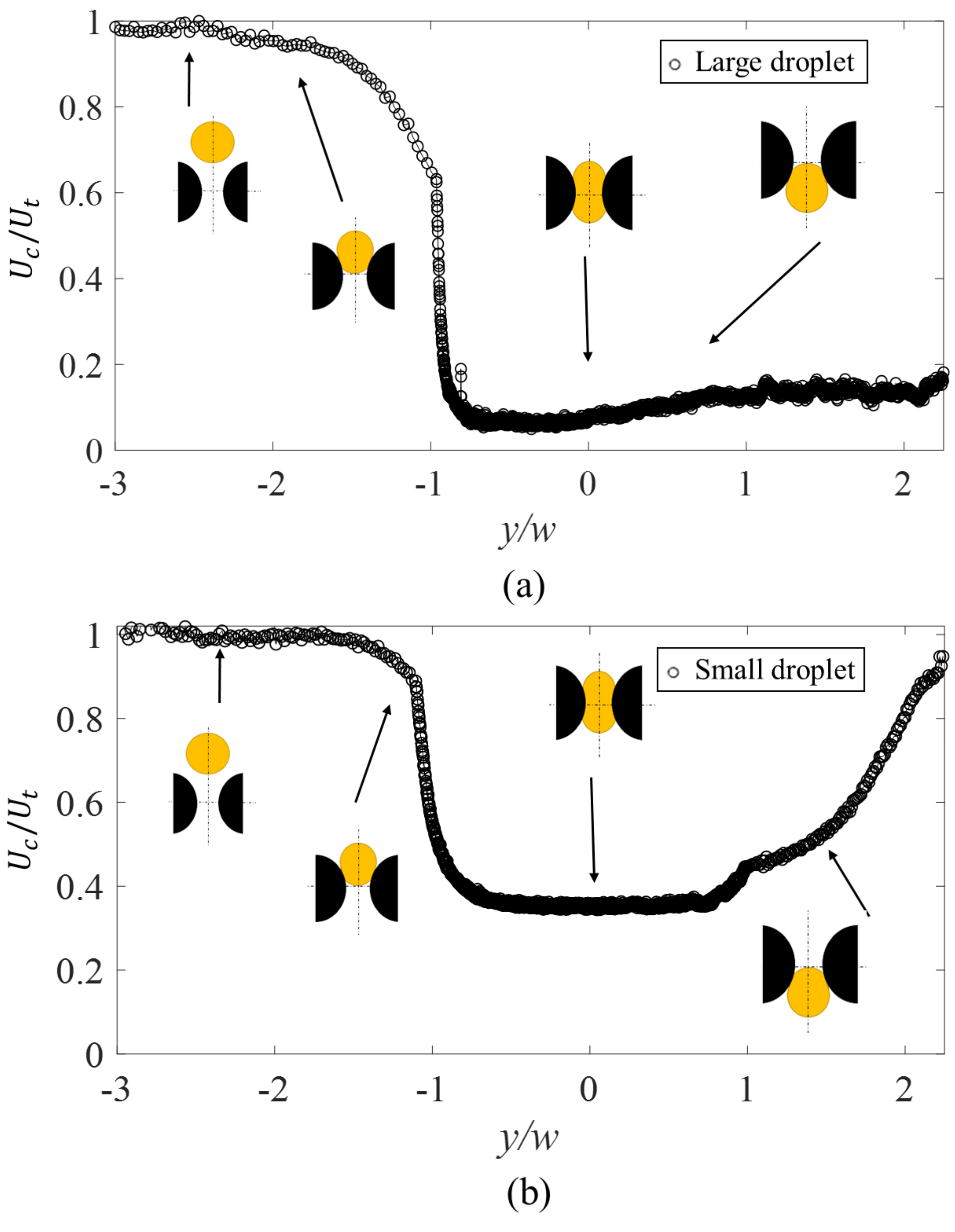

Figure 4-12. The change in the centroid velocities (u_c) normalized by the terminal velocity(u_t) with respect to the position of the center of their projected areas and the location of pore throat for (a) the large and (b) small droplets

The change in the centroid velocities (u_c) of the large and small droplets with respect to the position of the center of their projected areas and the location of the pore throat are given in Figure 4-12 (a) and (b), respectively. In both cases, the velocity is normalized by the corresponding terminal velocity of the droplet. It can be seen that the velocities are the highest at a location prior to the pore entrance. At positions closer to the pore, however, the velocities decrease. The velocity of the larger droplet decreases to less than 10% of its initial velocity, Figure 4-12 (a), while for the smaller droplet the velocity reduces only to ~ 40% of its terminal velocity. It is evident that the velocity history of the droplet is affected by the deformation of the droplet which is a strong function of its size.

Deformation starts as the droplet begins to enter the pore which results in the development of an internal pressure gradient. In addition to the buoyancy force, capillary pressure also acts on the droplet. This results in a reduction of the velocity of the droplet as it enters the pore and it continues to decrease until it reaches the pore throat as shown in Figure 4-11 (c) and (g). At this location, the velocity within the droplet becomes constant since its center of the projected area is aligned with the pore throat. The same phenomena are observed for both sizes of the droplet at this location which is shown as $y/w = 0$ in Figure 4-12 (a) and (b). After passing this location, both droplets accelerate, faster for the smaller droplet than the larger one. As shown in Figure 4-11 (i), the small droplet regains its spherical shape after it exits the pore throat. For the case of the larger droplet, however, this condition is not as clearly observed in the field of view of the experiments.

The trend of change in the velocity of the droplet in Figure 4-12 is similar for both cases. The locations where the velocity changes, however, are different. In the case of the larger droplet, shown in Figure 4-12 (a), the droplet has its highest velocity before it reaches the pore throat ($-3 \leq y/w \leq -2$) which is essentially its terminal velocity where the gradient in capillary pressure is zero. The velocity remains constant up to $y/w \leq \sim -2.5$ which is the beginning of the converging zone. Beyond this location the droplet decelerates as the capillary forces become more significant. It reaches its minimum value at $y/w = -1$. Compared to the smaller droplet which only begins to decelerate at $y/w = -1$, the larger droplet starts to decelerate further upstream. The velocity of larger droplet reaches its minimum value at $y/w = -1$ which is where the droplet enters the area of the pore geometry. At this location, until the center of the droplet aligns with the pore throat, the droplet velocity remains constant. After the droplets pass this stage, the velocity starts to increase again. In comparison with the smaller droplet, the increase in the velocity of the larger droplet occurs farther downstream of the pore throat even though it does not reach the same value. The length available for the droplet to recover its velocity is much smaller in the case of a small droplet than the length of the larger droplet. This is due to the change in the capillary pressure introduced to the droplet as it passes through the pore. The droplets reach their terminal velocity after $y/w =$~ 2 which is not shown in the figure since it is outside the field of view.

4.5.2 Pressure determined from velocity measurement

The change in velocity affects the distribution of the pressure gradient within the droplet. The field distributions of the pressure gradient, which correspond to the velocity fields shown in Figure 4-11 (a) to (i), are shown in Figure 4-13 (a) to (i), in the same order. When the droplet moves at a constant velocity in regions with no influence from the pore throat, the pressure difference is uniform within the droplet since it has maintained its spherical shape as shown in Figure 4-13 (a) and (e). There is, however, a step-change in the pressure difference between the two phases due to capillary pressure as shown in the color bar. A more detailed description of the changes in the velocity and pressure at the center of the large droplet ($y/w = -3$) along the x-axis is shown in Figure 4-14. A uniform span-wise velocity can be seen within the droplet ($-0.8 \leq x/w \leq 0.8$) in Figure 4-14 (II) having the same value as its terminal velocity. The velocity has a minimum value at $x/w = -1$ and 1 which are regions for the reverse flow of the continuous phase. The pressure profile at this location shows that the pressure change is zero at the wall and decreases to negative values at $x/w = -1$ and 1. It increases up to 80 Pa at $x/w = -0.8$ and 0.8 due to the capillary pressure dominating at the boundaries of the droplet.

There is generally no relative motion inside the droplet as its viscosity is noticeably higher than the surrounding fluid. Hence, the low-pressure change inside the droplet. As shown in Figure 4-14 (IV), a flat velocity profile is observed in the continuous phase in the stationary regions in front of the leading edge of the droplet. As a result of no flow in this region, there is no change in pressure as shown in Figure 4-14 (VIII). The change in the velocity along the y-axis is also given in Figure 4-14. (I) and (III). The corresponding pressure change is shown in Figure 4-14 (VI) and (VII). The step-wise effect of capillary pressure between the phases can be seen at $y / w \approx -4.0$ and –2 in Figure 4-14 (VII).

As the droplet draws closer to the pore, its deformation will result in the higher velocity of the leading face than the trailing-face, leading to a higher pressure change in the vicinity of the leading-face, Figure 4-13 (b) and (f). When the droplet reaches the pore throat, the pressure change within the droplet becomes constant with equalization of the leading- and trailing- curvatures of the droplet as shown in Figure 4-13 (c) and (g). As the droplet passes through the pore, the trailing face of the droplet accelerates, thus increasing the pressure gradient as shown in Figure 4-13 (d) and (h). Once the droplet passes the pore, the pressure drop continues to increase until it reaches a constant value, which corresponds to the terminal velocity of the droplet after the pore location in Figure 4-13 (i).

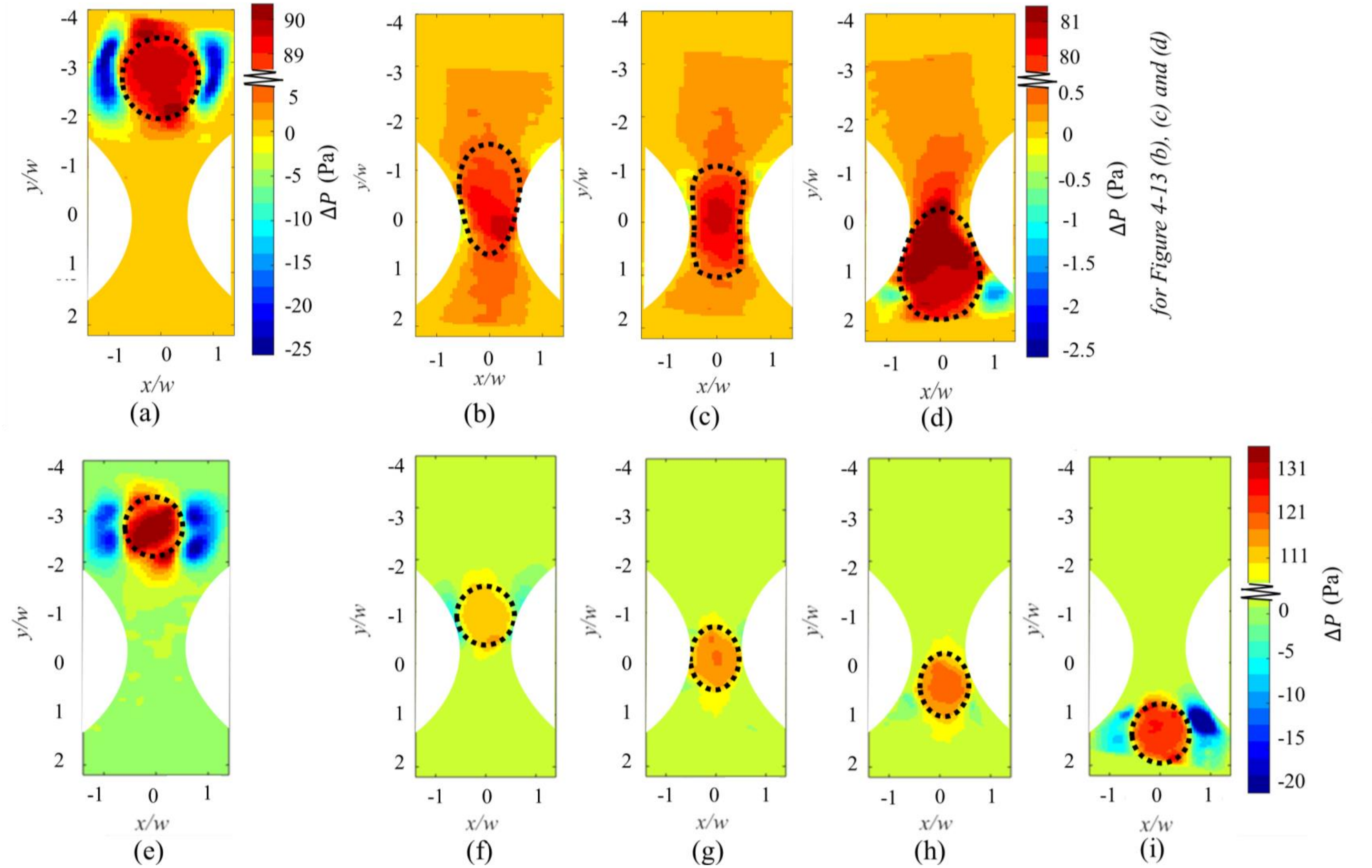

Figure 4-13. Pressure color map and the anticipated location of the larger droplet (a) before droplet enters the pore (b) as it enters (c) in the pore throat and (d) exiting the pore throat and smaller droplet (e) before droplet enters the pore (f) as it enters (g) in the pore throat and (h) exiting the pore throat, (i) after pore throat. Note that there is a step-change in the color bars.

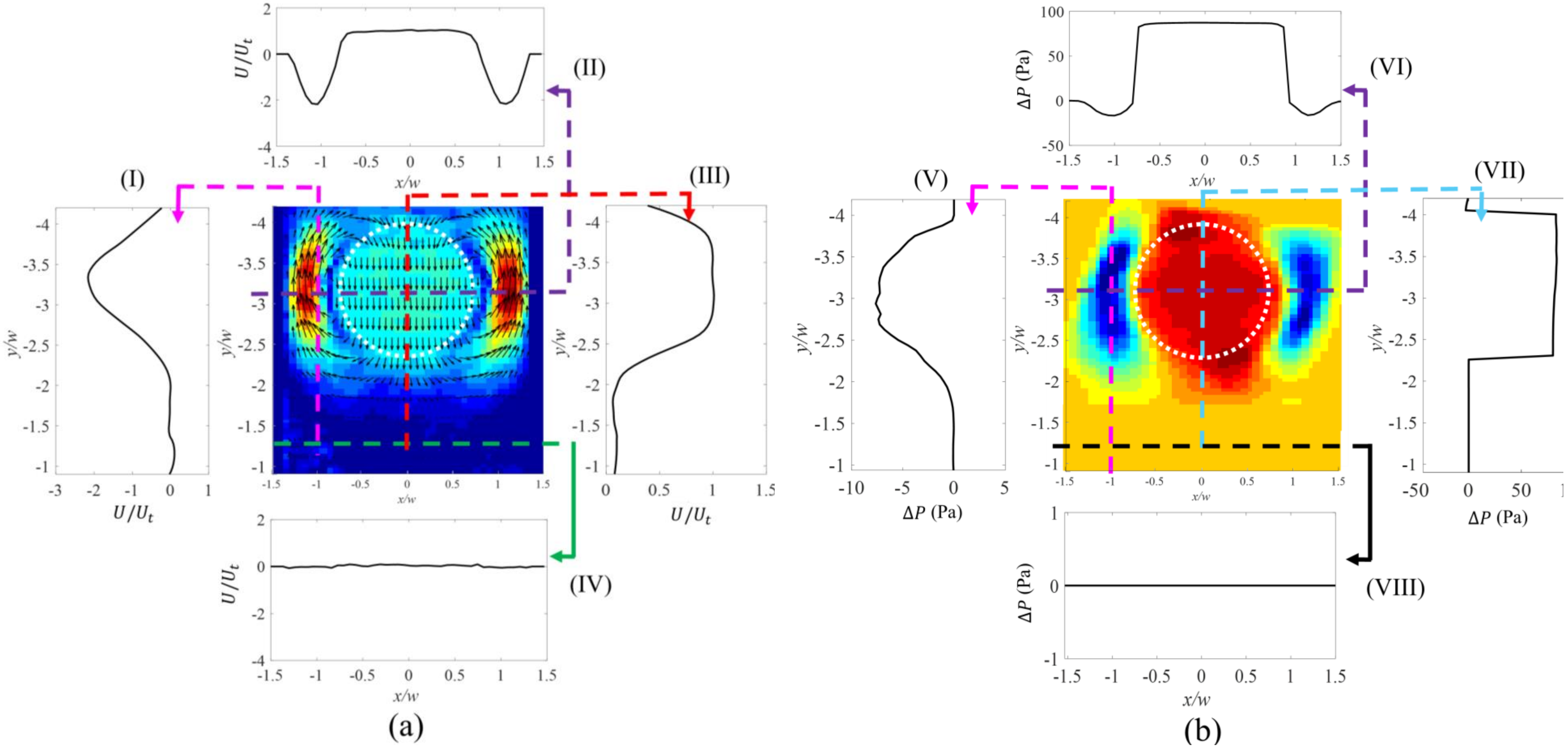

Figure 4-14. (a) velocity and (b) pressure distribution with their corresponding profiles at $x/w = -1$ shown in (I) and (V); $y/w = -3.1$ shown in (II) and (VI); $x/w = 0$ shown in (III) and (VII); and $y/w = -1$ shown in (IV) and (VIII). Colour map as per Figure 4-13.

The pressure gradient across the droplet can be calculated based on the instantaneous pressure change at the leading and the trailing edges of the droplet as described in Figure 4-13. The results from this measurement for small and large droplets are shown in Figure 4-15 (a) and (b), respectively. As shown in Figure 4-15 (a), at y/w = - 2 the pressure change within the large droplet increases which introduces an extra resistance to the fluid resulting in a reduction of the velocity. The pressure change continues to increase until y/w= -1. As the droplet passes this location, the pressure decreases back to zero at y/w = 0 which represents the position of the droplet where the centre of its projected area is aligned with the pore throat.

The pressure change continues to decrease to a negative value which accelerates the motion of the droplet. After the droplet passes y/w = 1, the pressure change increases resulting in a change in the acceleration of the droplet. Past the location of y/w = 2, the pressure change returns to zero within the droplet at the value needed for the terminal velocity of the droplet. Overall, similar trends are seen in the pressure change experienced by the droplets in both cases. The locations where the trend changes, however, are different for each case.

For the smaller droplet, as shown in Figure 4-15 (b), the magnitude of the pressure change is not significant as for the larger droplet. The location at which the droplet begins to be influenced by the effect from the pore occurs farther downstream for the small droplet (y/w=- 1 vs. y/w =- 2 for larger droplet). The pressure change within the droplet also returns to a value of zero at closer distance from the pore throat for the smaller droplet (y/w=1) as compared to larger droplet (y/w=2). This variation signifies the importance of the droplet deformation on the pressure drop along the pore throat.

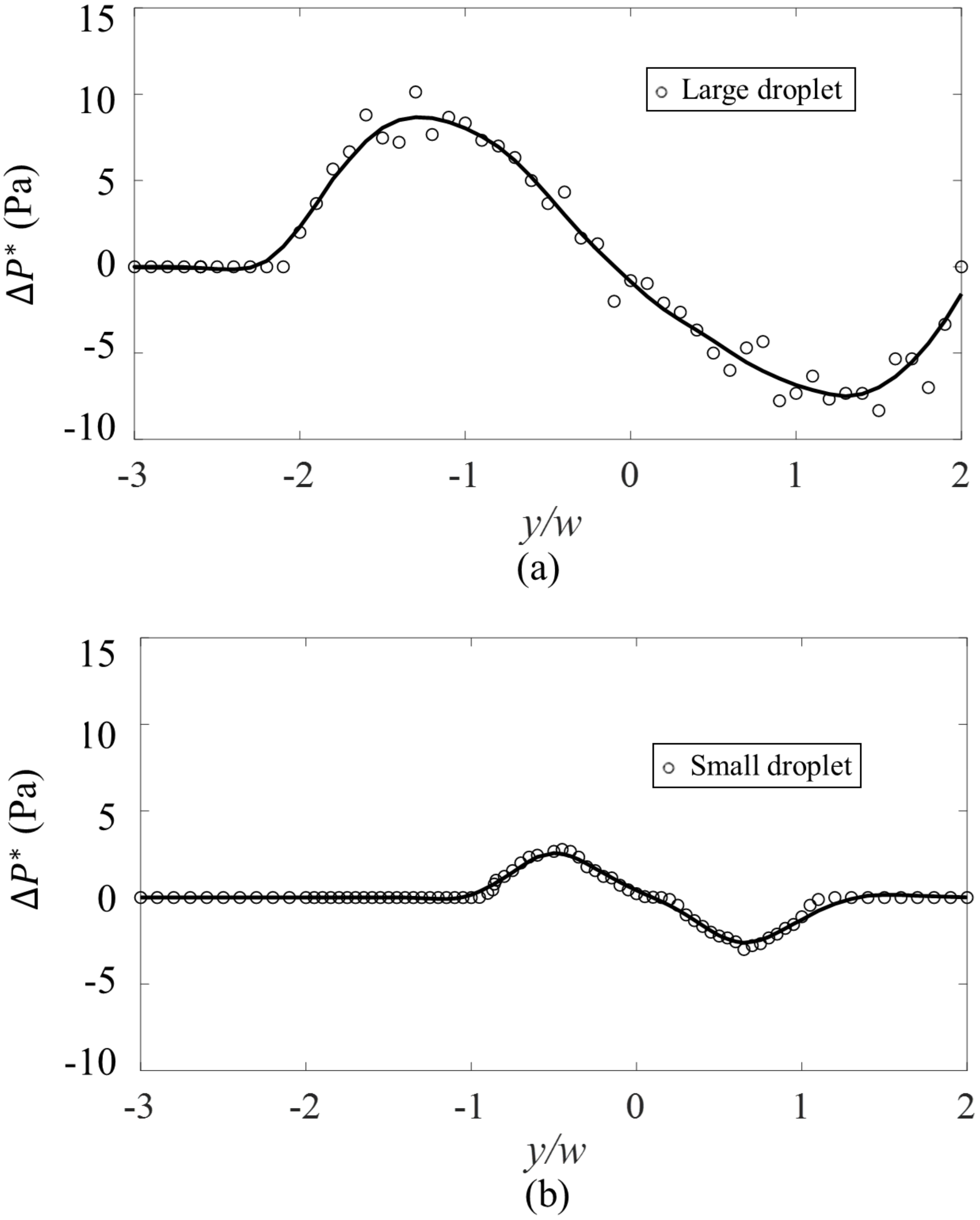

Figure 4-15. The pressure drop introduced to the droplet calculated from the velocity measurement for (a) large and (b) small droplet.

4.5.3 Pressure calculated from analysis of droplet deformation

The change in the velocity of the droplet can be further explained by examining the capillary pressure which is a function of the droplet deformation. A sample of the change in the shape of the droplet and the corresponding change in the radii of curvatures at different stages along the pore is shown in Figure 4-16 for both droplets. The instantaneous change in the leading- and the trailing-face radius of curvatures with respect to the position of the droplets are shown in Figure 4-17 (a) and (b). The droplet has a spherical shape before entering the converging zone as shown in Figure 4-16 (a) and (e). It maintains its spherical shape until it reaches the pore as shown in Region Aof Figure 4-17 (a) and (b). In this region the radius of curvatures of the leading- and the trailing- faces are constant at 0.8 mm for larger droplet and 0.55 mm for small droplet, respectively.

As the droplet enters the pore the radius of curvature of the leading-face becomes smaller than that of the trailing-face and an example of this condition is shown in Figure 4-16 (b) and (f). The change in the radii of curvatures of the faces at this location is shown in Region B in Figure 4-17. It can be seen that the curvatures of both faces decrease as they enter the pore. In all cases, the radius of the curvature of the leading-face is lower than that of the trailing-face. The respective minimum radius of curvatures for large and small droplets is 0.5 mm and 0.46 mm. The minimum values are reached when the leading-face of the droplet is aligned with the pore throat. After the droplet passes this location, the radius of curvature of the leading-face increases and reaches the same value as the trailing-face at ($y/w = 0$ for both cases) which is when the centre of area of the droplet is aligned with the pore throat in Figure 4-16 (c) and (g). Analogously, the radius of curvature of the trailing-face reaches its minimum when it is leveled with the pore throat in Figure 4-16 (d) and (h). The radius of curvatures of both faces increases as shown as Region C in

Figure 4-17 when the droplet has passed the pore and regains its spherical shape in Region D shown in Figure 4-16 (e). For the larger droplet, the radius of curvature reduces up to ~63% of its initial curvature. For the smaller droplet, however, it decreases to ~83% of its radius of curvature as a sphere. The change in the radius of curvature of the leading- and trailing-faces is not as significant for the case of a smaller droplet since the droplet is only slightly bigger than the pore throat.

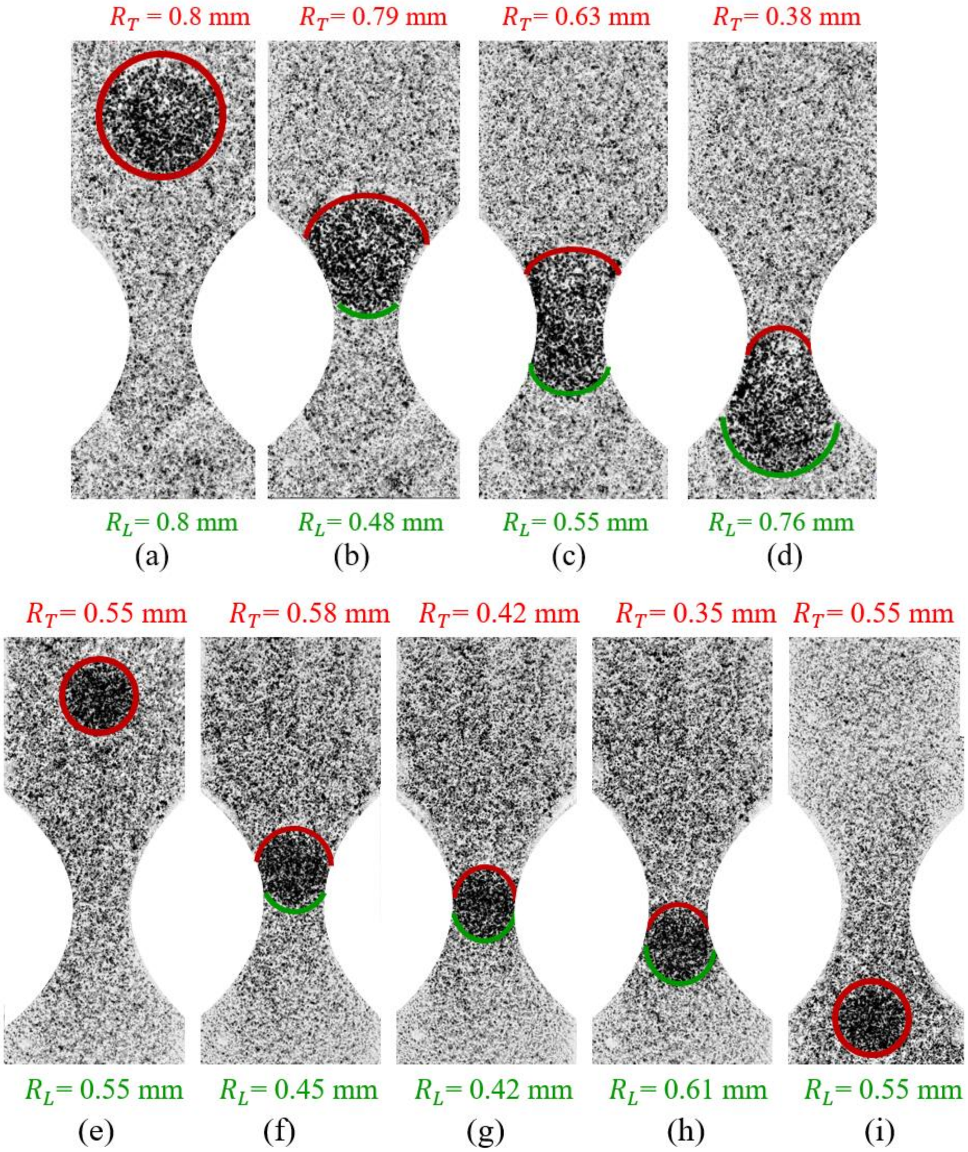

Figure 4-16. the droplet shape analysis (a) before droplet enters the pore (b)as it enters (c)in the pore throat, (d) exiting the pore throat, and (e) after pore throat.

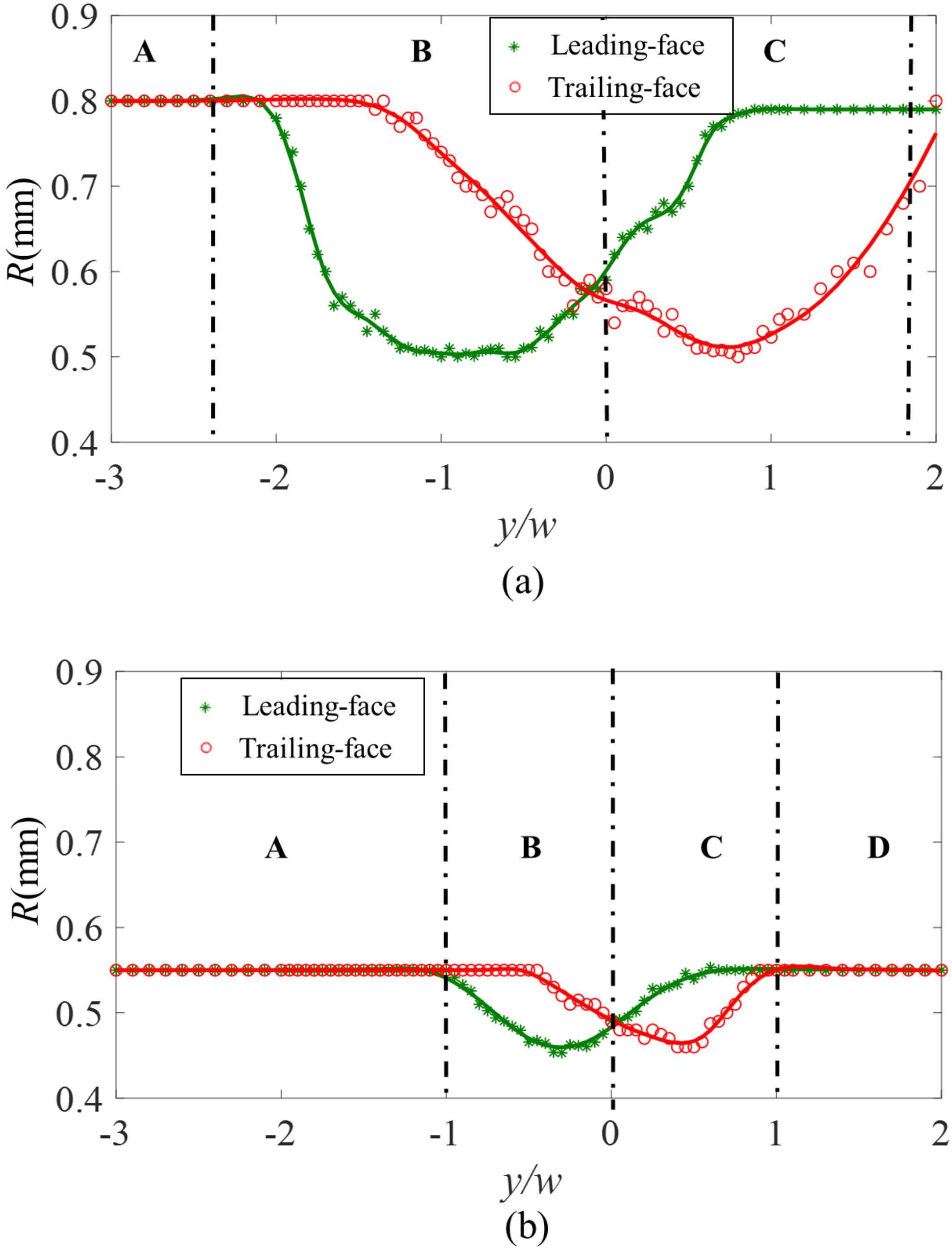

(a)

(b)

Figure 4-17. Measured leading and trailing edge curvature for (a) the large and (b) the small droplet.

Applying the measured radius of curvatures from the shape analysis in Eq. (4-3) shows that the capillary pressure distribution follows the same trend for both sizes as shown in Figure 4-18. The capillary pressure is zero before the droplet enters the converging zone due to its spherical shape where $y/w <$-2 and $y/w <$-1 for large and small droplets, respectively. The pressure change increases after the droplet deforms and reaches its maximum when the leading-face of the droplet is aligned with the pore throat ($y/w =$ -1 for large droplet, and y/w = - 0.5 for small droplet). This location has the most resistance to the droplet motion and in order for the droplet to stay in motion, the pressure drop should exceed the maximum capillary pressure. After this stage, the pressure change reduces to its minimum value which corresponds to the least resistance to the flow.

The numerical values of the pressure change also show that the variation in the capillary pressure intensifies as the size of the droplet increases. The capillary pressure in the case of the larger droplet increases as high as 55% whereas for the smaller droplet the increase is ~40%. The greater change in the capillary pressure results in a significant decrease in the velocity of the droplet. This phenomenon can also be seen from Figure 4-13, which shows that the capillary pressure gradient becomes more pronounced as the droplet moves along the pore geometry.

The velocity and pressure gradient distributions show the significance of the size of the droplet. The respective trends in the results from the calculation of pressure from the shape analysis in Figure 4-18 appear similar to the one seen in the velocity measurement analysis in Figure 4-13. This confirms the action of the Jamin effect for the motion of the droplet passing through a pore. The values of the pressure drop in these cases are not the same. This is most likely due to the oversimplification of the edge detection used in the shape analysis to determine droplet curvature.

The results of this study show that the motion of the smaller droplet has been less affected by the pore geometry and the variation in the pressure drop is not as significant as for the larger droplet.

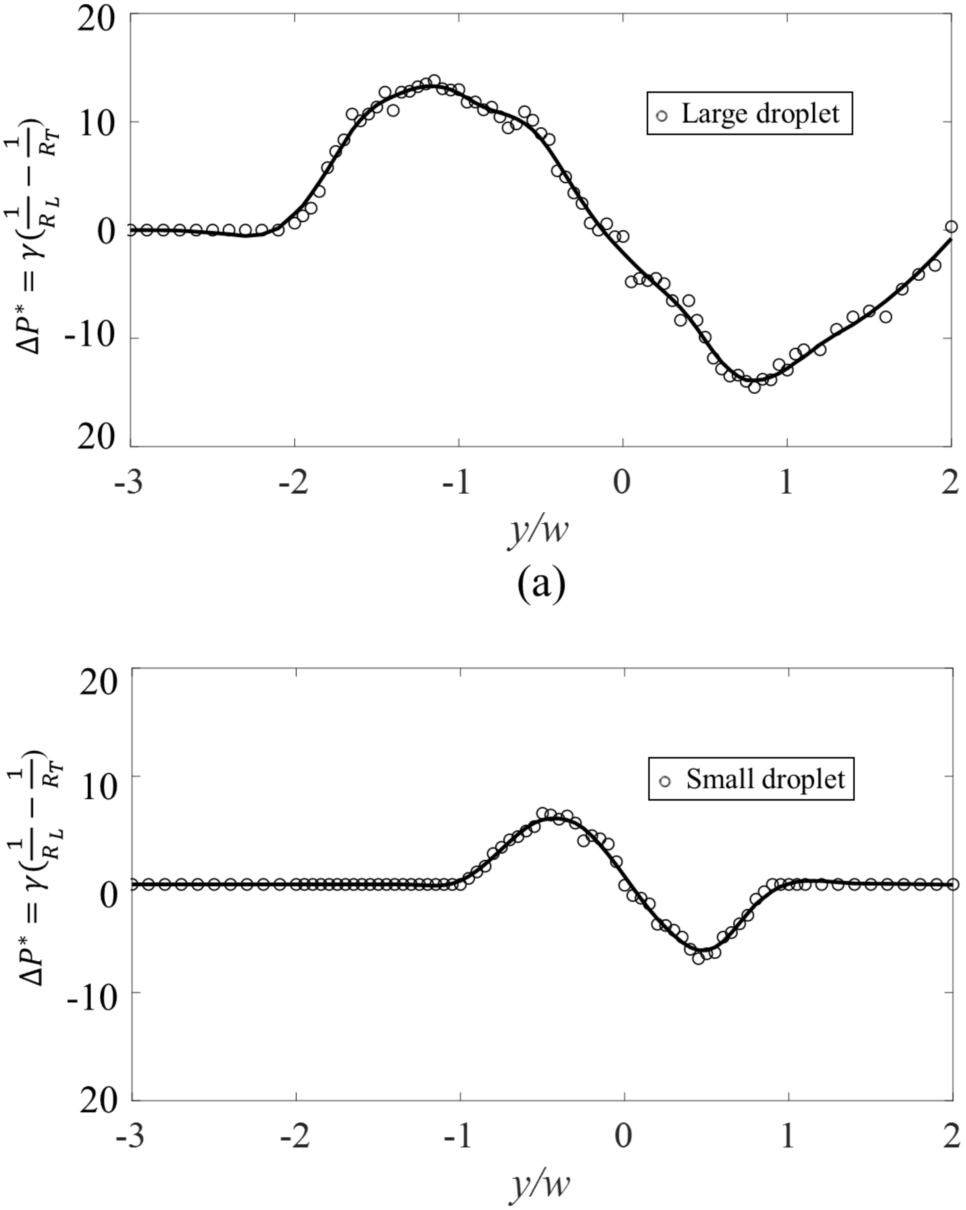

(a)

(b)

Figure 4-18. Capillary force introduced to by the small droplet as a result of deformation-calculated using the shape analysis.

4.6 Conclusion

The velocity and pressure distributions for the flow of a droplet through a pore geometry inside a stationary continuous phase were considered in this study. The velocity field was measured using μ-PSV and the results were used to calculate the corresponding pressure field. Two droplet sizes were studied whereby imaging-based shape characterization offered instantaneous information regarding their deformation. Capillary pressure distribution was determined from measurement of the leading- and trailing-edge radius of curvature of the droplets based on the theory given by the Jamin effect.

The results of this study showed that there is a significant effect of the size of the droplet. For both sizes, however, the droplet has its terminal velocity before it reaches the pore throat. This motion of the droplet before it enters the pore results in a reverse flow of the stationary phase between the droplet edge and the confining wall. As the droplet draws closer to the pore its velocity decreases and deformation causes the capillary forces to become more dominant compared to buoyancy. Beyond this location, the droplet accelerates and ultimately returns to its terminal velocity.

The change in velocity of both sizes of the droplet followed the same trend. The range of the velocity gradients and their distribution along the channel, however, varied with the size of the droplet. The capillary pressure distribution determined from both velocity measurements and shape analysis showed a similar trend with a greater variation for the larger droplet. While the refractive index matching of the two fluids worked well, it provided a significant challenge in the shape analysis and overall accuracy of deterring the curvature of the droplet. This impacted the accuracy of the measurement.

Chapter 5: Effect of the pore geometry on pressure distribution within a bubble penetrating a single pore[7]

This chapter describes and discusses the experimental investigation of the effect of the surface roughness and pore geometry on pressure distribution and predict the effect of the pore geometry on the required energy to mobilize a trapped phase. This goal was achieved by tracking the motion of an isolated bubble passing through four different pore geometries having the same pore throat size of 1 mm. Three circular pores, a smooth pore and 2 with different roughness (0.2 and 0.4 mm height saw-tooth) and a sharp triangular pore were considered in this study.

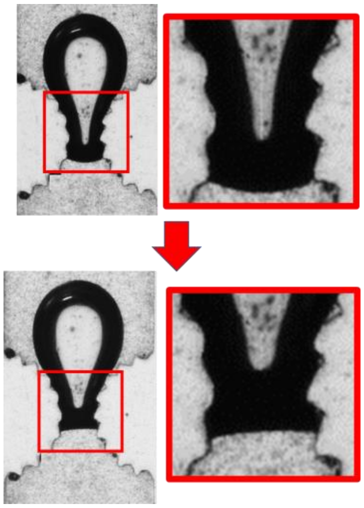

Graphical Abstract
Chapter 4

5.1 Introduction

Multi-phase flow motion in a porous media is broadly observed in different applications such as oil recovery [4], food processing [212], and macromolecular delivery [2]. The motion of the immiscible phases having different motilities in the pore space will lead to the phase trapping caused by the snap-off or the bypass of the phases in the pore structures [236], [237]. The mobilization of the trapped phase is important for many applications such as trap oxygen gas bubbles in contaminated groundwater or oil residual in the recovery oil reserves [236]–[240].

---

[7] This chapter with some modifications will be submitted as Ansari, S., and Nobes, D. S. (2020). “The effect of surface properties of a pore-scale confined geometry on the passage of a multi-phase flow”. Manuscript is prepared for submission.

Having a better understanding of the motion of the phases and their interaction with the surrounding fluid and solid geometry is beneficial to predict the required energy needed to mobilize the isolated phase.

Over the past decade, the motion of multi-phase flows in the porous media has been studied by groups of researchers on a macro and micro scale [244]–[253] . The comparison between the motion of single-phase and multi-phase flow indicates that higher resistance to the flow is observed for multi-phase flows [64]. The resistance is introduced due to the deformation of the dispersed phase which arises from the interfacial interaction between the phases and the flow passage [38]. The phase trapping in the pore geometry occurs due to the critical pressure introduced by the interaction of the dispersed phase and the solid interface at the entrance of the confined geometry [7]. To mobilize the trapped phase in the pore geometry, a critical driving force is needed to overcome the entrance pressure.

Various factors have an impact on the motion of the isolated dispersed phase in a pore structure such as the velocity of the carrying fluid [211], [232], [256], the pressure of the system [162], the relative size of the dispersed phase compared to the pore [257] and the capillary number [13], [26], [158], [258]. Studies on the interaction of the solid surface and the trapped isolated phase showed that pore structure, grain morphology, and wettability of the surface play important roles in the motion of isolated dispersed phases in the pore structure [10]–[17]. Other studies [237], [238], [242], [243], [247], [254] on the effect of the pore structure on the motion of multi-phase flow mainly focused on the overall phase trapping in the pore space and phase residual. Overall, these studies didn’t focus on the fundamentals of the interaction of an isolated dispersed phase and solid geometry and the effect of the grain morphology on the motion of the phase in pore geometry.

Research work focusing on the pore-scale interaction of an isolated dispersed phase and pore geometry [38], [39]showed that in addition to the entrance critical pressure, the strong interaction of the solid interface and the pore geometry can lead to an extra critical pressure at the exit of the pore geometry[25], [257]. The introduced flow restrictions will lead to different flow motions within the geometry and the calculation of the critical entrance pressure is not sufficient to predict the required driving force for the mobilization of the trapped phase in the solid geometry. The surface properties of the confined geometry are an important component for emulsion flows in porous media [239]–[243] . This indicates a need to study the effect of the pore geometry on the change in the phase pinning critical pressure.

The main objective of this study is to investigate the pore-scale effect of shape and surface roughness of a confined geometry on pressure distribution within the multi-phase flow and the required transit time for the phase to pass the confined geometry. To achieve this goal, an isolated bubble is considered as a dispersed phase to pass through pore space and the deformation and velocity will be monitored using a particle image velocimetry method. The interaction of the bubble and the interface is visualized by the deformation of the phase at different stages and velocity and pressure distribution were selected as representative parameters for the flow properties. The pressure in this study is calculated using an indirect method proposed in our previous studies [34], [232]. The results of this study will aim to provide a better understanding of the effect of pore surface properties on pore-scale capillary pressure and fluid motion within a porous media.

5.2 Pressure calculation from shape analysis

The pressure change of a dispersed phase passing through a confined geometry can be determined using the theory introduced by Jamin (1860) [35] which was derived from the Young–Laplace equation. According to this theory, the pressure change within the deformed dispersed phase (ΔP^*) is inversely proportional to the change in the radii of curvature of the trailing (R_{T}) and leading-edge (R_{L}) and proportional to the interfacial tension as (γ_{cd}):

$$\Delta P^* = \gamma_{cd}\left(\frac{1}{R_{\mathrm{L}}} - \frac{1}{R_{\mathrm{T}}}\right) \tag{5-1}$$

An image processing technique developed in our previous studies (POF) can be utilized to monitor the instantaneous change in the motion of isolated bubbles passing through a pore geometry. The details of the development of the image processing methodology can be seen in Chapter 3. A sample of the different stages of bubble deformation and their corresponding change in the pressure of the phase is shown in Figure 5-1. The change in the pressure within the phase (ΔP^*) and the location of the centroid of the bubble (y_c) with respect to the pore throat (y_p) showed that a different local pressure distribution can be expected depending on the location of the dispersed phase in the pore geometry. It can be seen that the proposed methodology to evaluate the motion of the phase can detect the critical pressure required for mobilization of the phase in the pore geometry. The critical pressure can be measured by the first peak detected in the flow motion in confined geometry.

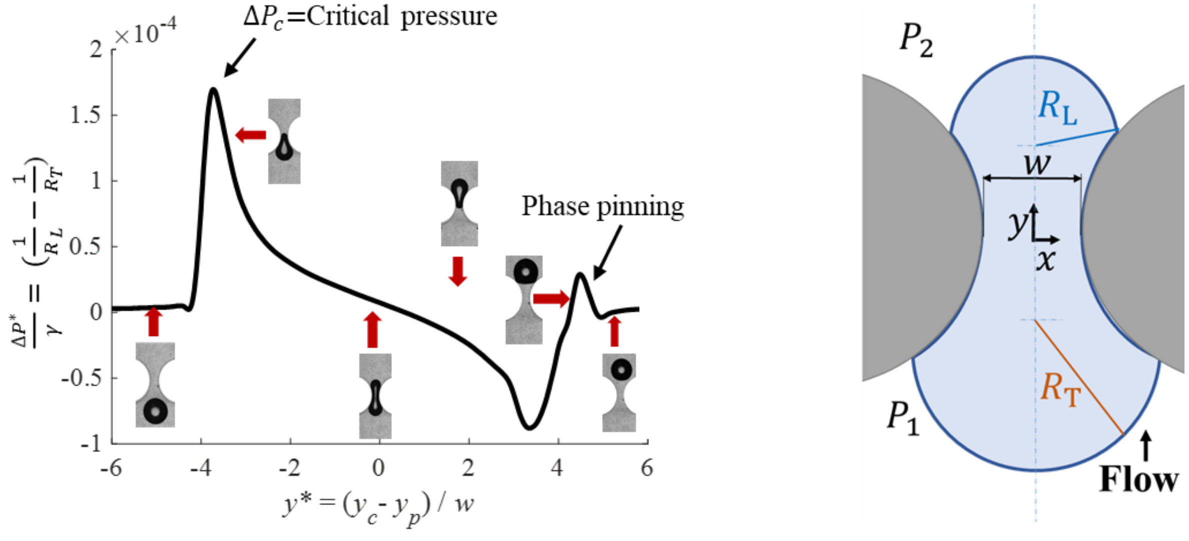

(a)

(b)

Figure 5-1. (a) An example of the determined pressure of an isolated bubble passing a pore and its corresponding locations and (b) schematic of bubble deformation.

5.3 Experimental setup and image processing

An optical setup was used to measure and track the motion and the deformation of a bubble passing through a pore geometry is shown in Figure 5-2. The setup consists of two main sections of the optical setup containing a camera (4M180, IO Industries Inc.), a light source (BX0404-520 nm; Advanced Illumination Inc.), and data acquisition (DVR Express Core 2, IO Industries Inc.). The flow loop, consisting of two syringe pumps for each phase (PHD 2000, Harvard Apparatus) and a flow channel, is highlighted in the figure.

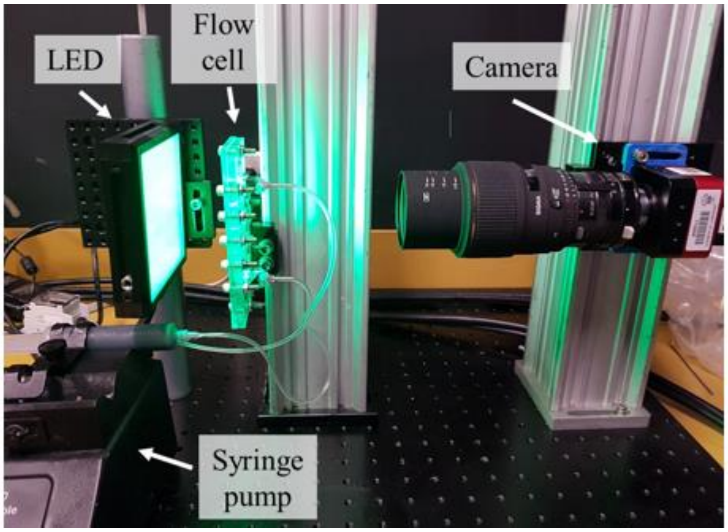

Figure 5-2. A picture of the experimental setup.

The designs of the flow channels used to study different pore geometries are shown in Figure 5-3. The flow channels consisted of two assembled layers of an optical access window and the main flow channel. The window access is made of acrylic sheet and manufactured using a laser cutter (VersaLaser VLS Version 3.50; Universal Laser Systems). The design main flow channels with the desired features were manufactured from a photo-reactive resin using the stereolithography (SLA) additive manufacturing technique (Form 2, Formlabs Inc. USA).

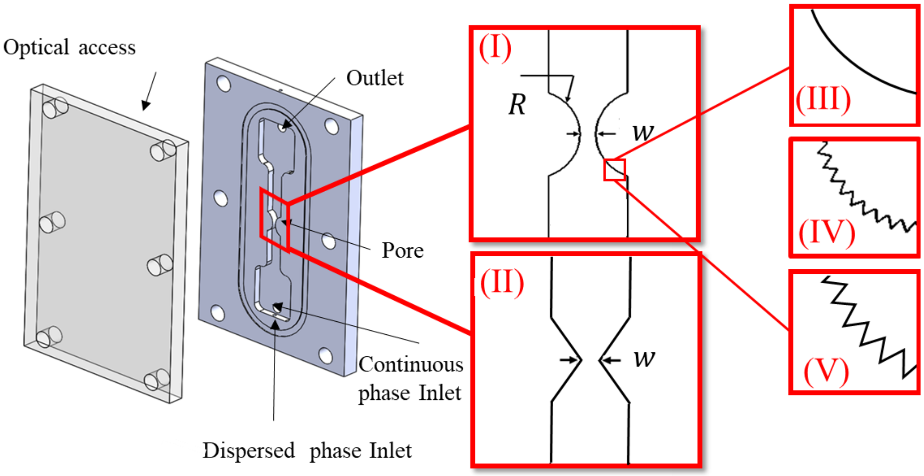

Figure 5-3. Design of flow channels containing different shapes of pore space.

Two separate inlets for the continuous and the dispersed phase were designed at the bottom of the flow channel as highlighted in Figure 3-3. Glycerol (100% Pure Glycerol (Molecular Biology), Fisher BioReagents™, USA) was used as the continuous flow and air was used as a dispersed phase. Glycerol had a viscosity 1.412 Pa.s, density 1.26 g/cm and surface tension 64 mN/m [209], [229]. The continuous phase in each experiment was injected with different flow rates of 0.1, 02, and 0.3 ml/min. Air, as a dispersed phase, was injected at time intervals to generate an isolated bubble.

The motion of the multi-phase flow in the pore space was studied by modeling the pore space of two adjacent particles in the flow channels. Four different pore geometries were designed and shown in the detailed views of Figure 5-3. These pore geometries are a smooth circular pore, circular pore with two different roughness (0.2 and 0.4 mm), and a sharp pore. In these channels, two cylindrical pillars were used to mimic the geometry of two adjacent particles in the pore space with smooth surfaces. The pillars were 2 mm in diameter and they were separated by 1 mm at the pore throat. The detail view (I) of Figure 5-3 represents the design of the smooth circular pore. Two different roughness of 0.2 and 0.4 mm, shown in the detail view (IV) and (V), were used to compare the effect of roughness. A sharp pore geometry with the same aperture was also considered to account for the effect of the change of the convergence of the pore on the pressure distribution. In this case, two adjacent rectangles were considered as shown in the detail view (II). The pictures of the pore geometries after manufacturing and their original designs are in Figure 5-4

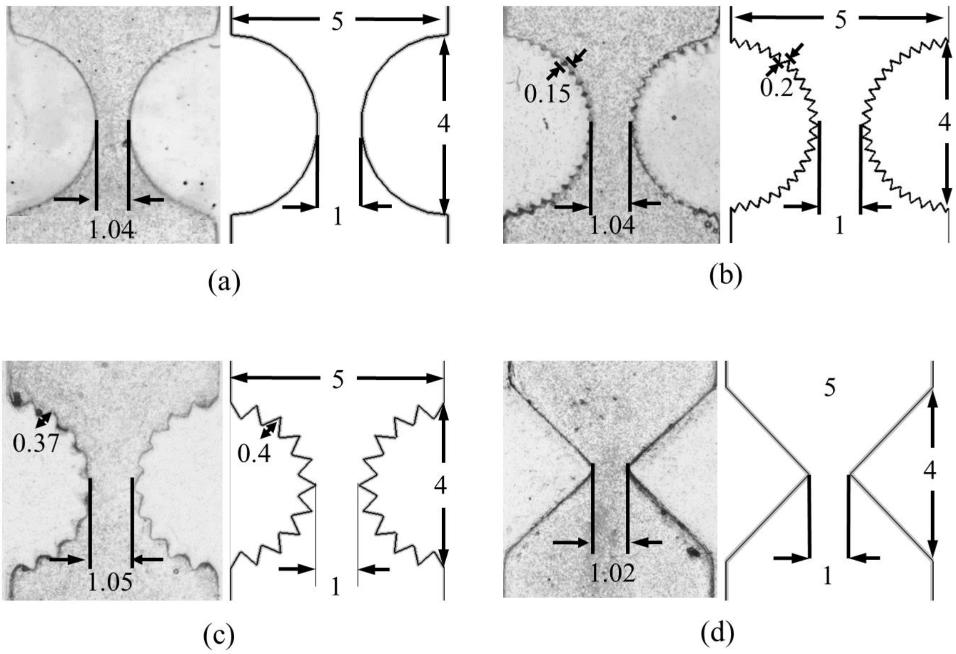

Figure 5-4. Picture of the designed and manufactured pore geometry (a) smooth circular pore, (b) sharp pore, (c) circular pore with 0.2 mm roughness, and (d) circular pore with 0.4 mm roughness (all dimensions are in mm).

A sample of a raw image of a bubble and the surrounding fluid passing through a circular pore is shown in Figure 5-5 (a). The bubble is reflected as a black hollow region as shown in the picture due to the difference between the refractive indexes of glycerol and air. To have better detection of the deformation of the bubble and remove noise of the background the images need to be pre-processed. The details of these procedures can be seen in [232], [258], [259]. The deformation of the dispersed phase in the pore geometry will be then detected by the radius of the leading and trailing edge at each location as shown in Figure 5-5 (c). Having the curvature of the leading and trailing edges, the pressure change along the faces of the bubble can be evaluated using Eq. (5-1).

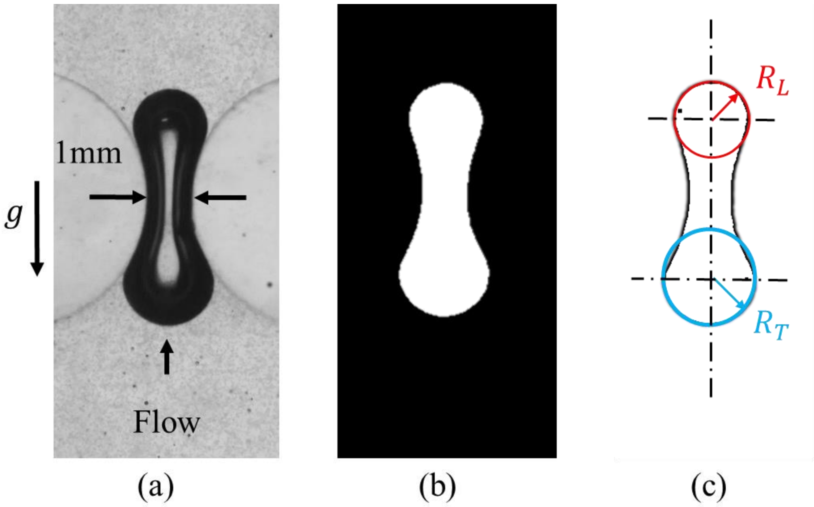

Figure 5-5. An example of (a) a raw image, (b) the isolated dispersed phase, and (c) processed image defining the leading and trailing geometry.

5.4 Results

5.4.1 Flow visualization of the deformation of the bubbles passing through different pore geometries

A series of images showing the passage of the bubble and its deformation for bubbles having a similar equivalent radius (R_b~3 mm) passing through the different pore geometries are shown in Figure 5-6. As the bubbles have slightly different velocities for these cases. Therefore, the images were selected based on the location of the centroid of the bubble from the pore throat to highlight the bubble shape at these locations for the different surface conditions. As shown in location (a) for all pore geometries, it can be seen that the bubbles are symmetric and have similar radius for the curvature of leading and trailing. They are slightly oval due to the presence of a confining wall effect on the bubble's interface as was reported in the literature [29]. As the bubbles approach the pore geometry, their leading-edge deforms slightly as shown in location (b). The deformation in this location leads to the decrease in the radius of curvature of the leading edge compared to the trailing edge of the bubble. The decrease in the leading edge continues until it passes the pore throat as shown inFigure 5-6 (c). After this location, the leading edge radius of curvature increases and reaches an equilibrium condition after the bubble has passed through the pore geometry.

As shown in Figure 5-6, there is a significant difference between the motions of bubble exiting the pore geometries with different roughness. The effect of the surface condition of the pore geometry on the motion of the bubble can be observed by the deformation of the trailing edge at different locations along the pore. It can be seen that in the case of a smooth circular pore, shown in Figure 5-6 (I), the bubbles trailing edge decreases as it enters the pore geometry. The trailing edge maintains its convex curvature during its passage in the pore. As it reaches the exit of the pore, in location (h) of the case (I), the interaction between the pore solid interface and the bubble leads to the development of phase pinning. Change in the detachment of the bubble exiting a circular pore geometry is highly affected by the relative size of the bubble with the pore and the continuous phase flow rate. A sample of the effect of the continuous phase flow rate is shown in Figure 5-7. It can be seen that the bubble's trailing edge interface becomes flat for lower flow rates and as the flow rate increases, the bubbles trailing interface becomes concave.

The motion of a bubble passing through a circular pore with roughness is shown in Figure 5-6 (II) and (III). Having a closer look at the interaction of the bubble and pore geometry shows that the bubble deforms to fill the pore roughness. It does not block the valleys of the pore roughness and the phases are mostly in contact at the peak of the roughness of the pore. The higher contact area between the bubble and the solid surface in this condition results in more interaction between the surface and the bubble at the lower portion of the bubble. Therefore, it can be seen that phase pinning occurs at each peak of the roughness of the pore interface shown in locations (g) (h) for cases (II), and (III).

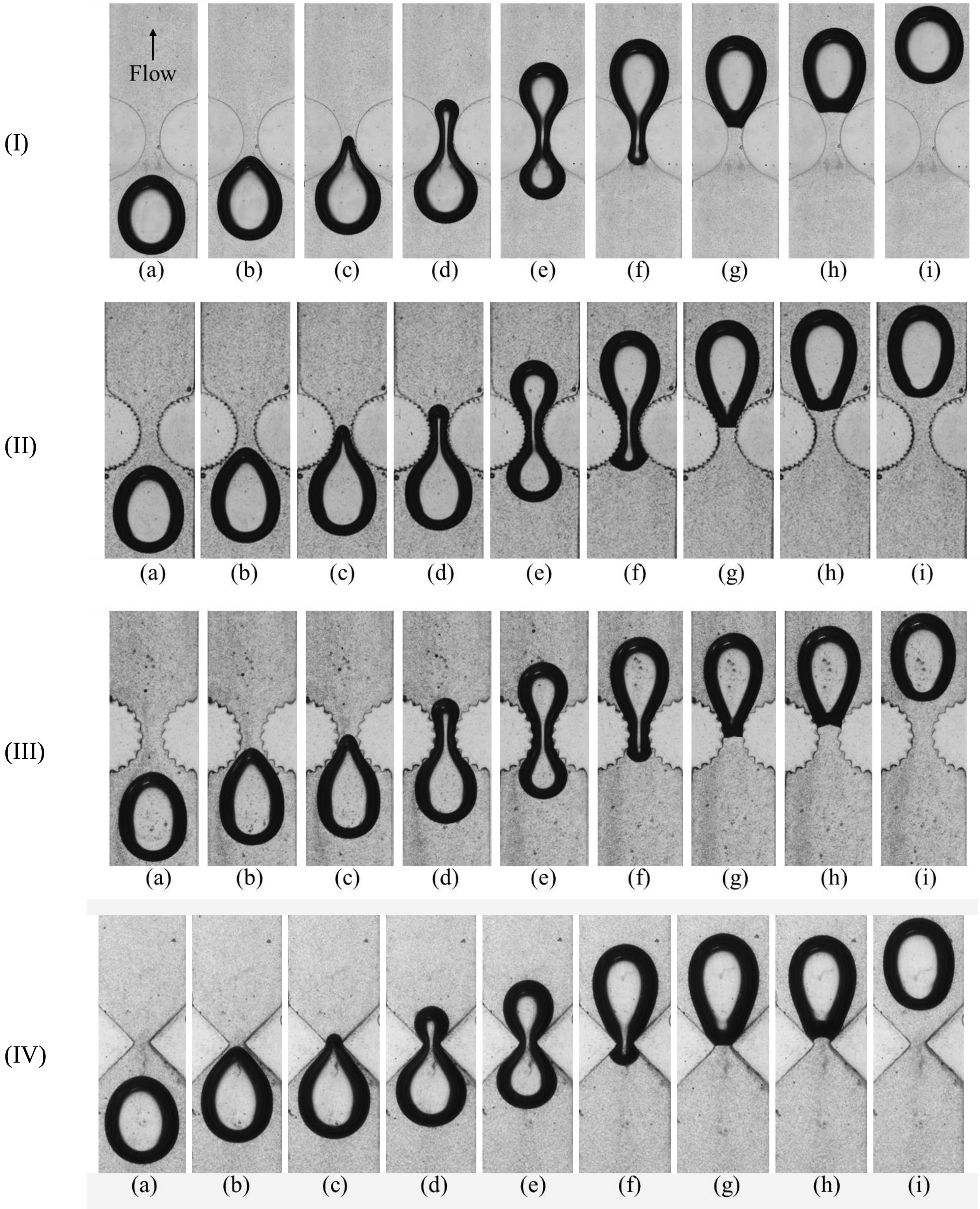

Figure 5-6. Bubble passing through (I) circular pore (II) circular pore with 0.2 mm surface roughness, (III) circular pore with 0.4 mm surface roughness, and (IV) pore with a sharp corner.

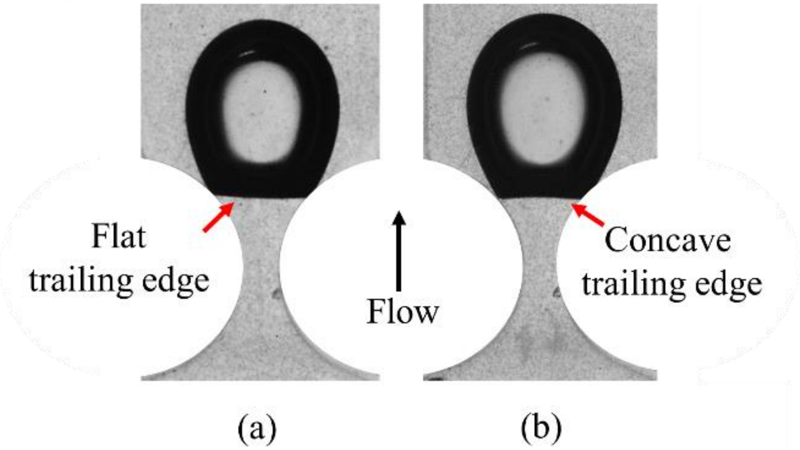

Figure 5-7. Pinning of a bubble existing a smooth pore interface at (a) 0.1 ml/min and (b) 0.3 ml/min.

The interface of the trailing edge of the bubble goes through different steps due to the pinning at each peak of the pore. The details of the change in the curvature of the bubble passing a 0.4 mm roughness are shown in Figure 5-8. As shown in the detailed view of Figure 5-8 (a), the bubble has a convex curvature before its trailing edge reaches the peak of the roughness. As the bubble moves further in the pore, the bubble’s trailing edge reaches the same elevation of the pore the roughness. It can be seen in Figure 5-8 (b), the bubble has a flat trailing edge due to the pinning of the phase. On breaking of the pinning, inFigure 5-8 (c) the trailing edge curvature has become convex. As the bubble is not in contact with the valleys of the pore, the trailing edge becomes unstable and the bubbles trailing edge moves to the next pore peak as shown in Figure 5-8 (d). The same deformation steps for the trailing edge were observed at each peak of the roughness. Similar interaction of the phase was observed in the case of bubble moving through a pore with a roughness of 0.2 mm.

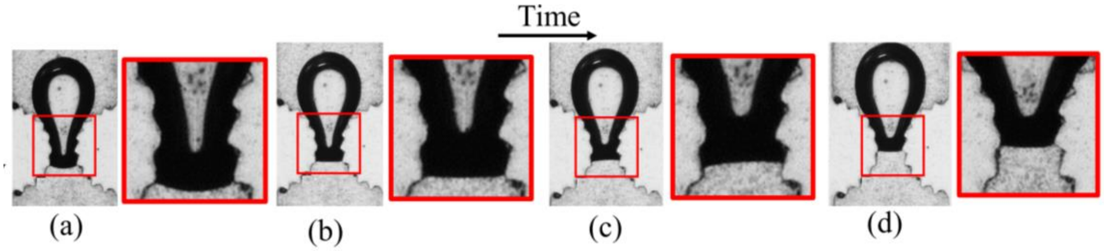

Figure 5-8. Phase pinning of a bubble (R_b~1.95 mm)at different stages passing through a rough pore space .

For the case of the flow in the sharp pore geometry shown in Figure 5-6 (IV), the bubble has a smooth transition in the pore geometry. It can be seen that due to the lower gradient of the change in the available cross-sectional area of the pore geometry, the curvature of the leading and trailing edges has more variation. The bubble has the same trend of the change in the leading and trailing edge. The pinning of the phase was observed after the bubble passes the pore throat as shown in location (g) of Figure 5-6 (IV).

5.4.2 The effect of pore geometry on the deformation, pressure, and velocity of the bubble passing through smooth circular pore

The instantaneous change of the absolute value of the radius of curvature of the leading and trailing edges of a bubble passing through a circular pore (geometry shown in Figure 5-4 a) is represented in Figure 5-9 (a). The location of the bubble, symbolized by y^*, is the normalized location of the centroid of the bubble (y_c) along the pore geometry by the width of the channel (w). The location was also offset by the pore throat (y_p) so the location y^*=0 represents the condition when the bubbles centroid is aligned with the pore throat.

As indicated in Figure 5-9 (a) the bubble has the same radius of curvature of the leading and trailing edge before it enters the pore geometry ($y^* < -4$). This condition is also shown in location (a) of Figure 5-6 (I). As the bubble enters the pore, indicated in location (b) in Figure 5-6 (I), the bubbles leading edge decreases due to the decrease in the available cross-sectional area. The minimum radius occurs at $y^{*} \sim -3$ where the leading edge is aligned with the pore throat. The deformation of the leading edge continuous until location (g) of Figure 5-6 (I) when the bubbles leading edge passes through the pore geometry and it regains its original radii of the curvature for $y^{*} > 4$.

It can be seen that the deformation of the bubble's trailing face occurs further in the pore ($y^{*} \sim -3$) compared to the leading edge. The bubbles trailing edge reaches its minimum value as it aligns with the pore throat ($y^{*} \sim 2.5$). It can be seen that at $y^{*} \sim 4.5$ the radius increases to infinity and decreases to a constant value. The increase in the radius is caused by the pinning of the bubbles trailing edge before it exits the pore. In this condition, the bubbles trailing edge becomes flat and again regains its convex shape. After $y^{*} > 5$, the bubble detaches from the surface, and its radius of curvature of leading and trailing edge becomes equal.

The change in the pressure of the bubble at different locations along the pore was determined by the change in the radius of the curvature shown in Figure 5-9 (a) and Eq. (5-1). As shown in Figure 5-9 (b), the bubble has similar pressure at the entrance and exit when the bubble is well away from the pore. As it enters the pore, the pressure drop increases to a maximum value at ($y^{*} \sim -3$). This positive pressure is known as the critical pressure required for the bubble to enter the pore. This pressure is highly affected by the relative size of the dispersed phase and pore geometry, flow rate, and interfacial tension of the phases. In the current study, the bubble can pass this stage as the driving force of the carrying fluid overcomes the introduced pressure and the phase can deform further to pass the pore geometry.

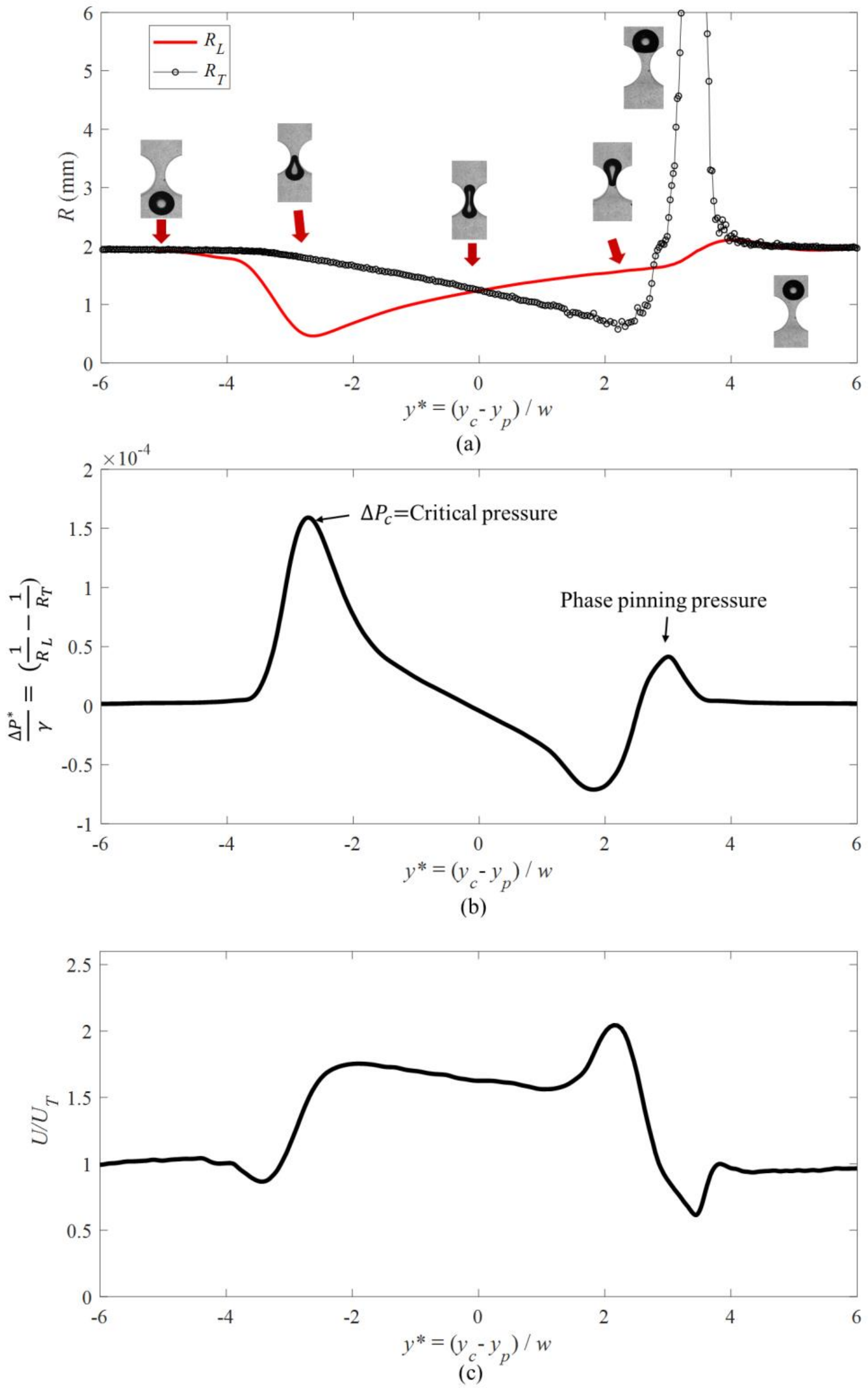

Figure 5-9. Plots of (a) change in the radii of curvature of leading and trailing edge of a bubble, (b) pressure along the bubble, and (c) velocity of the centroid of a bubble ($R_b \sim 1.95$ mm) passing through a smooth circular pore surface.

As the bubble passes the stages corresponding to the critical pressure, the pressure drop along the bubble decrease and it reaches a minimum value. The pinning of the phase at the exit of the pore results in another positive pressure. It can be seen that the introduced pressure due to the pinning of the bubble, in this case, is lower than the critical pressure at the entrance. The driving force also can again overcome this pressure and the bubble can exit the pore geometry.

The change in the pressure of the bubble results in a variation in the velocity of the centroid of the bubble as depicted in Figure 5-9 (c). It can be seen that the bubble reaches the pore geometry with a constant velocity. A slight decrease in the velocity is detected as the bubble gets closer to the pore geometry. The deceleration is caused by the development of the critical pressure needed to deform the bubble, allowing it to enter the pore. As the bubble passes this location it accelerates as it enters the pore throat. The introduced pinning pressure will result in a decrease of the velocity at the exit of the pore. The bubble accelerates as it detaches from the surface of the pore, returning to its terminal velocity.

5.4.3 The effect of pore geometry on the deformation, pressure, and velocity of the bubble passing through circular pore with 0.2 mm roughness

The variation in the radius of curvature, pressure, and velocity of a bubble passing through a circular pore with 0.2 mm roughness are shown in Figure 5-10. It can be seen that the leading edge experiences the same deformation as discussed for the smooth circular pore. The trailing edge, however, has a different set of deformation characteristics as the bubbles centroid passes through the pore throat ($y^* > 0$). The interaction of the moving interface of the bubble and the peaks of the solid interface leads to pinning of the phase at different locations after the pore throat. The bubble interface shape change at each peaks of the pore roughness which result in increase in the radius of curvature. These conditions are represented by the peaks detected in Figure 5-10 (a).

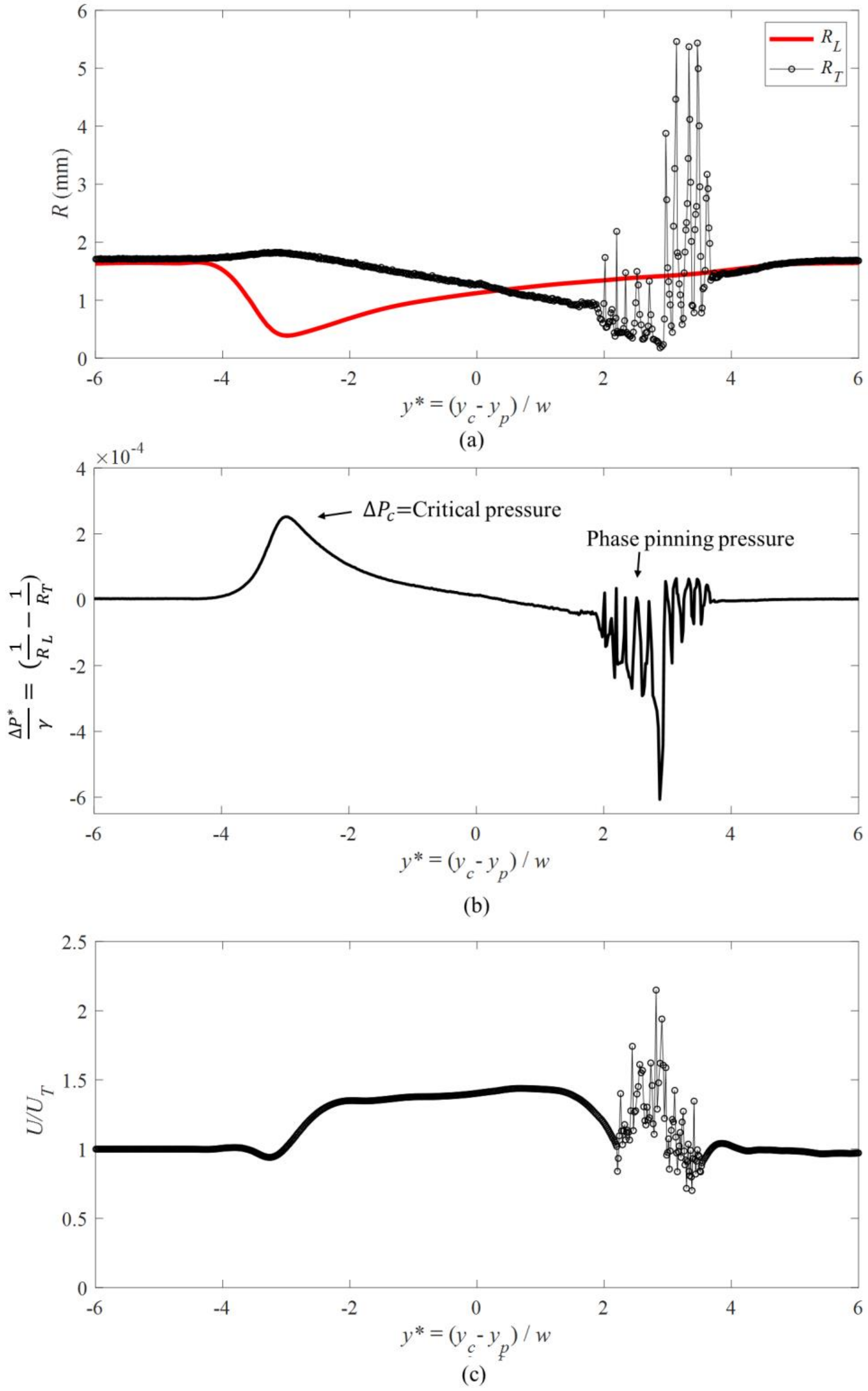

Figure 5-10. Plots of (a) change in the radii of curvature of leading and trailing edge of a bubble, (b) pressure along the bubble, and (c) velocity of the centroid of a bubble ($R_b \sim 1.95$ mm) passing through a circular pore with 0.2 mm roughness on the surface.

The effect of the pinning of the phase in this pore geometry on the instantaneous change in the pressure of the bubble at different locations is shown in Figure 5-10 (b). It can be seen that the overall trend of the change in the pressure is similar to the circular pore discussed in the previous section. Similar critical pressure is detected in this case as shown for the smooth surface. The phase pinning of the bubble trailing edge at different locations along the pore results in multiple positive pressure peak detection as the bubble passes the pore throat.

The velocity of the centroid of the bubble passing through the rough pore is shown in Figure 5-10 (c). The velocity of the bubble is constant before it reaches the pore and as it enters the pore, the bubble accelerates due to the decrease in the available area. The bubble decelerates as its centroid passes the pore throat as the area available for the flow increases. It can be seen that at each pinning location, there is an acceleration and deceleration of the bubble. In these locations, the bubble decelerates as the pinning occurs and it accelerates as it detaches from the surface. The acceleration occurs due to the instability between the roughness peaks which results in a rapid motion of the trailing edge toward the next peak of the surface roughness. These phenomena can be seen for all cases of the pinning and the motion of the bubble as it exits the pore.

5.4.4 The effect of pore geometry on the deformation, pressure, and velocity of the bubble passing through circular pore with 0.4 mm roughness

The effect of the pore roughness identified by the change in the radius of the curvature of a bubble passing through a circular pore with 0.4 mm roughness as shown in Figure 5-11 (a). A similar trend of the change in the radius of curvature detected for the case of 0.2 mm roughness. The number of the detected peaks of the change in the curvature is lower due to the lower number of the pore roughness objects. The variation of the radius is higher due to the stronger interaction of the bubble and solid interface. The bubble interface shape changes from convex to concave which results in discontinuities in the instantaneous change of the radius of curvature. For the clarity of the discussion, the details of the stages of the change in the curvature highlighted by the blue box inFigure 5-11 (a), are represented in Figure 5-12 (a)

As shown in Figure 5-12 (a), the bubble passes through the different stages of deformation and these stages are numbered and displayed in Figure 5-12 (b). The bubble has a convex trailing interface before the pinning of the phase. It can be seen that there is a slight increase in curvature of the trailing edge at the location (1). This is due to the pinning of the bubble that occurs at this condition leading to the higher curvature for the bubble's interface. As the bubble moves further in the pore, it can be seen that the bubble moves to the next peak of the pore roughness. The smaller cross-sectional area available for the bubble's trailing edge in location (2) leads to a decrease in the curvature of the bubble which can be seen by the local minimum at $y^{*} \sim 1.9$. The bubbles interface becomes a flat surface at the location (3) which leads to $R \rightarrow \infty$ at location $y^{*} \sim 2.25$ in Figure 5-11 (a) and Figure 5-12 (a). The driving force of the continuous phase moves the bubble forward leading to the change in the curvature of the bubble to be concave as shown in location (4).

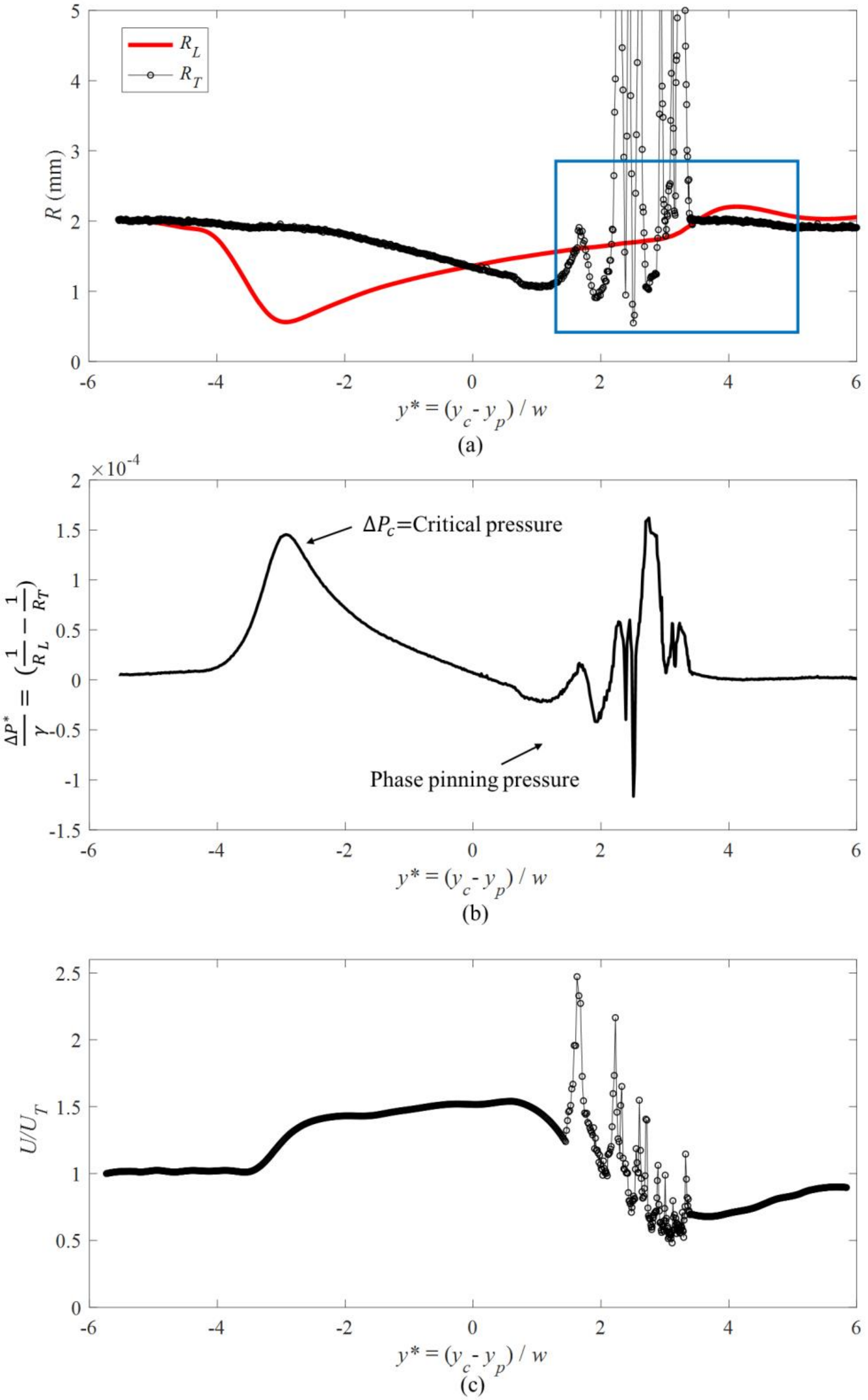

Figure 5-11. Plots of (a) change in the radii of curvature of leading and trailing edge of a bubble, (b) pressure along the bubble, and (c) velocity of the centroid of a bubble (R_b~1.95 mm) passing through a circular pore with 0.4 mm roughness on the surface.

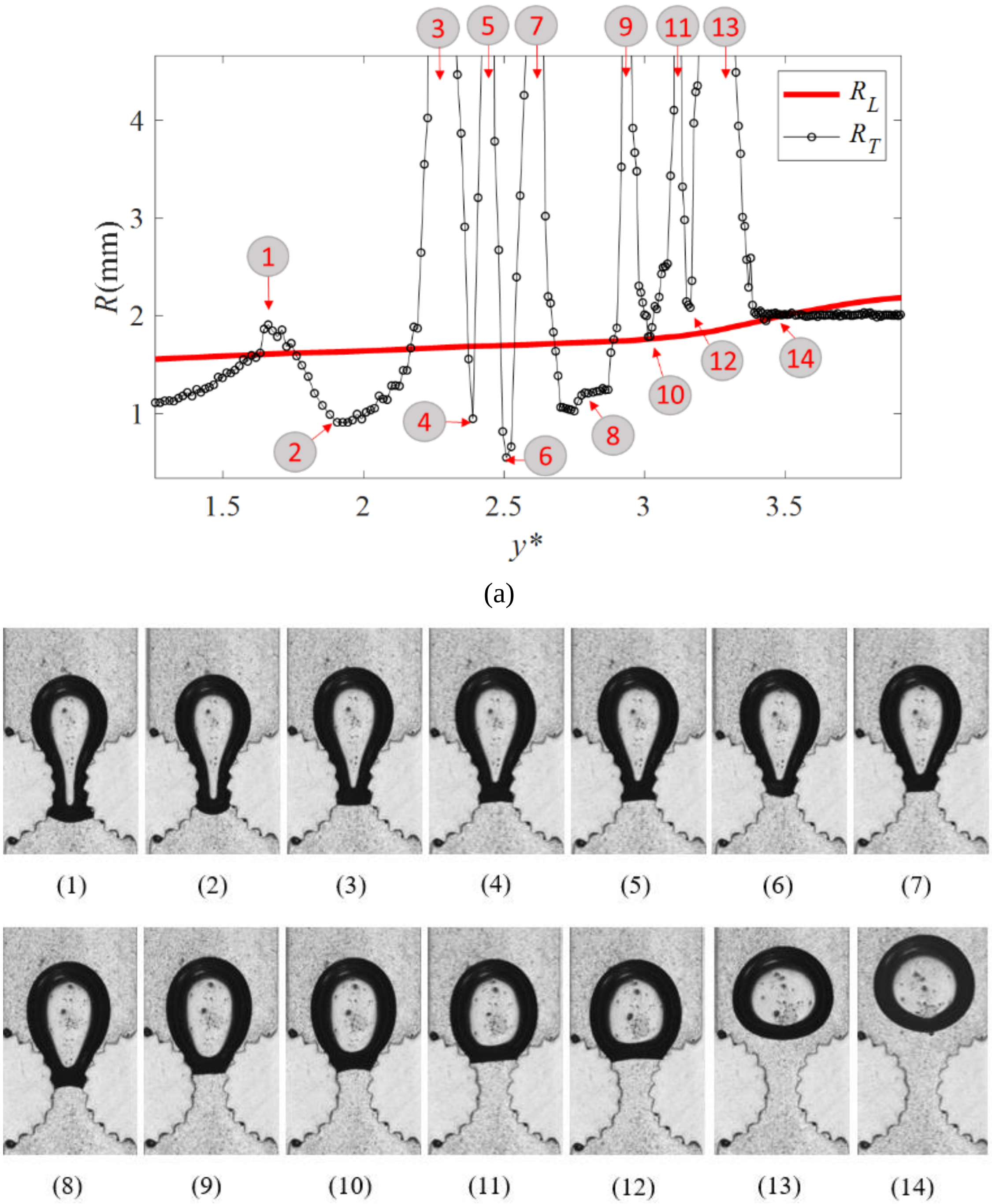

(a)

(b)

Figure 5-12. (a) zoomed-in condition represented in Figure 5-10(a) and (b) stages of bubble pinning in a pore.

The change in the direction of the curvature of the bubble occurs at each peak of the surface roughness before the trailing edge reaches the pore throat at location (6). The bubble radius of the curvature is the smallest in the location (6) as its interface is aligned with the smallest cross-sectional area available for the bubble passage at the pore throat. After this location, the curvature of bubbles trailing edge increases and it becomes convex again at a location (8). The convex interface of the bubble at the pore throat holds for the longest time at this stage due to the strong pinning force compared to the other stages. This is due to the smallest cross-sectional area available for the bubble passage. As the bubble's trailing edge passes the pore throat, it only has a concave and flat surface in the transit between each peak of the pore. The last pinning occurs before the bubble exists the pore at the location (12) and after this location, the bubble detaches from the pore surface and it goes back to its spherical shape as shown in location (14).

The effect of the pinning of the phase in this pore geometry on the instantaneous change in the pressure of the bubble at different locations is shown in Figure 5-11 (b). It can be seen that the overall trend of the change in the pressure is similar to the circular pore discussed in the previous section. A similar critical pressure is detected in this case as shown for the smooth surface as the bubble enters the pore. The phase pinning pressure, however, is different in this condition due to the multiple pinning in the flow passage. It can be seen that the pressure of the pinning occurs at different locations the bubble passes the pore throat result in the region with a variation in the pressure drop. In the location where the pinning occurs series of peaks are detected. The lowest pressure difference along the bubble occurs when the bubble has the smallest curvature of the trailing edge location (6) and the largest pressure is detected for the phase pinning at the pore throat having the smallest negative curvature of the bubble at location (8).

The velocity of the centroid of the bubble passing through the rough pore is shown in Figure 5-11 (b). It can be seen that the velocity of the bubble is constant before it reaches the pore. As it enters the pore, the bubble accelerates due to the decrease in the available area. The bubble decelerates as its centroid passes the pore throat as the area available for the flow increases. It can be seen that at each pinning location, there is an acceleration and deceleration of the bubble. In these locations, the bubble decelerates as the pinning occurs and it accelerates as it detaches from the surface. The acceleration occurs due to the instability between the roughness peaks which results in a rapid motion of the trailing edge toward the next peak of the surface roughness. These phenomena can be seen for all cases of the pinning and the motion of the bubble as it passes through the pore.

5.4.5 The effect of pore geometry on the deformation, pressure, and velocity of the bubble passing through sharp pore

The variation in the radius of the curvature of the leading and trailing edge of a bubble passing through a sharp pore is shown in Figure 5-13. It can be seen that the bubbles leading and trailing edge have a similar trend as observed for the bubble flow in a circular pore. Only one phase pinning can be observed as the bubble passes through the sharp geometry. Comparing the location of the pinning of the bubble in this case and the smooth round pore, it can be seen that the pinning in the case of sharp pore occurs further into the pore ($y^{*}\sim 4$ for circular pore and $y^{*}\sim 3$ for the sharp pore). This is due to the difference in the structure of the pore throat. In a sharp pore, the bubble detaches from the solid geometry right after it passes through the pore throat. In the case of the circular pore, however, the bubble is in contact with the pore further in the axial direction due to the gradual change in the pore geometry.

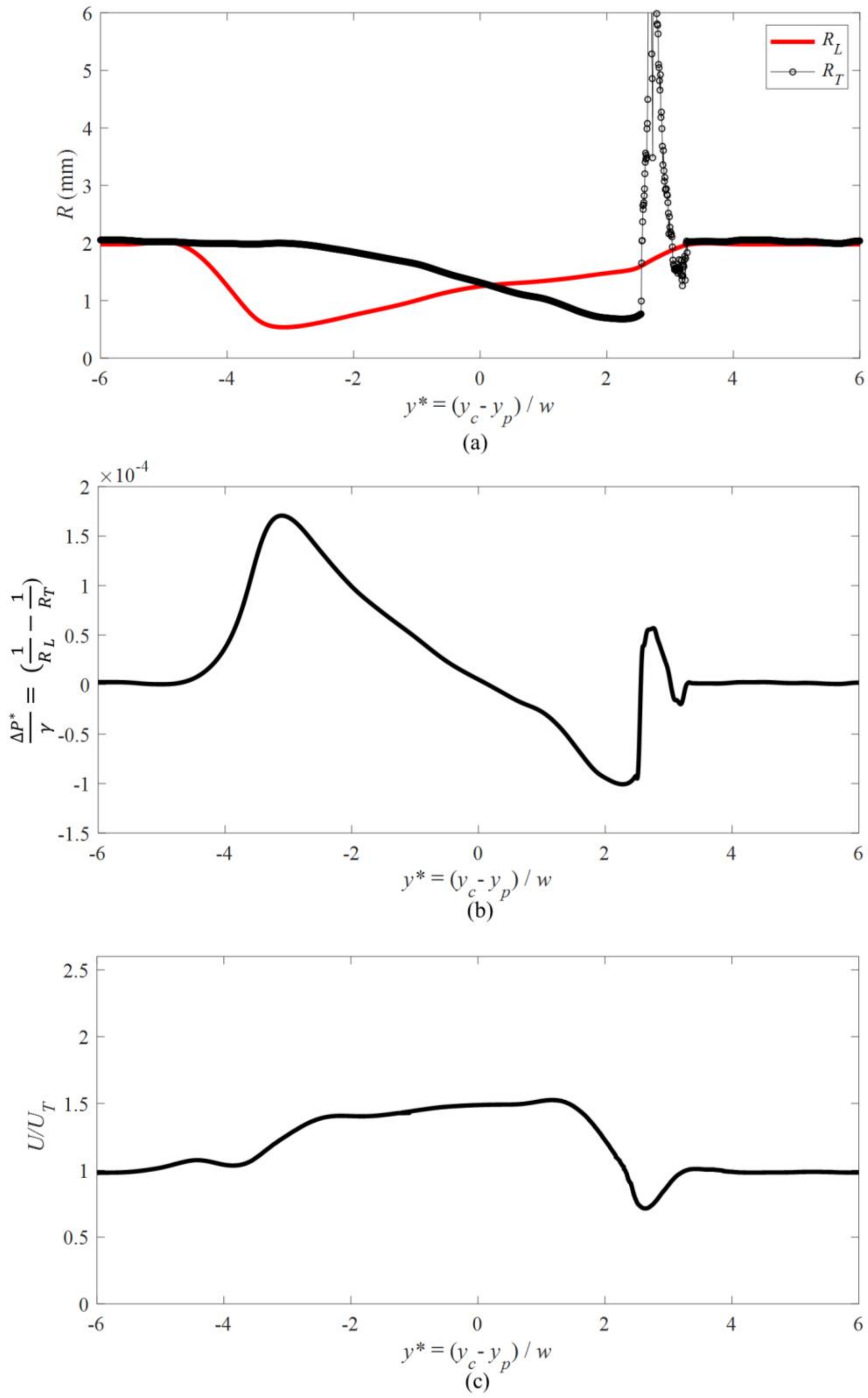

Figure 5-13. Plots of (a) change in the radii of curvature of leading and trailing edge of a bubble, (b) pressure along the bubble, and (c) velocity of the centroid of a bubble (R_b~1.95 mm) passing through a sharp pore

The critical pressure and the pinning pressure of the sharp pore can also be seen in the peaks shown in Figure 5-13(b). It can be seen that the phase pinning pressure in this condition is slightly larger than the one detected for a circular pore. This is because the pinning in the sharp pore occurs closer to the pore throat and the available cross-sectional area in this location is smaller. The smaller gap between the pore results in more deformation and a higher pressure gradient. The effect of the change in the pressure on the velocity is shown in Figure 5-13 (c). It can be seen that a lower acceleration is observed in this case due to the difference in the available cross-sectional area at different locations along the pore.

5.5 Bubble's Transit Time in different pore geometries

The variation of the transit time required for bubbles of different sizes passing through different pore geometries is represented in Figure 5-14. The transit time in this study is measured time required for the bubble leading edge enter the pore structure and the trailing edge exit the pore structure determined from image analysis images obtained using the optical setup. The overall trend of the change in the transit time at the same flow rate in the confined geometry is represented by the fitted line for each collected data set moving.

For all conditions, it can be seen that the bubble's transit time increases linearly as the size of the bubble increases. This is due to the higher volume of the larger bubbles which results in lower mobility of the bubble in the pore geometry. From the figure, it can be seen that the highest transit time corresponds to the motion of the bubble carried with lower flow rates of the continuous phase. The lower flow rate provides a lower driving force for the bubble passage which leads to the slower bubble motion in the pore geometry.

As the figure shows, there is a significant difference between the transit times of bubbles moving through different geometries. The transit time for the bubble flow in the sharp pore is the highest as the available cross-sectional area in this case is larger than the circular pores. The lower gradient in the decrease in the available area for the flow in this case results in lower acceleration of the bubble and slower motion of the phase in this geometry. The lower acceleration of bubble in sharp pore can be also observed by comparing the velocity reported in Figure 5-9 and Figure 5-13.

It can be seen that at the same flow rate, the lowest transit time occurs in the case of bubble flow in the smooth circular surface. This condition occurs since the only resistance, in this case, arises due to the critical pressure at the entrance and the phase pinning at the exit of the pore geometry. The transit time increases as the roughness on the wall of the pore geometry increases. The increase in the transit time is due to the multiple phase pinning that occurs for the bubble passage after the pore throat. For the case of bubble flow in the smooth circular pore, as shown in Figure 5-9, the bubble only pins on the exist of the channel and the reduction in the velocity occurs only in this location. For the bubble passing through the 0.4 mm the pinning is a more severe result in the change in the direction of the curvature (concave to convex and vice versa). The change in the trailing interface results in more delay in the motion of the bubble passage.

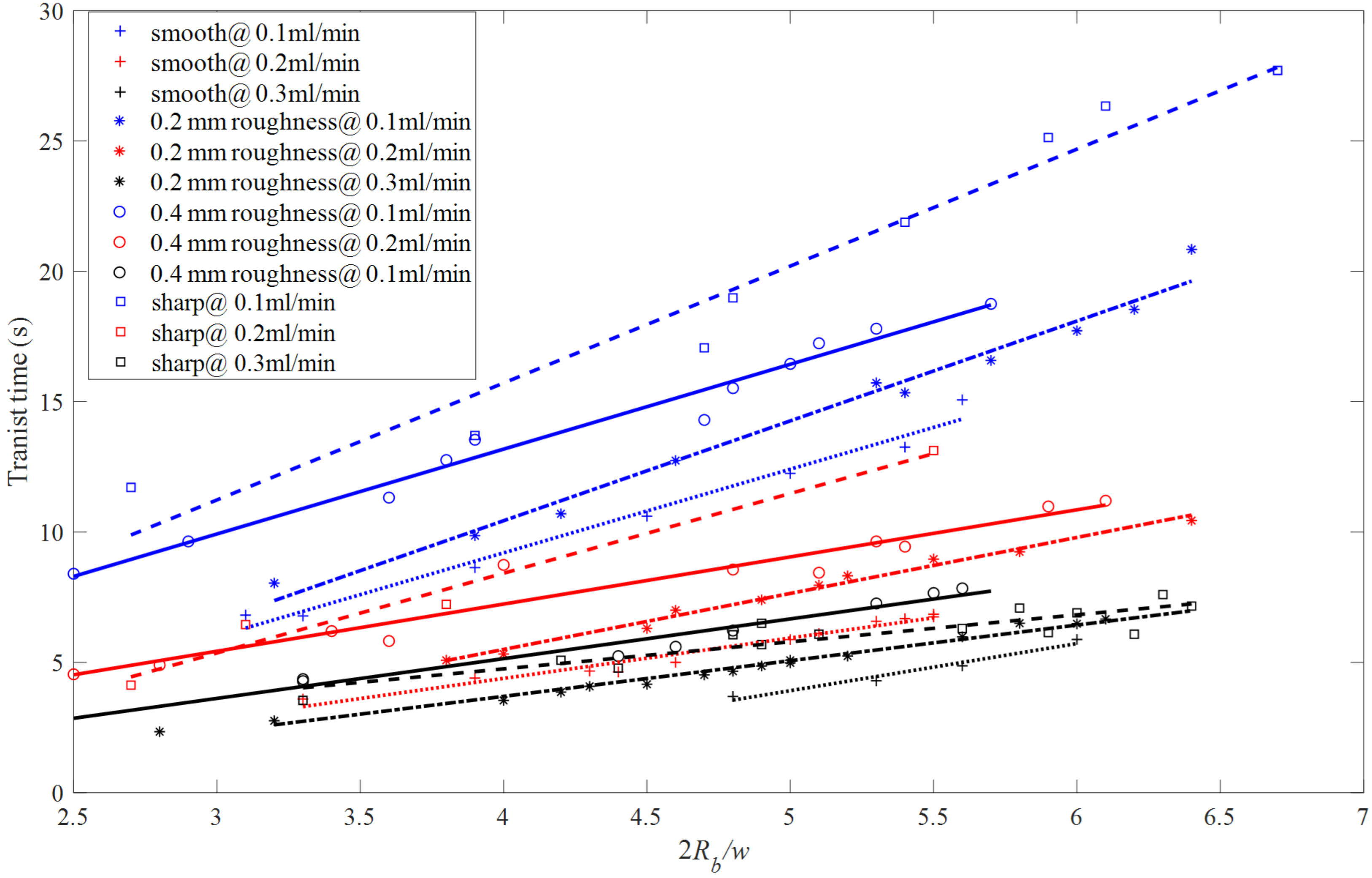

Figure 5-14. Plots of change in the transit time of bubble at different flow rates, size, and pore geometry. The flowrates are color-coded where black, red and blue corresponds to 0.1, 0.2 and 0.3 mm/min, respectively.

5.6 Conclusion

The main goal of the current study was to determine the effect of pore geometry on the motion and mobilization of an isolated bubble passing through a pore. The effect of pore’s structure was studied by the tracking of bubble deformation, pressure, the velocity of the centroid, and the required transit time for the phase passage. Four different pore geometry of circular with a smooth surface, circular with 0.2 mm and 0.4 mm roughness, and sharp pore were considered for this study. The evidence from this study suggests that the motion of the bubble passing through a pore space is highly affected by the geometry of the pore solid interface.

Investigation of the deformation of the bubble has shown that the different pore structures considered in this study all have a similar effect on the leading edge. However, significant differences were observed for the deformation of the bubble’s trailing edges. For the smooth circular pore structure and sharp pore, only one phase pinning event was observed before bubble detachment from the pore surface. For a bubble passing through a rough pore, the bubble has many pinning events for each peak of the roughness after the pore throat. The number of pinning events increases by the number of roughness structures on the pore surface. The strength of the interaction also increases by the height of each peak of the pore roughness.

The results of the pressure the change across the bubble showed that in addition to the critical pressure introduced by the entrance of the pore, a phase pinning pressure is also introduced during the phase passage in the pore. For all cases, similar critical pressure for the entrance is observed. The pinning pressure was highly affected by the properties of the pore structure. The change in the pressure due to the phase pinning was observed with a higher number of peaks and a wider range of pressure effect for pores having a rough surface structure. The applied pinning pressure at each pore roughness result in the positive pressure difference along the bubble and ultimately deceleration of the phase motion.

This study has found that generally, the transit time of the bubble through the pore structure increases with an increase in the pore surface roughness and the size of the dispersed phase. A shorter transit time was observed for the case of the smooth pore due to the minor effect of the phase pinning at the exit of the pore. The phase pinning in the rough structures leads to the delayed passage of the bubble in these pore geometries.

This research extends our knowledge of the pore-scale interactions of pore structure and multi-phase flow on the mobilization of the pore. The results of this research support the bulk flow studies that a higher driving force is required for the mobilization of trapped phase in rough and unstructured pore geometries. The findings from this study suggest that the critical pressure for mobilization of trapped isolated phase in a pore geometry can be predicted by the study of the motion of an individual isolated phase. The current study was also able to detect the phase pinning introduced pressure which results in the delayed passage of multi-phase flows in the pore structure.

Chapter 6: Interaction of loosely packed bubbly flow passing through a pore space [8]

This chapter describes the experimental investigation of the interaction of bubbles in a loosely packed bubbly flow passing through a single pore space. The motion of the bubbles has been evaluated by considering shape analysis of their deformation and the variation in the velocity and pressure distribution of the phase. Two cases of a linear array and a matrix of bubbles were considered to study the effect of the arrangement on the deformation and motion of the dispersed phase in the pore space. The result of this study showed emphasizes the importance of the location of the bubbles on their corresponding change in the pressure and the velocity.

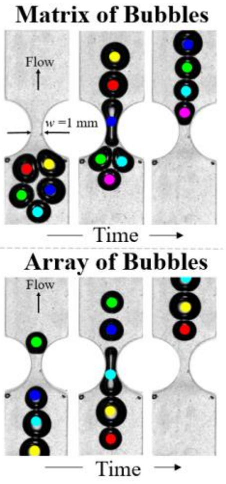

Graphical Abstract Chapter 6

6.1 Introduction

Multi-phase flow transportation of fluids with a continuous phase and a discrete, dispersed phase of particles, bubbles, or droplets in confined geometries have been described for various applications such as the food industry [1], oil reservoirs [17], and flow control devices such as orifice valve [189]. The interaction between the phases and confining flow passages has been shown to enhance or decrease the performance of that particular application. In the transport of

---

[8] This chapter with some modifications has been published as Ansari, S., & Nobes, D. S. (2020). Interaction of loosely packed bubbly flow passing through a pore space. *Journal of Visualization*. 23: 649-660.

bacteria [195] and drugs [6] removal of the dispersed phased is desired from the surface of the confining geometry. The interaction between a bubble or a liquid droplet and the dispersed phase enhances the transportation of the contaminate by encapsulation of the target material at the interface of the dispersed phase [3], [6], [212]. In the oil and gas industries, however, the transport of solid fines in the reservoir is not desirable. It can lead to fouling which decreases oil production [260]. Despite the wide range of applications, little is known about the interaction of the phases flowing through confining geometries of changing shape. This indicates a need to understand what effect the confining geometry has on the deformation and transport of the dispersed phase interface and its impact on dispersed phase interaction.

Several attempts have been made to study the motion of multiphase flows through confining channels [13], [22], [23]. The complexity of the interaction between the phases results in the simplification of the cases used when modeling to capture these phenomena. Research to date has tended to focus on a single bubble [13] and its motion in the confined space rather than multiple bubbles or droplets. It has been reported that the dispersed phase's viscosity, surface tension, and the velocity of the dispersed phase described by the capillary number has a significant effect on the deformation and the interaction of the phase with the confined geometry [13], [19], [20], [23], [27]. The results investigating the transportation of material within multi-phase flow have shown that a bubble with higher velocity (higher capillary number) results in lower material encapsulation [195]. Studies on the morphology of the deformed bubble also reported that the film thickness between the bubble and the surface of confined geometry can be characterized using the capillary number[22], [23]. The effect of the parameters on the motion of the phases becomes more pronounced in the case of confined geometries with varying cross-sectional areas such as a pore space, where the capillary number varies due to the change in the velocity of the dispersed phase.

A number of studies have reported the effect of the pore geometries on the velocity of isolated dispersed phase as a function of pressure distribution and the deformation of the dispersed phase [25], [34], [35]. These studies indicated that the pressure within the dispersed phase is not uniform due to the deformation of the phase as it passes through the pore space [27]. The pressure can be determined using the shape of the deformed dispersed phase and theory describing the Jamin effect [35], [37]. Based on this theory, there is a change in the pressure gradient within the dispersed phase that leads to the deceleration/acceleration phenomena of the dispersed phase when passing through a pore space [25]. Previous studies investigating the pressure and the deformation in the multi-phase flows [25], [34], [35], however, have not dealt with the interaction between the phases entering in the pore scale. Comparing the constant velocity reported for the motion of dispersed phase through uniform channels and the change in the velocity of the phase passing through a pore space emphasizes the importance of the flow conditions and the interaction with surrounding fluid and walls on the motion of the multi-phase flow.

Bubbly flows [33], [261], emulsions [21] and their interaction within porous media has been mainly studied at a bulk scale. This analysis of the motion of the multi-phase flow in the porous media has indicated that the flow will have more resistance to passage through the geometries as a result of pore interaction between the phases [21]. So far, however, there has been little discussion about the pore level mechanisms and the interaction of the phases in the pore space. There has been qualitative analysis of the interaction of bubbles in a high-quality foam in the pore space [28] that has shown the importance of the orientation of the dispersed phase approaching the pore space on their existing orientation of the dispersed phase. The dispersed phase can follow in the same path or they can experience reorientation or pinch-off as they pass through the pore space [28]. Research on the subject has been mostly restricted to limited comparisons of compact foam where the volume of the continuous phase is negligible and the interaction between the dispersed phase with the continuous phase is not studied in detail [28], [30], [121]. However, little is known about the quantitative interaction between the dispersed phase and the continuous phase such as a change in the velocity, pressure, and the shape of the dispersed phase in low-quality foams at the micro-scale. The results of the studies on the emulsion flows showed that there is a limited understanding of the motion of the dispersed phase and its interaction in loosely packed emulsions and foams.

The major objective of this study is to investigate the interaction of a dispersed phase of bubbles passing through a simulated pore space. This will be undertaken using image analysis techniques to track the position of the bubbles and their change in shape. Two different cases of a linear array of bubbles and a loosely packed matrix of bubbles are studied to investigate the effect of the number and the arrangement of bubbles on their entrance and exit to a single pore space. The shape of the dispersed phase will be analyzed in different time frames to study the velocity and pressure change of the dispersed phases. This combination of findings will provide a better understanding of the multi-phase flow interaction and the importance of the dispersed phase orientation when a loose-packed dispersed phase passing through the pore space geometries.

6.2 Experimental setup

The velocity, deformation, and interaction between the bubbles in the pore space were determined using a micro-shadowgraphic imaging technique. Details and arrangement of the equipment setup are shown in Figure 6-1 (a). The optical setup consists of a camera (4M180, IO Industries Inc.) operating at a frame rate of 149 Hz coupled with a 105 mm SLR lens with extension tubes to capture the flow over a 12 mm × 12 mm field-of-view. The system was back-illuminated using a high current LED panel (BX0404-520 nm; Advanced Illumination Inc.) with a uniform light distribution working in continuous mode. The flow cell containing the fluid and the pore space is placed between the camera and LED at the focal plane of the camera lens to capture the fluid and bubble motion.

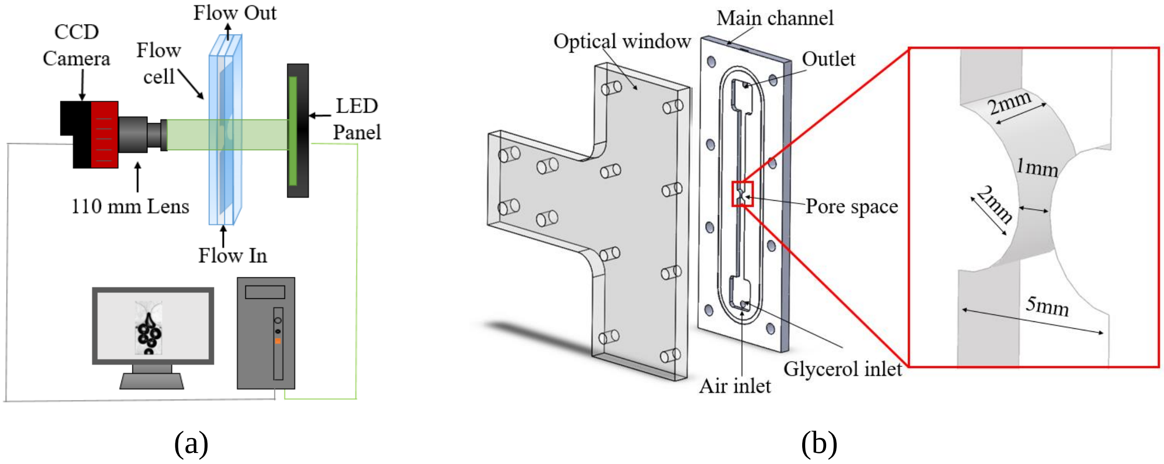

(a) (b)

Figure 6-1. (a) A schematic of the experimental setup and (b) the flow cell assembly with a detailed view

As shown in Figure 6-1 (b), the flow cell was an assembly of two components. Optical access to the main flow cell was achieved by using a clear window made from transparent acrylic. The main channel was manufactured using the stereolithography (SLA) additive manufacturing technique (Form 2, Formlabs Inc. USA) from a transparent, photoreactive resin material. The main 2D channel contains the pore space that was designed using two aligned semi-cylinders with a 1 mm aperture to represent the single pore space between two adjacent particles in a porous media. The continuous phase (liquid) and the dispersed phase (air) were injected separately through two inlets at the bottom of the flow cell and after their interaction with each other, they exit the flow cell via the outlet port. The continuous phase used in this study was 100% pure glycerol (Glycerol-Molecular Biology; Fisher BioReagents™, USA) with a density of 1.261 g/cm³ and viscosity of 1.412 Pa.s. This was injected at a constant flow rate of 0.2 ml/min using a syringe pump (PHD 2000; Harvard Apparatus). Air was also used as the dispersed phase in the experiments by injecting bubbles manually using a syringe.

6.3 Image data analysis

A sample raw image obtained using the experimental setup is shown in Figure 6-2 (a). As indicated in the figure, the flow direction is from bottom to top in the opposite direction to gravity. The air bubbles can be identified by their hollow black regions in the flow field due to the difference between the refractive index of the phases. The contact point between each bubble can also be seen by the bright regions on the surface of the bubbles. Represented in the detailed view of (I) of Figure 6-2 (a), the contact points between individual bubbles were also reflected on the inner surface of the bubbles.

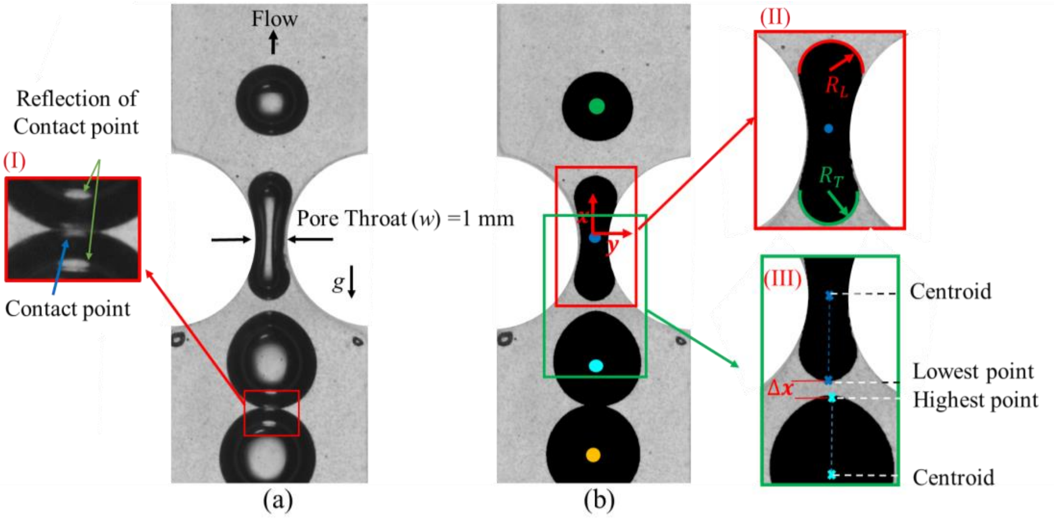

Figure 6-2. (a) A sample of raw and (b) processed images highlighting the pore throat, bubble locations, and definition of variables.

The presence of the bright regions and the contact points in the bubbles can result in uncertainty of the deformation calculation. To remove their influence, a dynamic mask was generated to remove the inner regions of the bubbles. The masking is achieved by detecting the outer shape of the bubbles (function edge, Matlab2018a; The MathWorks, Inc.) in each image. This region was identified by the change in intensity between the bubbles and the continuous phase. Having the location of the bubbles, the bright regions were removed from individual images as shown in Figure 6-2 (b). A geometric mask was also applied on the solid walls to remove the stationary locations to have a better indication of the pore space. The pre-processed images were then used to determine the center of the projected area, velocity, deformation, and distance between individual bubbles of the dispersed phases.

The motion of the individual bubbles was tracked in 2000 images captured over 13.5 s of fluid motion. To capture the motion of the bubbles, each of the bubbles was isolated using their unique labels in the images (function bwlabel, Matlab2018a; The MathWorks, Inc.). The velocity of the bubble was calculated by detecting and tracking the centroid (function regionprops, Matlab2018a; The MathWorks, Inc.) of each bubble as indicated by the color-coded circle shown in Figure 6-2 (b)in the sequential images. The distance between the bubbles (Δx) were also determined by the distance between the trailing edge of the leading bubble and the leading edge of the trailing bubble as shown in detailed view (III) of Figure 6-2 (b).

Having the location and the shape of the individual images, the change in the pressure distribution within the dispersed phase can also be calculated. The pressure change within the bubbles (ΔP) can be determined using the radii of the curvature of the leading (R_L) and trailing (R_T) edge as indicated in detailed view (II) of Figure 6-2 (b)and the theory introduced by Jamin [35], [37] as:

$$\Delta P = P_1 - P_2 = \gamma_{cd}\left(\frac{1}{R_{\mathrm{L}}} - \frac{1}{R_{\mathrm{T}}}\right) \tag{6-1}$$

where $P_1$and P_2 are the pressure of the dispersed phase at the leading and trailing face and γ_{cd} is the interfacial tension between the continuous and dispersed phases. Details of the pressure calculation within the dispersed phase passing through the pore space using the shape analysis can be found in our previous study [25].

6.4 Results and discussion

The results of this study focus on two different cases of a vertical linear array and a loose matrix of bubbles. The vertical linear array of bubbles were injected over a long time interval providing enough time for the bubbles to move independently along the centerline of the channel. For the loose matrix or grouping of bubbles, the bubbles were injected over a shorter time interval and are in contact with each other. Therefore, these bubbles will compete with each other to enter the pore. The interaction in these cases will be different due to their arrangement. To study these interactions, the change in the gap between the bubbles and their change in the pressure across the leading and trailing edge as they pass through the pore space has been considered.

6.4.1 Visualization flow of a vertical linear array of bubble entering a pore space

Sequential images showing the motion of a vertical linear array of bubble passing through a pore space at different times from the starting point (t = 0) with a constant time step of 0.6 s are presented in Figure 6-3. Using image analysis (function regionprops, Matlab2018a; The MathWorks, Inc.), the diameter of the bubbles are calculated and they were named and color-coded according to their position in the array. The bubbles' terminal velocity, U_T determined before entering the pore throat are represented in Table 6-1. It can be seen in Figure 6-3 (t = 0), the majority of bubbles in this linear arrangement are in contact with each other before they enter the pore space. The first bubble (B_A1), however, was injected earlier than the linear array of bubbles to highlight the effect of spacing between the bubbles at different stages. The distance between the bubbles varies depending on the location of the bubbles as they pass through the pore space. The distance between the bubbles (Δx) were calculated using the shown in Figure 6-2 (b)and plotted with respect to the normalized position of the centroid of the trailing bubble along the vertical direction (x/w) in Figure 6-4.

Table 6-1. The properties of the bubbles in the array arrangement

Bubble label	Color	Diameter in mm (D)	Max normalized velocity (U/U_T)
1	Green	1.9	-
B$_A$2	Blue	1.9	2.44
B$_A$3	Cyan	2.3	1.78
B$_A$4	Yellow	2.4	1.62
B$_A$5	Red	1.7	2.77

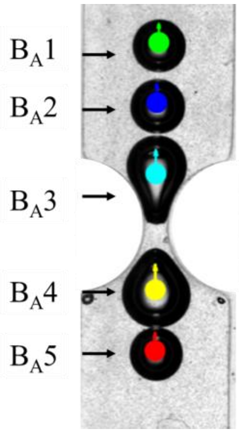

For the case of the bubble with the initial spacing, bubble B$_A$1 (green), it can be seen that it maintains the spacing to bubble B$_A$2 (blue) as it passes through the pore as shown in the images of Figure 6-3. This spacing between these bubbles is quantitatively shown as the blue line in Figure 6-4, which highlights the variation of the gap with respect to the position of the centroid of B$_A$2 (blue). In general, the spacing between the bubbles increases as they enter the pore and decreases as they move further away from the pore space. The spacing is larger when the leading bubble is within the pore space as shown in Figure 6-3 (t = 0) to (t = 0.6 s) and the peak spacing for all cases is shown to be where the trailing bubble is before the pore throat (at $x/w < 0$ in Figure 6-4). As the B$_A$2 (blue) passes the pore throat ($x/w > 0$ of Figure 6-4), represented in Figure 6-3 (t = 1.2 s) to (t = 2.4 s), the spacing between the bubble pair (B$_A$1 to B$_A$2) decreases. It can be seen in Figure 6-3 (t = 0) to (t = 7.2 s), B$_A$1 moves through the entire set of images collect while maintaining a spacing to B$_A$2 which was not able to accelerate enough to attach to B$_A$1.

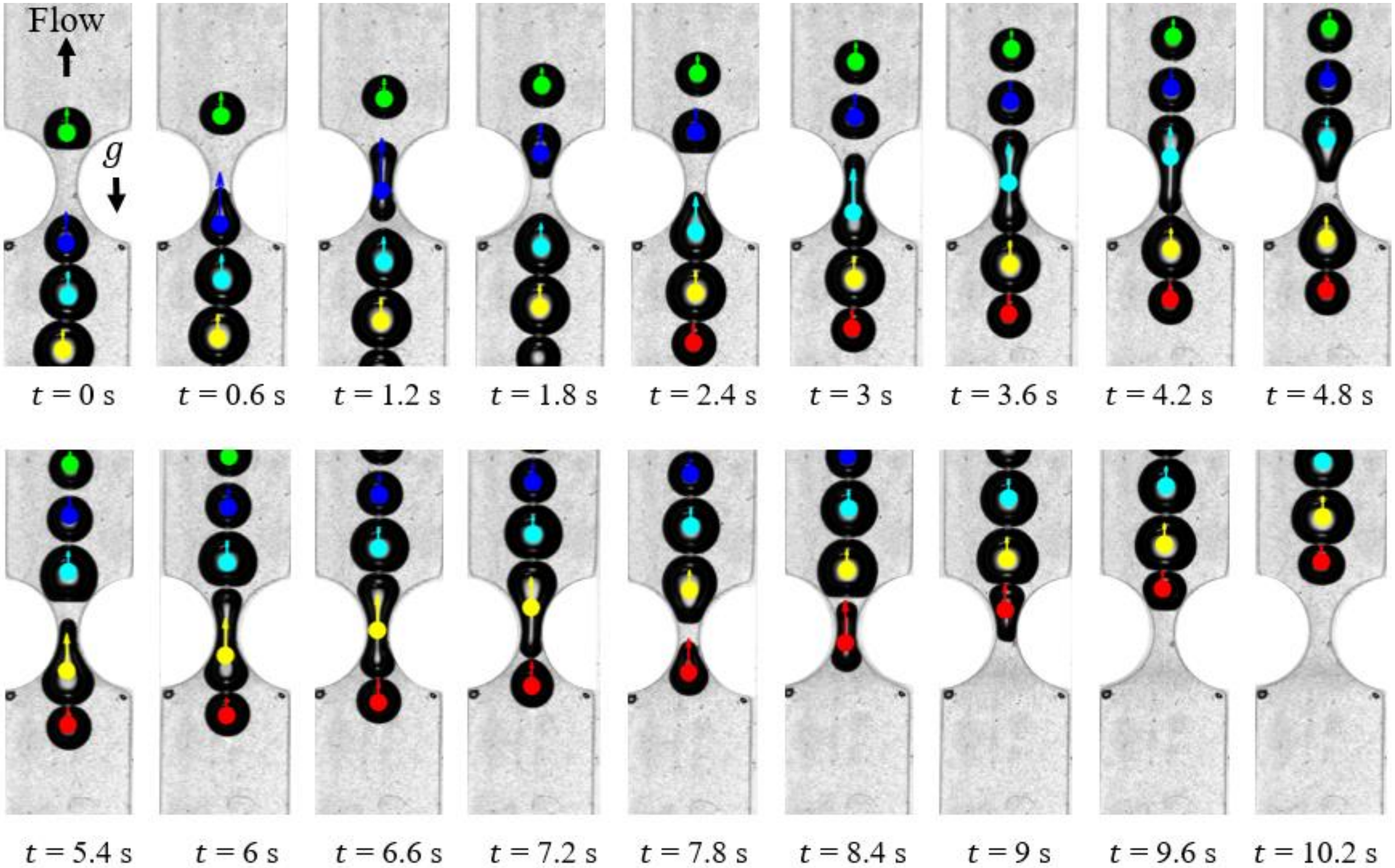

$t = 0$ s $t = 0.6$ s $t = 1.2$ s $t = 1.8$ s $t = 2.4$ s $t = 3$ s $t = 3.6$ s $t = 4.2$ s $t = 4.8$ s

$t = 5.4$ s $t = 6$ s $t = 6.6$ s $t = 7.2$ s $t = 7.8$ s $t = 8.4$ s $t = 9$ s $t = 9.6$ s $t = 10.2$ s

Figure 6-3. Image plots of bubbles array entering a pore space at different times with a constant time step of 0.6 s.

For the case of the bubbles in contact (B_A2 and B_A3) as shown in Figure 6-3 (t = 0 s), it can be seen that they stay in contact from before they enter the pore throat (t = 0 s) to (t = 0.6 s). This stage can be also seen by the zero spacing (Δx) at $x/w < -2$ shown in cyan line of Figure 6-4. The bubbles detach when the leading face of the B_A2 has passed through the pore throat represented in Figure 6-3 (t = 1.2 s). This is due the deformation of the bubbles in this condition. As bubble B_A2 (blue) gets closer to the pore it starts to deform from a spheroid shape to a tear-drop. The radius of the leading edge of B_A2 becomes smaller, making it ready to pass through the smaller pore throat. This location is also represented at $x/w > -1$ of cyan line shown in Figure 6-4. The spacing between the bubbles increases and reaches a maximum value at $x/w \sim -$ 0.3. As the bubbles pass through the pore space, the spacing between them decreases. The bubbles come back into contact at $x/w \sim 2.7$ of cyan line of Figure 6-4. A similar phenomena of the detachment and the attachment occur for all the bubbles (B_A3, B_A4, and B_A5) that start in contact with each other. The spacing and the location where the detachment and the attachment varies depending on the location of the bubbles in the row as well as the size of the bubbles.

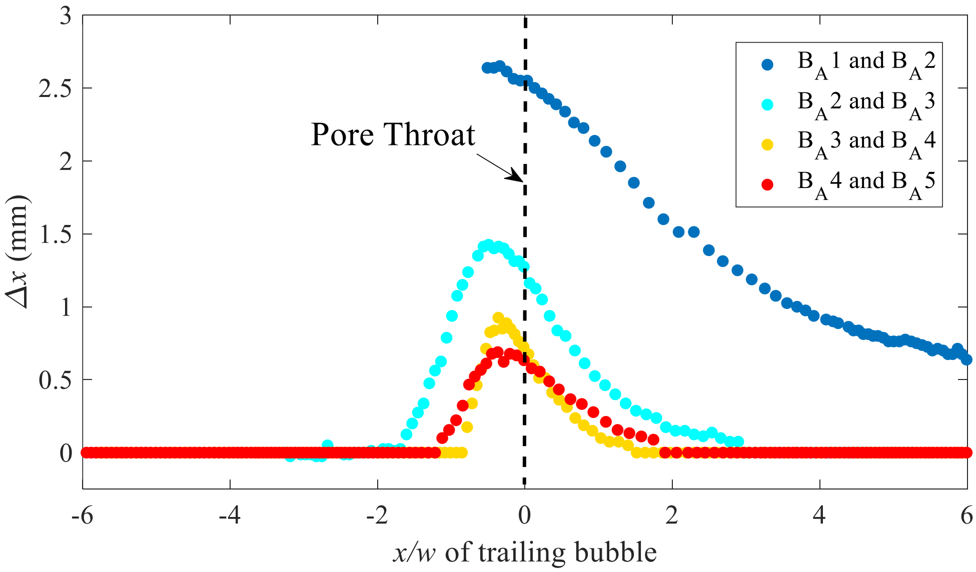

Figure 6-4. A graph of the gap between the bubbles along the pore space

The detachment and the attachment of the bubbles may be explained due to the different stages of deformation of the front bubbles (e.g. B_A2) and the leading edge of the following bubbles (e.g. B_A3) as they pass through the pore geometry. The deformation of the bubbles results in the asymmetric shapes of the bubble interface before the pore throat. Therefore, an excessive pressure drop will be introduced to the bubble by the presence of interfacial forces described by the Jamin effect. To have a better understanding of this phenomena, the change in the pressure distribution of each bubble scaled by the interfacial tension was determined by measuring the curvature of the leading and trailing edge (shown in detailed view (II) of Figure 6-2 b) and using Eq. (6-1) and plotted in Figure 6-5 (a). The change in the pressure in the dispersed phase ultimately leads to the change in the velocity of the bubbles as they pass through the pore. The normalized velocity of the bubble with their terminal velocity before they enter the pore throat, U_T, with respect to their location of the centroid of the trailing bubbles along the pore space are plotted in Figure 6-5 (b).

The observed detachment of the bubbles can be explained by the acceleration of the front bubble (B_A2) and deceleration of the trailing bubble (B_A3). As an example in the case of bubbles B_A2 and B_A3, the position of the bubble shown in Figure 6-3 (t =1.2 s) corresponds to $x/w \sim -1.5$ of the B_A2 and $x/w \sim -3$ of B_A3 in Figure 6-5. In this condition, the pressure difference between the front and back face of B_A2 is positive and the pressure difference for B_A3 is zero. The positive pressure change in the B_A2 results in the deceleration of the bubble and especially at the trailing edge as shown in Figure 6-5 (b). At this location, the bubbles are still in contact with each other. As B_A2 passes the location with the highest positive pressure at $x/w \sim -2$, it begins to accelerate which results in detachment of the leading bubble from the trailing bubble. The distance between the bubble increases and reaches its maximum at the pore throat. As the bubble reaches the exit of the pore space, it decelerates and the bubbles come into contact as shown in Figure 6-3 (t =4.8 s).

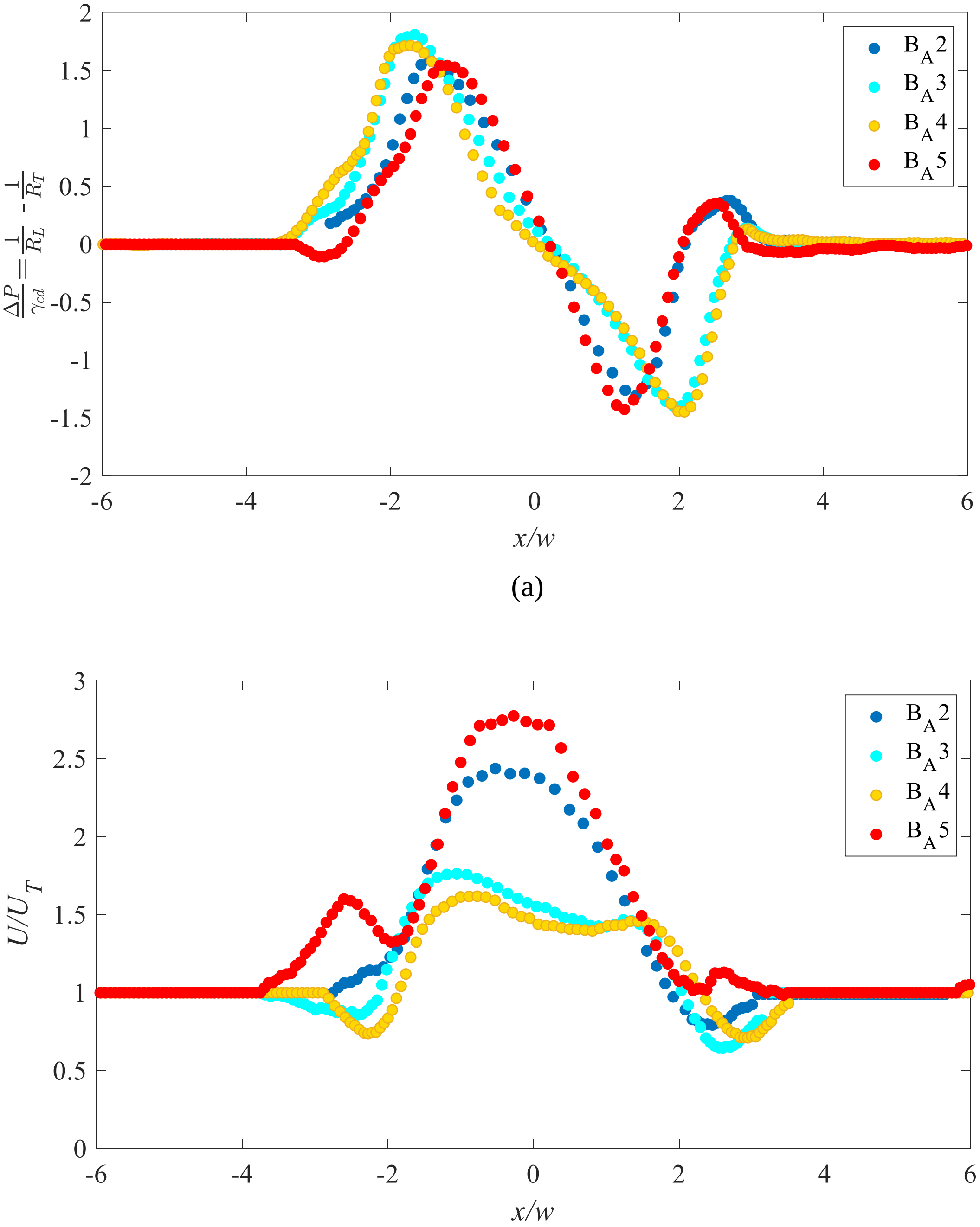

(a)

(b)

Figure 6-5. The graphs the change in (a) the pressure leading and trailing edge of the bubble due to its deformation and (b) velocity of bubbles with position along the pore.

The observed detachment of the bubbles can be explained by the acceleration of the front bubble (B_A2) and deceleration of the trailing bubble (B_A3). As an example in the case of bubbles B_A2 and B_A3, the position of the bubble shown in Figure 6-3 (t =1.2 s) corresponds to x/w ~ - 1.5 of the B_A2 and x/w ~ -3 of B_A3 in Figure 6-5. In this condition, the pressure difference between the front and back face of B_A2 has a positive value and the pressure difference for B_A3 is zero. The positive pressure change in the B_A2 results in the deceleration of the bubble and especially at the trailing edge as shown in Figure 6-5 (b). At this location, the bubbles are still in contact with each other. As B_A2 passes the location with the highest positive pressure at $x/w \sim -2$, it begins to accelerate which results in detachment of the leading bubble from the trailing bubble. The distance between the bubble increases and reaches its maximum at the pore throat. As the bubble reaches the exit of the pore space, it decelerates again and the bubbles again come into contact as shown in Figure 6-3 (t =4.8 s).

In addition to the acceleration of B_A2, the deceleration of B_A3 results in the variation in the change in spacing between the bubbles. As B_A3 enters the pore as shown in Figure 6-3 (t = 1.8 s) and $x/w\sim -2$ of Figure 6-5 (a)., it starts to deform. This deformation results in the deceleration of the bubble in this stage. The decrease in the velocity of the bubble results in the increase in the spacing between the bubbles shown in Figure 6-3 (t = 1.8 s) to (t = 2.4 s). This condition represents the location where the leading bubble is in its acceleration stage and the following bubble is in its deceleration stage. As the center of mass of the bubble passes through the pore presented in Figure 6-3 (t = 3.6 s), it begins to accelerate and the spacing between the bubbles decreases and the bubbles (B_A2 and B_A3) come again into contact in Figure 6-3 (t = 7.2 s).

Similar observations of the phenomenon of change in the pressure and velocity were observed for all bubbles in the linear array. It can be seen in Figure 6-5 (b). that all of the bubbles approach the pore throat with the terminal velocity of each bubble (U_T). As they approach the pore they start to accelerate as they enter the pore space and after they pass the pore throat the velocity decreases. The bubble again reaches its terminal velocity after its passes through the pore space geometry. The increase in the velocity of the bubble also varies by the size of the individual bubble resulting in the different magnitudes of the spacing between the bubbles shown in Figure 6-4. A higher increase in the velocity was observed for the case of smaller bubbles (B_A2 and B_A5). This is due to the smaller deformation which results in a lower change in the internal pressure.

One of the more interesting observations of this study is the phenomenon of pinning [262] of the bubble observed in Figure 6-3 (t = 8.4 s). As a result of this, all of the bubbles decelerate as they pass through the pore space shown in location of the bubbles where $2 < x/w < 3$ in Figure 6-5 (b). It can be seen in Table 6-1 that B_A4 has the largest size among the all injected bubbles. As such, it can be expected that this bubble will deform more and will therefore have more variation in its velocity. Pinning can be seen clearly for bubble B_A4 is more due to the larger deformation which leads to higher excessive pressure change across the leading and trailing edge of the bubble as shown in Figure 6-5 (b). This case allows interfacial forces to become significant. To have a clear perception of this phenomenon, the interaction of the bubble, B_A4, and the pore surface at different times is represented in Figure 6-6 (a) in more detail. The first image is the interaction of the bubble with the exit wall of the pore at location Figure 6-3 (t = 7.8 s) and the last image in Figure 6-3 (t = 8.4 s). The red dashed line shows the location of the contact point of the bubble and the pore surface. It can be seen that, as the bubble passes through the pore space, it maintains its contact line due to the interfacial tension between the bubble and the pore surface. This interaction results in a pinning point that can be seen in all the images which ultimately leads to a concave curvature of the bubble's trailing edge.

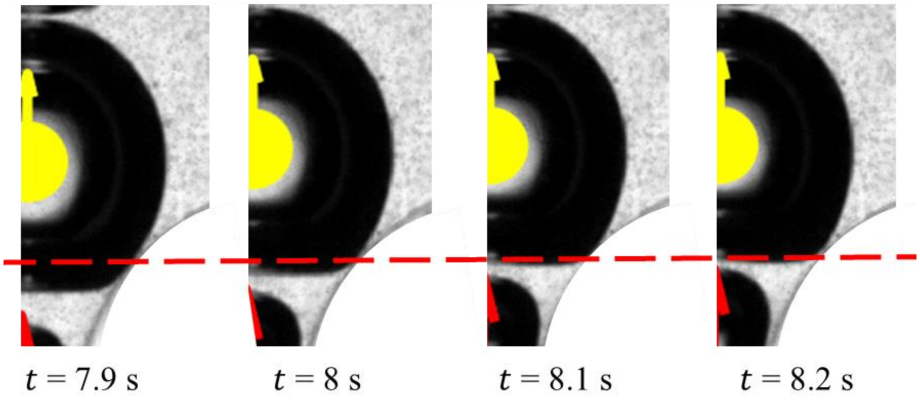

(a)

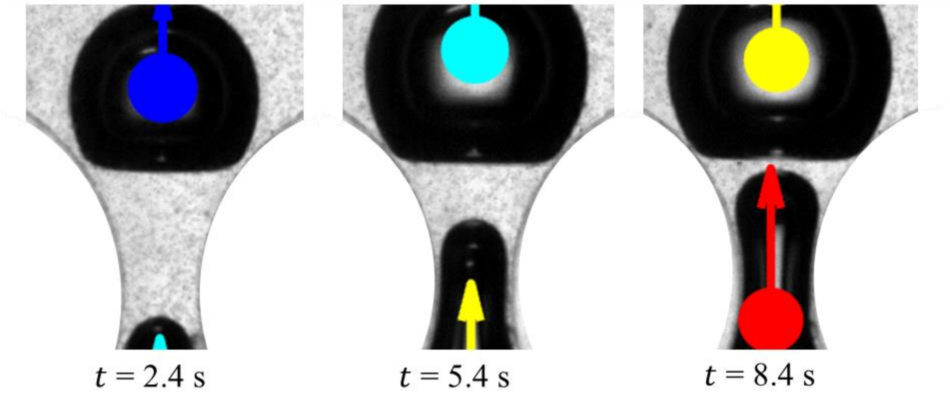

(b)

Figure 6-6. Detailed views of (a) the interaction of the bubble, B_A4, and the pore space with respect to time, and (b) the spacing between different size bubbles on exiting the pore.

It is interesting to note that for bubbles in the array at the same position from the pore exit and the same location of the contact point shown in Figure 6-6 (b), there is a change in the spacing between the bubbles. It can be seen that the distance between the individual bubbles decreases as the number of bubbles in the array in front of the exiting bubble after the pore increases. The higher number of bubbles in the flow results in the slower motion of the dispersed phase compared to the surrounding fluid. The motion of the bubbles entering the pore space can also result in the deformation of the bubbles that have already passed through the pore space as can be seen in the bubble at (t = 8.4 s) shown in Figure 6-6 (b). This shows that the trailing edge of the bubble has become concave. The other possible reason for the decrease in the spacing is the size of bubbles observed in these cases. As shown in Figure 6-6 (b), the bubble (B_A2) in (t = 2.4 s) is smaller than the others, which will have more acceleration as it passes through the pore. In the other cases (t = 5.4 s) and (t = 8.4 s) the bubbles are comparable in size and it can be seen that the gap is higher for the first case and the gap decreases as the number of bubbles in the array after the pore increases.

6.4.2 Visualization of the flow of a matrix of bubbles competing to enter a single pore space

Images of a matrix of bubbles approaching and passing through a single pore space with respect to time are shown in Figure 6-7. This condition was considered to study the effect of competing bubbles on the motion and the spacing between the bubbles. The images are selected with the same time intervals of 0.23 s from the starting point of Figure 6-7 (t = 0). The size of bubbles and their labeling are summarized in Table 6-2. The velocity of the bubbles in Figure 6-7 is indicated by the arrow starting from their center of the projected area of each bubble. The length of the arrows represents the instantaneous velocity magnitude of the bubble at that location. The variation in the velocity of the bubble changes as they compete to enter the pore throat. The change in the velocity of the bubble varies based on the location and the direction of the bubble compared to the competing bubble.

Table 6-2. The properties of the bubbles in the matrix arrangement

Name of the bubble	Color	Diameter in mm (D)
B_M1	Yellow	3.08
B_M2	Red	3.02
B_M3	Blue	2.88
B_M4	Green	2.66
B_M5	Cyan	2.5
B_M6	Purple	2.38

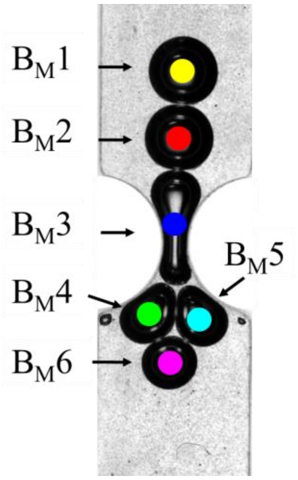

As can be seen in Figure 6-7 (t = 0), two bubbles with similar size B_M1 and B_M2 (yellow and red) are approaching the pore space at the same time. In this condition, both of the bubbles are moving upward as a result of the bulk motion of the continuous phase. As they approach the pore as shown in Figure 6-7 (t = 0.23 s), it can be seen that the leading edge of B_M1 is closer to the pore throat allowing it to interact with the pore first. This misalignment between the leading edges of the bubbles will result in the delayed entrance of B_M2 compared to the competing bubble, B_M1. As B_M1 enters the pore space, Figure 6-7 (t = 0.46 s), the effect of upward motion of the bubble results in B_M2 being repelled from the pore. Bubble B_M2 continues to move backward until the leading edge of the B_M1 passes into the pore throat as represented in Figure 6-7 (t = 0.9 s). After this the B_M2 starts to move forward again and competes to enter the pore space with a new bubble approaching the pore, B_M3 (blue). The same phenomena of the alternating entrance to the pore were observed for all following bubbles

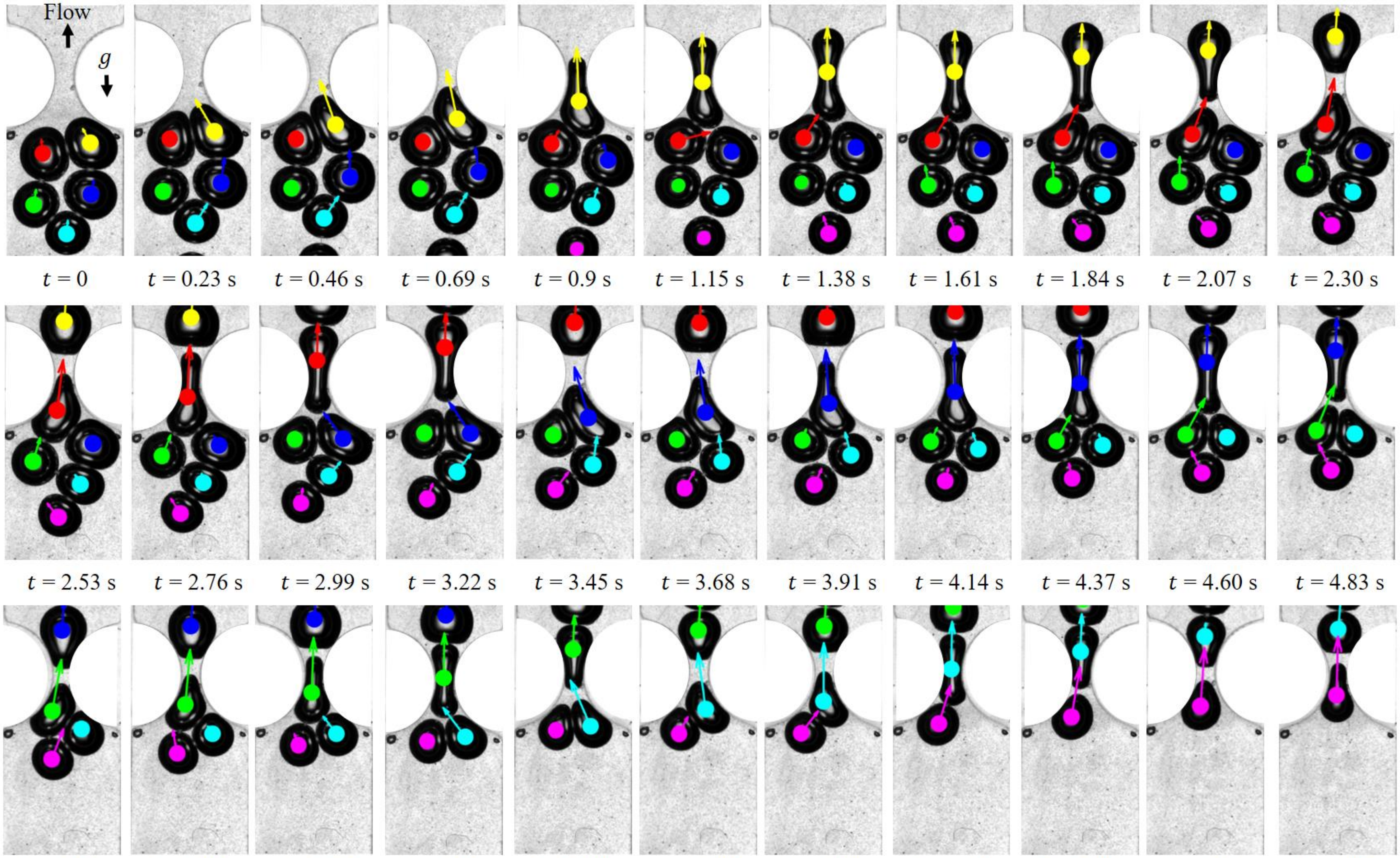

t = 0 *t* = 0.23 s *t* = 0.46 s *t* = 0.69 s *t* = 0.9 s *t* = 1.15 s *t* = 1.38 s *t* = 1.61 s *t* = 1.84 s *t* = 2.07 s *t* = 2.30 s

t = 2.53 s *t* = 2.76 s *t* = 2.99 s *t* = 3.22 s *t* = 3.45 s *t* = 3.68 s *t* = 3.91 s *t* = 4.14 s *t* = 4.37 s *t* = 4.60 s *t* = 4.83 s

t = 5.06 s *t* = 5.29 s *t* = 5.52 s *t* = 5.75 s *t* = 5.98 s *t* = 6.21 s *t* = 6.44 s *t* = 6.67 s *t* = 6.90 s *t* = 7.13 s *t* = 7.36 s

Figure 6-7. Picture of merging bubbles to enter a pore space with respect to time (with a constant time step of 0.23 s).

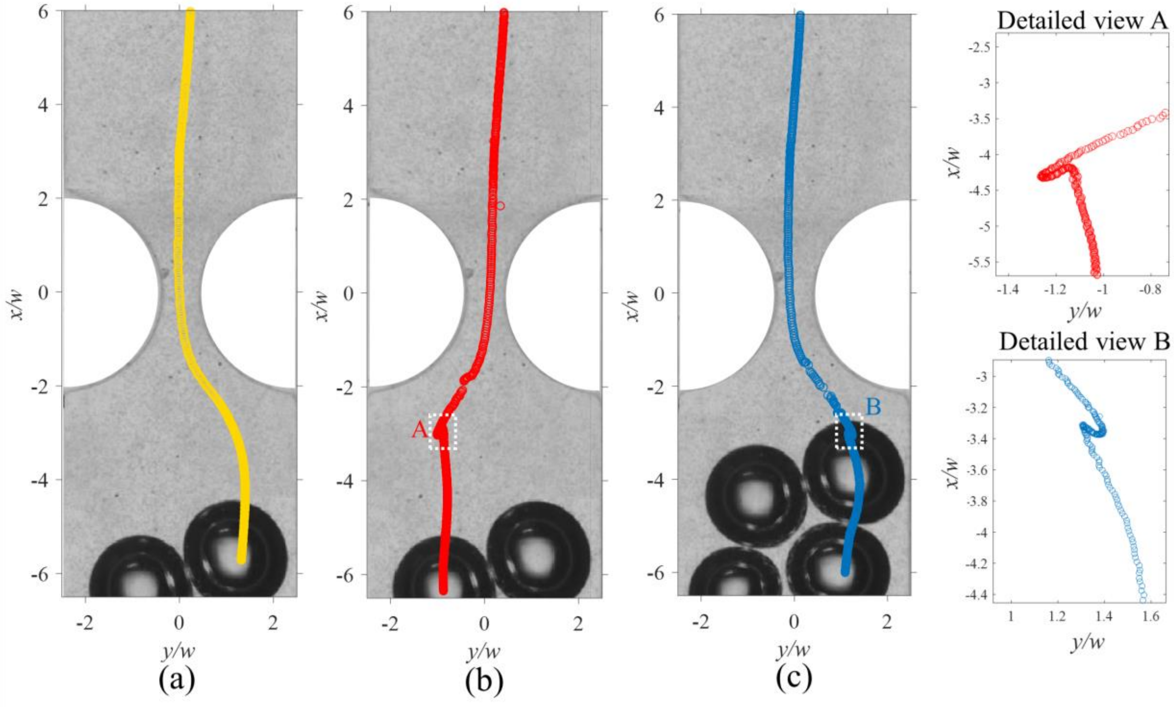

Figure 6-8. Flow path of (a) $\mathrm{B_M}$1, (b) $\mathrm{B_M}$2, and (c) $\mathrm{B_M}$3 passing through the pore space tracked within 2000 images.

The path of motion of the first three bubbles ($\mathrm{B_M}$1, 2, and 3) passing through the pore space is shown in Figure 6-8. In Figure 6-8 (a), $\mathrm{B_M}$1 enters the pore from the right side and after it passes the pore space it follows the centerline of the channel. In this case, since the bubble is leading the matrix of bubbles, it enters the pore space without any repulsion. For the case of $\mathrm{B_M}$2 and $\mathrm{B_M}$3 as it can be seen in Figure 6-8 (b) and c that the bubbles were repelled to the wall of the channel as they get closer to the pore space. This phenomenon can be clearly seen in Figure 6-8 (b) detailed views A and B. The same phenomena of repulsion were observed for $\mathrm{B_M}$4, 5,6 as it can be seen in Figure 6-7 at distinct times (t = 2.99, 4.6 and 5.98 s).

Another observation is that the contact point between the bubbles also changes as the bubbles compete to enter the pore. As represented in Figure 6-9 (a) by the glare points, the contact point is small in the case of upward-moving bubbles. The small contact point is an indication of a small deformation of the interface of the bubbles. As shown in Figure 6-9 (b), when the red bubble enters the pore, the contact point increases, which represents higher bubble deformation. This deformation results in a backward motion of the blue bubble which continuous up to the location where the contact point and the deformation are less, Figure 6-9 (d). The decrease in the deformation allows the red bubble to move upward shown in Figure 6-9 (d) and (e).

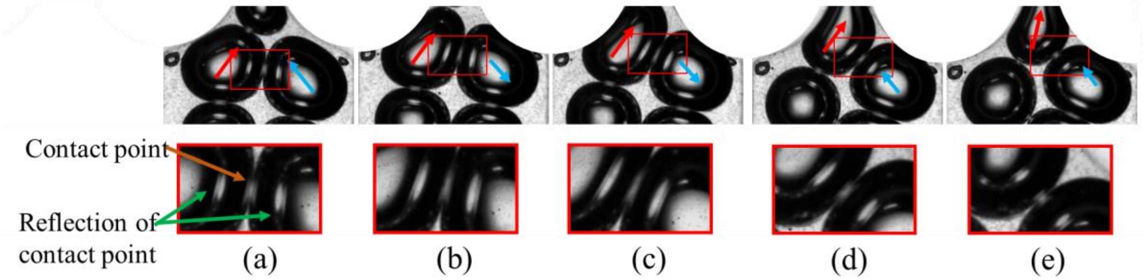

Figure 6-9. The change in the contact point of the competing bubble with respect to time.

There are several similarities between the motion of an array and the matrix of bubbles entering the pore. As shown in Figure 6-7 (t = 1.61 s) to (t = 4.37 s), the same phenomena of the presence of the spacing between two bubbles entering the pore exists for the matrix of bubbles as well. As it can be seen in Figure 6-10, the bubbles have a negative spacing as the trailing edge of the B_M1 is behind the leading edge of B_M2. As the bubbles start to compete to enter the pore, the spacing increases due to the repulsion of the B_M2. The spacing between the leading edge decreases as B_M1 enters the pore and it can be seen the bubble detaches at $x/w > -2$. The spacing reaches a maximum when the first bubble's trailing edge passes and the leading edge of the next bubble are before the pore throat. The spacing decreases as the leading edge of the next bubble passes the pore throat. The bubbles come back into contact when the first bubble passes the pore and the majority of the second one is on the existing part of the pore.

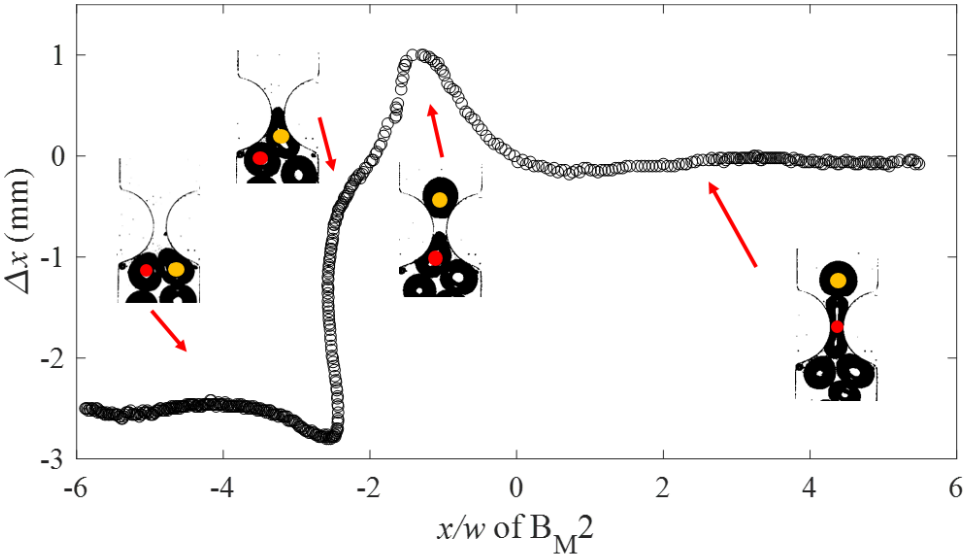

Figure 6-10. A graph of the change of the gap between two competing bubbles (B_M1 and B_M2) with position along the pore space.

Bubble layout or arrangement relative to each other within a channel can change from before the entrance to after the exit of the pore throat. As shown in Figure 6-11 (t = 0), the bubbles are arranged in a loose matrix competing to enter the pore throat. As the bubbles pass through the pore space, shown in Figure 6-11 (t = 4.60 s) they continue to move to the center of the channel. Once all of the bubbles are have passed the pore throat, represented in Figure 6-11 (t = 8.38 s), they are ordered into a linear array within the channel as they exist in the pore space and the bubbles are all in contact with each other. This phenomenon is similar to the motion of the linear array bubbles discussed in Figure 6-3 (t = 9 s).

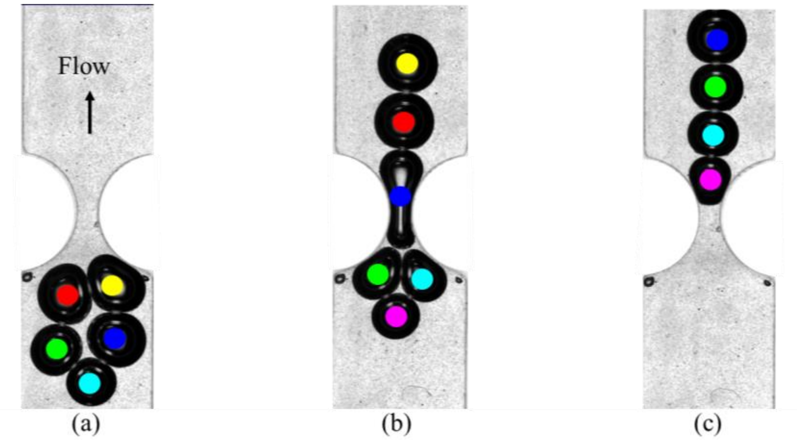

Figure 6-11. Picture of bubble arrangement with time (a) before bubbles enter, (b) three bubbles have passed, and (c) all of the bubbles have passed through the pore.

6.5 Conclusion

The present study was designed to visualize the interaction and motion of a dispersed phase of loosely packed bubbly flow passing through a pore space. The study has been considered for two cases of an array and a loose matrix of bubbles entering a pore space where of the size of the bubbles in the flow are larger than the pore throat. The phase interaction was investigated by tracking the motion and deformation of the dispersed phase competing to enter the pore space with respect to their influence on the velocity, bubble spacing, and pressure distribution within the dispersed phase.

Bubbles in both arrangements undergo deformation as they pass through the pore spaces. As a result of this deformation, the bubbles decelerate before they enter the pore and accelerate as they pass through the pore throat. The change in the velocity of the bubbles results in spacing between two sequential bubbles within the pore space. The spacing increases as the following bubble enters the pore and it decreases after it exits the pore space. In addition to the motion of individual bubbles, the orientation of the existing bubbles shows a similar trend after the pore space. In both cases of the bubble’s arrangements, as the bubbles pass through the pore, they align on the centerline of the vertically orientated channel as a single linear array.

The difference between the cases arises by comparison of the order of bubbles entering the pore space. The results of the motion of the flow in matrix of bubbles showed that the bubbles are entering from left and right in an alternating manner due to interaction between the bubbles themselves and the geometry of the pore. The bubbles competing to enter the pore as they get closer to the pore space and the bubble, having its leading interface closer to the pore throat, enters the pore first. The motion of the bubble entering the pore leads to a temporary repelling of the competing bubble from the pore. The present study raises the importance of the effect of the arrangements on multi-phase flow by demonstrating the interaction of the dispersed and the continuous phase in the pore space and their influence on the motion of the fluid.

Chapter 7: Conclusion

This study set out with the aim of assessing the importance of emulsification in applications where single-phase flow was assumed as a pronounced phenomenon such as the SAGD process and to experimentally study the pore-scale interaction of multi-phase flow motion in solid confined geometries and the impact of different flow conditions on the pressure distribution. The question posed at the beginning of this study on the importance of the emulsion formation in the performance of SAGD process has been investigated by reviewing more than a hundred papers. The presence of emulsions in SAGD condition is confirmed by reviewing the physics of the emulsification process in SAGD reservoirs. The evidence presented in this section and the results of experimental studies reported in the literature confirm that SAGD conditions lead to the formation of stable emulsions in the reservoir. It is suggested that the edges of the steam chamber in the region having the highest effect on emulsion formation. The emulsification also occurs in other regions such as the sub-cool zone and the near-entrance regions of the sand/flow control devices.

The review of the literature provide evidence that the variation in the reported oil production from the reservoir and estimated production using popular SAGD models arises due to the assumption of the single-phase flow phenomenon in the reservoir condition. Considering the emulsification phenomena that could prevail in oil reservoirs, however, this could be seen as a significant limitation. The outcome of this review strengthens the idea that a multiphase flow scenario needs to be considered when studying all flow-related phenomena in enhanced oil recovery (EOR) processes and hence SAGD. The presence of emulsions significantly affects the bulk properties of the porous media, such as relative permeability, and properties that are related to the flow, such as viscosity, and density, and ultimately pressure drop. Lower oil production in multi-phase flows is due to the higher pressure drop required to mobilize the emulsions in the reservoir condition.

The second aim of this study on the pore-scale interaction of the phases is considered by studying the relative motion of a dispersed phase moving in/with a continuous phase in confined geometry. This motion was evaluated by considering the isolated dispersed phase deformation, velocity, and pressure change. These characteristics of the phase were evaluated experimentally by utilizing a non-intrusive imaging system. The collected images were analyzed to track the interface between the phases and the relative location of the phase in the confined geometry.

A novel methodology to evaluate the pressure change of an isolated bubble is introduced using a combination of existing theoretical models and optical diagnosis. According to the Laplace equation, the change in the pressure along a deformed bubble is proportional to the change in the curvature of the leading and the trailing edge. The location of the curvature evaluation was determined using two proposed approaches. The first method is based on the relative location of the leading and trailing edge of the bubble compared to the pore throat. In the second approach, the location is determined by the change in the curvature along with the bubble. The methodology showed repeatable results and the maximum uncertainty introduced by the edge detection was 5.5%.

The proposed approach was used to evaluate the motion of an isolated bubble passing through a 1 mm pore geometry. Different sizes of bubbles and flow rates of the continuous phase were considered to study the effect of flow conditions on the deformation, velocity, and acceleration of the bubble. The results obtained from the analysis showed that the motion of bubbles having different sizes and flow rates follow the same trend. The deformation of the bubbles passing through the pore intensifies as the relative bubble size compared to the pore geometry increase. It was observed that the bubble deformation occurs at different locations relative to the pore throat depending on the size of the bubble. The bubble starts to deform further in the pore for smaller bubble sizes and regains its spherical phase faster as it exists the pore geometry.

The strong interaction between the interface of the solid geometry and the bubble leads to phase pinning of the bubble as it existing the pore geometry. Phase pinning leads to the increase in the curvature of the bubbles trailing edge at this location. The bubbles phase pinning also intensified as the size of the bubble and the flow rate increased. Based on the results obtained from tracking the velocity of the bubble passage in the pore, it can be seen that a higher flow rate of the continuous phase results in the faster passage of the bubble in the confined geometry. However, the effect of pinning results in the slower motion of the bubble and an increase in the transit time required in the system.

Tracking the change in the pressure obtained from the shape analysis showed that the proposed method is capable of evaluating the critical pressure required for the phase passage. It was observed that the critical pressure introduced at the entrance of the confined geometry increases as the size of the bubble increases. The phase pinning at the exit of the pore geometry also resulted in the extra positive pressure change leading to the decrease in the mobility of the phase. The introduced pressure due to the pinning also intensifies as the size and the deformation of the bubble increase.

The motion of a liquid-liquid flow was also considered to expand the capability of the proposed method. To track the internal motion of the oil droplet, a glycerol droplet having the same refractive index of canola oil is selected for the study. The velocity field was measured using µ-PSV and the results were used to calculate the corresponding pressure field in both droplet and continuous phase. Two different sizes of droplets were studied to evaluate the instantaneous information regarding their deformation. The results of this study further support the results obtained from the bubble flow. The velocity of the phases showed that the droplets decelerate as they enter the pore geometry due to the influence of the confining wall. As the droplet gets closer to the pore throat the deformation caused by the capillary forces becomes more dominant compared to buoyancy. The change in the velocity of the droplet having a larger size is higher due to the higher deformation of the phase. The capillary pressure distribution determined from both velocity measurements and shape analysis showed a similar trend with a greater variation for the larger droplet.

The effect of the solid interface properties on the motion of isolated bubbles was studied using four pore shape geometries. A circular pore with a smooth surface, ×2 surfaces with different roughness, and sharp pore were considered in this study. The results of the change in the curvature of the bubbles showed that the bubbles' transit time is the smallest in the smooth channel. The transit time in the pore geometry increases as the roughness of the channel increases. This is caused by the strong interaction of the phase and solid surface resulting in phase pinning during the flow passage and ultimately the deceleration of the phase in the confined geometry.

The results of the pressure evaluation also confirm that the change in the critical pressure introduced at the entrance is due to the pinning increase as the size of the bubble increases. The pinning of the phase in the smooth and the sharp pore showed that only one phase pinning event occurs at the exit of the pore geometry. In the case of rough circular pores, however, phase pinning events occur at each peak of the pore roughness. It was observed that in the case of the higher roughness, intensified pinning results in a change in the direction of the curvature of the phase. In this case, the bubble interface approaches the roughness with a convex shape and due to the pinning its curvature becomes flat and in some cases it becomes concave. This extensive change n the curvature results in a higher phase pinning critical pressure required for the bubble to pass through the confined geometry.

The interaction between the dispersed phase moving in a loosely packed bubbly flow passing through a pore space was also showed the importance of the bubble arrangement on the motion of the phase-in pore geometry. Two cases of an array and a loose matrix of bubbles entering a pore space were studied in this case. It was observed that the bubbles in both arrangements undergo similar deformation as they pass through the pore spaces. The bubbles decelerate before they enter the pore and accelerate as exit the pore due to their deformation. The spacing between the following bubble changes as a result of the change in the velocity of the bubbles in the pore. The spacing increases as the following bubble enters the pore and it decreases after it exits the pore space. The bubbles exiting the pore align on the centerline of the vertically orientated channel as a single linear array for both bubble's arrangement.

The results of the motion of the flow in the matrix of bubbles showed the interaction between the bubbles themselves and the geometry of the pore results in the entering of the bubbles in an alternating manner. As the bubbles in the matrix arrangement get closer to the pore geometry, they compete to enter the pore first. The bubble having a closer leading edge and the pore throat enters the pore first and its motion leads to a temporary repelling of the competing bubble from the pore.

This work contributes to the existing knowledge of multi-phase flow through porous media. It provides experimental insights on the limitation of previous studies by accounting for phase pinning when a dispersed phase passes through a pore space. The present study confirms previous findings on the reduction in the mobility of multi-phase flow in porous media and contributes additional evidence that the pore-scale interactions of the phases and solid interface are the main cause for the change in the phase mobility. This is the first study reporting that in addition to the critical pressure required for the phase entrance, the three-phase contact line pinning results in further complications for the flow passage. The analysis of the effect of dispersed size, the flow rate of the continuous phase, and the solid interface properties undertaken here, has extended knowledge on phase pinning and the required energy for the mobilization of the trapped phases in the porous media.

Future work

The present study provides a novel methodology to evaluate the pressure change results due to the deformation of the phase. It also provided insights on some important parameters affecting isolated flow passage. More research is required to expand the capability of the introduced method and evaluate the importance of the studied parameters in more applications. Several possible future studies using a similar approach are recommended.

Further research needs to examine more closely on the effect of 3D motion on the pressure determined by using the Laplace equation. The 3D detection of the isolated interface will address the effect of the asymmetric shape of the interface on the flow passage. It can be also beneficial to have detailed detection of the 3-phase contact line pinning in the pore geometry.

It would be interesting to assess and the motion of multi-bubble/droplet flow in porous media. The effects of pore structure having different roughness on a case of bubble competing to enter the pore will be an interesting flow investigation. The effect of bubble size, velocity, and pore structure will be more significant as the pinning of the phase results in slower motion of the phase exiting a pore and entering the next pore.

The pressure field in a multi-phase flow has a strong impact on the migration of fine particles. Physical phenomena that occur at the interface level will determine whether carried particles will remain attached to the dispersed phase or stick to the solid surface of the pore. A future study investigating the motion of the oil droplet on the removal of the fines from the oil reservoir would be very interesting. The refractive index matching approach introduced in this study can be applied to study the effect of carried particles and the effect of the 3-phase interaction on the particle deposition and removal from the surface of confining geometries.

References

[1] G. Muschiolik, “Multiple emulsions for food use,” *Curr. Opin. Colloid Interface Sci.*, vol. 12, no. 4–5, pp. 213–220, 2007.

[2] M. Nakano, “Places of emulsions in drug delivery,” *Adv. Drug Deliv. Rev.*, vol. 45, no. 1, pp. 1–4, 2000.

[3] F. L. Sousa, M. Santos, and S. M. Rocha, “Encapsulation of essential oils in SiO2 microcapsules and release behaviour of volatile compounds,” *J. Microencapsul.*, vol. 31, no. 7, pp. 627–635, 2014.

[4] J. S. Huang and R. Varadaraj, “Colloid and interface science in the oil industry,” *Curr. Opin. Colloid Interface Sci.*, vol. 1, no. 4, pp. 535–539, 1996.

[5] M. Murtaza, Z. He, and H. Dehghanpour, “An approach to model three-phase flow coupling during steam chamber rise,” *Can. J. Chem. Eng.*, vol. 92, no. 6, pp. 1100–1112, 2014.

[6] H. Qi, P. Hu, J. Xu, and A. Wang, “Encapsulation of drug reservoirs in fibers by emulsion electrospinning: Morphology characterization and preliminary release assessment,” *Biomacromolecules*, vol. 7, no. 8, pp. 2327–2330, 2006.

[7] E. Benet and F. J. Vernerey, “Mechanics and stability of vesicles and droplets in confined spaces,” *Phys. Rev. E*, vol. 94, no. December, p. 062613, 2016.

[8] J. Fournier and P. Galatola, “Corrections to the Laplace law for vesicle aspiration in micropipettes and other confined geometries,” *Soft Matter*, vol. 4, pp. 2463–2470, 2008.

[9] F. Mugele, “On the shape of a droplet in a wedge: new insight from electrowetting,” *Soft Matter*, vol. 11, no. 39, pp. 7717–7721, 2015.

[10] J. L. Drury and M. Dembo, “Hydrodynamics of micropipette aspiration,” *Biophys. J.*, vol. 76, no. 1, pp. 110–128, 1999.

[11] H. Mohamed, M. Murray, J. N. Turner, and M. Caggana, “Isolation of tumor cells using size and deformation,” *J. Chromatogr. A J.*, vol. 1216, pp. 8289–8295, 2009.

[12] S. Ansari, R. Sabbagh, Y. Yusuf, and D. S. Nobes, “The role of emulsions in steam-assisted-gravity-drainage (SAGD) oil-production process: a review,” *SPE J.*, vol. 25, no. 02, pp. 0969–0989, 2020.

[13] H. Soltani, R. Sabbagh, and D. S. Nobes, “The passage of bubbles rising through a confining rectangular geometry,” *Phys. Fluids*, vol. 10, no. 30, p. 103302, 2018.

[14] G. Chen, X. Huang, A. Zhang, S. Wang, and T. Li, “Three-dimensional simulation of a rising bubble in the presence of spherical obstacles by the immersed boundary – lattice Boltzmann method,” *Phys. Fluids*, vol. 31, p. 097104, 2019.

[15] V. T. Hoang, J. Lim, C. Byon, and J. Min, “Three-dimensional simulation of droplet dynamics in planar contraction microchannel,” *Chem. Eng. Sci.*, vol. 176, pp. 59–65, 2018.

[16] W. Lian, V. Mx, M. Ulloa, F. V. Martin, A. Fr, and M. M. Samuel, “Relative permeability modification,” vol. 2, no. 12, 2013.

[17] P. Azom and S. Srinivasan, “Mechanistic modeling of emulsion formation and heat transfer during the steam-assisted gravity drainage (SAGD) process,” in *SPE Annual Technical Conference and Exhibition, New Orleans, Louisiana, USA*, 2009, pp. 1–14.

[18] T. Patel, D. Patel, N. Thakkar, and A. Lakdawala, “A numerical study on bubble dynamics in sinusoidal channels A numerical study on bubble dynamics in sinusoidal channels,” *Phys. Fluids*, vol. 31, no. February, p. 052103, 2019.

[19] F. Huang, Y. Kang, L. You, X. Li, and Z. You, “Massive fines detachment induced by moving gas-water interfaces during early stage two-phase flow in coalbed methane reservoirs,” *Fuel*, vol. 222, no. November 2017, pp. 193–206, 2018.

[20] M. Menesses, J. Belden, N. Dickenson, and J. Bird, “Measuring a critical stress for continuous prevention of marine biofouling accumulation with aeration,” *Biofouling*, vol. 33, no. 9, pp. 703–711, 2017.

[21] L. Yu, Q. Sang, M. Dong, and Y. Yuan, “Effects of interfacial tension and droplet size on the plugging performance of oil-in-water emulsions in porous media,” *Ind. Eng. Chem. Res.*, vol. 56, no. 32, pp. 9237–9246, 2017.

[22] M. Magnini, A. M. Beisel, A. Ferrari, and J. R. Thome, “Pore-scale analysis of the minimum liquid film thickness around elongated bubbles in confined gas-liquid flows,” *Adv. Water Resour.*, vol. 109, pp. 84–93, 2017.

[23] M. Magnini, A. Ferrari, and J. R. Thome, “Undulations on the surface of elongated bubbles in confined gas-liquid flow,” *Phys. Rev. Fluids*, vol. 2, no. 8, pp. 1–21, 2017.

[24] Y. Liu, Q. Wang, and A. Zhang, “Surface stability of a bubble in a liquid fully confined by an elastic solid,” *Phys. Fluids*, vol. 30, no. December 2018, 2019.

[25] S. Ansari, Y. Yusuf, R. Sabbagh, and D. S. Nobes, “Determining the pressure distribution of a multi-phase flow through a pore space using velocity measurement and shape analysis,” *J. Meas. Sci. Technol.*, vol. 30, no. 5, 2019.

[26] S. Ansari and D. S. Nobes, “Interaction of loosely packed bubbly flow passing through a pore space,” *J. Vis.*, vol. 23, pp. 649–660, 2020.

[27] S. Ansari, Y. Yusuf, R. Sabbagh, H. Soltani, and D. S. Nobes, “An imaging derivation of the pressure field of a multi-phase flow in a porous media using µ-SPIV,” in *19th International Symposium on the Application of Laser and Imaging Techniques to Fluid Mechanics*, 2018.

[28] R. Liontas, K. Ma, G. J. Hirasaki, and S. L. Biswal, “Neighbor-induced bubble pinch-off:

novel mechanisms of in situ foam generation in microfluidic channels," *R. Soc. Chem.*, vol. 9, no. 46, pp. 10971–10984, 2013.

[29] R. Azadi, J. Wong, and D. S. Nobes, "Experimental and analytical investigation of meso-scale slug bubble dynamics in a square capillary channel Experimental and analytical investigation of meso-scale slug bubble dynamics in a square capillary channel," *Phys. Fluids,* vol. 32, no. June, 2020.

[30] C. Dai, S. Fang, Y. Wu, *et al.*, "Experimental study of bubble breakup process in non-Newtonian fluid in 3-D pore-throat microchannels," *Colloids Surfaces A Physicochem. Eng. Asp.*, vol. 535, pp. 130–138, 2017.

[31] H. Soltani, R. Azadi, A. Baldygin, S. Ansari, and D. S. Nobes, "Developing quantitative information of oil droplets rising through a rectangular confinement," in *5th International Conference on Experimental Fluid Mechanics –*, 2018.

[32] Y. Wu, S. Fang, C. Dai, *et al.*, "Investigation on bubble snap-off in 3-D pore-throat micro-structures," *J. Ind. Eng. Chem.*, vol. 54, pp. 69–74, 2017.

[33] J. Jin, Y. Wang, M. Wei, H. Ma, and K. Wang, "Coreflooding and pore-scale visualization of foamed gel flowed in porous network media," *J. Dispers. Sci. Technol.*, vol. 37, no. 10, pp. 1436–1443, 2015.

[34] S. Ansari, R. Sabbagh, H. Soltani, and D. S. Nobes, "Flow visualization of a bubble penetration through porous media in SAGD process using μSPIV," in *5th International Conference on Experimental Fluid Mechanics – ICEFM 2018 Munich*, 2018, vol. 1, no. 1.

[35] E. Benet, A. Badran, J. Pellegrino, and F. Vernerey, "The porous media's effect on the permeation of elastic (soft) particles," *J. Memb. Sci.*, vol. 535, no. January, pp. 10–19, 2017.

[36] R. Wright, "Jamin effect in oil production," *Bull. Am. Assoc. Pet. Geol.*, vol. 17, no. 12, pp.

1521–1525, 1933.

[37] M. J. Jamin, “Memoire sur l’equilibre et les mouvements de liquides dans corps poreux,” *Compt. Rend. Acad. Sci.*, vol. 50, pp. 172–76, 1860.

[38] W. O. Smith and M. D. Crane, “The Jamin effect in cylindrical tubes,” *J. Am. Chem. Soc.*, vol. 52, no. 4, pp. 1345–1349, 1930.

[39] A. F. Sarioglu, N. Aceto, N. Kojic, *et al.*, “A microfluidic device for label-free , physical capture of circulating tumor cell clusters,” *Nat. Methods*, vol. 12, no. 7, 2015.

[40] P. Preira, V. Grandne, J.-M. Forel, S. Gabriele, M. Camara, and and O. Theodoly, “Passive circulating cell sorting by deformability using a microfluidic gradual filter,” *Lab Chip*, vol. 13, pp. 161–170, 2013.

[41] S. M. Mcfaul, K. Lin, and H. Ma, “Cell separation based on size and deformability using microfluidic funnel ratchets,” *Lab Chip*, vol. 12, pp. 2369–2376, 2012.

[42] Z. Zhang, C. Drapaca, D. Gritsenko, and J. Xu, “Pressure of a viscous droplet squeezing through a short circular constriction : An analytical model,” *Phys. Fluids*, vol. 30, no. June, p. 102004, 2018.

[43] M. Nagel, P.-T. Brun, and F. Gallaire, “A numerical study of droplet trapping in microfluidic devices,” *Phys. Fluids*, vol. 26, no. 032002, 2016.

[44] Z. Zhang, C. Drapaca, X. Chen, and J. Xu, “Droplet squeezing through a narrow constriction : Minimum impulse and critical velocity,” *Phys. Fluids*, vol. 29, no. January 2017, p. 072102, 2018.

[45] Y. Guan, M. Zhu, B. Li, J. Tu, L. Xing, and X. Chen, “Numerical investigation of continuous droplet transport in parallel-plate electrowetting-on-dielectric digital microfluidics (EWOD DMF) with stripped electrodes,” *Phys. Fluids*, vol. 32, no. 2019, p.

062002, 2020.

[46] CAPP, “Oil Sands,” *Canadian Association of Petroleum Producers*, Jul-2018.

[47] J. Guan, “Physical properties of Athabasca bitumen and liquid solvent mixtures,” MSc Thesis, University of Calgary, 2013.

[48] M. Abram, G. Cain, and D. Canada, “Particle-size analysis for the pike 1 project , McMurray formation,” *J. Can. Pet. Technol.*, vol. 53, pp. 339–354, 2014.

[49] M. Carrigy, “Lithology of the Athabasca oil sands,” *Res. Counc. Alberta, Bull. 18, Edmont.*, 1966.

[50] H. Devold, *Oil and gas production Handbook - An introduction to oil and gas production, transport, refiening and petrochemical industry*. ABB Oil and Gas, 2013.

[51] V. Alvarado and E. Manrique, “Enhanced oil recovery concepts,” in *Enhanced oil recovery*, Burlington, USA: Elsevier Inc., 2010, pp. 9–10.

[52] S. Thomas, “Enhanced oil recovery-an overview,” *Oil Gas Sci. Technol.*, vol. 63, no. 1, pp. 9–19, 2008.

[53] R. Butler, “inverntor, ExxonMobil Upstream Research Co, assignee. Method for continuously producing viscous hydrocarbons by gravity drainage while injecting heated fluids,” *United States Pat.*, p. US 4,344,485, 1982.

[54] C. S. Matthews, “Steamflooding,” *SPE J.*, vol. 35, no. 03, pp. 465–471, 1983.

[55] R. Butler, “SAGD comes of age!,” *J. Can. Pet. Technol.*, vol. 37, no. 7, pp. 9–12, 1998.

[56] B. Orr, “ES-SAGD; past, present and future,” *2009 SPE Int. Student Pap. Contest SPE Annu. Tech. Conf. Exhib. New Orleans, Louisiana, USA*, vol. SPE-129518, no. October, pp. 4–7, 2009.

[57] R. Butler, “Steam-assisted gravity drainage: concept, development, performance and

future," *J. Can. Pet. Technol.*, vol. 33, no. 02, pp. 44–50, 1994.

[58] C. Shen, "SAGD for heavy oil recovery," in *Enhanced Oil Recovery Field Case Studies*, First Edit., Elsevier Inc., 2013, pp. 413–445.

[59] J. Zhang, X. Fan, B. Xu, Y. Yuan, and Y. Yu, "Steam circulation strategies for SAGD wells after geomechanical dilation," *SPE Canada Heavy Oil Tech. Conf. Calgary, Canada*, vol. SPE-180705, 2016.

[60] J.-Y. Yuan and R. Mcfarlane, "Evaluation of steam circulation strategies for SAGD start-up," *J. Can. Pet. Technol.*, vol. 50, no. 01, pp. 20–32, 2011.

[61] A. Haddadnia, B. Azinfar, M. Zirrahi, H. Hassanzadeh, and J. Abedi, "Thermophysical properties of dimethyl ether/Athabasca bitumen system," *Can. J. Chem. Eng.*, vol. 96, pp. 597–604, 2018.

[62] N. Sabet, H. Hassanzadeh, and J. Abedi, "Selection of efficient solvent in solvent-aided thermal recovery of bitumen," *Chem. Eng. Sci.*, vol. 161, pp. 198–205, 2017.

[63] M. Razi, S. Sinha, P. R. Waghmare, S. Das, and T. Thundat, "Effect of steam-assisted gravity drainage produced water properties on oil/water transient interfacial tension," *Energy and Fuels*, vol. 30, no. 12, pp. 10714–10720, 2016.

[64] C. Ezeuko, J. Wang, and I. Gates, "Investigation of emulsion flow in SAGD and ES-SAGD," *Proc. SPE Heavy Oil Conf. Canada,Calgary, Canada, SPE-157830*, pp. 1–16, 2012.

[65] M. Leitch, "Personal communication, January 19, 2017." 2017.

[66] M. Kyanpour, "Thermal energy distribution in the steam assisted gravity drainage," PhD Thesis, University of Calgary, 2015.

[67] P. Li, M. Chan, and W. Froehlich, "Steam injection pressure and the SAGD ramp-up

process," *J. Can. Pet. Technol.*, vol. 48, no. 1, pp. 36–41, 2009.

[68] Y. Yusuf and Y. Ma, "Design of a simulation tool for SAGD based on the concept of unified feature modeling scheme," *Proc. TMCE 2016*, pp. 1–12, 2016.

[69] H. Nourozieh, M. Kariznovi, and J. Abedi, "Density and viscosity of Athabasca bitumen samples at temperatures up to 200C and pressures up to 10 MPa," *SPE Reserv. Eval. Eng.*, vol. 18, no. 03, pp. 375–386, 2015.

[70] C. Ezeuko, J. Wang, and I. D. Gates, "Investigation of emulsion flow in steam-assisted gravity drainage," *SPE J.*, vol. 18, no. 03, pp. 440–447, 2013.

[71] W. H. Goodman, M. R. Godfrey, and T. M. Miller, "Scale and deposit formation in steam assisted gravity drainage (SAGD) facilities," in *the International Water Conference, San Antonio, Texas*, 2010, p. International Water Conference in San Antonio, Tex.

[72] A. Azad and R. J. Chalaturnyk, "Geomechanical coupling simulation in SAGD process ; a linear geometry model," in *Proceedings of the 3rd CANUS Rock Mechanics Symposium,Toronto, Canada*, 2009.

[73] X. Bao, "Thermal simulation and optimization of SAGD process: case study on surmont pilot project," MSc Thesis, University of Calgary, 2012.

[74] R. Butler, "Rise of interfering steam chambers," *J. Can. Pet. Technol.*, vol. 26, no. 3, pp. 70–75, 1987.

[75] R. Butler, G. S. McNab, and H. Y. Lo, "Theoretical studies on the gravity drainage of heavy oil during insitu steam heating," *Can. J. Chem. Eng.*, vol. 59, no. 4, pp. 455–460, 1981.

[76] D. Denney, "Net pay: What is it? What does it do? How do we quantify it? How do we use it?," *J. Pet. Technol.*, vol. 62, no. 08, pp. 46–48, 2010.

[77] V. Dehdari, "Development and applications of a semi-analytical approximate thermal

simulator," *2014 Gussow Geosci. Conf. Banff, Canada*, pp. 1–5, 2014.

[78] N. Alali, M. R. Pishvaie, and H. Jabbari, "A new semi-analytical modeling of steam-assisted gravity drainage in heavy oil reservoirs," *J. Pet. Sci. Eng.*, vol. 69, no. 3–4, pp. 261–270, 2009.

[79] M. Mojarad and H. Dehghanpour, "Analytical modeling of emulsion flow at the edge of a steam chamber during a steam-assisted-gravity-drainage process," *SPE J.*, vol. 21, no. 02, pp. 353–363, 2016.

[80] X. Shi and R. Okuno, "Analytical solution for steam-assisted gravity drainage with consideration of temperature variation along the edge of a steam chamber," *Fuel*, vol. 217, pp. 262–274, 2018.

[81] Q. Chen, "Assessing and improving steam-assisted gravity drainage: reservoir heterogeneities, hydraulic fractures, and mobility control foams," PhD Thesis, Standford University, 2009.

[82] M. Irani and S. Ghannadi, "Understanding the heat-transfer mechanism in the steam-assisted gravity-drainage (SAGD) process and comparing the conduction and convection flux in bitumen reservoirs," *SPE J.*, vol. 18, no. 01, pp. 134–145, 2013.

[83] J. Sharma and I. D. Gates, "Multiphase flow at the edge of a steam chamber," *Can. J. Chem. Eng.*, vol. 88, no. 3, pp. 312–321, 2010.

[84] R. Butler, "A new approach to the modelling of steam-assisted gravity drainage," *J. Can. Pet. Technol.*, vol. 24, no. 03, pp. 42–51, 2013.

[85] K. Patel, E. M. Aske, and M. Fredriksen, "Integrating reservoir simulator and model predictive control software for automating SAGD well pair operations," *SPE Heavy Oil Conf. Canada, Calgary, Canada*, p. SPE-165535, 2013.

[86] S. M. Farouq-Ali, “Is there life after SAGD?,” *J. Can. Pet. Technol.*, vol. 36, no. 6, pp. 20–23, 1997.

[87] K. Sasaki, S. Akibayashi, N. Yazawa, and F. Kaneko, “Microscopic visualization with high resolution optical-fiber scope at steam chamber interface on initial stage of SAGD process,” *SPE - DOE Improv. Oil Recover. Symp. Proceedings, Tulsa, Oklahoma,* p. SPE-75241, 2002.

[88] O. Mohammadzadeh, N. Rezaei, and I. Chatzis, “More insight into the pore-level physics of the solvent-aided SAGD (SA-SAGD) process for heavy oil and bitumen recovery,” *Soc. Pet. Eng. - SPE Heavy Oil Conf. Canada 2012*, vol. 1, pp. 588–633, 2012.

[89] A.-M. Al-Bahlani and T. Babadagli, “SAGD laboratory experimental and numerical simulation studies: A review of current status and future issues,” *J. Pet. Sci. Eng.*, vol. 68, no. 3–4, pp. 135–150, Oct. 2009.

[90] C. Lu, H. Liu, and W. Zhao, “Visualized study of displacement mechanisms by injecting viscosity reducer and non-condensable gas to assist steam injection,” *J. Energy Inst.*, vol. 90, no. 1, pp. 73–81, 2017.

[91] F. J. Argüelles-Vivas and T. Babadagli, “Pore-scale investigations on the dynamics of gravity-driven steam-displacement process for heavy-oil recovery and development of residual oil saturation : a 2D visual analysis,” *SPE J.*, vol. 21, pp. 1–943, 2016.

[92] O. Mohammadzadeh and I. Chatzis, “Pore-level investigation of heavy oil recovery using steam assisted gravity drainage (SAGD),” *Can. Int. Pet. Conf. (CIPC), Doha, Qatar,* vol. IPTC 13403, 2009.

[93] R. Bosch, E. Axcell, V. Little, *et al.*, “A novel approach for resolving reverse emulsions in SAGD production systems,” *Can. J. Chem. Eng.*, vol. 82, no. 4, pp. 836–839, 2004.

[94] C. Noik, C. Dalmazzone, C. Goulay, and P. Glenat, “Characterisation and emulsion behaviour of Athabasca extra-heavy-oil produced by SAGD,” *Proc. SPE/PS-CIM/CHOA Int. Therm. Oper. Heavy Oil Symp. Canada*, p. SPE-97748-MS, 2005.

[95] S. Kokal, “Crude oil emulsions: a state-of-the-art review,” *SPE Prod. Facil.*, vol. 20, pp. 5–13, 2005.

[96] S. F. Wong, J. S. Lim, and S. S. Dol, “Crude oil emulsion: A review on formation, classification and stability of water-in-oil emulsions,” *J. Pet. Sci. Eng.*, vol. 135, pp. 498–504, 2015.

[97] T. Tadros, “Emulsion formation,” in *Encyclopedia of colloid and interface science*, Berlin Heidelberg: Springer-Verlag, 2013, pp. 366–375.

[98] O. K. Kimbler, R. L. Reed, and I. H. Silberberg, “Physical characteristics of natural films formed at crude oil-water interfaces,” *Soc. Pet. Eng. J.*, vol. 6, no. 02, pp. 153–165, 1966.

[99] T. J. Jones, E. L. Neustadter, and K. P. Whittingham, “Water-in-crude oil emulsion stability and emulsion destabilization by chemical demulsifiers.,” *J. Can. Pet. Technol.*, vol. 17, no. 2, pp. 100–108, 1978.

[100] D. D. Eley, M. J. Hey, and J. D. Symonds, “Emulsions of water in asphaltene-containing oils 1. Droplet size distribution and emulsification rates,” *Colloids and Surfaces*, vol. 32, no. C, pp. 87–101, 1988.

[101] D. E. Tambe and M. M. Sharma, “Factors controlling the stability of colloid-stabilized emulsions. I. An experimental investigation,” *J. Colloid Interface Sci.*, vol. 157, no. 1, pp. 244–253, 1993.

[102] R. Butler, *Thermal recovery of oil and bitumen*. Englewood Cliffs, New Jersey, USA: Prentice Hall, 1991.

[103] G. I. Taylor, “The viscosity of a fluid containing small drops of another fluid,” *Proc. R. Soc. A Math. Phys. Eng. Sci.*, vol. 138, no. 834, pp. 41–48, 1932.

[104] E. Kreyszig, *Advanced engineering mathematics*, 10th ed. Boston: John Wiley & Sons Inc., 2011.

[105] R. H. Brooks and A. T. Corey, “Hydraulic properties of porous media,” *Color. State Univ. Fort Collins Color.*, vol. 3, pp. 1–27, 1964.

[106] S. Wang, E. Axcell, R. Cleary, V. Little, and L. Pinkoski, “Application of a reverse-emulsion-breaker at a SAGD pilot plant in northern Alberta,” *SPE Int. Therm. Oper. Heavy Oil Symp. West. Reg. Meet. held Bak. California, U.S.A*, 2004.

[107] T. N. Nasr, D. Law, H. Golbeck, and G. Korpany, “Counter-current aspect of the SAGD process,” *J. Can. Pet. Technol.*, vol. 39, no. 1, pp. 41–47, 2000.

[108] A. M. Albahlani and T. Babadagli, “A critical review of the status of SAGD : where are we and what is next?,” *SPE West. Reg. Pacific Sect. AAPG Jt. Meet. Bak. California, U.S.A.*, pp. 1–22, 2008.

[109] K. Chung and R. Butler, “In-situ emulsification by the condensation of steam in contact with bitumen,” *J. Can. Pet. Technol.*, vol. 28, no. 01, pp. 48–55, 1989.

[110] W. M. Mahmud and V. H. Nguyen, “Effects of snap-off in imbibition in porous media with different spatial correlations,” *Transp. Porous Media*, vol. 64, no. 3, pp. 279–300, 2006.

[111] Y. Ito and G. Ipek, “Steam fingering phenomenon during SAGD process,” *SPE Int. Therm. Oper. Heavy Oil Symp. Calgary, Canada*, pp. 1–9, 2005.

[112] R. Butler and K. Chung, “Geometrical effect of steam injection on the formation of emulsions in the steam-assisted gravity drainage process,” *38th Annu. Meet. Pet. Soc. CIM, Calgary, Canada*, pp. 373–392, 1987.

[113] D. Letourneau, “Flow control devices : an emerging SAGD technology,” *Journal of the Canadian Heavy Oil Association*, pp. 14–18, Jun-2015.

[114] I. D. Gates and N. Chakrabarty, “Optimization of steam-assisted gravity drainage in McMurray reservoir,” *Can. Int. Pet. Conf.*, vol. 45, pp. 54–62, 2006.

[115] E. Walls, C. Palmgren, and K. Kisman, “Residual oil saturation inside the steam chamber during SAGD,” *J. Can. Pet. Technol.*, vol. 42, no. 1, pp. 39–47, 2003.

[116] D. R. Gotawala and I. D. Gates, “Steam fingering at the edge of a steam chamber in a heavy oil reservoir,” *Can. J. Chem. Eng.*, vol. 86, no. 6, pp. 1011–1022, 2008.

[117] J. Ratulowski and H. Chang, “Snap off at strong constrictions : effect of pore geometry,” *ACS Symp. Ser. Am. Chem. Soc. Washington, DC*, pp. 282–294, 1988.

[118] W. M. Mahmud, “Effect of snap-off on two- and three-phase relative permeabilities and residual saturations using a network model,” PhD Thesis, University of New South Wales, 2004.

[119] W. Abdallah, J. S. Buckley, A. Carnegie, *et al.*, “Fundamentals of wettability,” *Oilf. Rev.*, pp. 44–61, 2007.

[120] M. J. Blunt, “Flow in porous media - Pore-network models and multiphase flow,” *Curr. Opin. Colloid Interface Sci.*, vol. 6, no. 3, pp. 197–207, 2001.

[121] C. A. Conn, K. Ma, G. J. Hirasaki, and S. L. Biswal, “Visualizing oil displacement with foam in a microfluidic device with permeability contrast,” *Lab Chip*, vol. 14, no. 20, pp. 3968–3977, 2014.

[122] R. Bilak, “inverntor, Terralog Technologies Inc, assignee. Enhanced oil recovery methods,” *United States Pat.*, p. US 7,069,990, 2006.

[123] O. Mohammadzadeh, N. Rezaei, and I. Chatzis, “Pore-level investigation of heavy oil and

bitumen recovery using solvent -Aided steam assisted gravity drainage (SA-SAGD) process," *Energy and Fuels*, vol. 24, no. 12, pp. 6327–6345, 2010.

[124] É. Lepercq-Bost, M. L. Giorgi, A. Isambert, and C. Arnaud, "Use of the capillary number for the prediction of droplet size in membrane emulsification," *J. Memb. Sci.*, vol. 314, no. 1–2, pp. 76–89, 2008.

[125] J. Sjoblom, O. Urdahl, H. Hoiland, A. A. Christy, and E. J. Johansen, "Water-in-crude oil emulsions. Formation, characterization, and destabilization," *Prog. Colloid Polym. Sci.*, vol. 82, pp. 131–139, 1990.

[126] J. D. McLean and P. K. Kilpatrick, "Effects of asphaltene solvency on stability of water-in-crude-oil emulsions," *J. Colloid Interface Sci.*, vol. 189, no. 2, pp. 242–253, 1997.

[127] R. A. Mohammed, A. I. Bailey, P. F. Luckham, and S. E. Taylor, "Dewatering of crude oil emulsions 2. Interfacial properties of the asphaltic constituents of crude oil," *Colloids Surfaces A Physicochem. Eng. Asp.*, vol. 80, no. 2–3, pp. 237–242, 1993.

[128] K. Kumar, A. D. Nikolov, and D. T. Wasan, "Mechanisms of stabilization of water-in-crude oil emulsions," *Ind. Eng. Chem. Res.*, vol. 40, no. 14, pp. 3009–3014, 2001.

[129] X. Yang, H. Hamza, and J. Czarnecki, "Investigation of subfractions of Athabasca asphaltenes and their role in emulsion stability," *Energy and Fuels*, vol. 18, no. 3, pp. 770–777, 2004.

[130] V. Balsamo, D. Nguyen, and J. Phan, "Non-conventional techniques to characterize complex SAGD emulsions and dilution effects on emulsion stabilization," *J. Pet. Sci. Eng.*, vol. 122, pp. 331–345, 2014.

[131] B. Zhao, M. Becerra, and J. M. Shaw, "On asphaltene and resin association in Athabasca bitumen and Maya crude oil," *Energy and Fuels*, vol. 23, no. 9, pp. 4431–4437, 2009.

[132] A. Mukhametshina, T. Kar, and B. Hascakir, “Asphaltene precipitation during bitumen extraction with expanding-solvent steam-assisted gravity drainage: Effects on pore-scale displacement,” *SPE J.*, vol. 21, no. 02, pp. 380–392, 2016.

[133] R. A. Mohammed, A. I. Bailey, P. F. Luckham, and S. E. Taylor, “Dewatering of crude oil emulsions 3. Emulsion resolution by chemical means,” *Colloids Surfaces A Physicochem. Eng. Asp.*, vol. 83, no. 3, pp. 261–271, 1994.

[134] P. Berger, C. Hsu, and J. Arendell, “Designing and selecting demulsifiers for optimum field performance based on production fluid characteristics,” *SPE Int. Symp. Oilf. Chem. Antonio, Texas*, pp. 457–461, 1987.

[135] R. A. Mohammed, A. I. Bailey, P. F. Luckham, and S. E. Taylor, “Dewatering of crude oil emulsions 1. Rheological behaviour of the crude oil-water interface,” *Colloids Surfaces A Physicochem. Eng. Asp.*, vol. 80, no. 2–3, pp. 23–235, 1993.

[136] H. A. W. Kaminsky, T. H. Etsell, D. G. Ivey, and O. Omotoso, “Distribution of clay minerals in the process streams produced by the extraction of bitumen from athabasca oil sands,” *Can. J. Chem. Eng.*, vol. 87, no. 1, pp. 85–93, 2009.

[137] D. M. Sztukowski and H. W. Yarranton, “Oilfield solids and water-in-oil emulsion stability,” *J. Colloid Interface Sci.*, vol. 285, no. 2, pp. 821–833, 2005.

[138] B. P. Binks and S. O. Lumsdon, “Catastrophic phase inversion of water-in-oil emulsions stabilized by hydrophobic silica,” *Langmuir*, vol. 16, no. 6, pp. 2539–2547, 2000.

[139] A. Borysenko, B. Clennell, R. Sedev, *et al.*, “Experimental investigations of the wettability of clays and shales,” *J. Geophys. Res. Solid Earth*, vol. 114, no. 7, pp. 1–11, 2009.

[140] K. A. Heiden and M. A. Holmes, “Grain-size distribution and significance of clay and clay-sized minerals in eocene to holocene sediments from sites 918 and 919 in the Irminger

basin," *Proc. Ocean Drill. Program, Sci. Results*, vol. 152, pp. 39–49, 1998.

[141] P. H. J. Mercier, Y. Le Page, Y. Tu, and L. Kotlyar, "Powder X-ray diffraction determination of phyllosilicate mass and area versus particle thickness distributions for clays from the athabasca Oil sands," *Pet. Sci. Technol.*, vol. 26, no. 3, pp. 307–321, 2008.

[142] O. E. Omotoso and R. J. Mikula, "High surface areas caused by smectitic interstratification of kaolinite and illite in Athabasca oil sands," *Appl. Clay Sci.*, vol. 25, no. 1–2, pp. 37–47, 2004.

[143] F. S. Manning and R. Thompson, *Oilfield processing of petroleum: crude oil, Volume 2*. Tulsa, Oklahoma ,USA: PennWell Corporation, 1991.

[144] V. Smith and K. Arnold, "Crude oil emulsions," in *Petroleum Engineering Handbook*, Richardson, TX: Society of Petroleum Engineers, 1987.

[145] J. E. Strassner, "Effect of pH on interfacial films and stability of crude oil-water emulsions," *J. Pet. Technol.*, vol. 20, no. 03, pp. 303–312, 1968.

[146] R. Valdya and H. Fogler, "Fines migration and formation damage: influence of pH and ion exchange," *SPE Prod. Eng.*, vol. 7, no. 4, pp. 325–330, 1992.

[147] J. J. Sheng, "Critical review of low-salinity waterflooding," *J. Pet. Sci. Eng.*, vol. 120, pp. 216–224, 2014.

[148] M. Mahmoudi, V. Fattahpour, and A. Nouri, "An experimental investigation of the effect of pH and salinity on sand control performance for heavy oil thermal production," *SPE Canada Heavy Oil Tech. Conf. ,Calgary, Alberta, Canada*, vol. SPE-180756, 2016.

[149] J. Hajinasiri, "Treatment of steam assisted gravity drainage produced water using polymeric membranes," MSc Thesis, University of Alberta, 2015.

[150] B. R. Hansen, "Review of potential technologies for the removal of dissolved components

from produced water," *Chem. Eng. Res. Des.*, vol. 72, no. A2, pp. 176–188, 1994.

[151] R. G. Pillai, N. Yang, S. Thi, J. Fatema, M. Sadrzadeh, and D. Pernitsky, "Characterization and comparison of dissolved organic matter signatures in steam-assisted gravity drainage process water samples from Athabasca oil sands.," *Energy and Fuels*, vol. 31, no. 8, pp. 8363–8373, 2017.

[152] P. Binks, R. Murakami, S. P. Armes, and S. Fujii, "Effects of pH and salt concentration on oil-in-water emulsions stabilized solely by nanocomposite microgel particles," *Langmuir*, vol. 22, pp. 2050–2057, 2006.

[153] L.-H. Hung, K. M. Choi, W.-Y. Tseng, Y.-C. Tan, K. J. Shea, and A. P. Lee, "Alternating droplet generation and controlled dynamic droplet fusion in microfluidic device for CdS nanoparticle synthesis," *Lab Chip*, vol. 6, no. 2, p. 174, 2006.

[154] H. Song, J. D. Tice, and R. F. Ismagilov, *A microfluidic system for controlling reaction networks in time*, vol. 115, no. 7. KGaA, Weinheim: Wiley-VCH Verlag GmbH & Co., 2003.

[155] C. Wang, N.-T. Nguyen, and T. N. Wong, "Optical measurement of flow field and concentration field inside a moving nanoliter droplet," *Sensors Actuators, A Phys.*, vol. 133, no. 2 SPEC. ISS., pp. 317–322, 2006.

[156] Y. C. Tan, Y. L. Ho, and A. P. Lee, "Droplet coalescence by geometrically mediated flow in microfluidic channels," *Microfluid. Nanofluidics*, vol. 3, no. 4, pp. 495–499, 2007.

[157] K. Liu, H. Ding, Y. Chen, and X. Z. Zhao, "Droplet-based synthetic method using microflow focusing and droplet fusion," *Microfluid. Nanofluidics*, vol. 3, no. 2, pp. 239–243, 2007.

[158] B. J. Jin, Y. W. Kim, Y. Lee, and J. Y. Yoo, "Droplet merging in a straight microchannel

using droplet size or viscosity difference,” *J. Micromechanics Microengineering*, vol. 20, no. 3, pp. 1–10, 2010.

[159] B. J. Jin and J. Y. Yoo, “Visualization of droplet merging in microchannels using micro-PIV,” *Exp. Fluids*, vol. 52, no. 1, pp. 235–245, 2012.

[160] K. Ahn, J. Agresti, H. Chong, M. Marquez, and D. A. Weitz, “Electrocoalescence of drops synchronized by size-dependent flow in microfluidic channels,” *Appl. Phys. Lett.*, vol. 88, no. 26, 2006.

[161] D. R. Link, E. Grasland-Mongrain, A. Duri, *et al.*, “Electric control of droplets in microfluidic devices,” *Angew. Chemie - Int. Ed.*, vol. 45, no. 16, pp. 2556–2560, 2006.

[162] F. Javadpour, “Bubble breakup in porous media,” *J. Can. Pet. Technol.*, vol. 46, no. 8, pp. 26–32, 2007.

[163] R. Kumar and M. Pooladi-Darvish, “Effect of viscosity and diffusion coefficient on the kinetics of bubble growth in solution-gas drive in heavy oil,” *J. Can. Pet. Technol.*, vol. 40, no. 3, pp. 30–37, 2001.

[164] K. Sasaki, S. Akibayashi, N. Yazawa, Q. T. Doan, and S. M. Farouq Ali, “Experimental modeling of the SAGD process - enhancing SAGD performance with periodic stimulation of the horizontal producer,” *SPE J.*, vol. 6, no. 01, pp. 89–97, 2001.

[165] J. Kumasaka, K. Sasaki, Y. Sugai, O. S. Alade, and M. Nakano, “Measurement of viscosity alteration for emulsion and numerical simulation on bitumen production by SAGD considering in-situ emulsification,” *J. Earth Sci. Eng.*, vol. 6, pp. 10–17, 2016.

[166] A. Cihan, “The rise velocity of an air bubble in coarse porous media: Theoretical studies,” MSc Thesis, Middle East Technical University, 2004.

[167] G. O. Brown, “Henry Darcy and the making of a law,” *Water Resour. Res.*, vol. 38, no. 7,

pp. 11_1-11_12, 2002.

[168] H. D. Beggs and J. . Robinson, “Estimating the viscosity of crude oil systems,” *J. Pet. Technol.*, vol. 27, no. 09, pp. 1140–1141, SPE-5434, 1975.

[169] M. Batzle, R. Hofmann, and D.-H. Han, “Heavy oils - Seismic properties,” *SEG int’l Expo. 74th Annu. Meet. , Denver, Color.*, vol. 25, no. 2006, pp. 673–792, 2006.

[170] A. K. Mehrotra and W. Y. Svrcek, “Viscosity of compressed Athabasca bitumen,” *Can. J. Chem. Eng.*, vol. 64, no. 5, pp. 844–847, 1986.

[171] N. Edmunds, “Investigation of SAGD steam trap control in two and three dimensions,” *J. Can. Pet. Technol.*, vol. 39, no. 1, pp. 30–40, 1998.

[172] A. Al-Gawfi, M. Zirrahi, H. Hassanzadeh, and J. Abedi, “Development of generalized correlations for thermophysical properties of light hydrocarbon solvents (C1 − C5)/ bitumen systems using genetic programming,” *ACS Omega*, vol. 4, pp. 6955–6967, 2019.

[173] G. De Ghetto, F. Paone, M. Viila, and S. A. Agip, “Pressure-volume-temperature correlations for heavy and extra heavy oils,” *Soc. Pet. Eng.*, pp. 647–662, SPE 30316, 1995.

[174] R. Simon and W. Poynter, “Down-hole emulsification for improving viscous crude production,” *J. Pet. Technol.*, pp. 1349–53, 1968.

[175] V. A. Bloomfield and R. K. Dewan, “Viscosity of liquid mixture,” *J. Phys. Chem*, vol. 75, no. 1, p. pp 3113–3119, 1971.

[176] J. P. Camy, S. S. Marsden, and N. Arihara, “The rheology of crude oil dispersions,” *Int. Symp. Oilf. Chem. of-the Soc. Pet. Eng. AIME*, pp. 51–57, 1975.

[177] E. Barnea and J. Mizrahi, “On the ‘effective’ viscosity of liquid-liquid dispersions,” *Ind. Eng. Chem. Fundam.*, vol. 15, no. 2, pp. 120–125, 1976.

[178] R. Pal and E. Rhodes, “Viscosity/concentration relationships for emulsions,” *J. Rheol. (N.*

Y. N. Y)., vol. 33, no. 7, pp. 1021–1045, 1989.

[179] R. Pal and E. Rhodes, "A novel viscosity correlation for non-Newtonian concentrated emulsions," *J. Colloid Interface Sci.*, vol. 107, no. 2, pp. 301–307, 1985.

[180] A. Elgibaly, I. Nashawi, and M. Tantawy, "Rheological characterization of Kuwaiti oil-lakes oils and their emulsions," in *International Symposium on Oilfield Chemistry, At Houston, Texas, USA*, 1997.

[181] R. Pal, "A novel method to correlate emulsion viscosity data," *Colloids surfaces A Physicochem. Eng. Asp.*, vol. 137, no. 1–3, pp. 275–286, 1998.

[182] G. Li-ping, W. Lei, and Z. Yi-min, "Applicability of emulsion viscosity models to crude oil emulsion," *Adv. Mater. Res.*, vol. 581–582, p. pp 50-53, 2012.

[183] D. Dou and J. Gong, "Experimental investigation on apparent viscosity of heavy oilwater emulsions," *Chem. Eng.*, vol. 34, no. 9, pp. 39–42, 2006.

[184] L. L. Schramm, *Emulsions: Fundamentals and applications in the petroleum industry*, vol. 16, no. 6. Washington, DC: American Chemical Society, 2001.

[185] W. J. McCaffrey and R. D. Bowman, "Recent successes in primary bitumen production," in *8th Annual Heavy Oil and Oil Sands Technical Symposium, Calgary, Alberta, Canada*, 1991.

[186] D. B. Robinson, "The thermodynamic and transport properties of bitumens and heavy oils," *Alberta Oil Sands Technol. Res. Authority, Edmonton, Canada*, pp. 9–12, 1984.

[187] K. Miller and B. Erno, "Use and misuse of heavy oil and bitumen viscosity data," in *46th Annual Technical Meeting of The Petroleum Society of CIM, Banff, Alberta, Canada*, 1995.

[188] D. Chisholm, "Two-phase flow in heat exchangers and pipelines," *Heat Transf. Eng.*, vol. 6, no. 2, pp. 48–57, Jul. 2007.

[189] C. Alimonti, G. Falcone, and O. Bello, “Two-phase flow characteristics in multiple orifice valves,” *Exp. Therm. Fluid Sci.*, vol. 34, no. 8, pp. 1324–1333, Nov. 2010.

[190] S. Ansari, R. Sabbagh, Y. Yusuf, and D. S. Nobes, “The role of emulsions in steam-assisted-gravity-drainage (SAGD) oil-production process: a review,” *SPE J.*, no. March, pp. 1–21, 2019.

[191] G. R. Guédon, J. D. H. Hyman, F. Inzoli, M. Riva, A. Guadagnini, and R. Gu, “Influence of capillary end effects on steady- state relative permeability estimates from direct pore-scale simulations estimates from direct pore-scale simulations,” *Phys. Fluids*, vol. 29, no. 123104, 2017.

[192] C. G. Suarez, J. Noordmans, H. C. van der Mei, and H. J. Busscher, “Detachment of colloidal particles from collector surfaces with different electrostatic charge and hydrophobicity by attachment to air bubbles in a parallel plate flow chamber,” *Phys. Chem. Chem. Phys.*, pp. 4423–4427, 1999.

[193] P. Sharma, M. Flury, and J. Zhou, “Detachment of colloids from a solid surface by a moving air-water interface,” *J. Colloid Interface Sci.*, vol. 326, no. 1, pp. 143–150, 2008.

[194] C. G. Suárez, J. Noordmans, H. C. Van Der Mei, and H. J. Busscher, “Removal of colloidal particles from quartz collector surfaces as stimulated by the passage of liquid-air interfaces,” *Langmuir*, vol. 15, no. 15, pp. 5123–5127, 1999.

[195] S. Khodaparast, M. K. Kim, J. E. Silpe, and H. A. Stone, “Bubble-driven detachment of bacteria from confined microgeometries,” *Environ. Sci. Technol.*, vol. 51, no. 3, pp. 1340–1347, 2017.

[196] F. de Gennes, Pierre-Gilles Brochard-Wyart and D. Quere, *Capillarity and wetting phenomena: drops, bubbles, pearls, waves*. Springer, New York, 2004.

[197] A. T. S. Cerdeira, J. B. L. M. Campos, J. M. Miranda, and J. D. P. Araújo, "Review on microbubbles and microdroplets flowing through microfluidic geometrical elements," *Micromachines*, vol. 11, no. 201, 2020.

[198] J. M. Kim, K. H. Ahn, and S. Lee, "Numerical study on the effect of viscoelasticity on pressure drop and film thickness for a droplet flow in a confined microchannel," *Korea-Australia Rheol. Journ*, vol. 21, no. 1, 2009.

[199] Z. Zhang, X. Chen, and J. Xu, "Entry effects of droplet in a micro confinement : Implications for deformation-based circulating tumor cell microfiltration," *Biomicrofluidics*, vol. 9, no. 024108, pp. 15–18, 2015.

[200] X. Zhang, M. Abul, X. Chen, and H. Tan, "On passing a non-Newtonian circulating tumor cell (CTC) through a deformation-based microfluidic chip," *Theor. Comput. Fluid Dyn.*, vol. 32, no. 6, pp. 753–764, 2018.

[201] Z. Zhang, J. Xu, B. Hong, and X. Chen, "The effects of 3D channel geometry on CTC passing pressure – towards deformability-based cancer cell separation," *Lab Chip*, vol. 14, pp. 2576–2584, 2014.

[202] Z. Zhang, C. Drapaca, D. Gritsenko, and J. Xu, "Pressure of a viscous droplet squeezing through a short circular constriction : An analytical model," *Phys. Fluids*, vol. 30, p. 102004, 2018.

[203] T. T. Shirai, A.; Fujita, R.; Hayase, "Transit Characteristics of a Neutrophil passing through two moderate constrictions in a cylindrical capillary vessel (effect of cell deformation on transit through the second constriction)," *JSME Int. J.*, vol. 46, no. 4, pp. 1198–1207, 2003.

[204] C. D. Tsai, S. Sakuma, F. Arai, and M. Kaneko, "A New Dimensionless Index for Evaluating Cell Stiffness-Based Deformability in Microchannel," *IEEE Trans. Biomed.*

Eng., vol. 61, no. 4, pp. 1187–1195, 2014.

[205] A. Z. Zinchenko and R. H. Davis, “Squeezing of a periodic emulsion through a cubic lattice of spheres,” *Phys. Fluids*, vol. 20, no. 4, p. 040803, 2008.

[206] S. Ansari, A. I. Rashid, O. Chatterjee, P. R. Waghmare, Y. Ma, and D. Nobes, “Visualization of the viscous effects of non - Newtonian fluids flowing in mini - channels,” *10th Pacific Symp. Flow Vis. Image Process. Naples*, pp. 15–18, 2015.

[207] S. Ansari, M. A. I. Rashid, P. R. Waghmare, and D. S. Nobes, “Measurement of the flow behavior index of Newtonian and shear-thinning fluids via analysis of the flow velocity characteristics in a mini-channel,” *SN Appl. Sci.*, 2020.

[208] S. Ansari, “Newtonian and non-Newtonian flows through mini-channels and micro-scale orifices for SAGD applications,” MSc thesis, University of Alberta, 2016.

[209] S. N. Sahasrabudhe, V. Rodriguez-Martinez, M. O’Meara, and B. E. Farkas, “Density, viscosity, and surface tension of five vegetable oils at elevated temperatures: Measurement and modeling,” *Int. J. Food Prop.*, vol. 20, no. 2, pp. 1965–1981, 2017.

[210] F. Leal-Calderon, F. Thivilliers, and V. Schmitt, “Structured emulsions,” *Curr. Opin. Colloid Interface Sci.*, vol. 12, no. 4–5, pp. 206–212, 2007.

[211] D. Vasiljevic, J. Parojcic, M. Primorac, and G. Vuleta, “An investigation into the characteristics and drug release properties of multiple W/O/W emulsion systems containing low concentration of lipophilic polymeric emulsifier,” *Int. J. Pharm.*, vol. 309, no. 1–2, pp. 171–177, 2006.

[212] A. Soottitantawat, F. Bigeard, H. Yoshii, T. Furuta, M. Ohkawara, and P. Linko, “Influence of emulsion and powder size on the stability of encapsulated D-limonene by spray drying,” *Innov. Food Sci. Emerg. Technol.*, vol. 6, no. 1, pp. 107–114, 2005.

[213] C. J. McDonald, K. J. Bouck, A. B. Chaput, and C. J. Stevens, "Emulsion polymerization of voided particles by encapsulation of a nonsolvent," *Macromolecules*, vol. 33, no. 5, pp. 1593–1605, 2000.

[214] O. Vetter and V. Kandarpa, "Prediction of CaCO3 scale under downhole conditions," *SPE Oilf. Geotherm. Chem.*, 1980.

[215] T. Cheung, M. Scheck, and S. C. Limited, "Novel scale remediation for steam assisted gravity drainage (SAGD) operations," *SPE Int.*, pp. 1–10, 2013.

[216] A. Kantzas, J. Bryan, and S. Taher, "Measurement of permeability," in *Fundamentals of fluid flow in porous media*, Special Core Analysis & EOR Laboratory, PERM Inc., 2016.

[217] A. Baldygin, D. S. Nobes, and S. K. Mitra, "New laboratory core flooding experimental system," *Ind. Eng. Chem. Res.*, vol. 53, no. 34, pp. 13497–13505, 2014.

[218] A. Baldygin, D. S. Nobes, and S. K. Mitra, "Water-alternate-emulsion (WAE): A new technique for enhanced oil recovery," *J. Pet. Sci. Eng.*, vol. 121, pp. 167–173, 2014.

[219] W. Barthlott and C. Neinhuis, "Purity of the sacred lotus, or escape from contamination in biological surfaces," *Planta*, vol. 202, no. 1, pp. 1–8, 1997.

[220] S. B. G. O'Brien and B. H. A. A. Van Den Brule, "A mathematical model for the cleansing of silicon substrates by fluid immersion," *J. Colloid Interface Sci.*, vol. 144, no. 1, pp. 210–221, 1991.

[221] J. O. Dabiri, S. Bose, B. J. Gemmell, S. P. Colin, and J. H. Costello, "An algorithm to estimate unsteady and quasi-steady pressure fields from velocity field measurements," *J. Exp. Biol.*, vol. 217, pp. 331–336, 2014.

[222] S. Ghaemi, D. Ragni, and F. Scarano, "PIV-based pressure fluctuations in the turbulent boundary layer," *Exp. Fluids*, vol. 53, no. 6, pp. 1823–1840, 2012.

[223] D. Violato, P. Moore, and F. Scarano, “Lagrangian and Eulerian pressure field evaluation of rod-airfoil flow from time-resolved tomographic PIV,” *Exp. Fluids*, vol. 50, no. 4, pp. 1057–1070, 2011.

[224] C. Soulaine, *Direct numerical simulation in fully saturated porous media*. Stanford Edu, 2015.

[225] A. Valli, J. Hyväluoma, A. Jäsberg, A. Koponen, and J. Timonen, “Pressure drop for low Reynolds-number flows through regular and random screens,” *Transp. Porous Media*, vol. 80, no. 2, pp. 193–208, 2009.

[226] J. H. Mathews and K. D. Fink, *Numerical methods using Matlab*, 4th Editio., no. 6. Upper Saddle River, New Jersey, USA: Prentice-Hall Inc., 2004.

[227] P. L. van Gent, D. Michaelis, B. W. van Oudheusden, *et al.*, “Comparative assessment of pressure field reconstructions from particle image velocimetry measurements and Lagrangian particle tracking,” *Exp. Fluids*, vol. 58, no. 4, pp. 1–23, 2017.

[228] T. M. V Kaiser, S. Wilson, M. Oil, and L. A. Venning, “Inflow analysis and optimization of slotted liners,” no. May 2001, 2002.

[229] J. B. Segur and H. E. Oderstar, “Viscosity of glycerol and its aqueous solutions,” *Ind. Eng. Chem.*, vol. 43, no. 9, pp. 2117–2120, 1951.

[230] M. Raffel, C. E. Willert, F. Scarano, C. J. Kähler, S. T. Wereley, and J. Kompenhans, “PIV uncertainty and measurement accuracy,” in *Particle Image Velocimetry: A Practical Guide*, Cham: Springer International Publishing, 2018, pp. 203–241.

[231] B. Wieneke, “PIV uncertainty quantification from correlation statistics,” *Meas. Sci. Technol.*, no. August, 2015.

[232] S. Ansari, Y. Yusuf, R. Sabbagh, H. Soltani, L. Kinsale, and D. S. Nobes, “An imaging

derivation of the pressure field of a multi-phase flow in a porous media using μ-SPIV," in *19th International Symposium on the Application of Laser and Imaging Techniques to Fluid Mechanics ・Lisbon, July16-19, 2018*, 2018.

[233] R. de Kat and B. W. van Oudheusden, "Instantaneous planar pressure from PIV : analytic and experimental test-cases," *15th Int Symp Appl. Laser Tech. to Fluid Mech.*, no. August 2002, 2010.

[234] V. Oudheusden, D. Version, M. Science, and V. Oudheusden, "PIV-based pressure measurement," 2013.

[235] I. Azijli, A. Sciacchitano, D. Ragni, A. Palha, and R. P. Dwight, "A posteriori uncertainty quantification of PIV-based pressure data," *Exp. Fluids*, vol. 57, no. 5, pp. 1–15, 2016.

[236] I. Chatzis, N. R. Morrow, and H. T. Lim, "Magnitude and Detailed Structure of Residual Oil Saturation.," *Soc. Pet. Eng. J.*, vol. 23, no. 2, pp. 311–326, 1983.

[237] H. Geistlinger and B. Zulfiqar, "The Impact of Wettability and Surface Roughness on Fluid Displacement and Capillary Trapping in 2-D and 3-D Porous Media: 1. Wettability-Controlled Phase Transition of Trapping Efficiency in Glass Beads Packs," *Water Resour. Res.*, vol. 56, no. 10, pp. 1–15, 2020.

[238] H. Geistlinger, I. Ataei-Dadavi, S. Mohammadian, and H. J. Vogel, "The impact of pore structure and surface roughness on capillary trapping for 2-D and 3-D porous media: Comparison with percolation theory," *Water Resour. Res.*, vol. 51, no. 11, pp. 9094–9111, 2015.

[239] P. C. Johnson, R. L. Johnson, C. L. Bruce, and A. Leeson, "Advances in in situ air sparging/biosparging," *Bioremediat. J.*, vol. 5, no. 4, pp. 251–266, 2001.

[240] S. Mohammadian, H. Geistlinger, and H.-J. Vogel, "Quantification of Gas-Phase Trapping

within the Capillary Fringe Using Computed Microtomography," *Vadose Zo. J.*, vol. 14, no. 5, p. vzj2014.06.0063, 2015.

[241] C. Xie, "Geometric criteria for the snap-off of a nonwetting droplet in pore-throat channels with rectangular cross-sections Geometric criteria for the snap-off of a nonwetting droplet in pore-throat channels with rectangular cross-sections Key Points :," no. December, 2020.

[242] A. Zou, "Effects of grain-size distribution and hysteresis on soil-water characteristic curve (SWCC)," 2018.

[243] H. Chen, M. Yang, K. Chen, and C. Zhang, "Relative Permeability of Porous Media with Nonuniform Pores," *Geofluids*, vol. 2020, 2020.

[244] I. L. Molnar, J. I. Gerhard, C. S. Willson, and D. M. O'Carroll, "Wettability Effects on Primary Drainage Mechanisms and NAPL Distribution: A Pore-Scale Study," *Water Resour. Res.*, vol. 56, no. 1, pp. 1–18, 2020.

[245] A. Mehmani, S. Kelly, C. Torres-Verdín, and M. Balhoff, "Capillary Trapping Following Imbibition in Porous Media: Microfluidic Quantification of the Impact of Pore-Scale Surface Roughness," *Water Resour. Res.*, vol. 55, no. 11, pp. 9905–9925, 2019.

[246] Z. Qiao, Z. Wang, C. Zhang, S. Yuan, Y. Zhu, and J. Wang, "PVAm–PIP/PS composite membrane with high performance for CO_2/N_2 separation," *AIChE J.*, vol. 59, no. 4, pp. 215–228, 2012.

[247] H. Jiang, B. Guo, and M. L. Brusseau, "Characterization of the micro-scale surface roughness effect on immiscible fluids and interfacial areas in porous media using the measurements of interfacial partitioning tracer tests," *Adv. Water Resour.*, vol. 146, no. January, p. 103789, 2020.

[248] M. Khishvand, M. Akbarabadi, and M. Piri, "Micro-scale experimental investigation of the

effect of flow rate on trapping in sandstone and carbonate rock samples," *Adv. Water Resour.*, vol. 94, pp. 379–399, 2016.

[249] R. Askari, S. Taheri, and S. H. Hejazi, "Thermal conductivity of granular porous media: A pore scale modeling approach," *AIP Adv.*, vol. 5, no. 9, 2015.

[250] Y. Cha, S. S. Park, K. Kim, M. Byeon, and C. A. Stow, "Water Resources Research," pp. 5375–5377, 2014.

[251] S. Ansari, R. Sabbagh, Y. Yusuf, and D. S. Nobes, "The role of emulsions in steam-assisted-gravity-drainage (SAGD) oil-production process: a review," *SPE J.*, no. August, pp. 1–21, 2019.

[252] D. Wildenschild and A. P. Sheppard, "X-ray imaging and analysis techniques for quantifying pore-scale structure and processes in subsurface porous medium systems," *Adv. Water Resour.*, vol. 51, pp. 217–246, 2013.

[253] A. Anbari, H. T. Chien, S. S. Datta, W. Deng, D. A. Weitz, and J. Fan, "Microfluidic Model Porous Media: Fabrication and Applications," *Small*, vol. 14, no. 18, pp. 1–15, 2018.

[254] Y. Tanino, A. Ibekwe, and D. Pokrajac, "Impact of grain roughness on residual nonwetting phase cluster size distribution in packed columns of uniform spheres," *Phys. Rev. E*, vol. 102, no. 1, p. 13109, 2020.

[255] R. Hu, T. Lan, G. J. Wei, and Y. F. Chen, "Phase diagram of quasi-static immiscible displacement in disordered porous media," *J. Fluid Mech.*, vol. 875, no. November, pp. 448–475, 2019.

[256] W. Y. Fowlkes and K. S. Robinson, *Particles on Surfaces 3*. 1989.

[257] S. Ansari and D. S. Nobes, "The effect of phase pinning on the passage of an isolated bubble passing through a confining pore," *Submitt. to Phys. Fluids*, 2021.

[258] S. Ansari, Y. Yusuf, R. Sabbagh, and david, “Determining the pressure distribution of a multi-phase flow through a pore space using velocity measurement and shape analysis,” *Meas. Sci. Technol.*, vol. 30, no. 5, 2019.

[259] S. Ansari and D. S. Nobes, “Effect of the pore geometry on pressure distribution within a bubble penetrating a single pore,” 2019.

[260] B. W. H. Goodman, M. R. Godfrey, and T. M. Miller, “Scale and deposit formation in steam assisted gravity drainage (SAGD) facilities,” in *International Water Conference in San Antonio, Texas, USA*, 2010.

[261] G. Bernard and L. . Holm, “Effect of foam on permeabily of porous media to gas,” *Soc. Pet. Eng. J.*, vol. SPE-983, pp. 267–274, 1964.

[262] J. Berthier, V. Tran, S. Schoumacker, F. Mittler, G. Marchand, and N. Sarrut, “On the pinning of interfaces on micropillar edges,” *J. Colloid Interface Sci.*, vol. 338, no. 1, pp. 296–303, 2009.

Appendix

A-1: MATLAB code for curvature calculation using the pore geometry

The presented code was used to evaluate the radius of the curvature of the leading and trailing edge of the bubble using its relative location with the pore throat. The details of the process can be found in section 3.4.1.

```
%%%%%%%%%%%%%%%%%%%%%%%%%%%%%%%%%%%%%%%%%%%%%%%%%%%%%%%%%%%%%%%%%
% DropletAnalysis.m
%
% Who    : Shadi Ansari
% When  : Jan2019
% Aim   : Load a Tiff file, analyze the droplets, filled the empty
regionst6gy7
% in the droplet finds the center of mass, radius, and the plots the
% equivalent circle.
%%%%%%%%%%%%%%%%%%%%%%%%%%%%%%%%%%%%%%%%%%%%%%%%%%%%%%%%%%%%%%%%%

close all; %closing all figures
clc; %clearing the command area
clear all

pixel_to_mm=50;%Physical scale conversion factor
% generating matrixes to store the data
R_trailing_save=zeros(1,2);
R_leading_save=zeros(1,2);
equvilantdiameter_save=zeros(1,2);
X_centroid_save=zeros(1,2);
Y_centroid_save=zeros(1,2);
X_Leading_save=zeros(1,2);
Y_Leading_save=zeros(1,2);
X_Trailing_save=zeros(1,2);
Y_Trailing_save=zeros(1,2);
NUmbertosave=1;
%%%%%%%%%%%%%%%%%%%%%%%%%%%%%%%%%%%%%%%%%%
%%%finding the location of pore throat %%%
%%%%%%%%%%%%%%%%%%%%%%%%%%%%%%%%%%%%%%%%%%
% Importing one of the images
Sample= imread(sprintf('Round pore_1mm_0pmlpermin_149frate_skiped5
images_Glycerol_#0062_3rd.tif'));
figure,imshow(Sample);
%selecting the  leading and trailing location of the pore
[xLeading_pore,yLeading_pore] = getpts;
[xTrailing_pore,yTrailing_pore] = getpts;
%calcaulating the location of the pore throat
ypore=yLeading_pore+(yTrailing_pore-yLeading_pore)/2;
for framenumbers =62:573 % defining the range of the number of images
close all;
```

```
%% %%%%%%%%%%%%%%%%%%%%%%%%%%%%%%%%%%%
%%%%%%%%%% importing Data %%%%%%%%%%%%
%%%%%%%%%%%%%%%%%%%%%%%%%%%%%%%%%%%%%%
filename=sprintf('Round pore_1mm_0pmlpermin_149frate_skiped5 
images_Glycerol_#%04i_3rd.tif',framenumbers);
I= imread(filename);

%%%%%%%%%%%%%%%%%%%%%%%%%%%%%%%%%%%%%
%%%%% Plotting the original image %%%
%%%%%%%%%%%%%%%%%%%%%%%%%%%%%%%%%%%%%
figure(1), set(gcf,'color','w');
sz_x = 400; sz_y = 400; % size of the figure
y_pos = 600; x_pos =1;  % position on the screen
set(1,'pos', [x_pos, y_pos, sz_x, sz_y]);
axes('position',[.1  .15  .8  .8]) % size of the plot in the figure
title('Original image')
figure (1)
hold on
imshow(I, []); %showing the raw image
axis on

%% %%%%%%%%%%%%%%%%%%%%%%%%%%%%%%%%%
%%%%% Binarization of the image %%%%
%%%%%%%%%%%%%%%%%%%%%%%%%%%%%%%%%%%%
numberOfcolum = size(I, 1);% calculating the size of the raw image
numberOfrows = size(I, 2);% calculating the size of the raw image
J=zeros(numberOfcolum,numberOfrows);

for i=1:numberOfcolum
    for j=1:numberOfrows
        if I(i,j) < 37
%%%%%%%%%%%%%Masking the lower intensity%%%%%%%%%%
            J(i,j)=1;
        else
            J(i,j)=0;
        end
      j=j+1;
    end
    i=i+1;
end
%figure,imshow(J); %shwoing the black and white image

%%%%%%%%%%%%%%%%%%      Fill Interior Gaps     %%%%%%%%%%%%%%%%%%%%%%
BWdfill = imfill(J, 'holes');
%figure, imshow(BWdfill);
title('binary image with filled holes');
BWnobord = BWdfill;
%%
BWnobord = bwareaopen(BWnobord,3000);
```

```
%%%%%%%%%%%%%Masking the smaller particles%%%%%%%%%%
%figure, imshow(BWnobord), title('cleared border image');
%%%%%%%%%%%%%%%%%%  Smoothen the Object   %%%%%%%%%%%%%%%%%%%%%%
% seD = strel('sphere',1);
% BWfinal = imerode(BWnobord,seD);
% BWfinal = imerode(BWfinal,seD);
%  figure, imshow(BWfinal), title('segmented image');

%%%%%%%%%%%%%%%%%%      outlined original image %%%%%%%%%%%%%%%%%%%%%
 BWoutline = bwperim(BWnobord);
Segout = BWnobord;
Segout(BWoutline) = 255;

figure, fig_outlined=imshow(Segout);

%% %%%%%%%%%%%%%%%%%%%%%%%%%%%%%%%%%%%%%%%%
%%%%%   Saving the fig_outlined plot %%%%%%
%%%%%%%%%%%%%%%%%%%%%%%%%%%%%%%%%%%%%%%%%%%
%%%%%%%%%%Location of the folder
fname = 'W:\Shadi Ansari\Tod _bubble
experiments\16_Jan\0p2mlpermin_20Micron
partilces_Glyecerol_149fps\Small\Round pore_Small-
1mm_0p2mlpermin_149frate_skiped5
images_Glycerol_4th\Preprocessed\Processed_image';
%%%%%%%%%%name of the file
%saveas(fig_outlined,fullfile(fname,sprintf('outlined_%04i.tiff',frame
numbers)),'tiff');
%%%%%%%%%%%%%%%% showing the center of the droplets%%%%%%%%%%
s  = regionprops(Segout, 'centroid');
centroids = cat(1, s.Centroid);

figure, fig_projected_area=imshow(Segout), %title('Center of mass and
equivalent radius ');
hold on
plot(centroids(:,1), centroids(:,2), 'r*')

%%%%%%%%%%%%%%%% plotting the circles around the droplets%%%%%%%%%%
stats = regionprops('table',BWnobord,'Centroid',...
    'MajorAxisLength','MinorAxisLength')
centers = stats.Centroid;
    diameters = mean([stats.MajorAxisLength stats.MinorAxisLength],2);
        radii = diameters/2;
        % Plot the circles
        hold on
        viscircles(centers,radii);
        hold off
   strmin = ['{\itR} = ',num2str(radii/pixel_to_mm,3),' mm'];
text(centroids(:,1)+radii+200,
centroids(:,2),strmin,'HorizontalAlignment','center','Color','red',
'FontSize',14);
axis on
```

```
%%%%%%%%%%%%%%%%%%%%%%%%%%%%%%%%%%%%%%%%%%%%%%%%%%%%%%%%
%%%%%%%%%%%%%Saving the projected area plot%%%%%%%%%%%%%
%%%%%%%%%%%%%%%%%%%%%%%%%%%%%%%%%%%%%%%%%%%%%%%%%%%%%%%%

%%%%%%%%%%Location of the folder
fname = 'W:\Shadi Ansari\Tod _bubble
experiments\16_Jan\0p2mlpermin_20Micron
partilces_Glyecerol_149fps\Small\Round pore_Small-
1mm_0p2mlpermin_149frate_skiped5
images_Glycerol_4th\Preprocessed\eq.Diameter';
%%%%%%%%%%name of the file
%saveas(fig_projected_area,fullfile(fname,sprintf('projected_area_%04i
.tiff',framenumbers)),'tiff');


%%%%%%%%%%%%%%%%%%%%%%%%%%%%%%%
%%%%%%%%%%%%%%%%%%%%%%%%%%%%%Original pic+the eq. diameter

figure, fig_projected_area_original=imshow(I),
%title('Center of mass and equivalent radius ');
hold on
plot(centroids(:,1), centroids(:,2), 'r*')


%%%%%%%%%%%%%%%% plotting the circles around the droplets%%%%%%%%%%
stats = regionprops('table',BWnobord,'Centroid',...
    'MajorAxisLength','MinorAxisLength')
centers = stats.Centroid;
        diameters = mean([stats.MajorAxisLength
stats.MinorAxisLength],2);
        radii = diameters/2;
        % Plot the circles
        hold on
        viscircles(centers,radii);
        hold off
strmin = ['{\itR} = ',num2str(radii/pixel_to_mm,3),' mm'];
text(centroids(:,1)+radii+200,
centroids(:,2),strmin,'HorizontalAlignment','center','Color','red','Fo
ntSize',14);
axis on

%%%%%%%%%%%%%%%%%%%%%%%%%%%%%%%%%%%%%%%%%%%%%%%%%%%%%%%%%%%%
%%%%%%%%%%%%% Saving the projected area plot %%%%%%%%%%%%%%%
%%%%%%%%%%%%%%%%%%%%%%%%%%%%%%%%%%%%%%%%%%%%%%%%%%%%%%%%%%%%
%%%%%%%%%%Location of the folder
fname = 'W:\Shadi Ansari\Tod _bubble
experiments\16_Jan\0p2mlpermin_20Micron
partilces_Glyecerol_149fps\Small\Round pore_Small-
1mm_0p2mlpermin_149frate_skiped5
images_Glycerol_4th\Preprocessed\eq.Diameter_original';
%saveas(fig_projected_area_original,fullfile(fname,sprintf('projected_
area_original_%04i.tiff',framenumbers)),'tiff');%%%%%%%%%%%%%%%%%%%%%
```

```
equvilantdiameter_save(1,NUmbertosave)=radii;
X_centroid_save(1,NUmbertosave)=centroids(:,1);
Y_centroid_save(1,NUmbertosave)=centroids(:,2);
%%%%%%%%%%%%%%%%%%%%%%%%% Ploting the contour of the edge
%%%%%%%%%%%%%%%%%%%%%%%
%    figure; imcontour(BWnobord,3), title('Countour of the outer part
');
if stats.MajorAxisLength/stats.MinorAxisLength>1.02
||stats.MinorAxisLength/stats.MajorAxisLength>1.02

%%%%%%%%%%%%%%%%%%% Cropping the images into two sections%%%%%%%%%%%%
distance=radii/2;
%%%%%%%%%%%%%%%%%%%%%%%%%%%%%%%%%%%%%%%%%%%%%%%%%%%%%%%%%%%%%%%%%%%%%%

YCenterOfMass=round(centroids(1,2));
TrailingCrop = BWnobord(YCenterOfMass:numberOfcolum, 1:numberOfrows);
Leadingcrop = BWnobord(1:YCenterOfMass, 1:numberOfrows);
%figure, imshow(TrailingCrop), title('Cropped image (Trailing part)');
%figure, imshow(Leadingcrop), title('Cropped image (Leading part)');
xcenter=round(centroids(:,1))
%%%%%%%%%%%%%%%Conditions for the Leading part
L=find(Leadingcrop(:,xcenter)==1, 1, 'first')
sizeofLeadingpart=size(Leadingcrop)
yoftehLeading=sizeofLeadingpart(1,1)

%%%%%%%%Leading part of bubble in the pore

%%%%%%%%%%%%%%%%%%%%%%%%%%%%%%%%%%%%%%%%%%%%%%%%%%%%%%%%%%%%%%%%%%%%
%%%%%%%% Defining the condition for cropping the image Leading%%%%%%
%%%%%%%%%%%%%%%%%%%%%%%%%%%%%%%%%%%%%%%%%%%%%%%%%%%%%%%%%%%%%%%%%%%%

if (L<ypore)&&YCenterOfMass>ypore % if the bubble is located
     YCenterOfMass_2=ypore;
else
     YCenterOfMass_2=YCenterOfMass;
end
Longest_width_Leading=zeros(1,1)
for number=L:YCenterOfMass_2
Longest_width_Leading(number)=find(Leadingcrop(number,:)==1, 1,
'first')-find(Leadingcrop(number,:)==1, 1, 'Last');
end
max_lenght_Leading=max(abs(Longest_width_Leading));
location_max_width=find(abs(Longest_width_Leading)==max_lenght_Leadin)

if (ypore<(L))&&((L)<yTrailing_pore)||((L)<
ypore)&&(yLeading_pore<(L))&&(max(location_max_width)>L)
      Ynewcut_Leading= round(L+(yoftehLeading-L)/4)
elseif location_max_width>L

%% if the Leading edge is before the pore throat
%if the bubble has a maximum width different from the cutting part
```

```
Ynewcut_Leading=location_max_width
 else
     Ynewcut_Leading=YCenterOfMass
  end
Leadingcrop = BWnobord(1:Ynewcut_Leading, 1:numberOfrows);

%%%%%%%%%%%%%%%%%%%%%%%%%%%%%%%%%%%%%%%%%%%%%%%%%%%%%%%%%%%%%%%%%
%%%%%%%%calcualting the maximum width of the Trailing part %%%%%%
%%%%%%%%%%%%%%%%%%%%%%%%%%%%%%%%%%%%%%%%%%%%%%%%%%%%%%%%%%%%%%%%%

End_of_Bubble=find(TrailingCrop(:,xcenter)==1, 1, 'last')
sizeofLeadingpart=size(TrailingCrop)
yoftehTrailing=sizeofLeadingpart(1,1)
n=End_of_Bubble+YCenterOfMass
%%%%%%%%%%%%%%%%%%%%%%%%%%%%%%%%%%%%%%%%%%%%%%%%%%%%%%%%%%%%%%%%%%
%%%%%%%%%%%%%generating a matrix of the maximum widths%%%%%%%%%%%%
%%%%%%%%%%%%%%%%%%%%%%%%%%%%%%%%%%%%%%%%%%%%%%%%%%%%%%%%%%%%%%%%%%

if (End_of_Bubble+YCenterOfMass>ypore)&&YCenterOfMass<ypore
     YCenterOfMass_2=ypore;
else
     YCenterOfMass_2=YCenterOfMass;
end

Longest_width_Trailing=zeros(1,1)
for number=floor(YCenterOfMass_2-YCenterOfMass+1):End_of_Bubble
Longest_width_Trailing(number)=find(TrailingCrop(number,:)==1, 1,
'first')-find(TrailingCrop(number,:)==1, 1, 'Last');
end
max_lenght_Trailing=max(abs(Longest_width_Trailing));%%%calcualting
the maximum width
location_max_width_Trailing=max(find(abs(Longest_width_Trailing)==max_
lenght_Trailing))
%%calculating the location of maximum width in the Trailing crop

%%%%%%%%%%%%%%%%%%%%%%%%%%%%%%%%%%%%%%%%%%%%%%%%%%%%%%%%%%%%%%%%%
%%%%% Defining the condition for cropping the images Trailing%%%%
%%%%%%%%%%%%%%%%%%%%%%%%%%%%%%%%%%%%%%%%%%%%%%%%%%%%%%%%%%%%%%%%%
   if
(yLeading_pore<n)&&(n<ypore)||(n<yTrailing_pore)&&(ypore<n)&&location_
max_width_Trailing<End_of_Bubble  %% if the trailing edge is after
pore throat
      Ynewcut_Trailing= round(3*End_of_Bubble/4)+YCenterOfMass
   elseif location_max_width_Trailing<End_of_Bubble
%%%%%%if the bubble has maximum width different from the cutting part
Ynewcut_Trailing=location_max_width_Trailing+YCenterOfMass
   else
     Ynewcut_Trailing=YCenterOfMass
   end
```

```
%%%%%%%%%%%%%%%%%%%%%%%%%%%%%%%%%%%%%%%%%%%%%%%%%%%%%%%%%%%%%%%%
%%%%%%%%%Plotting the cropped images%%%%%%%%%%%%%%%%%%%%%%%%%%%
%%%%%%%%%%%%%%%%%%%%%%%%%%%%%%%%%%%%%%%%%%%%%%%%%%%%%%%%%%%%%%%%
TrailingCrop_second = BWnobord(Ynewcut_Trailing:numberOfcolum,
1:numberOfrows);
Leadingcrop_second = BWnobord(1:Ynewcut_Leading, 1:numberOfrows);
figure, imshow(TrailingCrop_second), title('Cropped image (Trailing
part)_02');
figure, imshow(Leadingcrop_second), title('Cropped image (Leading
part)_02');

%%%%%%%%%%%%%%%%%%%%%%%%%%%%%%%%%%%%%%%%%%%%%%%%%%%%%%%%%%%%%%%%%
%%%%calculating the maximum width of the Leading part after crop
%%%%%%%%%%%%%%%%%%%%%%%%%%%%%%%%%%%%%%%%%%%%%%%%%%%%%%%%%%%%%%%%%

Longest_width_Leading=zeros(1,1)k

for number=L:Ynewcut_Leading
Longest_width_Leading(number)=find(Leadingcrop(number,:)==1, 1,
'first')-find(Leadingcrop(number,:)==1, 1, 'Last');
end
max_lenght_Leading=max(abs(Longest_width_Leading));
%%%calcualting the maximum width
location_max_width=find(abs(Longest_width_Leading)==max_lenght_Leading)
%%calculating the location of maximum width in the Leading crop

%%%%%%%%%%%%%%%%%%%%%%%%%%%%%%%%%%%%%%%%%%%%%%%%%%%%%%%%%%%%%%%%%%%
%%calculating the maximum width of the Trailing part after crop%%%%
%%%%%%%%%%%%%%%%%%%%%%%%%%%%%%%%%%%%%%%%%%%%%%%%%%%%%%%%%%%%%%%%%%%

Longest_width_Trailing=zeros(1,1)
for number=1:End_of_Bubble-(Ynewcut_Trailing-YCenterOfMass)
Longest_width_Trailing(number)=find(TrailingCrop_second(number,:)==1,
1, 'first')-find(TrailingCrop_second(number,:)==1, 1, 'Last');
end
max_lenght_Trailing=max(abs(Longest_width_Trailing));
%%%calcualting the maximum width
location_max_width_Trailing=find(abs(Longest_width_Trailing)==max_leng
ht_Trailing)
%%calculating the location of maximum width in the trailing crop


%%%%%%%%%%%%%%%%%%%%%%%%%%%%%%%%%%%%%%%%%%%%%%%%%%%%%%%%%%%%%%%%%
%%%%calculating the radius of the leading edge%%%%%%%%%%%%%%%%%
%%%%%%%%%%%%%%%%%%%%%%%%%%%%%%%%%%%%%%%%%%%%%%%%%%%%%%%%%%%%%%%%%

H_Leading=max(location_max_width)-L;
width_Leading=max_lenght_Leading;
R_Leading=((H_Leading/2)+((width_Leading^2)/(8*H_Leading)))
```

```
%%%%%%%%%%%%%%%%%%%%%%%%%%%%%%%%%%%%%%%%%%%%%%%%%%%%%%%%%%%%%%%%%
%%%%calculating the radius of the Trailing edge%%%%%%%%%%%%%%%%%%
%%%%%%%%%%%%%%%%%%%%%%%%%%%%%%%%%%%%%%%%%%%%%%%%%%%%%%%%%%%%%%%%%
H_Trailing=End_of_Bubble-(Ynewcut_Trailing-YCenterOfMass);
width_Trailing=max_lenght_Trailing;
R_Trailing=((H_Trailing/2)+((width_Trailing^2)/(8*H_Trailing)))
%%%%%%%%%%%%%%%%%%%%%%%%%%%%%%%%%%%%%%%%%%%%%%%%%%%%%%%%%%%%%%%%%
%%%%%%%%%%Plotting the bubble with the radius of curvature%%%%%%
%%%%%%%%%%%%%%%%%%%%%%%%%%%%%%%%%%%%%%%%%%%%%%%%%%%%%%%%%%%%%%%%%
figure,fig_final=imshow(BWnobord);
hold on
%%%%%%%%%%%%%%%%%%%%%%%%%%%%%%%%%%%%%%%%%%%%%%%%%%%%%%%%%%%%%%%%%
%%%%Plotting the radius of the leading edge%%%%%%%%%%%%%%%%%%%%%
%%%%%%%%%%%%%%%%%%%%%%%%%%%%%%%%%%%%%%%%%%%%%%%%%%%%%%%%%%%%%%%%%
xCenter= centroids(1,1); %%% x-center of the leading curvature
yCenterpoint= centroids(1,2);
yCenter_Leading =L+R_Leading;%%% y-center of the leading curvature
theta = 0 : 0.01 : 2*pi;
radius =  R_Leading;
xR_TOP= radius * cos(theta) + xCenter;
%%% x locations of the leading curvature
yR_TOP = radius * sin(theta) + yCenter_Leading;
%%% y locations of the leading curvature

%%%%%%%%%%%%Saving the data

R_leading_save(1,NUmbertosave)=R_Leading;
X_Leading_save(1,NUmbertosave)=centroids(1,1);
Y_Leading_save(1,NUmbertosave)=L;
plot(xR_TOP, yR_TOP,'g','LineWidth',2);
sizeofR_TOP = ['{\itR_L} = ',num2str(radius/pixel_to_mm,3),' mm'];
%%%% value of the leading edge
hold on
axis on
plot(xCenter,yCenter_Leading,'g*')
%%%%%Plotting the center of fitted circle for leading
hold on

%%%%%%%%%%%%%%%%%%%%%%%%%%%%%%%%%%%%%%%%%%%%%%%%%%%%%%%%%%%%%%%%%
%%%%Plotting the radius of the Trailing edge%%%%%%%%%%%%%%%%%%%%
%%%%%%%%%%%%%%%%%%%%%%%%%%%%%%%%%%%%%%%%%%%%%%%%%%%%%%%%%%%%%%%%%

yCenter_Trailing =End_of_Bubble-R_Trailing+YCenterOfMass;
%%% y-center of the Trailing curvature
theta = 0 : 0.01 : 2*pi;
radius2 =  R_Trailing;
sizeofR_Botttom = ['{\it R_T} = ',num2str(radius2/pixel_to_mm,3),'
mm'];
xR_Trailing= radius2 * cos(theta) + xCenter;
%%% x locations of the Trailing curvature
yR2_Trailing= radius2 * sin(theta) + yCenter_Trailing;
%%% y locations of the Trailing curvature
```

```
plot(xR_Trailing, yR2_Trailing,'r','LineWidth',2);
%%%%%%%%%%%%Saving the data
R_trailing_save(1,NUmbertosave)=R_Trailing;
X_Trailing_save(1,NUmbertosave)=centroids(1,1);
Y_Trailing_save(1,NUmbertosave)=End_of_Bubble+YCenterOfMass;

hold on
axis on
plot(xCenter,yCenter_Trailing,'r*')
%%%%%Ploting the center of the fitted circle for Trailing
hold on
%%%%%%%%%%%%%%%%%%%%%%%%%%%%%%%%%%%%%%%%%%%%%%%%%%%%%%%%%%%%%%%%%
%%%%%%%%%%%%%%%% writing the Radius of the Leading and Trailing%%
%%%%%%%%%%%%%%%%%%%%%%%%%%%%%%%%%%%%%%%%%%%%%%%%%%%%%%%%%%%%%%%%%
text(xCenter,
yCenter_Trailing+radius2+50,sizeofR_Botttom,'HorizontalAlignment','cen
ter','Color','red','FontSize',14);
hold on
text(xCenter, yCenter_Leading-radius-
50,sizeofR_TOP,'HorizontalAlignment','center','Color','green','FontSiz
e',14);
%%%%%%%%%%%%%%%%%%%%%%%%%%%%%%%%%%%%%%%%%%%%%%%%%%%%%%%%%%%%%%%%%%%%
%%%%%%%%%Plotting the original bubble with the radius of curvature%%
%%%%%%%%%%%%%%%%%%%%%%%%%%%%%%%%%%%%%%%%%%%%%%%%%%%%%%%%%%%%%%%%%%%%
figure,fig_Original_final= figure,imshow(I);
hold on
%%%%%%%%%%%%%%%%%%%%%%%%%%%%%%%%%%%%%%%%%%%%%%%%%%%%%%%%%%%%%%%%%
%%%%Plotting the radius of the leading edge%%%%%%%%%%%%%%%%%%%%%%
%%%%%%%%%%%%%%%%%%%%%%%%%%%%%%%%%%%%%%%%%%%%%%%%%%%%%%%%%%%%%%%%%
xCenter= centroids(1,1); %%% x-center of the leading curvature
yCenterpoint= centroids(1,2);
yCenter_Leading =L+R_Leading;%%% y-center of the leading curvature
theta = 0 : 0.01 : 2*pi;
radius =  R_Leading;
xR_TOP= radius * cos(theta) + xCenter;
%%% x locations of the leading curvature
yR_TOP = radius * sin(theta) + yCenter_Leading;
%%% y locations of the leading curvature
%%%%%%%%%%%%Saving the data
R_leading_save(1,NUmbertosave)=R_Leading;
X_Leading_save(1,NUmbertosave)=centroids(1,1);
Y_Leading_save(1,NUmbertosave)=L;
plot(xR_TOP, yR_TOP,'g','LineWidth',2);
sizeofR_TOP = ['{\itR_L} = ',num2str(radius/pixel_to_mm,3),' mm'];
%%%% value of the leading edge
hold on
axis on
plot(xCenter,yCenter_Leading,'g*')
%%%%%Plotting the center of fitted circle for leading
hold on
```

```
%%%%%%%%%%%%%%%%%%%%%%%%%%%%%%%%%%%%%%%%%%%%%%%%%%%%%%%%%%%%%%%%%
%%%%Plotting the radius of the Trailing edge%%%%%%%%%%%%%%%%%%%%%
%%%%%%%%%%%%%%%%%%%%%%%%%%%%%%%%%%%%%%%%%%%%%%%%%%%%%%%%%%%%%%%%%

yCenter_Trailing =End_of_Bubble-R_Trailing+YCenterOfMass;
%%% y-center of the Trailing curvature
theta = 0 : 0.01 : 2*pi;
radius2 =  R_Trailing;
sizeofR_Botttom = ['{\it R_T} = ',num2str(radius2/pixel_to_mm,3),'
mm'];
xR_Trailing= radius2 * cos(theta) + xCenter;
%%% x locations of the Trailing curvature
yR2_Trailing= radius2 * sin(theta) + yCenter_Trailing;
%%% y locations of the Trailing curvature
plot(xR_Trailing, yR2_Trailing,'r','LineWidth',2);
%%%%%%%%%%%%Saving the data
R_trailing_save(1,NUmbertosave)=R_Trailing;
X_Trailing_save(1,NUmbertosave)=centroids(1,1);
Y_Trailing_save(1,NUmbertosave)=End_of_Bubble+YCenterOfMass;

hold on
axis on

plot(xCenter,yCenter_Trailing,'r*')
%%%%%Plotting the center of the fitted circle for Trailing
hold on

%%%%%%%%%%%%%%%%%%%%%%%%%%%%%%%%%%%%%%%%%%%%%%%%%%%%%%%%%%%%%%%%%%%%%
%%%%%%%%%%%%%%%% writing the Radius of the Leading and Trailing%%%%%%
%%%%%%%%%%%%%%%%%%%%%%%%%%%%%%%%%%%%%%%%%%%%%%%%%%%%%%%%%%%%%%%%%%%%%

text(xCenter,
yCenter_Trailing+radius2+50,sizeofR_Botttom,'HorizontalAlignment','cen
ter','Color','red','FontSize',14);
hold on
text(xCenter, yCenter_Leading-radius-
50,sizeofR_TOP,'HorizontalAlignment','center','Color','green','FontSiz
e',14);
%%%%%%%%%%%%%%%%%%%%%%%%%%%%%%%%%%%%%%%%%%%%%%%%%%%%%%%%%%
%%%%%%%%%%%%%%%%%%%%%%%Saving the curvature plot%%%%%%%%%%
%%%%%%%%%%%%%%%%%%%%%%%%%%%%%%%%%%%%%%%%%%%%%%%%%%%%%%%%%%
%%%%%%%%%%Location of the folder
fname = 'W:\Shadi Ansari\Tod _bubble
experiments\16_Jan\0p2mlpermin_20Micron
partilces_Glyecerol_149fps\Small\Round pore_Small-
1mm_0p2mlpermin_149frate_skiped5
images_Glycerol_4th\Preprocessed\radius of curvature-Original';
%%%%%%%%%%name of the file
%saveas(fig_Original_final,fullfile(fname,sprintf('curvature_original_
%04i.tiff',framenumbers)),'tiff');
else
```

```
fname = 'W:\Shadi Ansari\Tod _bubble
experiments\16_Jan\0p2mlpermin_20Micron
partilces_Glyecerol_149fps\Small\Round pore_Small-
1mm_0p2mlpermin_149frate_skiped5
images_Glycerol_4th\Preprocessed\radius of curvature';
%%%%%%%%%name of the file
%saveas(fig_projected_area,fullfile(fname,sprintf('curvature_%04i.tiff
%',framenumbers)),'tiff');
fname = 'W:\Shadi Ansari\Tod _bubble
experiments\16_Jan\0p2mlpermin_20Micron
partilces_Glyecerol_149fps\Small\Round pore_Small-
1mm_0p2mlpermin_149frate_skiped5 images_Glycerol_4th\radius of
curvature-Original';
%saveas(fig_projected_area_original,fullfile(fname,sprintf('curvature_
%original_%04i.tiff',framenumbers)),'tiff');

R_trailing_save(1,NUmbertosave)=radii;
R_leading_save(1,NUmbertosave)=radii;
X_Trailing_save(1,NUmbertosave)=centroids(1,1);
Y_Trailing_save(1,NUmbertosave)=centroids(1,2)+radii;
X_Leading_save(1,NUmbertosave)=centroids(1,1);
Y_Leading_save(1,NUmbertosave)=centroids(1,2)-radii;
end
NUmbertosave=NUmbertosave+1
end
%generating the result matrix
C =
horzcat(equvilantdiameter_save',X_centroid_save',Y_centroid_save',R_tr
ailing_save',X_Trailing_save',Y_Trailing_save',R_leading_save',X_Leadi
ng_save',Y_Leading_save');
%name of the headers in the excel file
col_header={'equvilantdiameter','X_centroid','Y_centroid','R_trailing'
,'X_Trailing','Y_Trailing','R_leading','X_Leading','Y_Leading'};
%generating the excel file
filename='Round
pore_Small_1mm_0pm1permin_149frate_skiped5images_Glycerol_3rd';
xlswrite(filename,C,'Sheet1','B2');      %Write data
xlswrite(filename,col_header,'Sheet1','B1');
```

A-2: MATLAB code for curvature calculation in Polar coordinate

The presented code was used to evaluate the radius of the curvature of the leading and trailing edge of the bubble using by tracking the change in the curvature along the bubble. The details of the process can be found in section 3.4.2.

```
%%%%%%%%%%%%%%%%%%%%%%%%%%%%%%%%%%%%%%%%%%%%%%%%%%%%%%%%%%%%%%%%%
% NOV20_2020_Curvature.m
%
% Who    : Shadi Ansari
% When   : Nov 2020
% Aim    : Analyzing bubble -radii of curvature based on the curvature
in
% polar coordinate system
%%%%%%%%%%%%%%%%%%%%%%%%%%%%%%%%%%%%%%%%%%%%%%%%%%%%%%%%%%%%%%%%%
clc
clear all
close all
set(0, 'DefaultAxesFontName', 'Times New Roman');
set(0, 'DefaultUIControlFontName', 'Times New Roman');
set(0, 'defaultUitableFontName', 'Times New Roman');
set(0, 'defaultTextFontName', 'Times New Roman');
set(0, 'defaultUipanelFontName', 'Times New Roman');
font_size = 16;
line_width_size=2;
J=zeros;
number=1;
pixelTomm=50; %Physical scale conversion factor

%% %%%%%%%%%%%%%%%%%%%%%%%%%%%%%%%%%%%
%%%%%%%%%% importing Data %%%%%%%%%%%%
%%%%%%%%%%%%%%%%%%%%%%%%%%%%%%%%%%%%%%

for framenumbers=53:576
% defining the range of the number of the images
close all
clear_all_but('number','framenumbers','xcentroid1','ycentroid1','xfit_
Leading','yfit_Leading','Rfit_Leading','xfit_trailing','yfit_trailing'
,'Rfit_trailing','Thetaleading','Thetatrailing')

%% %%%%%%%%%%%%%%%%%%%%%%%%%%%%%%%%%%%
%%%%%%%%%% importing Data %%%%%%%%%%%%
%%%%%%%%%%%%%%%%%%%%%%%%%%%%%%%%%%%%%%

I = imread(sprintf('Name of the picture.tif',framenumbers));
%Importing tif
I(:,:,3) = []; %%% removing the second and third layer of the image
I(:,:,2) = [];
```

```
%%%%%%%%%%%%%%%%%%%%%%%%%%%%%%%%%%%%%
%%%%% Plotting the original image %%%
%%%%%%%%%%%%%%%%%%%%%%%%%%%%%%%%%%%%%

figure(1), set(gcf,'color','w');
sz_x = 400; sz_y = 400; % size of the figure
y_pos = 600; x_pos =1;  % position on the screen
set(1,'pos', [x_pos, y_pos, sz_x, sz_y]);
axes('position',[.1  .15  .8  .8]) % size of the plot in the figure
title('Original image')
figure (1)
hold on
imshow(I, []); %showing the raw image
axis on

%% %%%%%%%%%%%%%%%%%%%%%%%%%%%%%%%%%
%%%%% Binarization of the image %%%%
%%%%%%%%%%%%%%%%%%%%%%%%%%%%%%%%%%%%

numberOfcolum = size(I, 1);% calculating the size of the raw image
numberOfrows = size(I, 2);% calculating the size of the raw image
J=zeros(numberOfcolum,numberOfrows);
% defining the matrix to store the Binarized image

for i=1:numberOfcolum
    for j=1:numberOfrows
        if I(i,j) < 37
%%%%%%%%%%%%%Masking the lower intensity%%%%%%%%%%
            J(i,j)=0;
        else
            J(i,j)=1;
        end
      j=j+1;
    end
    i=i+1;
end
figure,imshow(J); %showing the black and white image
J = bwareaopen(J,20000); %Remove small objects from binary image
figure,imshow(J);

%% %%%%%%%%%%%%%%%%%%%%%%%%%%%%%%%%%%%%%%%%%%%%%%%%%%%%
%%%% Detect Entire droplet and fill the hollow region %%%
%%%%%%%%%%%%%%%%%%%%%%%%%%%%%%%%%%%%%%%%%%%%%%%%%%%%%%%%%

[~, threshold] = edge(J, 'sobel'); %findig the edge of the bubble
fudgeFactor = .9;
BWs = edge(J,'sobel', threshold * fudgeFactor);
figure, imshow(BWs), title('binary gradient mask');
%showing the detected bubble
```

```
%%%%%%%%%%%%%     Fill Interior Gaps     %%%%%%%%%%%%

BWdfill = imfill(BWsdil, 'holes');
figure, imshow(BWdfill);

Preprocessed_Image = imcrop(BWdfill,[778.5 10.5 783 2038]);
%Cropping the original image to remove the white border
figure, imshow(BWdfill);

%%%%%%%%%%%%%%%%%%%%%%%%%%%%%%%%%%%%%%%
%%%%%% Plotting cropped image   %%%%%%
%%%%%%%%%%%%%%%%%%%%%%%%%%%%%%%%%%%%%%%

figure(2), set(gcf,'color','w');
sz_x = 400; sz_y = 400; % size of the figure
y_pos = 600; x_pos =401;  % position on the screen
set(2,'pos', [x_pos, y_pos, sz_x, sz_y])
axes('position',[.1  .15  .8  .8])   % size of the plot in the figure
title('Pre-processed image')
figure(2)
imshow(Preprocessed_Image);
axis on

%%%%%%%%%%%%%%%%%%%%%%%%%%%%%%%%%%%%%%%%%%%%%%%%%%%%%%%%%%%%%%%%%%%%%%%%
%%% finding the centroid, leading and trailing edge of the bubble   %%
%%%%%%%%%%%%%%%%%%%%%%%%%%%%%%%%%%%%%%%%%%%%%%%%%%%%%%%%%%%%%%%%%%%%%%%%

stats = regionprops('table',Preprocessed_Image,'Centroid',...
    'MajorAxisLength','MinorAxisLength');
xcentroid=stats.Centroid(1,1);              % x of the centroid
x_centroid(number)=xcentroid;               % storing x-location
ycentroid=stats.Centroid(1,2);              % y of the centroid
y_centroid(number)=ycentroid;               % storing y-location
MinorAxisLength=stats.MinorAxisLength(1);   % length of Minor axis
MajorAxisLength=stats.MajorAxisLength(1);   % length of Minor axis


%% %%%%%%%%%%%%%%%%%%%%%%%%%%%%%%%%%%%%%%%%%%%%%%%%%%%%%%%%%%%%%%%%%%%
%%%%%Processing the images to evaluate the radii of the curvature%%%%
%%%%%%%%%%%%%%%%%%%%%%%%%%%%%%%%%%%%%%%%%%%%%%%%%%%%%%%%%%%%%%%%%%%%%%

if stats.MajorAxisLength(1)/stats.MinorAxisLength(1)>1.015
||stats.MinorAxisLength(1)/stats.MajorAxisLength(1)>1.025
%defining the threshold to determine the sphericity of the bubble

Ymin_atcentroid=find(Preprocessed_Image(:,floor(xcentroid))==255,1,
'first'); %determine the y-location of the trailing edge
Ymax_atcentroid=find(Preprocessed_Image(:,floor(xcentroid))==255,1,
'last');  %determine the y-location of the leading edge
```

```
figure(3), set(gcf,'color','w');
sz_x = 400; sz_y = 400; % size of the figure
y_pos = 600; x_pos =801;  % position on the screen
set(3,'pos', [x_pos, y_pos, sz_x, sz_y])
axes('position',[.1  .15  .8  .8]) % size of the plot in the figure
title(' Image with smooth boundary')
figure(3)
imshow(Preprocessed_Image) %%plotting the image
axis on
hold on
plot(xcentroid, ycentroid, 'r*')       %plotting the centroid  point
hold on
plot(xcentroid, Ymin_atcentroid, 'b*')
%plotting the leading edge point
hold on
plot(xcentroid, Ymax_atcentroid, 'g*') %plotting the trailing edge
point

%% %%%%%%%%%%%%%%%%%%%%%%%%%%%%%%%%%%%%%%%%%%%%%%%%%%%%%%%%%%%
%%%%%% defining boundary and the curvature of the image  %%%%%
%%%%%%%%%%%%%%%%%%%%%%%%%%%%%%%%%%%%%%%%%%%%%%%%%%%%%%%%%%%%%%

boundaries=zeros(1)
%defining matrix to store the detected boundary of the bubble
x_boundary=zeros(1);
%defining matrix to store the x-location of the boundary
y_boundary=zeros(1);
%defining matrix to store the y-location of the boundary
thisBoundary=zeros(1)
boundaries = bwboundaries(Preprocessed_Image);
% detecting the boundary of the bubble
x_boundary = boundaries{1}(:, 2); %the x-location of the boundary
y_boundary = boundaries{1}(:, 1); %the y-location of the boundary
numberOfBoundaries = size(boundaries, 1);

%%%%%%%%%%%%%%%%%%%%%%%%%%%%%%%%%%%%%
%%%%%% Smoothing the boundary   %%%%%
%%%%%%%%%%%%%%%%%%%%%%%%%%%%%%%%%%%%%

for k = 1 : numberOfBoundaries

% Plot original boundary in green.
plot(x_boundary, y_boundary, 'g-', 'LineWidth', 2);
boundaryLength = length(x_boundary);
fprintf('Length of boundary #%d = %d pixels\n', k, boundaryLength);

% Smooth the boundary.  First subsample it.
subSamplingFactor =25;
xSubsampled = x_boundary(1 : subSamplingFactor : end);
ySubsampled = y_boundary(1 : subSamplingFactor : end);
numInterpolatingPoints = length(xSubsampled);
```

```
if numInterpolatingPoints <= 1
% Skip boundaries of length 1.
continue;
end

% Smooth x coordinates.
t = 1 : boundaryLength;
tx = linspace(1, boundaryLength, numInterpolatingPoints);
x_smooth = pchip(tx, xSubsampled, t);

% Smooth y coordinates.
y_smooth = pchip(tx, ySubsampled, t);

% Plot smoothed boundary in magenta.
plot(x_smooth, y_smooth, 'm-', 'LineWidth', 2);
end

xcentroid_smooth=find(abs(x_smooth-xcentroid)<1);
xleading_location=max(xcentroid_smooth);
xtrailing_location=min(xcentroid_smooth);
yTrailing=y_smooth(xleading_location);
xTrailing=x_smooth(xleading_location);
yleading=y_smooth(xtrailing_location);
xleading=x_smooth(xtrailing_location);
figure(4), set(gcf,'color','w');
sz_x = 400; sz_y = 400; % size of the figure
y_pos = 600; x_pos =1200;  % position on the screen
set(4,'pos', [x_pos, y_pos, sz_x, sz_y])
axes('position',[.1  .15  .8  .8]) % size of the plot in the figure
figure(4)
imshow(Preprocessed_Image)
hold on
plot(x_smooth, y_smooth)
hold on
plot(xTrailing, yTrailing, 'b*') %plotting the leading edge point
hold on

plot(xleading, yleading, 'g*') %plotting the trailing edge point
x_half_bubble=x_smooth(xtrailing_location:xleading_location);
y_half_bubble=y_smooth(xtrailing_location:xleading_location);
figure(5), set(gcf,'color','w');
sz_x = 300; sz_y = 400; % size of the figure
y_pos = 600; x_pos =1600;  % position on the screen
set(5,'pos', [x_pos, y_pos, sz_x, sz_y])
axes('position',[.1  .15  .8  .8]) % size of the plot in the figure
title('half of smooth boundaries')
figure(5)
hold on
plot(x_half_bubble, y_half_bubble)
```

```
%%%%%%%%%%%%%%%%%%%%%%%%%%%%%%%%%%%
%%%%%%  finding the curvature %%%%%
%%%%%%%%%%%%%%%%%%%%%%%%%%%%%%%%%%%

windowSize_Curvature = 20;
% window size to capture the local curvature
halfWidth = floor(windowSize_Curvature/2);   %half window size
curvatures = zeros(size(x_half_bubble));

for k = halfWidth+1 : length(x_half_bubble) - halfWidth
  theseX = x_half_bubble(k-halfWidth:k+halfWidth);   % 19 element of x
  theseY = y_half_bubble(k-halfWidth:k+halfWidth);   % 19 element of y
  % Get a fit in the window.
  coefficients = polyfit(theseX, theseY, 2);

  % Get the curvature
  curvatures(k) = coefficients(1);
  xc(k) = x_half_bubble(k);
  yc(k) = y_half_bubble(k);
end
for number22=1:length(x_half_bubble)
theta_curvature(number22)=atan((y_half_bubble(number22)-
ycentroid)/(x_half_bubble(number22)-xcentroid));
% determine the angle of corresponding to the location
end
theta_curvature(1)=[];
theta_curvature(length(theta_curvature))=[];
curvatures(1)=[];
curvatures(length(curvatures))=[];

%%%%%%%%%%%%%%%%%%%%%%%%%%%%%%%%%%%%%%%%%%%%%%%%%%%%%%%%%%%%%
%%%%%%  Plotting the curvature around half of the bubble%%%%%
%%%%%%%%%%%%%%%%%%%%%%%%%%%%%%%%%%%%%%%%%%%%%%%%%%%%%%%%%%%%%

figure(6), set(gcf,'color','w');
sz_x = 800; sz_y = 400; % size of the figure
y_pos = 120; x_pos =1;  % position on the screen
set(6,'pos', [x_pos, y_pos, sz_x, sz_y])
axes('position',[.1  .15  .8  .8]) % size of the plot in the figure
title('plot of curvature of the half of bubble')

figure(6)
plot(theta_curvature*180/3.14+180,flip(curvatures)/pixelTomm,'o-')
axis
xlabel('Angle (^{\circ})')
ylabel('Curvature (mm)')
xlim([90 270])
ylim([-0.1 0.1])
```

```
%%%%%%%%%%%%%%%%%%%%%%%%%%%%%%%%%%%%%%%%%%%%%%%%%%%%%%%%%%%%%
%%%% determining the change in the curvature of the bubble%%%
%%%%%%%%%%%%%%%%%%%%%%%%%%%%%%%%%%%%%%%%%%%%%%%%%%%%%%%%%%%%%

Number33=1;
for number44=2:length(curvatures)
    delta(Number33)=curvatures(number44)-curvatures(number44-1);
    Number33=Number33+1;
end
figure(6), set(gcf,'color','w');
sz_x = 400; sz_y = 400; % size of the figure
y_pos = 120; x_pos =1;  % position on the screen
set(6,'pos', [x_pos, y_pos, sz_x, sz_y])
axes('position',[.1  .15  .8  .8]) % size of the plot in the figure
title('plot of change in curvature of the half of bubble')
figure(6)
plot(delta,'*') %plotting the change in the curvature around the
bubble

yfirst=find(abs(delta(windowSize_Curvature/2+1:length(delta)))>0.001,1
, 'first')+windowSize_Curvature/2;
%finding the first location where the curvature changes more than0.001
ylast=find(abs(delta(1:length(delta)-windowSize_Curvature/2-
1))>0.001,1, 'last');
%finding the last location where the curvature changes more than 0.001

%%%%%%%%%%%%%%%%%%%%%%%%%%%%%%%%%%%%%%%%%%%%%%%%%%%%%%%%%%
%%%%%%  Plotting the Cropping location of the bubble%%%%
%%%%%%%%%%%%%%%%%%%%%%%%%%%%%%%%%%%%%%%%%%%%%%%%%%%%%%%%%%

figure(7), set(gcf,'color','w');
sz_x = 400; sz_y = 400; % size of the figure
y_pos = 120; x_pos =401;  % position on the screen
set(7,'pos', [x_pos, y_pos, sz_x, sz_y])
axes('position',[.1  .15  .8  .8]) % size of the plot in the figure
title('Cropping locations')
figure(7)
hold on
plot(x_half_bubble, y_half_bubble)
hold on
plot(x_half_bubble(ylast), y_half_bubble(ylast), 'g*')
%plotting the leading edge point
hold on
plot(x_half_bubble(yfirst), y_half_bubble(yfirst), 'b*')
%plotting the trailing edge point

figure(8), set(gcf,'color','w');
sz_x = 400; sz_y = 400; % size of the figure
y_pos = 120; x_pos =401;  % position on the screen
set(8,'pos', [x_pos, y_pos, sz_x, sz_y])
axes('position',[.1  .15  .8  .8]) % size of the plot in the figure
```

```
title('Cropping locations')
figure(8)
hold on
plot(px, py)
hold on
plot(px(yfirst+xtrailing_location), py(yfirst+xtrailing_location),
'b*') %plotting the leading edge point
hold on
plot(px(xtrailing_location-yfirst), py(xtrailing_location-yfirst),
'b*') %plotting the leading edge point
hold on
plot(px(ylast+xtrailing_location), py(ylast+xtrailing_location), 'g*')
%plotiing the trailing edge point
hold on
plot(px(xleading_location+(xleading_location-ylast-
xtrailing_location)), py(xleading_location+(xleading_location-ylast-
xtrailing_location)), 'g*') %plotting the trailing edge point

%%%%%%%%%%%%%%%%%%%%%%%%%%%%%%%%%%%%%%%%%%%%%%%%%%%%%%%%%%%%%%%%%%%%
%%%%%% determining the curvature of the leading and trailing   %%%%%
%%%%%%%%%%%%%%%%%%%%%%%%%%%%%%%%%%%%%%%%%%%%%%%%%%%%%%%%%%%%%%%%%%%%
%%%curvature of leading

trailing_location_x=x_smooth((xtrailing_location-
yfirst):yfirst+xtrailing_location);
% defining the location of trailing for 50 points after and before
trailing_location_y=y_smooth((xtrailing_location-
yfirst):yfirst+xtrailing_location);
leading_location_x=x_smooth((ylast+xtrailing_location):xleading_locati
on+(xleading_location-ylast-xtrailing_location));
% defining the location of leading for 50 points after and before
leading_location_y=y_smooth((ylast+xtrailing_location):xleading_locati
on+(xleading_location-ylast-xtrailing_location));
% Get a fit.
coefficients_L = polyfit(leading_location_x, leading_location_y, 2);
% Get the curvature
curvatures_L= coefficients_L(1);

%%%curvature of trailing
% Get a fit.
coefficients_T = polyfit(trailing_location_x, trailing_location_y, 2);
% Get the curvature
curvatures_T= coefficients_T(1);
[xfit_L,yfit_L,Rfit_L]=
circfit(leading_location_x,leading_location_y);
[xfit_T,yfit_T,Rfit_T]=
circfit(trailing_location_x,trailing_location_y);

%storing data
xfit_Leading(number)=xfit_L;
yfit_Leading(number)=yfit_L;
Rfit_Leading(number)=Rfit_L;
```

```
xfit_trailing(number)=xfit_T;
yfit_trailing(number)=yfit_T;
Rfit_trailing(number)=Rfit_T;


figure(9), set(gcf,'color','w');
sz_x = 400; sz_y = 800; % size of the figure
y_pos = 120; x_pos =801; % position on the screen
set(9,'pos', [x_pos, y_pos, sz_x, sz_y])
% axes('position',[.1  .15  .8  .8]) % size of the plot in the figure
fig=figure(9)
hold on
imshow(Preprocessed_Image, []);
hold on
rectangle('position',[xfit_L-Rfit_L,yfit_L-
Rfit_L,Rfit_L*2,Rfit_L*2],...
    'curvature',[1,1],'linestyle','-','edgecolor','r');
plot(xfit_L,yfit_L,'r*')
hold on
rectangle('position',[xfit_T-Rfit_T,yfit_T-
Rfit_T,Rfit_T*2,Rfit_T*2],...
    'curvature',[1,1],'linestyle','-','edgecolor','g');
plot(xfit_T,yfit_T,'g*')
%%%%%%%%%%%%%%%%%%%%%%%%%%%%%%%%%%%%%%%%%%%%%%%%%%%%%%%
%%%%%% Plotting the bubble in polar coordinate %%%%%%
%%%%%%%%%%%%%%%%%%%%%%%%%%%%%%%%%%%%%%%%%%%%%%%%%%%%%%%

location_leading=find(x_boundary(:)==floor(xcentroid),1, 'first');
location_trailing=find(x_boundary(:)==floor(xcentroid),1, 'last');
theta=zeros(1,1); % defining the theta
redia=zeros(1,1); % defining the Radius
%
L=1;
LL=1;
% defining the y-location of right side of the bubble
 for i=location_leading:location_trailing
 y_firstpart(L)=(y_boundary(i));
 x_firstpart(L)=(x_boundary(i))
 L=L+1;
 end
% defining the y-location of left side of the bubble
 for ii=1:location_leading
 y_seconpart(LL)=y_boundary(ii);
 x_seconpart(LL)=(x_boundary(ii));
 LL=LL+1;
 end
 for ii= location_trailing:length(y_smooth)
 y_seconpart(LL)=y_boundary(ii);
 x_seconpart(LL)=(x_boundary(ii));
 LL=LL+1;
 end
```

```
% defining the polar location of the right side of the bubble
xpolar=x_firstpart-xcentroid;
%offsetting x so the bubble is @ center of the polar coordinate

ypolar=y_firstpart-ycentroid;
%offsetting y so the bubble is @ center of the polar coordinate

for i=1:length(y_firstpart)
     theta(i)=atan(ypolar(i)/xpolar(i));          % defining the theta
     redia(i)=sqrt((ypolar(i)^2)+(xpolar(i)^2));
% defining the radius
 end

% defining the polar location of the of left side of the bubble with
180 degree rotation
xpolar2=x_seconpart-xcentroid;
ypolar2=y_seconpart-ycentroid;
for i=1:length(y_seconpart)
     theta21(i)=atan(ypolar2(i)/xpolar2(i))+3.14;
     redia2(i)=sqrt((ypolar2(i)^2)+(xpolar2(i)^2));
end
%%%first curve

xc =xfit_L-xcentroid; yc =yfit_L-ycentroid;
th = linspace(0,2*pi,50);
[x_boundary,y_boundary] = pol2cart(th,Rfit_L);
[th1, r1] = cart2pol( x_boundary+xc, y_boundary+yc );
xct =xfit_T-xcentroid; yct =yfit_T-ycentroid;
%the work
th2 = linspace(0,2*pi,50);
[x222,y222] = pol2cart(th2,Rfit_T);
[th2, r2] = cart2pol( x222+xct, y222+yct);
theta(1)=[];
theta21(1)=[];
theta(length(theta)-1)=[];
theta21(length(theta21)-1)=[];
redia(1)=[];
redia2(1)=[];
redia(length(redia)-1)=[];
redia2(length(redia2)-1)=[];
tehta=[theta theta21];
redian=[redia redia2];
%% sorting the second part
[tehta,idx]=sort(tehta,'ascend');
redian=redian(idx);
```

```
figure(10), set(gcf,'color','w');
sz_x = 400; sz_y = 400; % size of the figure
y_pos = 120; x_pos =1200; % position on the screen
set(10,'pos', [x_pos, y_pos, sz_x, sz_y])
% axes('position',[.1  .1  .8  .8]) % size of the plot in the figure
pax = polaraxes;
pax.ThetaZeroLocation = 'right'
pax.ThetaDir = 'clockwise';
pax.FontSize = 12
pax.RLim = [0 3.5]
hold on
figure(10)
polarplot(tehta,redian/pixelTomm,'k',...
    'LineWidth',2)% Plotting in the right side in polar coordinate
hold on
polarplot(th1, r1/pixelTomm,'r',...
    'LineWidth',2)
hold on
polarplot(th2, r2/pixelTomm,'b',...
    'LineWidth',2)

rightCrop_x_T=x_smooth(yfirst+xtrailing_location)-xcentroid;
rightCrop_y_T=y_smooth(yfirst+xtrailing_location)-ycentroid;
theta_x_T_R=atan(rightCrop_x_T/rightCrop_y_T)-1.57;
% definding the theta
redia_x_T_R=sqrt((rightCrop_x_T^2)+(rightCrop_y_T^2));

leftCrop_x_T=x_smooth(xtrailing_location-yfirst)-xcentroid;
leftCrop_y_T=y_smooth(xtrailing_location-yfirst)-ycentroid;
theta_T_L=atan(leftCrop_x_T/leftCrop_y_T)-1.57;
% defining the theta
redia_T_L=sqrt((leftCrop_x_T^2)+(leftCrop_y_T^2));

rightCrop_x_L=x_smooth(ylast+xtrailing_location)-xcentroid;
rightCrop_y_L=y_smooth(ylast+xtrailing_location)-ycentroid;
theta_L_R=atan(rightCrop_x_L/rightCrop_y_L)+1.57;
% defining the theta
redia_L_R=sqrt((rightCrop_x_L^2)+(rightCrop_y_L^2));

leftCrop_x_L=x_smooth(xleading_location+(xleading_location-ylast-
xtrailing_location))-xcentroid;
leftCrop_y_L=y_smooth(xleading_location+(xleading_location-ylast-
xtrailing_location))-ycentroid;
theta_L_L=atan(leftCrop_x_L/leftCrop_y_L)+1.57;
% defining the theta
redia_L_L=sqrt((leftCrop_x_L^2)+(leftCrop_y_L^2));

Thetaleading(number)=abs(theta_L_L-theta_L_R)/3.14*180;
Thetatrailing(number)=abs(theta_T_L-theta_x_T_R)/3.14*180;

else
```

```
% %%%%%%%%%%%%%%%%%%%%%%%%%%%%%%%%%%%%%%%%%%%%%%%%%%%%%%%%%%%%%%%%
%%%%% determining the curvature of the leading and trailing %%%%
%%%%%%%%%%%%%% for bubbles with sphericity around one %%%%%%%%
%%%%%%%%%%%%%%%%%%%%%%%%%%%%%%%%%%%%%%%%%%%%%%%%%%%%%%%%%%%%%%%%

figure(9), set(gcf,'color','w');
sz_x = 400; sz_y = 800; % size of the figure
y_pos = 120; x_pos =801;  % position on the screen
set(9,'pos', [x_pos, y_pos, sz_x, sz_y])
% axes('position',[.1  .15  .8  .8]) % size of the plot in the figure
fig=figure(9)
hold on
imshow(Preprocessed_Image, []);
hold on
centers = stats.Centroid;
        diameters = mean([stats.MajorAxisLength
stats.MinorAxisLength],2);
        radii = diameters/2; % determine the radius of the bubble
        % Plot the circles
hold on
viscircles(centers,radii);
xfit_Leading(number)=xcentroid;
yfit_Leading(number)=ycentroid;
Rfit_Leading(number)=radii(1);
% defining the radius of leading to be radius of the bubble
xfit_trailing(number)=xcentroid;
yfit_trailing(number)=ycentroid;
Rfit_trailing(number)=radii(1);
% defining the radius of trailing to be radius of the bubble
Thetaleading(number)=180;
Thetatrailing(number)=180;
end
number=number+1;
end
%generating the result matrix
C =
horzcat(x_centroid',y_centroid',xfit_Leading',yfit_Leading',Rfit_Leadi
ng',xfit_trailing',yfit_trailing',Rfit_trailing',Thetaleading',Thetatr
ailing');

%name of the headers in the excel file
col_header={'X_centroid','Y_centroid','X_Trailing','Y_Trailing','R_tra
iling','X_Leading','Y_Leading','R_leading','Thetatrailing','Thetaleadi
ng'};

% name of the file
filename='196_Round pore_Small-1mm_0p2mlpermin_149frate_skiped5
images_Glycerol_5th';

%generating the excel file
xlswrite(filename,C,'Sheet1','B2');     %Write data
xlswrite(filename,col_header,'Sheet1','B1');
```

```
%% %%%%%%%%%%%%%%%%%%%%%%%%%%%%%%%%%%%%%%
%%%%%% Functions used in the code   %%%%%
%%%%%%%%%%%%%%%%%%%%%%%%%%%%%%%%%%%%%%%%%

%%%%%%%%%%%%First function

 function   [xc,yc,R,a] = circfit(x,y)
%
%   [xc yx R] = circfit(x,y)
%
%   fits a circle  in x,y plane in a more accurate
%   (less prone to ill condition )
%  procedure than circfit2 but using more memory
%  x,y are column vector where (x(i),y(i)) is a measured point
%
%  result is center point (yc,xc) and radius R
%  an optional output is the vector of coefficient a
% describing the circle's equation
%
%   x^2+y^2+a(1)*x+a(2)*y+a(3)=0
%
%  By:  Izhak bucher 25/oct /1991,
    x=x(:); y=y(:);
   a=[x y ones(size(x))]\[-(x.^2+y.^2)];
   xc = -.5*a(1);
   yc = -.5*a(2);
   R  =  sqrt((a(1)^2+a(2)^2)/4-a(3));
 end

%%
%%%%%%%%%% Second function
 function clear_all_but(varargin)
%%
<><><><><><><><><><><><><><><><><><><><><><><><><><><><><><><><><><><>
%%
% <><><><><><>         Clear All But Some Variables
<><><><><><> %
%
<><><><><><><><><><><><><><><><><><><><><><><><><><><><><><><><><><><><><>
%
%                                                 Version:
16.09.2009 %
%                                                     (c) Roland
Pfister %
%                                             roland_pfister@t-
online.de %
% 1. Synopsis
%
%
%
% The workspace is cleared as if the 'clear all' command was used but
it %
```

```
% is possible to keep some of your most beloved variables. Simply
enter  %
% these variables as input arguments.
%
%
%
% 2. Example
%
%
%
% The command "clear_all_but('var_a','var_b')" clears all variables
but  %
% var_a and var_b.
%
%
%
%
<><><><><><><><><><><><><><><><><><><><><><><><><><><><><><><><><><><><>
%

%% Get a list of workspace variables.
workspace_variables = evalin('caller','who');

%% Go through the list...
for workspace_index_1 = 1:size(workspace_variables,1)
    workspace_index_3 = 0;
    % ... and check whether the current variable
    % name is among the input arguments.
    for workspace_index_2 = 1:nargin
        if strcmp(workspace_variables{workspace_index_1,1},...
           varargin{1,workspace_index_2}) == 1
            workspace_index_3 = 1;
        end;
    end;
    % If it's not: clear.
    if workspace_index_3 == 0
        workspace_index_4 = ['clear(' char(39) ...
            workspace_variables{workspace_index_1,1} char(39) ')'];
        evalin('base',workspace_index_4);
    end;
end;


%% Cleaning up the function workspace.
clear workspace_variables;
clear workspace_index_1;
clear workspace_index_2;
clear workspace_index_3;
clear workspace_index_4;
end
```

A-3: MATLAB code for alley and matrix of bubbles

The presented code was used to evaluate the location of individual bubbles in a matrix and array arrangement of the bubble. Plotting their centroid and instantaneous velocity. The result obtained from the process can be found in Chapter 6:

```
%%%%%%%%%%%%%%%%%%%%%%%%%%%%%%%%%%%%%%%%%%%%%%%%%%%%%%%%%%%%%%%%%
% J_Viz_Imageprocessing.m
%
% Who    : Shadi Ansari
% When   : Jan2019
% Aim    : Load the excel file containing the location of bubbles and
plotting them
%%%%%%%%%%%%%%%%%%%%%%%%%%%%%%%%%%%%%%%%%%%%%%%%%%%%%%%%%%%%%%%%%

close all
clear all
clc
%%%Importing the excel files of the locations
location1=xlsread('location_1st_deshaked.xls');%% 126...1378
location2=xlsread('location_2nd_deshaked.xls');%%126...1218
location3=xlsread('location_3rd_deshaked.xls');%% 126...1378
location4=xlsread('location_4th_deshaked.xls');%%126...1218
location5=xlsread('location_5th_deshaked.xls');%%250...1500
location6=xlsread('location_6th_deshaked.xls');%%300...1700
location7=xlsread('location_7th_deshaked.xls');%%510...1820
location8=xlsread('location_8th_deshaked.xls');%%738...1800
%%%%Importing the location of the centroid of 6 bubbles
x_cenroid_1=location1(:,1);
y_cenroid_1=location1(:,2);
x_cenroid_2=location2(:,1);
y_cenroid_2=location2(:,2);
x_cenroid_3=location3(:,1);
y_cenroid_3=location3(:,2);
x_cenroid_4=location4(:,1);
y_cenroid_4=location4(:,2);
x_cenroid_5=location5(:,1);
y_cenroid_5=location5(:,2);
x_cenroid_6=location6(:,1);
y_cenroid_6=location6(:,2);
x_cenroid_7=location7(:,1);
y_cenroid_7=location7(:,2);
x_cenroid_8=location8(:,1);
y_cenroid_8=location8(:,2);

 for framenumbers=715:2:1401 % defining the range of images to import
%%%%%%%%%%%%%%%%%%
%%%RED Bubble%%%%%
%%%%%%%%%%%%%%%%%%
```

```
% defining the range to recall the bubbles centroid based on the
% location in the image
if framenumbers<270
xOR=2.55; %conversion factor
yOR=2.8;  %conversion factor
elseif  270<framenumbers && framenumbers<500
xOR=2.55-0.000022*(framenumbers-271);
yOR=2.8-0.0022*(framenumbers-271);
elseif  500<framenumbers && framenumbers<720
xOR=2.55-0.000022*(framenumbers-271);
yOR=2.3-0.00225*(framenumbers-501);
elseif  720<framenumbers && framenumbers<792
xOR=2.55-0.000022*(framenumbers-271);
yOR=1.8050-((1.8050-1.45)/(792-721))*(framenumbers-721);
end
%%
%%%%%%%%%%%%%%%%%%
%%%Yellow ONE%%%%%%
%%%%%%%%%%%%%%%%%%
% defining the range to recall the bubbles centroid based on the
% location in the image
if framenumbers<320
xOy=2.45;  %conversion factor
yOy=3.05;  %conversion factor
elseif  320<framenumbers && framenumbers<520
xOy=2.45+0.0005*(framenumbers-321);
yOy=3.05-0.00125*(framenumbers-321);
elseif 520<framenumbers && framenumbers<784
xOy=2.55;
yOy=2.8-0.0000875*(framenumbers-521);
elseif 784<framenumbers && framenumbers<988
xOy=2.55;
yOy=2.7594-((2.7594-2.2)/(988-784))*(framenumbers-784);
end
%%
%%%%%%%%%%%%%%%%%%
%%%Blue ONE%%%%%%%
%%%%%%%%%%%%%%%%%%
if framenumbers<300
xOB=2.6;
yOB=3.07;
elseif  300<framenumbers && framenumbers<451
xOB=2.6+0.00006*(framenumbers-300);
yOB=3.07;
elseif  450<framenumbers && framenumbers<701
xOB=2.6089-0.000245*(framenumbers-451);
yOB=3.07-0.0006*(framenumbers-451);
elseif  700<framenumbers && framenumbers<760
xOB=2.55;
yOB=3.07-0.00065*(framenumbers-451);
elseif  760<framenumbers && framenumbers<992
xOB=2.55;
```

```
yOB=3.07-0.00065*(framenumbers-451);
elseif  992<framenumbers && framenumbers<1162
xOB=2.55;
yOB=2.7184-(0.7184/(1162-992))*(framenumbers-992);
end
%%
%%%%%%%%%%%%%%%%%%
%%%Green ONE%%%%%%
%%%%%%%%%%%%%%%%%%

if framenumbers<700
xOG=2.45;
yOG=3.05;
elseif  700<framenumbers && framenumbers<899
xOG=2.45+0.0005*(framenumbers-700);
yOG=3.1-0.001*(framenumbers-700);
elseif 898<framenumbers && framenumbers<1204
xOG=2.54;
yOG=2.9-0.0011*(framenumbers-901);
elseif 1204<framenumbers && framenumbers<1400
xOG=2.54;
yOG=2.5667-((2.5667-2.25)/(1299-1204))*(framenumbers-1204);
end

%%%%%%%%%%%%%%%%%%
%%%Cyan ONE%%%%%%%
%%%%%%%%%%%%%%%%%%

if framenumbers<572
xOC=2.52;
yOC=3.12;
elseif  572<framenumbers && framenumbers<672
xOC=2.52+(0.08/100)*(framenumbers-572);
yOC=3.12;
elseif  672<framenumbers && framenumbers<724
xOC=2.6-(0.04/(723-673))*(framenumbers-672);
yOC=3.12-(0.08/(723-673))*(framenumbers-672);
elseif  724<framenumbers && framenumbers<872
xOC=2.55+(0.05/(150))*(framenumbers-724);
yOC=3.04
elseif  873<framenumbers && framenumbers<936
xOC=2.6-(0.08/(50))*(framenumbers-873);
yOC=3.04-((3.04-2.8)/50)*(framenumbers-873);
elseif  936<framenumbers && framenumbers<1071
xOC=2.52;
yOC=3.05;
elseif  1071<framenumbers && framenumbers<1402
xOC=2.52+((2.56-2.52)/(1401-1071))*(framenumbers-1071);
yOC=3.05-((3.05-2.4)/(1401-1071))*(framenumbers-1071);
end
```

```
%%%%%%%%%%%%%%%%%%
%%%Magenta ONE%%%%
%%%%%%%%%%%%%%%%%%

if framenumbers<400
xOM=2.53
yOM=3.1;
elseif  400<framenumbers && framenumbers<855
xOM=2.53-(0.03/(200))*(framenumbers-400);
yOM=3.1-(0.05/(200))*(framenumbers-400)
elseif 854<framenumbers && framenumbers<956
xOM= 2.4617-(0.0117/(935-855))*(framenumbers-854);
yOM=2.9863+((3.3-2.9863)/(935-855))*(framenumbers-854);
elseif 956<framenumbers && framenumbers<1110
xOM= 2.45+((2.54-2.45)/(1151-956))*(framenumbers-956);
yOM=3;
elseif 1110<framenumbers && framenumbers<1800
xOM= 2.5211;
yOM=3-((3-2.8)/(1301-1110))*(framenumbers-1110);
%     xOM=2.55-0.000022*(framenumbers-271);
%     yOM=2.3-0.00225*(framenumbers-501);
    end
i=round(framenumbers/2);
close all;
%name of the image to plot the location of centroid
filename=sprintf('matrix_Deshaked_%05i.tiff',framenumbers);
%importing the image file
I= imread(filename);
I(:,:,3) = [];
I(:,:,2) = [];
I = imadjust(I);
%Plotting the raw image
fig=figure,imshow(I);
axis on
% funcation to draw an arrow
drawArrow = @(x,y,varargin) quiver( x(1),y(1),x(2)-x(1),y(2)-y(1),0,
varargin{:} )
%%%%%%%%%%%%%%%%%%%%%%%%%%%%
%%%%%%%%%% 1st bubble%%%%%%%
%%%%%%%%%%%%%%%%%%%%%%%%%%%%
 hold on
if 1<framenumbers && framenumbers<115
% range where the first bubble appears
plot(2.54*x_cenroid_1(i),2.5*y_cenroid_1(i),'.k', 'MarkerSize',80)
% Plotting the bubble centroid as a circle
hold on
if  framenumbers<(115-60)
```

```
% defining the location of the start and the end of the arrow based on
% the velocity and location of the centroid in the 30 image after
x1 = [2.54*x_cenroid_1(i) 2.54*x_cenroid_1(i+60/2) ];
y1 = [2.5*y_cenroid_1(i) 2.5*(y_cenroid_1(i+60/2))];
drawArrow(x1,y1,'MaxHeadSize',0.8,'Color','k','LineWidth',3);
end
end
hold on
%%%%%%%%%%%%%%%%%%%%%%%%%%%%
%%%%%%%%%% 2nd bubble%%%%%%%
%%%%%%%%%%%%%%%%%%%%%%%%%%%%
if 1<framenumbers && framenumbers<359
  plot(2.54*x_cenroid_2(i),2.7*y_cenroid_2(i),'.w', 'MarkerSize',80)
  hold on
 if  framenumbers<(359-90)
x2 = [2.54*x_cenroid_2(i) 2.54*x_cenroid_2(i+90/2) ];
y2 = [2.7*y_cenroid_2(i) 2.7*(y_cenroid_2(i+90/2))];
drawArrow(x2,y2,'MaxHeadSize',0.8,'Color','w','LineWidth',3);
 end
end


%%%%%%%%%%%%%%%%%%%%%%%%%%%%
%%%%%%%%%% 3rd bubble%%%%%%%
%%%%%%%%%%%%%%%%%%%%%%%%%%%%
hold on
if 1<framenumbers && framenumbers<793
    plot(xOR*x_cenroid_3(i),yOR*(y_cenroid_3(i)+40),'.r',
'MarkerSize',80)
    hold on
if  framenumbers<(793-90)
x1 = [xOR*x_cenroid_3(i) xOR*x_cenroid_3(i+90/2) ];
y1 = [yOR*(y_cenroid_3(i)+40) yOR*(y_cenroid_3(i+90/2)+40)];
drawArrow(x1,y1,'MaxHeadSize',0.8,'Color','r','LineWidth',3);
end
end
hold on
%%%%%%%%%%%%%%%%%%%%%%%%%%%%
%%%%%%%%%% 4th bubble%%%%%%%
%%%%%%%%%%%%%%%%%%%%%%%%%%%%

if 1<framenumbers && framenumbers<987
  plot(xOy*x_cenroid_4(i),yOy*y_cenroid_4(i),'.y', 'MarkerSize',80)
  hold on
if  framenumbers<(987-90)
x2 = [xOy*x_cenroid_4(i) xOy*x_cenroid_4(i+90/2) ];
y2 = [yOy*y_cenroid_4(i) yOy*(y_cenroid_4(i+90/2))];
drawArrow(x2,y2,'MaxHeadSize',0.8,'Color','y','LineWidth',3);
 end
end
hold on
```

```
%%%%%%%%%%%%%%%%%%%%%%%%%%%%
%%%%%%%%%% 5th bubble%%%%%%%
%%%%%%%%%%%%%%%%%%%%%%%%%%%%
if 1<framenumbers && framenumbers<1163
plot(xOB*x_cenroid_5(i),yOB*y_cenroid_5(i),'.b', 'MarkerSize',80)
 if  framenumbers<(1163-90)
x3 = [xOB*x_cenroid_5(i) xOB*x_cenroid_5(i+90/2) ];
y3 = [yOB*y_cenroid_5(i) yOB*(y_cenroid_5(i+90/2))];
drawArrow(x3,y3,'MaxHeadSize',0.8,'Color','b','LineWidth',3);
hold on
 end
end
%%%%%%%%%%%%%%%%%%%%%%%%%%%%
%%%%%%%%%% 6th bubble%%%%%%%
%%%%%%%%%%%%%%%%%%%%%%%%%%%%
if 1<framenumbers && framenumbers<1300
plot(xOG*x_cenroid_4(i),yOG*y_cenroid_6(i),'.g', 'MarkerSize',80)
      drawArrow = @(x,y,varargin) quiver( x(1),y(1),x(2)-x(1),y(2)-
y(1),0, varargin{:} )  ;
if  1<framenumbers && framenumbers<(1220)
x4 = [xOG*x_cenroid_4(i) xOG*x_cenroid_4(i+90/2) ];
y4 = [yOG*y_cenroid_6(i) yOG*(y_cenroid_6(i+90/2))];
drawArrow(x4,y4,'MaxHeadSize',0.8,'Color','g','LineWidth',3);
hold on
 end
end

%%%%%%%%%%%%%%%%%%%%%%%%%%%%
%%%%%%%%%% 7th bubble%%%%%%%
%%%%%%%%%%%%%%%%%%%%%%%%%%%%
if 21<framenumbers && framenumbers<1485
plot(xOC*x_cenroid_7(i),yOC*y_cenroid_7(i),'.c', 'MarkerSize',80)
      drawArrow = @(x,y,varargin) quiver( x(1),y(1),x(2)-x(1),y(2)-
y(1),0, varargin{:} )  ;
 if  framenumbers<(1485-round(21/2)-90)
x4 = [xOC*x_cenroid_7(i) xOC*x_cenroid_7(90/2+i)];
y4 = [yOC*y_cenroid_7(i) yOC*(y_cenroid_7(90/2+i))];
drawArrow(x4,y4,'MaxHeadSize',0.8,'Color','c','LineWidth',3);
 end
end
%%%%%%%%%%%%%%%%%%%%%%%%%%%%
%%%%%%%%%% 8th bubble%%%%%%%
%%%%%%%%%%%%%%%%%%%%%%%%%%%%
if 261<framenumbers && framenumbers<1519
 plot(xOM*x_cenroid_8(i-round(261/2)),yOM*y_cenroid_8(i-
round(261/2)),'.m', 'MarkerSize',80)
      drawArrow = @(x,y,varargin) quiver( x(1),y(1),x(2)-x(1),y(2)-
y(1),0, varargin{:} )  ;
if  framenumbers<(1519-90)
x4 = [xOM*x_cenroid_8(i-round(261/2)) xOM*x_cenroid_8(i+90/2-
round(261/2))];
```

```
y4 = [yOM*y_cenroid_8(i-round(261/2)) yOM*(y_cenroid_8(i+90/2-
round(261/2)))];
drawArrow(x4,y4,'MaxHeadSize',0.8,'Color','m','LineWidth',3);
 end
end
i=i+1;
fname = 'W:\Shadi Ansari\Tod _bubble
experiments\16_Jan\INTERSTING\Competing_149fps\processed\GIF\new';
%%%%%%%%%%name of the file
saveas(fig,fullfile(fname,sprintf('matrix_%04i.tiff',framenumbers)),'t
iff');
 end
```

A-4: Solid Model Drawing

This section represents the design of the channels and the optical access used in this study. The solid models have been generated using a commercial software package for solid modeling and simulation (SolidWorks 2018/19, Dassault Systèmes). The channels are manufactured using 3D printer, and laser cutting was used to manufacture the optical access window.

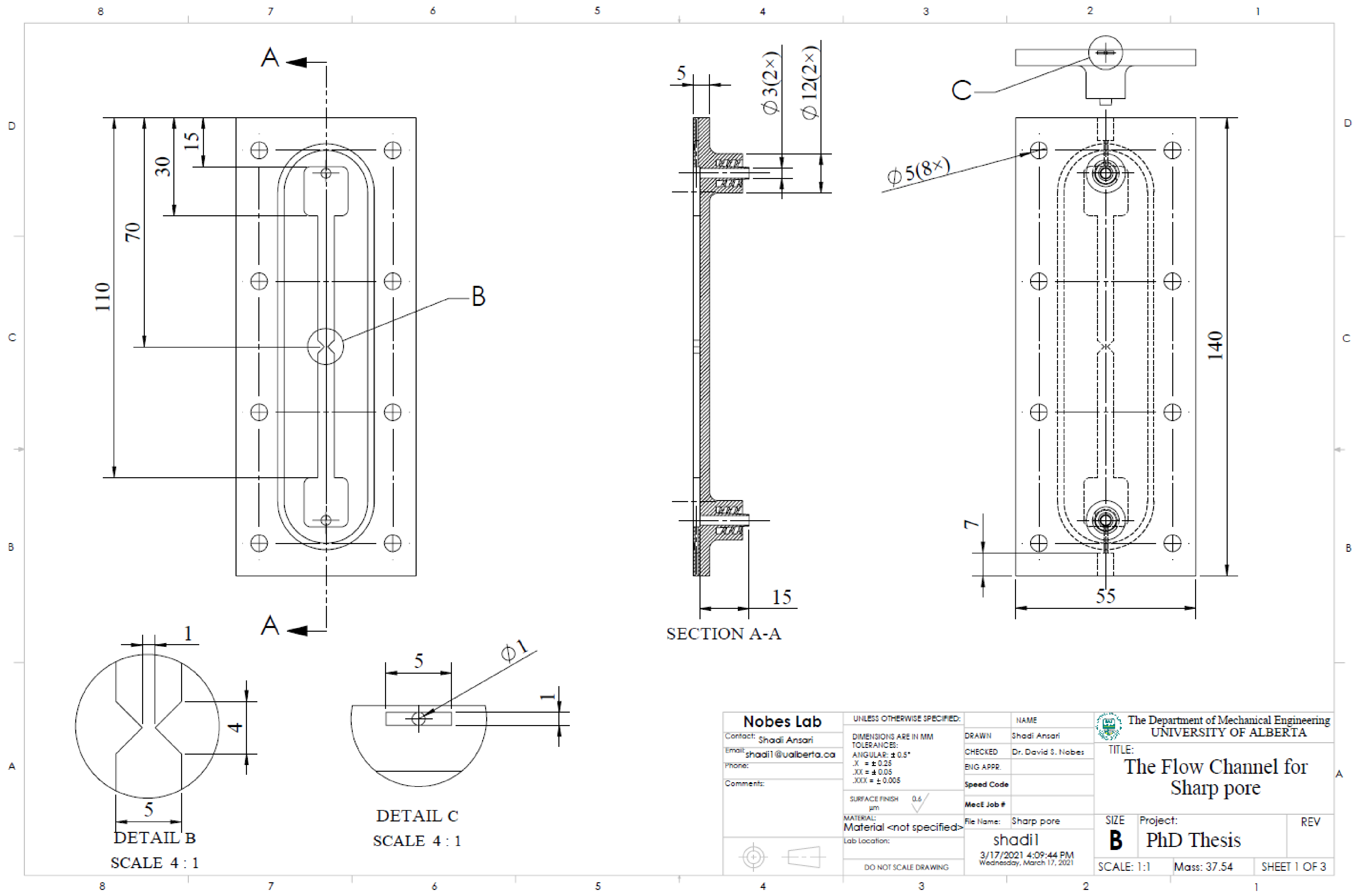

Nobes Lab
Contact: Shadi Ansari
Email: shadi1@ualberta.ca
Phone:
Comments:

UNLESS OTHERWISE SPECIFIED:
DIMENSIONS ARE IN MM
TOLERANCES:
ANGULAR: ± 0.5°
.X = ± 0.25
.XX = ± 0.05
.XXX = ± 0.005
SURFACE FINISH µm 0.6
MATERIAL: Material <not specified>
Lab Location:
DO NOT SCALE DRAWING

	NAME
DRAWN	Shadi Ansari
CHECKED	Dr. David S. Nobes
ENG APPR.	
Speed Code	
MecE Job #	
File Name:	Sharp pore

shadi1
3/17/2021 4:09:44 PM
Wednesday, March 17, 2021

The Department of Mechanical Engineering
UNIVERSITY OF ALBERTA

TITLE:
The Flow Channel for Sharp pore

SIZE B
Project: PhD Thesis
REV
SCALE: 1:1
Mass: 37.54
SHEET 1 OF 3

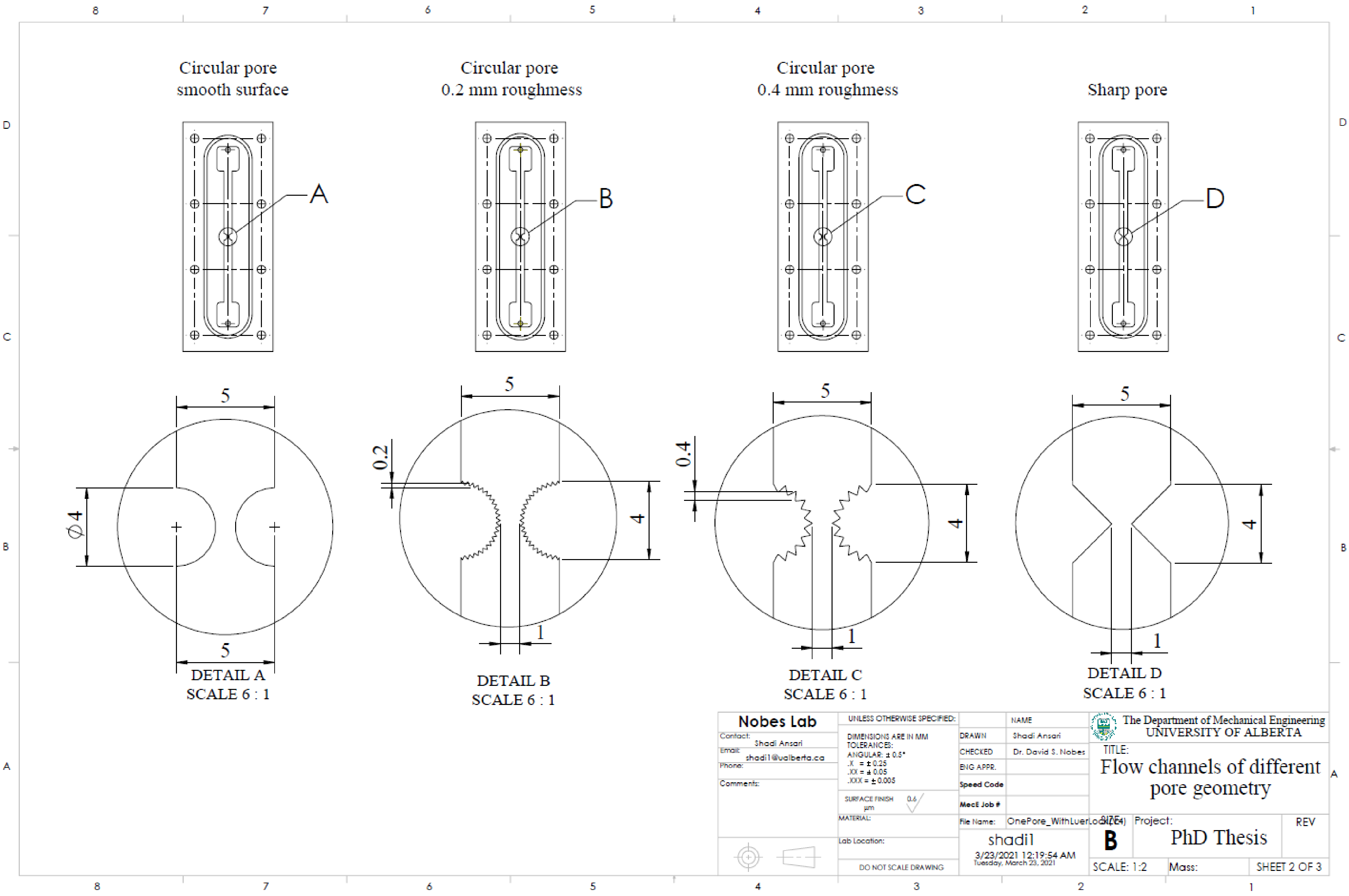

Nobes Lab
Contact: Shadi Ansari
Email: shadi1@ualberta.ca
Phone:
Comments:

UNLESS OTHERWISE SPECIFIED:
DIMENSIONS ARE IN MM
TOLERANCES:
ANGULAR: ± 0.5°
.X = ± 0.25
.XX = ± 0.05
.XXX = ± 0.005
SURFACE FINISH µm 0.6
MATERIAL:
Lab Location:
DO NOT SCALE DRAWING

	NAME
DRAWN	Shadi Ansari
CHECKED	Dr. David S. Nobes
ENG APPR.	
Speed Code	
MecE Job #	
File Name:	OnePore_WithLuerLock(E4)

shadi1
3/23/2021 12:19:54 AM
Tuesday, March 23, 2021

The Department of Mechanical Engineering
UNIVERSITY OF ALBERTA

TITLE:
Flow channels of different pore geometry

SIZE **B**
Project: PhD Thesis
REV
SCALE: 1:2
Mass:
SHEET 2 OF 3

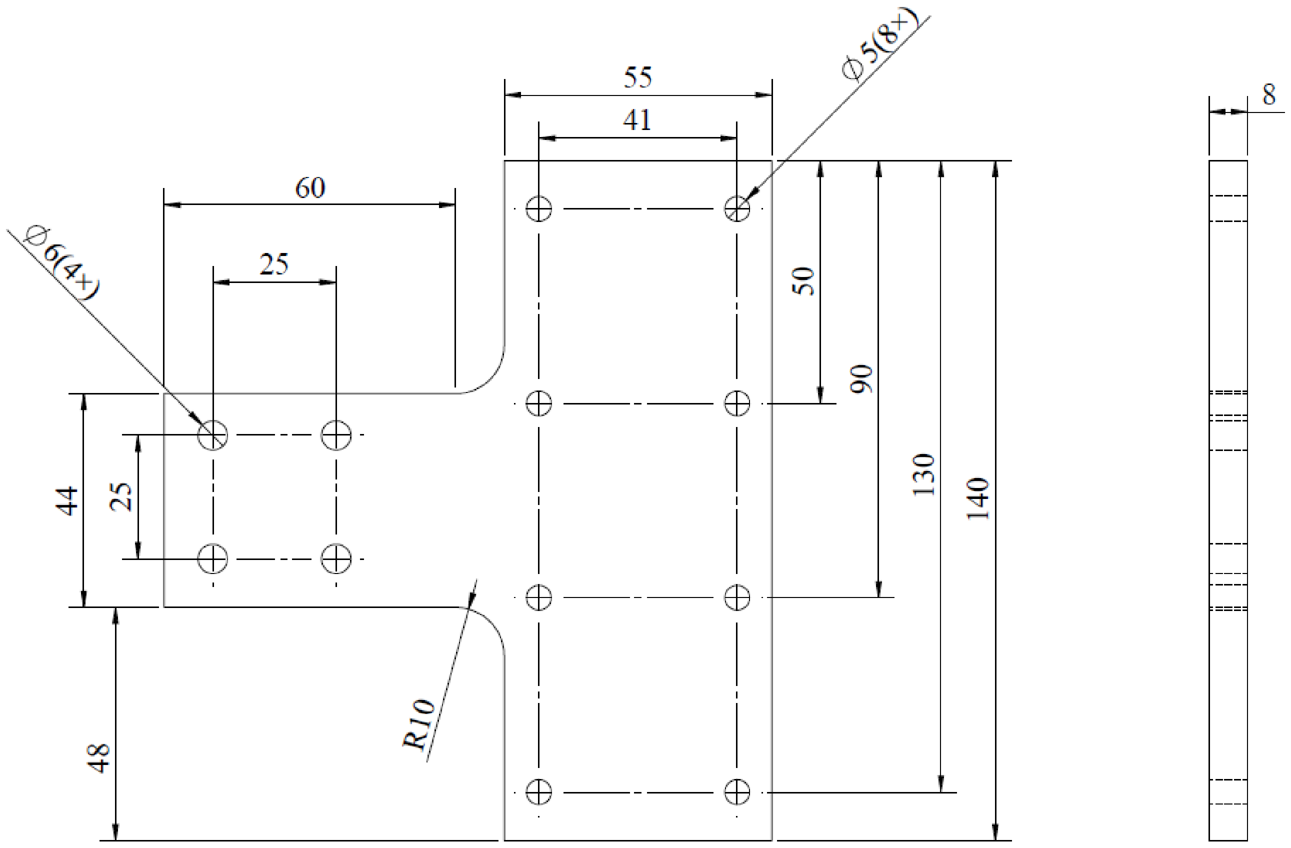

Nobes Lab

Contact: Shadi Ansari
Email: shadi1@ualberta.ca
Phone:
Comments:

UNLESS OTHERWISE SPECIFIED:
DIMENSIONS ARE IN MM
TOLERANCES:
ANGULAR: ± 0.5°
.X = ± 0.25
.XX = ± 0.05
.XXX = ± 0.005
SURFACE FINISH µm 0.6
MATERIAL:
Lab Location:
DO NOT SCALE DRAWING

	NAME
DRAWN	Shadi Ansari
CHECKED	Dr. David S. Nobes
ENG APPR.	
Speed Code	
MecE Job #	
File Name:	window

shadi1
3/17/2021 4:06:33 PM
Wednesday, March 17, 2021

The Department of Mechanical Engineering
UNIVERSITY OF ALBERTA

TITLE:
Optical window access

SIZE **B**
Project: PhD Thesis
REV
SCALE: 1:1
Mass:
SHEET 3 OF 3